MODIFIED FRACTIONAL ORDER SLIDING MODE CONTROL FOR SPEED CONTROL OF PERMANENT MAGNET SYNCHRONOUS MOTOR

FARDILA BINTI MOHD ZAIHIDEE

FACULTY OF ENGINEERING
UNIVERSITY OF MALAYA
KUALA LUMPUR

2020

MODIFIED FRACTIONAL ORDER SLIDING MODE CONTROL FOR SPEED CONTROL OF PERMANENT MAGNET SYNCHRONOUS MOTOR

FARDILA BINTI MOHD ZAIHIDEE

THESIS SUBMITTED IN FULFILLMENT OF THE REQUIREMENTS FOR THE DEGREE OF DOCTOR OF PHILOSOPHY IN ENGINEERING

FACULTY OF ENGINEERING
UNIVERSITY OF MALAYA
KUALA LUMPUR

2020

UNIVERSITI MALAYA

ORIGINAL LITERARY WORK DECLARATION

Name of Candidate: Fardila binti Mohd Zaihidee

Matric No.: 17048411/2 (KHA140070)

Title of Thesis: Modified Fractional Order Sliding Mode Control for Speed Control of

Permanent Magnet Synchronous Motor

Field of Study: Motor drives

I do solemnly and sincerely declare that:

(1) I am the sole author/writer of this Work;
(2) This Work is original;
(3) Any use of any work in which copyright exists was done by way of fair dealing and for permitted purposes and any excerpt or extract from, or reference to or reproduction of any copyright work has been disclosed expressly and sufficiently and the title of the Work and its authorship have been acknowledged in this Work;
(4) I do not have any actual knowledge nor do I ought reasonably to know that the making of this Work constitutes an infringement of any copyright work;
(5) I hereby assign all and every rights in the copyright to this Work to the University of Malaya ("UM"), who henceforth shall be owner of the copyright of this Work and that any reproduction or use in any form or by any means whatsoever is prohibited without the written consent of UM having been first had and obtained;
(6) I am fully aware that if in the course of making this Work I have infringed any copyright whether intentionally or otherwise, I may be subject to legal action or any other action as may be determined by UM.

Candidate's Signature: Date:

Subscribed and solemnly declared before:

Witness's Signature: Date:

Name:
Designation:

Abstract

In recent years, energy saving research activities have focused on electric motors and their systems since they are the main consumer of electricity in the industrial sector. Permanent magnet synchronous motor is known as a high-efficiency motor and slowly replacing induction motors in the industries. For speed control of PMSM, the sliding mode controller (SMC) has been widely used due to its robustness, high accuracy, and simplicity. The main disadvantage of the SMC method is the chattering phenomenon, which should be reduced or eliminated without compromising the controller's robustness. Fractional order sliding mode speed control (FOSMC) of PMSM is proposed in this research to overcome the above-stated problem. This controller incorporates fractional calculus which theoretically has a slower energy transfer compared to integer order calculus in order to suppress the chattering phenomenon. The stability of this controller is analysed using Lyapunov stability theorem. Firstly, the evaluation of the proposed controller is executed by simulation in MATLAB/Simulink environment. Then, a closed-loop PMSM drive prototype is developed to run experimental verification of the control system. The designed FOSMC provides a reference value for the current controller in the inner loop, which will then provide the required reference voltage for the PWM to generate switching signals for the inverter. With speed reference of 500 rpm, transient overshoot of only 8.18% is recorded in the experiment. When a load torque of 0.5 Nm is applied, the PMSM experiences only 9.36% of speed drop and then recovered back to the reference speed after 3.36 seconds. At a steady state, the speed command is tracked with only 1.14% error and low torque ripple of only 3.88%. Performance comparison with IOSMC shows that the proposed FOSMC system experiences up to 5 times less overshoot and up to 60% less speed drop. In addition, FOSMC with PID sliding surface as proposed

resulted in less overshoot of up to 14% and less speed drop of up to 20% compared to FOSMC-PI and FOSMC-PD. In terms of torque ripple, the designed controller outperforms IOSMC and other FOSMCs with up to 7% and 23% less ripple respectively. Similarly, the current ripple of IOSMC is almost double the current ripple of FOSMC. On the other hand, when compared with FOSMC-PD, the proposed system experiences a 10% less current ripple. Simulation and experimental results prove that the proposed FOSMC speed controller performs as a robust and fast anti-disturbance controller to regulate the speed of a PMSM. In addition, it also has shown remarkable performance in terms of transient response and anti-disturbance properties compared to conventional integer order SMC. In its own fractional-order SMC group, the proposed controller has shown its advantages in balancing the individual strength and weaknesses of FOSMC-PI and FOSMC-PD. Small torque and current ripple prove that the chattering phenomenon has been successfully suppressed by this controller design. Hence, the proposed FOSMC is suitable to be used in a high-performance application of PMSM.

Keywords: Fractional calculus, permanent magnet synchronous motor, sliding mode control, speed control.

Abstrak

Kebelakangan ini, aktiviti-aktiviti kajian tentang penjimatan tenaga memfokuskan kepada motor elektrik dan sistem-sistem berkaitan dengannya kerana motor elektrik merupakan pengguna utama tenaga elektrik dalam sektor perindustrian. Motor segerak magnet kekal (PMSM) terkenal sebagai motor yang berkecekapan tinggi dan sedikit demi sedikit menggantikan motor aruhan dalam industri. Untuk mengawal kelajuan PMSM, kawalan mod gelongsor (SMC) telah digunakan dengan meluas kerana keteguhan, ketepatan and keringkasannya. Kekurangan utama kaedah SMC ialah fenomena penggelatukan yang perlu dikurangkan atau disisihkan tanpa menjejaskan keteguhan pengawal tersebut. Satu kawalan mod gelongsor tertib pecahan (FOSMC) untuk PMSM dicadangkan dalam kajian ini untuk menyelesaikan masalah di atas. Pengawal ini menggabungkan kalkulus pecahan yang secara teorinya mempunyai pindahan tenaga yang lebih perlahan berbanding kalkulus integer untuk mengurangkan fenomena penggelatukan. Kestabilan pengawal ini dianalisa menggunakan teorem kestabilan Lyapunov. Pertamanya, penilaian pengawal yang dicadangkan dijalankan melalui simulasi dalam persekitaran MATLAB/Simulink. Kemudian, satu prototaip sistem pandu PMSM lingkaran tertutup telah dibangunkan bagi menjalankan penentusahan sistem pengawal secara eksperimen. Pengawal yang direka bentuk menyediakan nilai rujukan bagi pengawal arus dalam gelung dalaman yang akan menyediakan rujukan voltan yang diperlukan oleh PWM untuk menghasilkan isyarat pensuisan bagi penyongsang. Dengan halaju rujukan sebanyak 500 ppm, hanya 8.18% lajakan fana direkodkan dalam eksperimen. Apabila tork beban sebanyak 0.5 Nm dikenakan, PMSM tersebut hanya mengalami 9.36% susut halaju dan kemudian pulih kembali kepada halaju rujukan selepas 3.36 saat. Pada keadaan mantap, halaju rujukan dituruti dengan hanya 1.14% ralat dan hanya 3.88% riak tork. Perbandingan prestasi dengan IOSMC menunjukkan bahawa

sistem FOSMC yang dicadangkan mengalami sehingga 5 kali kurang lajakan dan sehingga 60% kurang susut halaju. Tambahan pula, FOSMC dengan permukaan gelongsor PID seperti yang dicadangkan menghasilkan sehingga 14% kurang lajakan dan 20% kurang susut halaju berbanding FOSMC-PI dan FOSMC-PD. Dari segi riak tork, pengawal yang direka bentuk mengatasi IOSMC dan FOSMC yang lain dengan sehingga 7% dan 23% kurang riak masing-masing. Demikian juga, riak arus IOSMC ialah hampir dua kali ganda riak arus FOSMC. Selain itu, apabila dibandingkan dengan FOSMC-PD, sistem yang dicadangkan mengalami 10% kurang riak arus. Keputusan simulasi dan eksperimen membuktikan bahawan pengawal yang dicadangkan telah menjalankan fungsi sebagai pengawal yang teguh dan anti-gangguan pantas untuk mengawal atur kelajuan sesebuah PMSM. Tambahan pula, ia menunjukkan prestasi luar biasa dari segi sambutan fana dan sifat anti-gangguan berbanding pengawal SMC tertib integer konvensional. Dalam kumpulan tertib pecahan SMC, pengawal yang dicadangkan telah menunjukkan kelebihan dalam mengimbangi kekuatan dan kelemahan individu FOSMC-PI dan FOSMC-PD. Riak tork dan riak arus yang kecil membuktikan bahawa fenomena penggelatukan telah berjaya dikurangkan oleh reka bentuk pengawal ini. Oleh itu, FOSMC yang dicadangkan sesuai untuk digunakan dalam aplikasi PMSM berprestasi tinggi.

Kata kunci: Kalkulus pecahan, motor segerak magnet kekal, kawalan mod gelongsor, kawalan kelajuan

ACKNOWLEDGEMENTS

Table of Contents

List of Figures

List of Tables

List of Symbols

α	Order of fractional integral sliding surface
a,b,c,p,q,j,K	Scalar coefficients in various sliding mode control
arg(.)	Argument of a complex number
A	n-by-n matrix
A_n, B_n	n-th quadrature signal
A_{n-1}, B_{n-1}	(n-1)-th quadrature signal
β	Order of fractional derivative sliding surface
B_m	Viscous friction coefficient
$C(s)$	Crone formula
$\Delta a, \Delta b, \Delta c$	Time-varying value of system parameters
$d-q$	Direct-quadrature
$_a D_t^r$	Fundamental operator of fractional calculus
δ	Torque angle
$\delta(t)$	Lumped uncertainty
$e(t)$	Tracking error
$eig(.)$	Eigenvalue of a matrix
$\Gamma(.)$	Gamma function
i_d	d-axis current
i_d^*	Reference d-axis current
i_q	q-axis current
$i_q^*, i_{q,ref}$	Reference q-axis current
I_{df}	Equivalent d-axis magnetizing current
$I_{\max}$	Maximum current
J	Moment of inertia
k	Constant in *nid* block
k_d	Derivative coefficient of fractional order sliding surface
k_i	Integral coefficient of fractional order sliding surface
k_p	Proportional coefficient of fractional order sliding surface
K_e	Back-emf constant

K_t	Torque constant
L_d	Direct axis inductance
L_{md}	d-axis mutual inductance
L_q	Quadrature axis inductance
λ_d	d-axis stator flux linkage
λ_q	q-axis stator flux linkage
M_0	Continuous stall torque
n	Parameter in *nid* block
$n_{\max}$	Maximum mechanical speed
n_p	Pole pair
n_s	Synchronous speed
Ω	Bound for lumped uncertainty
p	Number of poles
P_N	Nominal output power
$PI\_K_p\_d$	Proportional coefficient of d-axis current PI controller
$PI\_K_p\_q$	Proportional coefficient of q-axis current PI controller
$PI\_K_i\_d$	Integral coefficient of d-axis current PI controller
$PI\_K_i\_q$	Integral coefficient of q-axis current PI controller
r	Order of fractional calculus
$\mathbb{R}$	Real numbers
$\mathbb{R}^+$	Positive real numbers
R_s	Stator resistance
$s, s(x), s(t)$	Sliding surface
$s^{(n-1)}(t)$	n-th derivative of sliding surface
$\dot{s}$	Time derivative of sliding surface
$sign(.)$	Sign function
T_L	Load torque
T_e	Electric torque
T_p	PWM period
T_s	Sampling time

T_{si}	Delay time constant
T_{sw}	Switching time constant
τ_d	d-axis electrical time constant
τ_q	q-axis electrical time constant
θ_e	Electrical angle
θ_m	Mechanical angle
u_d^*	d-axis stator voltage
u_q^*	q-axis stator voltage
$U_{\max}$	Maximum voltage
v	Order of fractional calculus in *nid* block
$V, V(t)$	Lyapunov candidate function
$\dot{V}$	Time derivative of Lyapunov candidate function
V_{dc}	Direct current voltage
V_{rms}	Root mean square voltage
ω_e	Electrical speed
ω_f	Inverter frequency
ω_m	Mechanical speed
ω_r	Rotor speed
ω_r^*	Reference/command speed
$\dot{\omega}_r$	Time derivative of rotor speed
w, k_s	Control law coefficients

List of Abbreviations

AC	Alternating current
ADC	Analog/Digital Converter
AI	Artificial intelligence
B-H	Magnetic energy product
BCLK	Bus clock
BLDC	Brushless DC
CFTSMC	Continuous fast terminal SMC
CMOS	Complementary Metal Oxide Semiconductor
CPU	Central processing unit
CSI	Current source inverter
CTA	Constant torque angle
DAC	Digital/Analog Converter
DC	Direct current
DOB	Disturbance observer
DRAM	Dynamic random-access memory
DSP	Digital signal processor
DTC	Direct torque control
EMDS	Electric motor driven system
EMF	Electromotive force
EPS	Electric power steering
ESMDO	Extended sliding mode disturbance observer
ESO	Extended state observer
F	Objective function
FIFO	First in first out
FLIS	Fuzzy logic inference scheme
FOC	Field oriented control
FOSMC	Fractional order sliding mode control
FOSMC-PI	FOSMC with PI sliding surface
FOSMC-PD	FOSMC with PD sliding surface
FOSMC-PID	FOSMC with PID sliding surface
FNN	Fuzzy neural network
GA	Genetic algorithm
GL	Grunwald-Letnikov

HOSMC	Higher order sliding mode control
IAE	Integral of absolute error
IEC	International Electrotechnical Commission
IGBT	Insulated-gate bipolar transistor
IOSMC	Integer order SMC
IPMSM	Interior permanent magnet synchronous motor
ISE	Integral of squared error
ISMC	Integral sliding mode control
ITAE	Integral of time-weighted absolute error
LC	Inductor-Capacitor
MLI	Multilevel inverter
NdBFe	Neodymium-Boron-Iron
NFC	Neuro-fuzzy controller
NFTSM	Non-singular fast terminal sliding mode
NN	Neural network
NPC	Neutral-point clamped
NSFT	Non-singular fast terminal
NTSM	Non-singular terminal sliding mode
PC	Personal computer
PCI	Peripheral Component Interconnect
PD	Proportional-derivative
PI	Proportional-integral
PID	Proportional-integral-derivative
PMSM	Permanent magnet synchronous motor
PPC	Power PC
PSO	Particle swarm optimisation
PWM	Pulse width modulation
RFNN	Recurrent fuzzy neural network
RL	Riemann-Liouville
RMS	Root mean square
SMC	Sliding mode control
SNTSMO	Second-order non-singular terminal sliding mode observer
SOSMC	Second order sliding mode control
SPWM	Sinusoidal pulse width modulation
T-NPC	T-type neutral-point clamped

TSM	Terminal sliding mode
TSMC	Terminal SMC
TTL	Transistor-Transistor Logic
UART	Universal Asynchronous Receiver/Transmitter
USSR	Union of Soviet Socialist Republics
VFD	Variable frequency drive
VSI	Voltage source inverter
VSS	Variable structure system
WFNN	Wavelet fuzzy neural network
WNN	Wavelet neural network

CHAPTER 1: INTRODUCTION

1.1   Research Background

World energy demand has shown significant growth in recent years. An increase of about 48% of total world consumption of marketed energy is projected in 28 years period between the year 2012 and 2040. The industrial sector has been the main consumer of delivered energy and this trend will continue at least until the year 2040. World electricity consumption in 2016 by industries was reported at about 54% which is approximately 65000 TWh. The average increment of energy consumption by the world's industrial sector is forecasted at 1.2% annually (Energy, 2016).

The largest end-user of electricity is electric motor driven systems (EMDS). These systems consume around 43-46% of total global electricity consumption, which is twice as much as the second largest end-user (lighting). EMDS is widely used in industries and consumes 69% of electricity within its sector. Other than the industrial sector, EMDS is also significantly employed in another three sectors which are commercial, residential and transport/agricultural sectors with 38%, 22% and 39% of the sector's electricity consumption respectively. Electricity used by an EMDS is mainly consumed by the electric motors inside the system, which convert electrical power into mechanical power. Almost one-third of electricity demand by electric motors is consumed by medium-sized motors with output power ranging from 0.75 to 375kW (Waide & Brunner, 2011).

Energy saving for EMDS does not lie only on the motor itself but in various areas of EMDS implementation. Electric motor applications usually have long operating hours but with variable loads. Traditionally, to cater to load variations, artificial brakes (e.g. control valves, dampers, throttles) and on/off cycle were used. Nowadays, motor control

technology with variable frequency drive (VFD) allows a more efficient and stable system that runs with modulation. Four main components of VFD system as shown in Figure 1.1 are electric machines as categorised in Figure 1.2, power converters (rectifiers, choppers, inverters, cycloconverters), controllers (to match the motor and power converter to meet the load requirements) and load (Krishnan, 2001).
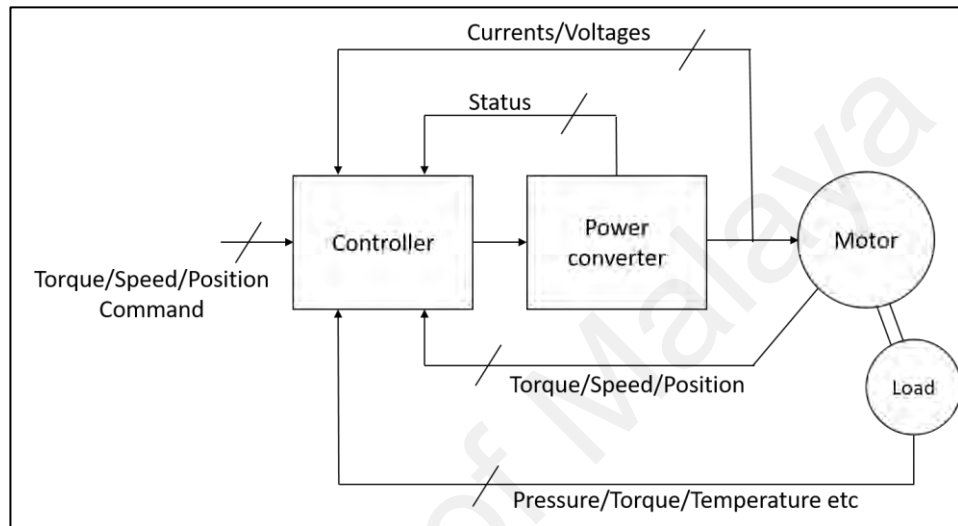
Figure 1.1: Motor drive schematic (Krishnan, 2001)
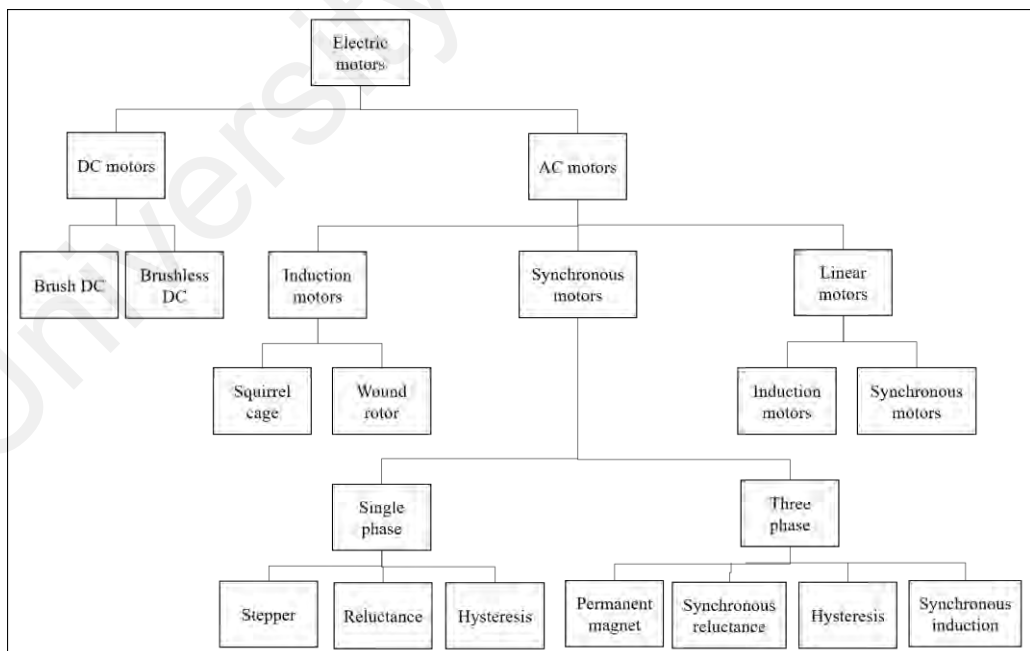
Figure 1.2: Electric machines categories

1.1.1 Permanent Magnet Synchronous Motors

Nowadays, electrical AC machines have been widely used especially in industries. Electrical AC drives are developed for various applications such as robot manipulators, conveyor belts, material processing lines, mills, etc. The invention of permanent magnet material, Alnico, in 1930 triggered the development of permanent magnet synchronous motors. Characteristics of large coercive force and high reminiscence are desirable in permanent magnets in order to avoid demagnetization during start and short conditions of motors and to obtain maximum air gap flux density respectively. Neodymium-Boron-Iron (NdBFe) is the most used permanent magnet material since it has 50 times higher B-H energy compared to Alnico (Abu-Rub, Iqbal, & Guzinski, 2012).

Permanent magnet synchronous motor (PMSM) has similar stator construction as in induction motors and similar field excitation concept as in brushless DC (BLDC) motor but has back EMF of sinusoidal type. The rotor consists of permanent magnets, which generate a substantial air gap magnetic flux. The electromagnetic torque of PMSM is proportional to stator-rotor flux linkages angle. Categorization of PMSM is done in terms of how the permanent magnets are mounted; surface-mounted or interior-mounted (Figure 1.3). For surface mounted PMSM, permanent magnets are mounted on the rotor surface. Their advantages lie on the ease of manufacture and cogging torque minimization. Interior permanent magnet synchronous motor (IPMSM) has magnets buried in the rotor core. PMSM design of this manner exhibits small effective air gap, robust rotor construction and non-salient rotor. The complex geometry of their rotors ensures the optimal usage of costly permanent magnet materials without jeopardizing the high magnetic field in the air gap (Uddin, Abido, & Rahman, 2004). Regardless of the magnet mounting manner, they have the same basic operating principle. The difference,

however, lies in the direct (L_d) and quadrature (L_q) axes inductance values. Surface mounted PMSM has $L_q = L_d$, whereas interior PMSM has $L_q > L_d$ (Krishnan, 2001).
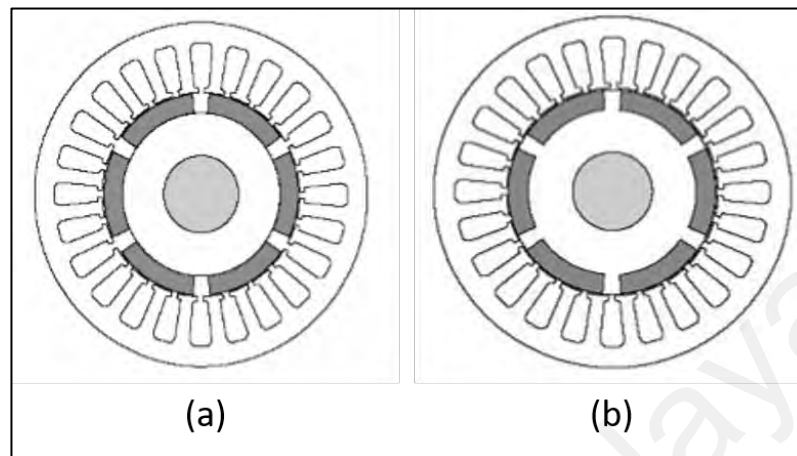
Figure 1.3: (a) Surface mounted PMSM (b) Interior PMSM (Krishnan, 2001)

VFD of permanent magnet synchronous motor system has become more popular in recent years compared to induction motor systems. The low maintenance properties of PMSM is a plus point in energy saving. PMSMs are widely used in low to mid-power applications and high-performance drives e.g. robotics, electric vehicles and machine tools. They are preferred over brush-type motors and gradually replacing induction motors in various fields of application due to its advantages such as compact structure, high air-gap flux density, high power density, high torque to inertia ratio, and high efficiency. However, the PMSM system is nonlinear and consists of time-varying parameters with high-order complex dynamics (Pillay & Krishnan, 1989; Shihua, Mingming, & Xinghuo, 2013).

In terms of AC machines control, various strategies have been established, as presented in Figure 1.4. Scalar-based controls offer easy implementation but result in sluggish dynamics. The vector control approach, combined with closed-loop feedback control, is preferable to obtain good dynamics and steady-state response. Field-oriented control (FOC) of PMSM is in the spotlight for many researchers in recent years. This

4

technique simplifies motor modelling, hence resulting in simplified controller design. Stator current is decoupled into torque and flux producing components to allow independent control of both parameters as in DC motors (Abu-Rub et al., 2012). FOC is used to achieve smooth starting, good acceleration and fast four-quadrant operation (Huang, Li, Teng, & Liu, 2012; B. Zhang, Pi, & Luo, 2012). Compared to the direct torque control (DTC) method, the FOC approach results in lower torque and current ripple (Garcia, Zigmund, Terlizzi, Pavlanin, & Salvatore, 2011; Maleki, Pahlavani, & Soltani, 2015). Hence, FOC approach is used in this research.
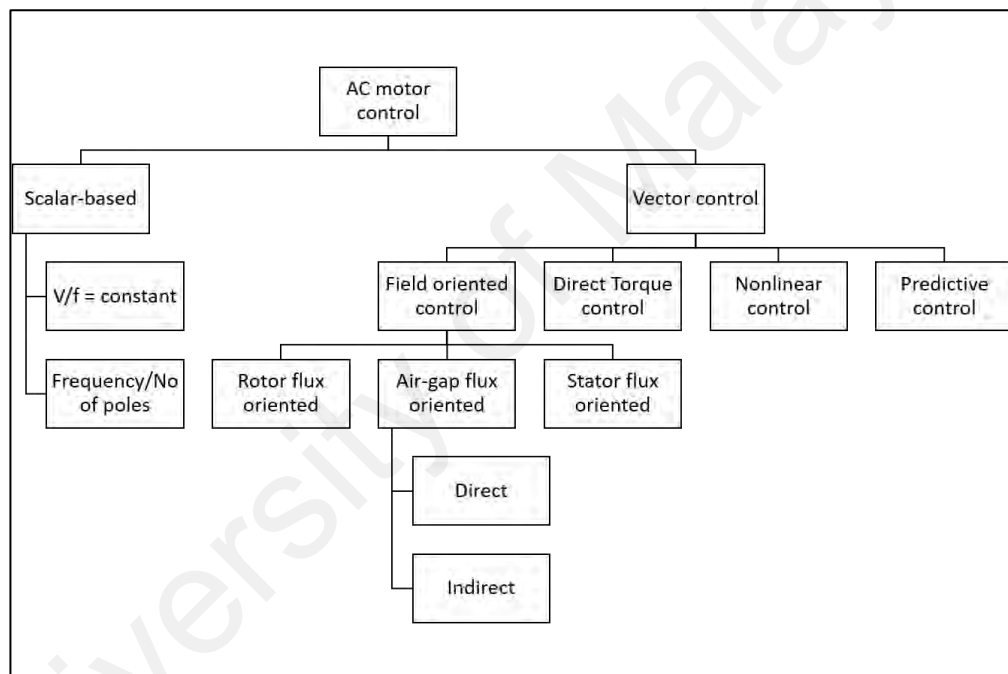
Figure 1.4: AC motor control strategies

1.1.2   Sliding Mode Control

Sliding mode control (SMC) is a class of variable structure systems (VSS). Its theory was originated in the late 1950s in the former USSR by Prof. V. I. Utkin and Prof. S. V. Emelyanov (Hung, Gao, & Hung, 1993; V. Utkin, 1977). The key idea of SMC is to reduce the complexity of high order systems to first order state variables namely the sliding function and its derivative (Fallaha, Saad, Kanaan, & Al-Haddad, 2011).

Designing a SMC requires two major steps; firstly, sliding surface design and secondly, control input design, so that sliding mode reaching condition is satisfied as in equation (1.1) and the system's state trajectory is forced towards the designed surface (Xiaoguang, Lizhi, Ke, & Li, 2013). Sliding surface design is crucial in SMC since the plant's dynamics e.g. stability to the origin, tracking and regulation that are restricted to the surface represent the controlled system's behaviour. Sliding surface or manifold defines the rule for switching in SMC. Once intercepted, the plant's state trajectory will maintain on the surface for all subsequent time and slide along this surface (Levine, 2010). The system trajectories when 'sliding' along the manifold $s(x) = 0$ is described by the equivalent control law (Vadim Utkin, Guldner, & Shi, 1999). Ideal sliding mode describes a sliding motion that occurs exactly on the sliding manifold, whereas in real sliding mode, the sliding motion takes place in a vicinity of the sliding manifold called boundary layer due to non-idealities of the control law implementation.

$$s \cdot \dot{s} < 0 \qquad (s \text{ is the sliding mode surface}) \qquad (1.1)$$

Challenges in SMC design are to ensure convergence of system state to the sliding surface, to ensure control target achieved on sliding surface (i.e. error converge to zero, ensure robustness), to minimize reaching phase and to reduce chattering during the sliding mode. Lyapunov stability analysis is widely used to analyse the stability of the developed SMC controllers, where the stable convergence property is proven and evaluated. Several Lyapunov functions were chosen by researchers to be employed in the analysis, but typically the function in equation (1.2) is chosen (Eker, 2010; B. Zhang et al., 2012) with the condition in equation (1.3). Reaching condition is satisfied when the condition in equation (1.4) is met.

$$V(t) = \frac{1}{2} s^2(t) \qquad (1.2)$$

$$V(0) = 0 \text{ and } V(t) > 0 \text{ for } s(t) \tag{1.3}$$

$$\dot{V}(t) = s(t)\dot{s}(t) < 0 \tag{1.4}$$

SMC has been successfully implemented in many fields (Bao-Lin, Qing-Long, Xian-Ming, & Xinghuo, 2014; Chih-Lyang, Li-Jui, & Yuan-Sheng, 2007; Chuan-Kai, 2006; Han & Lee, 2015; Jeng-Dao, Suiyang, & Zhi-Bin, 2013; Rong-Jong, Kun-Lun, & Jeng-Dao, 2010; Syuan-Yi & Faa-Jeng, 2011) and applied to many machine types e.g. induction motor (El-Sousy, 2013; Faa-Jeng, Chih-Kai, & Po-Kai, 2007; Rong-Jong et al., 2010; Veselic, Perunicic-Drazenovic, & Milosavljevic, 2010), linear variable reluctance motor (Pupadubsin et al., 2012) and brushless DC motor (Jian-Bo & Bing-Gang, 2009; Yaonan, Xizheng, Xiaofang, & Guorong, 2011).

1.2 Problem Statement

High performance application of PMSM requires its speed controller to result in fast response, precise tracking, small overshoot and strong disturbance rejection ability. Linear control algorithms e.g. PI controller has been widely used for speed control of PMSM, but the performances were unsatisfactory in terms of tracking ability and robustness (Gou-Jen, Chuan-Tzueng, & Chang, 2001). Hence, robust nonlinear control methods have been proposed and used to enhance the speed control performance of PMSM. These methods include sliding mode control (El-Sousy, 2011; Shihua et al., 2013; Shihua Li, Kai Zong, & Huixian Liu, 2011; Xiaoguang et al., 2013; B. Zhang et al., 2012), predictive control (Errouissi, Ouhrouche, Wen-Hua, & Trzynadlowski, 2012; Huixian & Shihua, 2012), backstepping control (J. Zhou & Wang, 2002), adaptive control (Han Ho, Nga Thi-Thuy, & Jin-Woo, 2011; Shihua & Zhigang, 2009; Vu, Choi, & Jung, 2012; J. Zhou & Wang, 2002), H∞ control (Hsien, Sun, & Tsai, 1997), automatic disturbance

7

rejection control (Su, Zheng, & Duan, 2005) and artificial intelligence incorporated controllers (El-Sousy, 2011; Han Ho & Jin-Woo, 2013).

The sliding mode controller has been widely used for speed control of PMSM. Sliding mode control is well known as a robust control method, which can guarantee excellent tracking although the system is exposed to internal parameter variations and external disturbances. Other remarkable features of SMC are its high accuracy and simplicity. The main disadvantage of the SMC method is the chattering phenomenon originated from high frequency switching near the sliding surface by discontinuous control law in SMC design and from parasitic dynamics interactions (Shihua et al., 2013; B. Zhang et al., 2012). Chattering can affect the system in terms of reducing control accuracy, resulting in high heat losses in electrical power circuits and high wear of moving mechanical parts (V. I. Utkin, 1993). On top of that, in the control of electrical machines, the chattering effect can cause unwanted vibrations in the rotor movement.

In order to successfully utilize the advantages of SMC in terms of robustness and simplicity, chattering effects in SMC should be eliminated or significantly reduced to obtain excellent control accuracy. The challenge in doing so lies in how robustness and chattering effect are closely related to each other, where robustness is jeopardized in order to suppress the chattering and vice versa. Recent research on SMC is focusing on SMC enhancement methods to balance both properties to come out with a robust, chattering-free sliding mode controller.

Several methods have been proposed to enhance SMC for speed control of PMSM. Reaching law method is used to minimize chattering at the end of the reaching phase. However, modification of control law in this approach can affect speed tracking in terms of steady-state error and reaching time (Lin, Hung, & Ruan, 2014; Xiaoguang et

al., 2013). Higher order SMC method aims to reduce chattering by characterizing system dynamics near the sliding surface, but its disadvantage lies in practical implementation due to measurement noise (Bartolini, Pisano, Punta, & Usai, 2003). Another way to enhance SMC is by designing composite SMC. Disturbance compensation mechanism is incorporated so that smaller switching gain can be chosen for the SMC and allow suppression of chattering. The main drawback of this method is its high dependency on the accuracy of the disturbance estimation algorithm used for compensation. In other works, artificial intelligence-based composite SMC is designed. However, for precise tracking, this method makes the system suffer from computational load due to parameter adjustments and intensive membership functions (Kuo, Hsu, & Tsai, 2007).

Another method proposed for PMSM sliding mode speed controller enhancement is sliding surface design modification. In this method, behaviour of control law of SMC is modified according to the system's dynamics determined by sliding surface design. Many designs have been proposed by previous researchers. One of them is integer order integral SMC, which aims to eliminate reaching phase and enforces sliding phase throughout the entire system response. Therefore, not only speed tracking properties is improved but also chattering is reduced due to smaller gain selection during sliding phase (Liang, Ting, & Lin, 2012).

In this research, the performance of integer order integral SMC (Zaky, 2012) is further enhanced by incorporating fractional calculus into the sliding surface. The proposed fractional order sliding mode speed controller is designed with a sliding surface that consists of both fractional differentiation and integration. Fractional order term provides an extra degree of freedom for the SMC which improves its robustness and accuracy. On top of that, properties of fractional calculus in fractional order SMC contributes to chattering reduction.

9

1.3   Research Objectives

The work aims to develop a robust speed control of a PMSM. The proposed sliding mode controller should enable the machine to track a given reference speed in any conditions of uncertainties and external disturbances. The specific project objectives are defined as follows:

a) To design a fractional order sliding mode controller for speed control of PMSM and prove the stability of the designed controller

b) To develop a closed-loop PMSM drive prototype

c) To validate the proposed control strategy using MATLAB/Simulink simulation and verify the simulation result experimentally

1.4   Scope and limitations

Scope and limitation of this work can be classified into two categories. Firstly, in terms of control, this work is limited to speed control of permanent magnet synchronous motor with encoder feedback data. Position control and sensorless control of PMSM are not considered. In addition, field-oriented approach with constant torque angle (CTA) strategy is used in this work. Hence, direct torque control approach and field weakening strategy are not within the scope of this work. Secondly, in terms of PMSM type, performance of the proposed control strategy is validated using interior type, Class I category of PMSM. Performance validation for surface-mounted and Class II-IV PMSMs is out of this work's scope.

1.5   Thesis Outline

The complete thesis has a total of five chapters. In Chapter 2, a comprehensive review of sliding mode control enhancement methods for PMSM control is presented. Other than that, previous works on fractional calculus application in control design state-of-the-art implementation of fractional order SMC is also discussed. In addition, inverter topologies proposed for application in the PMSM drive system are reviewed and compared.

Chapter 3 presents the controller design, stability analysis and methodology used in this research. Firstly, the PMSM mathematical model based on field-oriented control is presented. Secondly, the controller is designed based on fractional calculus and sliding mode control theories, where a control law is derived. Stability analysis is executed based on Lyapunov stability theorem. Methodology for controller programming in MATLAB/Simulink simulation is also detailed. In addition, components of the developed closed loop PMSM drive system prototype for experimental verification are thoroughly presented.

Chapter 4 is comprised of simulation and experimental results. In this chapter, the performance of the proposed controller as a robust anti-disturbance speed control of PMSM is presented. Its performance is also compared with a few relevant controllers to show its advantages against the other controllers in terms of robustness, response and torque ripple. The verification of simulation results through the experiment is also presented.   In this chapter, the obtained results are also analysed and discussed. Remarkable properties of the proposed controller are summarized and compared with relevant previous works.

Finally, Chapter 5 presents the research conclusions. Future works on this research are also explained. The outline of this thesis is summarized in the form of a flowchart, as shown in Figure 1.5.
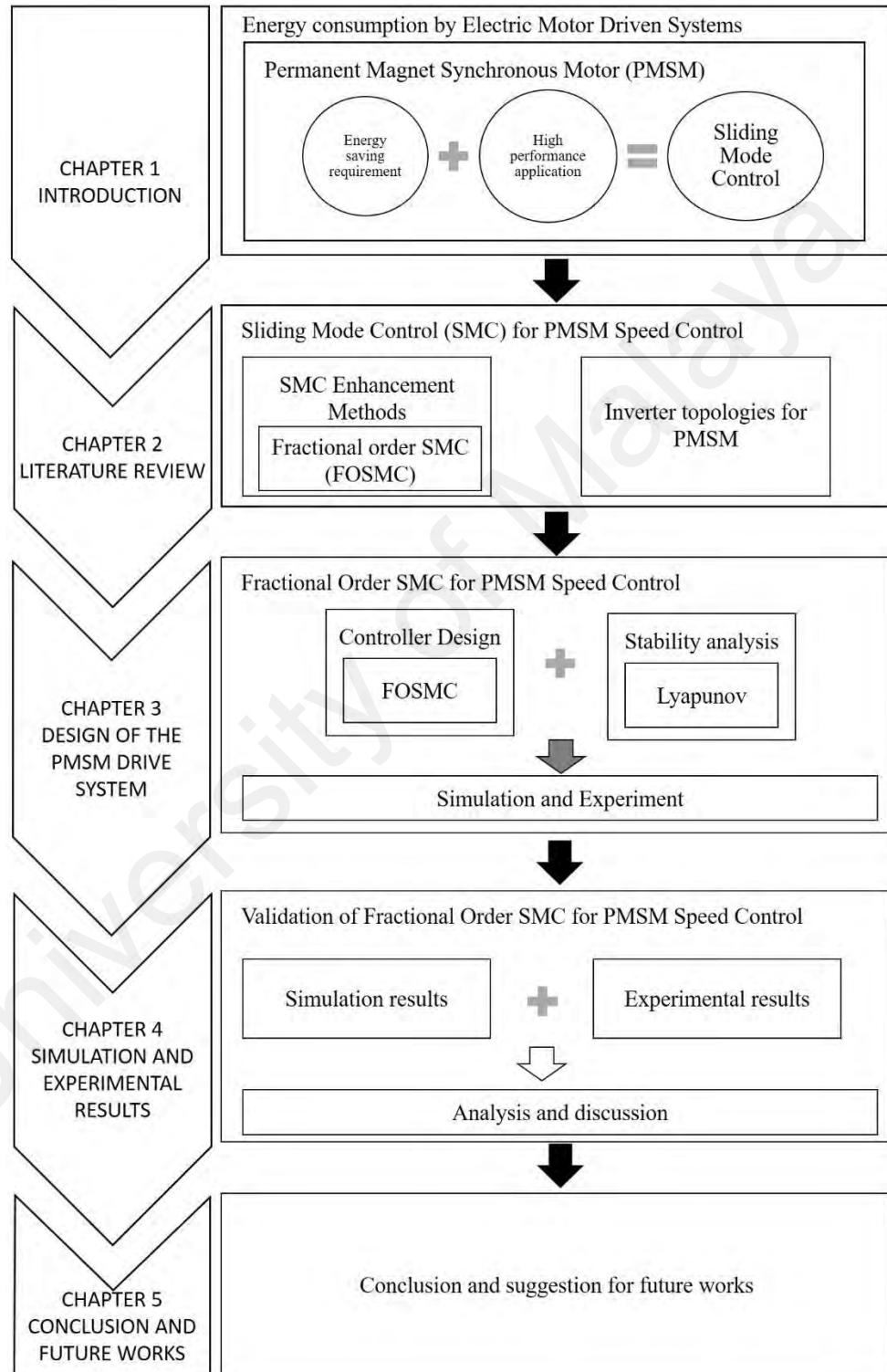
Figure 1.5: Summary of thesis outline.

CHAPTER 2: LITERATURE REVIEW

2.1   Introduction

A comprehensive critical literature review is presented in this chapter to demonstrate various sliding mode controller enhancements that led to the present standing of SMC for PMSM speed control. Conventional SMC is enhanced to improve controller's robustness and reduce chattering effect of SMC. Among the discussed methods, fractional order SMC (FOSMC) is introduced based on fractional calculus theory. FOSMC characteristics and state-of-the-art implementations are elaborated. In addition, inverter topologies employed for PMSM are reviewed.

2.2   Sliding Mode Controller Enhancement in PMSM Speed Control

The performance of sliding mode controllers as a robust control method for PMSM speed control has been proven in many previous works. However, chattering phenomena remains a crucial issue to be solved in this variable structure control. Researchers have proposed various methods to overcome this chattering issue, whereby in doing so, the controller's performance in terms of disturbance rejection properties and/or tracking are also affected, either in an advantageous or deteriorative way. SMC enhancement methods proposed in previous works for PMSM speed control are summarized in Figure 2.1 and discussed further in Subsection 2.2.1 until 2.2.5. Sensorless PMSM control is not considered in this work.
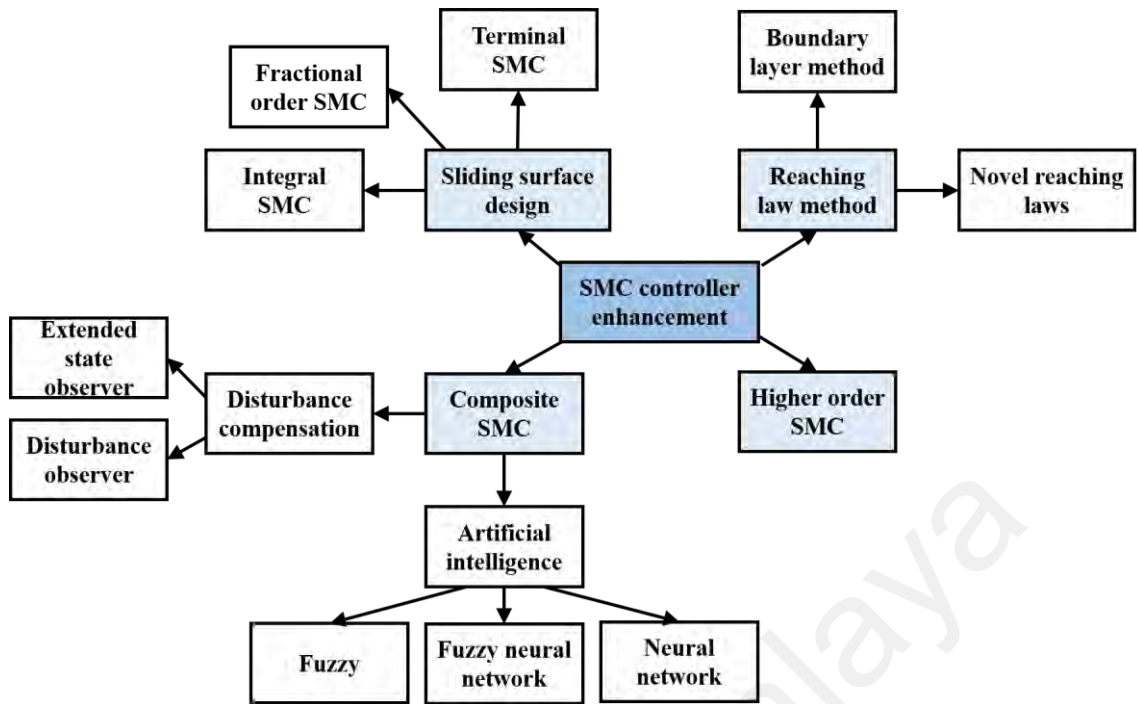
Figure 2.1: SMC enhancement methods for PMSM speed control

2.2.1 Reaching Law Method

One of the common methods to improve SMC is the reaching law method. In the sliding mode control theory, reaching law is the differential equation that specifies the dynamics of switching around the sliding surface. Conventionally, for PMSM speed control, a constant rate signum function is used as reaching law (Y. Zhao & Dong, 2019). The performance of SMC designed using this reaching law is highly dependent on the constant parameter chosen, where good tracking performance causes the system to suffer from large chattering as well and vice versa (Xiaoguang et al., 2013). A constant and proportional rate reaching law is proposed to solve this issue. With this design, the state is forced to approach the switching manifolds faster when s is large (Xudong Liu & Li, 2018).

2.2.1.1 Boundary Layer Method

The boundary layer method is proposed to replace the conventional sign function to further improve non-ideal reaching at the end of reaching phase. In this method, a thin boundary layer, Ω, is introduced around the sliding surface. When the state trajectories lie within this layer, the smooth approximation is obtained using either saturation function (Delavari, Ghaderi, Ranjbar, & Momani, 2010; Z. Zhou, Zhang, & Mao, 2018) or hyperbolic tangent function (Eker, 2010) to alleviate chattering. However, this method can sacrifice the system's anti-disturbance performance (Shihua et al., 2013) and causes steady-state error depending on boundary layer selection (Lin et al., 2014).

2.2.1.2 Novel Reaching Law Method

Apart from the boundary layer method, several works have proposed their own novel reaching law to come out with a chattering-free sliding mode controller. Instead of using a constant gain like reaching laws mentioned above, an adaptive gain is incorporated by Ke, Xiao-guang, Li, and Chang (2011). The gain consists of the absolute value of system state variable term and reaching law is designed so that the speed of convergence depends on the distance of state variables from the sliding surface. When the sliding surface is reached, the trajectory will become stable and low convergence speed allows the chattering phenomenon to be suppressed. However, in an effort to solve the chattering issue, the performance of SMC with this reaching law design becomes unsatisfactory as the state approaches the sliding surface, where reaching time increases and controller robustness is reduced (Xiaoguang et al., 2013).

To overcome this unbalance, another reaching law with gain adaptive to system state variables is proposed by Xiaoguang et al. (2013). As system states approaching the sliding surface, this design decreases not only the gain but in addition, it also gradually

decreases the width of the sliding mode band to suppress chattering without affecting the performance of the controller. Figure 2.2 shows the switching band around the sliding surface narrows down to almost zero at the equilibrium point in SMC with this reaching law compared to constant band width in conventional reaching law. As a result, under disturbance-free conditions, chattering suppression of more than 50% and 90% improvement in convergence rate was recorded.
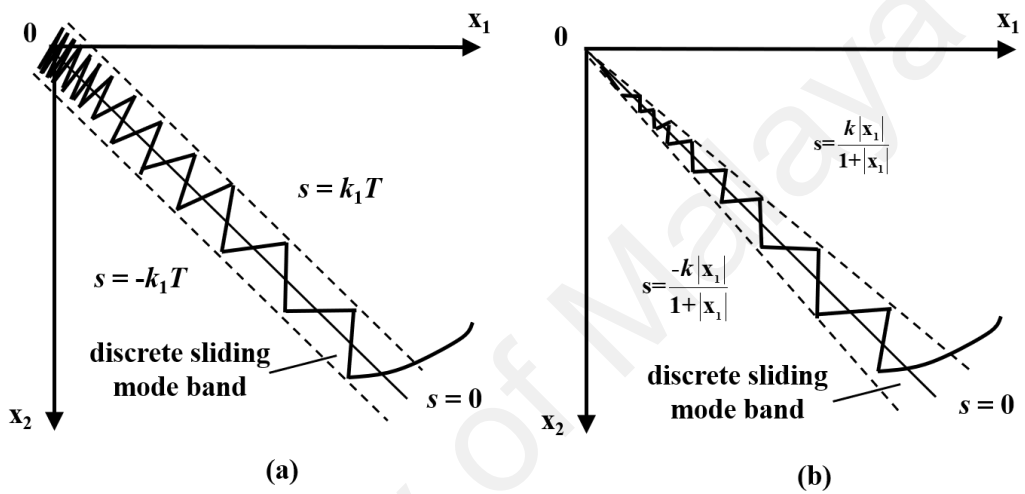
Figure 2.2: Sliding mode band of (a) conventional reaching law and (b) novel reaching law (Xiaoguang et al., 2013).

Last but not least, another novel reaching law was proposed by Xiaoguang Zhang, Zhao, and Sun (2011). In their design, sign function is omitted and replaced with a terminal attractor term. However, the chattering reduction was not clearly quantitatively documented and compared. Finally, a comparison of reaching law designs in the PMSM sliding mode speed controller is detailed in Table 2.1.

Table 2.1: Comparison of reaching laws in SMC for PMSM speed control

Reaching law design		Convergence rate	Adaptive gain	Chattering reduction ability	Smooth switching pattern
Conventional	Constant rate (Y. Zhao & Dong, 2019)	Low	No	No	No
	Constant and proportional rate (Xudong Liu & Li, 2018)	Medium	No	No	No
Boundary layer method	Saturation function (Z. Zhou et al., 2018)	Medium	No	Low	Yes
	Hyperbolic tangent function (Eker, 2010)	Medium	No	Low	Yes
Novel reaching law method	Proposed by Ke et al. (2011)	Medium	Yes	High	No
	Proposed by Xiaoguang et al. (2013)	Adaptive	Yes	High	No
	Proposed by Xiaoguang Zhang et al. (2011)	Adaptive	Yes	High	No

2.2.2 Higher Order SMC

Apart from the reaching law method, conventional SMC is also enhanced with higher order SMC design. Higher order sliding mode control (HOSMC) was first introduced by Levant (1993). In higher order SMC, control input acts on higher derivatives of the sliding surface, compared to on the first derivative in first order SMC. A sliding mode is defined as an n-th order sliding mode when equation (2.1) is satisfied (Eker, 2010). The n-th derivative is predominantly supposed to be discontinuous or non-existent (Levant, 2007). The sliding order, n characterizes the system dynamics in the

vicinity of the sliding mode in terms of the degree of smoothness (Bartolini, Ferrara, Levant, & Usai, 1999).

$$s(t) = \dot{s}(t) = ... = s^{(n-1)}(t) = 0 \qquad (2.1)$$

When compared to first order SMC, HOSMC provides smoother control, better performance in terms of switching delays in control implementation, eliminates the requirement of derivative information for the control and is better in chattering effects suppression while still preserving the main advantages of the conventional SMC approach in terms of robustness and easiness of implementation (Khan & Spurgeon, 2006; Levant, 1993; Xinghuo & Kaynak, 2009). On the other hand, the challenge in HOSMC lies in the usage of differentiators, where their practical behaviour requires particular care in real implementation due to measurement noise. The deteriorative effects on overall closed-loop performance increase dramatically with the number of differentiation stages (Bartolini et al., 2003).

Second order SMC (SOSMC) is the most common HOSMC design. Its control acts on the first derivative of the sliding surface and the sliding phase occurs when both sliding surface, *s* and its derivative is zero, as shown in equation(2.2), with its trajectory illustrated in Figure 2.3.

$$s(t) = \dot{s}(t) = 0 \qquad (2.2)$$
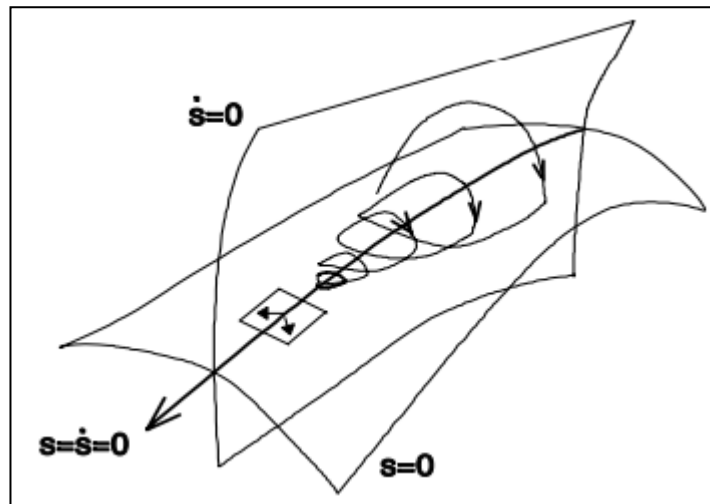
Figure 2.3: Second order sliding mode trajectory (Bartolini et al., 1999)

Different algorithms have been proposed in literature to ensure SOSMC finite time convergence to zero such as suboptimal (Matraji, Laghrouche, Jemei, & Wack, 2013), twisting, super-twisting (Bounasla & Hemsas, 2013; Damiano, Gatto, Marongiu, & Pisano, 2004), drift and algorithm with a prescribed law of variation of s (Bartolini et al., 1999). Phase trajectories of these algorithms are shown in Figure 2.4.
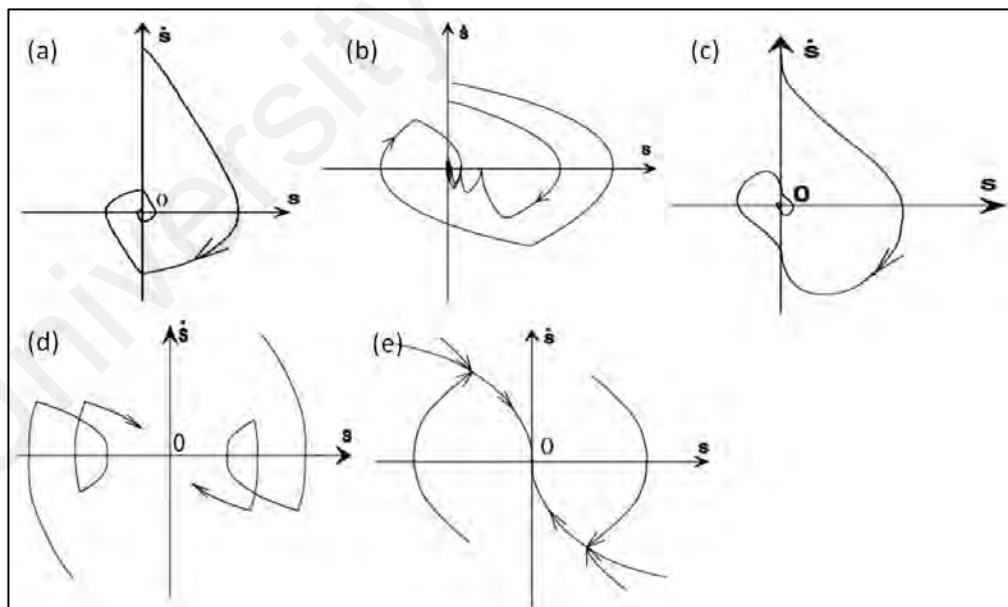
Figure 2.4: Phase trajectory of different SOSMC algorithm (a) twisting (b) suboptimal
(c) super-twisting (d) drift (e) algorithm with a prescribed law of variation of s
(Bartolini et al., 1999)

Second order SMC has been implemented in many systems (Bartolini, Pisano, & Usai, 2002; Ebrahimi et al., 2014; Ferrara & Incremona, 2015; Lin et al., 2014; Ling, Maksimovic, & Leyva, 2016; Shtessel, Shkolnikov, & Levant, 2009) and for many machine types, e.g., DC motors (Damiano et al., 2004; Eker, 2010; Pisano, Davila, Fridman, & Usai, 2008), PMSM (Laghrouche, Plestan, Glumineau, & Boisliveau, 2003), induction motors (Kommuri, Rath, Veluvolu, Defoort, & Soh, 2015) and induction generators (Beltran, Benbouzid, & Ahmed-Ali, 2012; Susperregui, Martinez, Tapia, & Vechiu, 2013). For speed control of PMSM, SOSMC resulted in smaller output deviations, smaller convergence time of up to 66% and smaller chattering in comparison with first order SMC (Bitao & Youguo, 2010; Bounasla & Hemsas, 2013; Qi & Shi, 2013b). Chattering analysis approach for systems with SOSMC has been proposed by Boiko, Fridman, Pisano, and Usai (2007), where it can be applied to perform in depth analysis of chattering for better comparison between SOSMC and first order SMC. Disadvantages of second order SMC in terms of robustness e.g. influences of measurement noise and unmodelled fast actuator dynamics have been described in detail by Levant and Fridman (2004) and Bartolini et al. (2003).

2.2.3 Composite SMC with Disturbance Compensation

Other than reaching law and higher order SMC method, the performance of conventional SMC can also be enhanced using additional control features. As far as speed control of PMSM is concerned, these composite SMCs are designed mainly by incorporating disturbance compensator or artificial intelligence. In standard sliding mode control theory, disturbances can be rejected completely when the selected switching gain is larger than the upper bound of disturbances. However, in practical applications, the upper bound of disturbances is difficult to be obtained. Hence, to ensure disturbance

rejection, a high value of the switching gain is normally chosen, due to which unwanted large chattering will occur.

SMC incorporated with disturbance compensation allows smaller value of switching gain to be selected since the gain value needs to be more than the bound of the disturbance compensation error instead of the lumped disturbances, which is usually larger. Hence, the disturbance rejection property of the controller is ensured without worsening the chattering effect (Shihua Li et al., 2011). Disturbance part required for compensation needs to be estimated, since direct measurement of the disturbances in PMSM applications is usually impossible. The estimated disturbance can be conventionally fed to the controller, but fast suppression is not guaranteed and can tremendously degrade the system's performance in cases of severe disturbances (Shihua et al., 2013). Therefore, it is usually fed as a feed-forward compensation part of the controller. Various disturbance estimation techniques as detailed in W. H. Chen, Yang, Guo, and Li (2016) have been proposed in other fields (Chiang & Tseng, 2004; SangJoo & Wan Kyun, 2003; She, Fang, Ohyama, Hashimoto, & Wu, 2008), but for PMSM applications, extended state observers, disturbance observers and artificial intelligence-based observers are widely used.

2.2.3.1 Extended State Observer

Extended state observer (ESO) was proposed by Jingqing (1995) and has been incorporated in composite SMC design in various fields (J. Wang, Li, Yang, Wu, & Li, 2015). In ESO, the lumped disturbances of the system i.e. external disturbances and internal dynamics are regarded as a new state of the system. It can estimate the states as well as the disturbances and its order is one magnitude higher than usual state observer. For PMSM speed control, a second order ESO has been composited in linear SMC by

Shihua Li et al. (2011). Experimental results proved good disturbance rejection capability with only 1% speed drop under load disturbance of 2 Nm. Furthermore, the SMC + ESO controller design managed to reduce approximately 40% chattering compared to the pure SMC controller.

Similar ESO design was incorporated in a continuous fast terminal SMC (CFTSMC) by W. Xu, Junejo, Liu, and Islam (2019). With disturbance compensation, the gain of the designed CFTSMC can be reduced to ensure chattering suppression. In addition, the composite SMC resulted in improved robustness against disturbance and better convergence with 30% higher reaching time compared to CFTSMC without ESO. Figure 2.5 shows the structure of composite SMC with ESO.
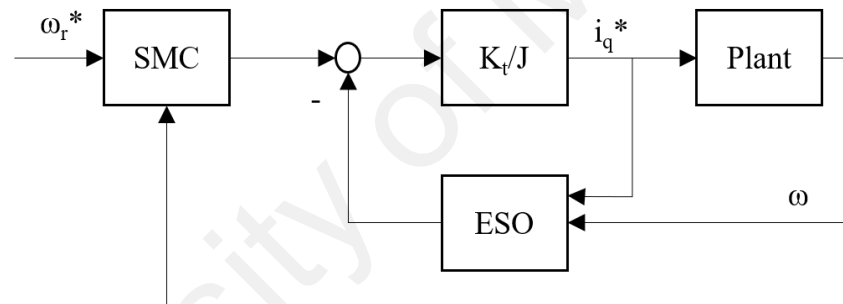
Figure 2.5: Composite SMC with ESO structure (W. Xu et al., 2019)

2.2.3.2 Disturbance Observer

Other than ESO, disturbance observer (DOB) originated by Ohnishi (1987) is also chosen by several researchers to estimate disturbance. In DOB, internal and external disturbances are estimated by using identified dynamics and measurable plant states. Disturbance observer-based SMC has been widely applied in various fields to improve the SMC in terms of disturbance rejection performance and chattering (Cao & Chen, 2014; Mu, Zong, Tian, & Xu, 2015; J. Zhang, Liu, Xia, Zuo, & Wang, 2016).

For speed control of PMSM, DOB is composited in SMC with a non-singular terminal sliding surface, which will be discussed further in Subsection 2.2.5.1. Simulation and experimental approaches in W. Xu, Jiang, and Mu (2016) showed that their proposed composite DOB-based SMC controller resulted in faster speed response with a tracking error of less than 0.2% and overshoot reduction by 50%. Furthermore, a remarkable improvement in current chattering was recorded, speed ripple was reduced by 80% as well as better robustness against step load torque compared to a conventional non-singular terminal sliding mode (NTSM) controller.

A composite nonlinear DOB with linear SMC was proposed by Nguyen, Basit, Choi, and Jung (2020), aiming to estimate the lumped disturbances to improve disturbance rejection ability as well as to act as a self-tuning mechanism for the observer gains to increase the convergence rate. Their simulation and experimental results proved improvement in tracking properties compared to SMC without the DOB. Unfortunately, chattering reduction analysis was not clearly executed.

A similar composite NTSM controller was proposed in E. Lu, Li, Yang, and Xu (2017), where a sliding mode based DOB is used to estimate disturbance, instead of a second order DOB in previously stated work. In their observer design, the conventional sliding mode is improved using the boundary layer reaching law method, as detailed in Subsection 2.2.1. A relevant comparison was made between their composite SMC and SMC without the observer, where the composite SMC showed smaller overshoot, better robust stability and reduction in the effect of random load on the system. In addition, when applied for a mining scraper conveyor system, a smooth starting and stable operation was achieved.

Another type of sliding mode based disturbance observer namely extended sliding mode disturbance observer (ESMDO) was developed by Xiaoguang et al. (2013) to provide disturbance compensation part to their main speed controller, SMC enhanced with novel reaching law, as detailed in Subsection 2.2.1. In this work, the chattering effect in the observer was suppressed using a low pass filter. The proposed composite SMC + ESMDO controller has better disturbance rejection ability than the PI controller, with smaller overshoot and shorter settling time. Quantitatively, under a load disturbance of 4 Nm, the speed drop of the proposed controller was reduced by 75%, the overshoot was reduced by 50% and settling time was 60% shorter.

In another work, sliding mode based disturbance observer was designed by combining the advantages of both NTSM sliding surface design and second order sliding mode, as presented in Subsection 2.2.2. Compared to the conventional sliding mode observer, the proposed second-order non-singular terminal sliding mode observer (SNTSMO) provides load estimation with lower estimation error and lower chattering. As a result, the overall performance of the composite controller, as shown in Figure 2.6, was improved in terms of robustness, disturbance rejection properties and speed fluctuation suppressions under load disturbance, therefore improving the dynamic performance of the system without affecting system's stability (En Lu, Li, Yang, & Liu, 2019).

Last but not least, in a most recent work, an extended sliding mode disturbance observer (ESMDO) using integral sliding surface was proposed in combination with novel reaching law design and continuous fast terminal sliding mode sliding surface design in the main speed controller to estimate the total system disturbances. Feed-forward compensation technique was used to reduce main controller's gain to suppress chattering (Junejo, Xu, Mu, Ismail, & Liu, 2020).
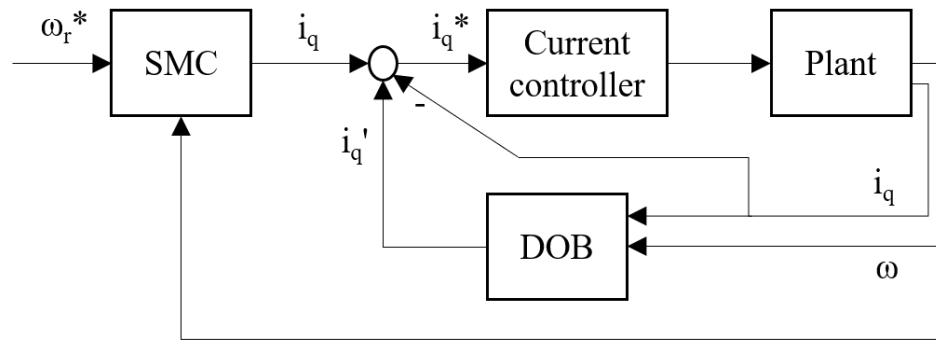
Figure 2.6: Structure of composite SMC with DOB (En Lu et al., 2019)

2.2.3.3 Artificial Intelligence-based Observer

Another type of observer used for disturbance compensation is artificial intelligence-based observers. Neural networks (NN) have characteristics of fault tolerance, parallelism and learning (Faa-Jeng & Po-Hung, 2006). Composite SMC with NN observer has been implemented in various applications (Pundir Avdesh & Singh, 2019; Sioud, Sharafin, Eliker, & Zhang, 2018; Y. Yin et al., 2019). For speed control of PMSM, uncertain system dynamics were predicted using a wavelet NN (WNN) bound observer to solve the issue of uncertainty bound in SMC design. Wavelet NN (WNN) combines the online learning ability of artificial NN and identification ability of wavelet decomposition. Its remarkable characteristics are quick convergence and high precision with reduced network size (Pan & Xia, 2008). The composite WNN-SMC controller allowed a robust speed control for a wide range of operating conditions as compared to a conventional PID controller (El-Sousy, 2011).

Other than pure NN observers, NN is also combined with fuzzy logic to design fuzzy neural network (FNN) observers. Both fuzzy logic and neural networks are universal approximators. However, the different characteristics of each of them are complementary. Fuzzy neural network (FNN) improves fuzzy logic-based controllers in terms of the learning abilities. Hence, it is capable of fuzzy reasoning in handling uncertain information as well as has the capability of artificial NN in learning from

25

processes. FNN observer is incorporated in SMC controllers in various fields (Yu, Fu, Li, & Zhang, 2018). For position control of PMSM, a recurrent fuzzy neural network (RFNN) intelligent observer was designed and combined with a SMC controller to facilitate real-time adjustment of the upper bound of the lumped uncertainty. The proposed composite controller resulted in a robust position control with less chattering and smaller control effort compared with SMC without RFNN observer (Wai, 2001). Similarly, for position control of PMSM, a wavelet FNN observer is applied with SMC. The experimental results proved that the WFNN can perform a reliable estimation of lumped uncertainty and the WFNN-SMC controller resulted in smaller tracking errors compared to a PI controller and SOSMC without WFNN lumped uncertainty estimator (Lin et al., 2014).

For speed control of PMSM, an uncertainty observer is designed using recurrent WFNN. This composite SMC resulted in precise tracking with smaller overshoot and smaller steady state error even under load disturbances due to lumped uncertainty suppression. In addition, electromagnetic impact and mechanical damage caused by excessively large and long torque overshoot are avoided by the resulting smaller torque response (Sheng, Xiaojie, & Lanyong, 2017).

The implementation of artificial intelligence-based observers has its drawbacks in terms of memory burden and complexity. It requires processors with fast data processing capability and optimization of network configuration parameters (Sheng et al., 2017). SMC controller enhancement through disturbance compensation depends heavily on the accuracy and speed of disturbance estimation, where careful selection of observer parameters is required. On top of that, the selected parameters must also ensure that the reachability condition of the main SMC controller is not jeopardized. In Table 2.2, disturbance estimation techniques in composite SMC are compared.

Table 2.2: Comparison of disturbance estimation techniques in SMC for PMSM speed control

Disturbance estimation technique		Main controller	Estimated parameter	Feed method
Extended state observer (ESO)	Second order ESO (Shihua Li et al., 2011)	Linear SMC	Speed, viscous friction and external load	Feed forward
	Second order ESO (W. Xu et al., 2019)	Fast terminal SMC	Speed, viscous friction and external load	Feed forward
Disturbance observer (DOB)	Nonlinear DOB (Nguyen et al., 2020)	Linear SMC	Lumped disturbances	Feedback
	Second order DOB (W. Xu et al., 2016)	Non-singular terminal SMC	Lumped disturbances	Feed forward
	Boundary layer sliding mode observer (E. Lu et al., 2017)	Non-singular terminal SMC	Load torque	Feed forward
	Extended sliding mode DOB (Xiaoguang et al., 2013)	Novel reaching law SMC	Lumped disturbances	Feed forward
	Extended sliding mode DOB (Junejo et al., 2020)	Fast terminal SMC	Lumped disturbances	Feed forward
	Second order non-singular terminal sliding mode observer (SNTSMO) (En Lu et al., 2019)	Linear SMC	Load torque	Feed forward
Artificial intelligence-based observer	Wavelet NN (El-Sousy, 2011)	WNN-SMC	Control gain	Feedback

2.2.4   Composite SMC with Artificial Intelligence

Apart from disturbance compensator, artificial intelligence (AI) is also a common feature incorporated to enhance SMC for speed control of PMSM. The integration of AI into SMC provides breakthrough to sliding mode theory that has been studied for over 50

years, where AI is incorporated to enhance the controller's performance. In general, composite SMC and computational intelligence controllers have been summarized technically by Kaynak, Erbatur, and Ertugnrl (2001), who discussed the possible ways of integration and by Xinghuo and Kaynak (2009), who emphasized the individual advantages and disadvantages of integrating various AI methods into SMC.

2.2.4.1 Fuzzy Logic

Fuzzy logic, which was proposed by Zadeh (1965), is one of the common AI incorporated in SMC. It uses linguistic information instead of mathematical tools to model complex industrial processes. Composite fuzzy sliding mode controllers have been implemented in various fields (Dasmahapatra et al., 2015; Belal A Elsayed, Hassan, & Mekhilef, 2013; Belal A. Elsayed, Hassan, & Mekhilef, 2015; Mohanty, Patra, & Ray, 2016; Saghafinia, Wooi Ping, & Nasir Uddin, 2014; X. X. Yin, Lin, Li, Liu, & Gu, 2015; X. Zhang, Wang, Liu, & Yuan, 2016).

For PMSM speed control, a composite fuzzy SMC was designed by Kuo et al. (2007). In this work, the control output was obtained using the fuzzy logic inference scheme (FLIS), depending on three sliding conditions namely reaching, sliding and stable. Since the input variable of the fuzzy inference rules is defined by the sliding conditions, the number of fuzzy rules can be minimized. The proposed controller improved the performance of a pure fuzzy controller in terms of eliminating overshoot, settling time, tracking precision and steady-state error elimination.

In Leu, Choi, and Jung (2012), instead of depending on sliding conditions like in the above-mentioned work, their fuzzy sets depending on the speed error. Based on five membership functions, switching control law in the main SMC controller adapts to speed difference with the reference speed, resulting in better transient response and smaller

chattering. Figure 2.7 shows two different control structures of composite SMC + fuzzy for speed control of PMSM.

(a)

(b)
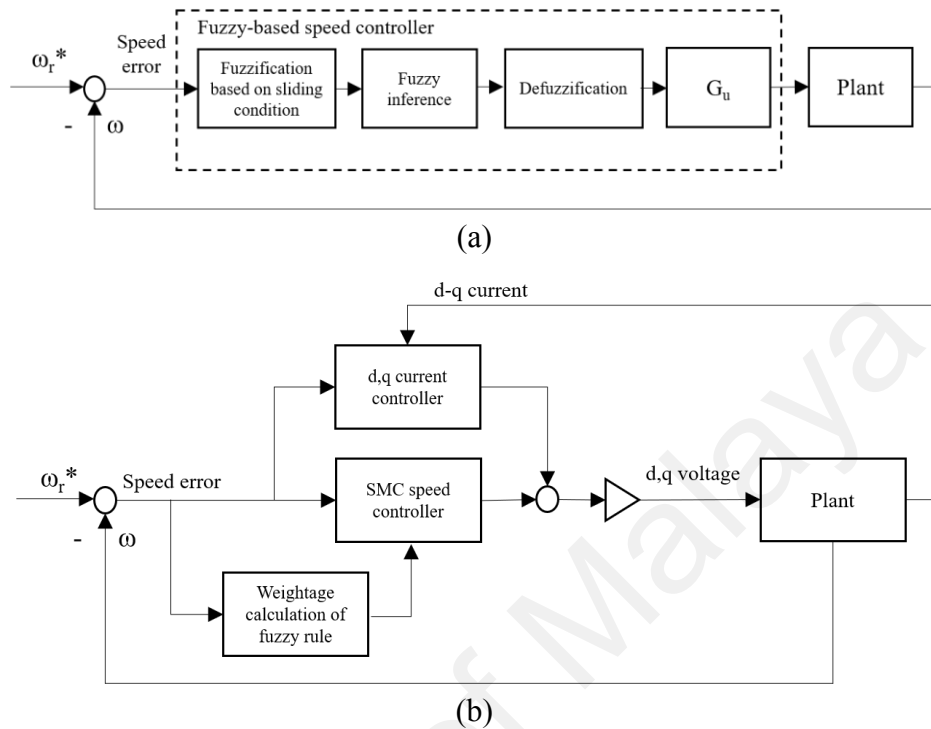
Figure 2.7: Two ways of fuzzy logic incorporation in SMC for speed control of PMSM (a) with output based on sliding condition (Kuo et al., 2007) (b) with adaptive reaching law gain based on speed error (Leu et al., 2012)

2.2.4.2 Neural Network

Other than fuzzy logic, a neural network is also applied to enhance sliding mode controller performance. In El-Sousy (2011), apart from incorporating a WNN observer as discussed in subsection 2.2.3.3, WNN theory is also integrated inside their SMC speed controller design for PMSM, to provide adaptive control signal based on the error between the selected reference model and the actual output of the PMSM drive. With this error, the connective weights of the WNN are trained to provide a good model-following response. This integrated WNN-SMC design allows a robust model-following tracking in the presence of parameter uncertainties and external load disturbances under a wide range of operating conditions.

2.2.4.3 Fuzzy Neural Network

Combining fuzzy logic and neural network theories, a neuro-fuzzy controller (NFC) is designed by Elmas and Ustun (2008) and is connected in parallel with a SMC controller for speed control of PMSM. The proposed hybrid controller uses error band method to determine which controller needs to be activated at a certain time. SMC is active during transient mode to get fast dynamic response whereas the NFC is active during steady-state mode to get a smooth, less chattering dynamic response. The idea is to use the advantages of both SMC and NFC as well as to eliminate the disadvantageous factors of both. The current chattering of the proposed hybrid controller is reduced by around 92% compared to a conventional SMC. However, the speed response of the hybrid controller is faster by more than 7% compared to a conventional SMC. The hybrid controller is also less sensitive to parameter variations and external load disturbances compared to a conventional NFC.

All works discussed above implement AI directly with SMC to design a composite SMC. However, it is also worth to mention that AI is also used indirectly in SMC design such as in observer design, as discussed earlier in subsection 2.2.3.3.

2.2.5 Sliding Surface Design Modification

Other than reaching law, higher order and composite methods, sliding mode controllers can also be enhanced by performing modification in their sliding surface design. Conventional SMC uses a linear sliding surface as in equation (2.3), with $c > 0$. This design guarantees sliding mode asymptotic stability with convergence rate, but the controller's performance is highly dependent on its gain value (Xiaoguang et al., 2013). The remarkable advantage of this design is its simplicity. However, the performance of

conventional linear sliding surfaces is proven to be less satisfactory in terms of convergence rate and settling time (Qi & Shi, 2013a; Shihua et al., 2013). The dynamic response of a closed-loop system can be improved by using nonlinear sliding surfaces. For PMSM speed control, several works have been executed using linear SMC, but the drawbacks of linear SMC were overcome by means of hybridization to develop composite SMC controllers (Elmas & Ustun, 2008; En Lu et al., 2019; Shihua Li et al., 2011; Yan, Ju-Beom, & Jang-myung, 2009) or modification of the reaching law (Xiaoguang et al., 2013).

$$s = cx_1 + x_2 \qquad (2.3)$$

2.2.5.1 Terminal SMC

To overcome issues in linear SMC design, nonlinear sliding surfaces are proposed. Terminal sliding surface is designed by replacing the linear term in linear sliding surface with a fractional power term to ensure fast and finite-time states convergence during the sliding mode phase. In this terminal sliding mode (TSM) control, rate of convergence increases near the equilibrium point which makes this controller preferred for high precision control. The drawback of conventional terminal SMC in equation (2.4) is its singularity problem that might occur if the initial conditions are not carefully selected, due to the recursive structure of switching manifolds (Feng, Yu, & Man, 2002; Shihua et al., 2013). Singularity in TSMC was overcome by using a two-phase control strategy by inducing the system state into a non-singular region, prior to finite-time convergence control (Wu, Yu, & Man, 1998). In Man and Xing Huo (1997), non-singularity was ensured by switching between TSM and linear hyperplane based sliding mode. However, as the boundary decreases to zero, the singularity effect is not fully eliminated.

Furthermore, when the boundary is relatively large, the advantage of TSM is diminished (Feng et al., 2002).

$$s = x_2 + bx_1^{\frac{q}{p}} \qquad\qquad b > 0; p, q \text{ are positive odd integers, } p > q \qquad (2.4)$$

To completely eliminate the singularity problem of conventional TSM control, non-singular terminal sliding mode (NTSM) controller in equation (2.4) was proposed. It has been applied to many systems (S. Y. Chen & Lin, 2011; Haibo, Heping, & Junlei, 2019; R. Zhang, Dong, & Sun, 2014; K. Zhao et al., 2019). Mu and He (2018) proposed two new definitions and theorems to specifically characterize the dynamic behaviour of TSM and NTSM for nonlinear systems. NTSM was applied for PMSM speed control and resulted in shorter settling time, better anti-disturbance ability, smaller tracking error and smaller chattering compared to conventional SMC (X. Liu, Yu, Yu, & Zhao, 2018; Shihua et al., 2013; W. Xu, Jiang, Mu, & Yue, 2015). However, controller enhancement still involves setting the switching gain at a higher value as per in SMC. Hence, large chattering cannot be avoided due to discontinuity term in order to improve the controller performance. Another drawback lies in providing good convergence especially when the system state is far from equilibrium (Qi & Shi, 2013a). Furthermore, improper parameter selection of NTSM can affect its convergence rate when its performance approaches that of linear SMC (Xinghuo & Man, 2002). Several works aimed to overcome these drawbacks using composite NTSM controllers (E. Lu et al., 2017; Mu, Xu, & Sun, 2016) as well as proposing a design principle of controller variables based on homogeneity analysis (Mu et al., 2016).

$$s = x_1 + \frac{1}{b} x_2^{\frac{p}{q}} \qquad\qquad b > 0; p, q \text{ are positive odd integers, } 1 < \frac{p}{q} < 2 \quad (2.5)$$

Another type of terminal sliding mode controller proposed in the literature is the non-singular fast terminal sliding mode (NFTSM) controller, as in equation (2.6). NFTSM retains the advantages of NTSM but with a faster state convergence. Near equilibrium, the convergence rate of linear sliding mode remains constant while the convergence rate of NFTSM grows exponentially (Xinghuo & Man, 2002). NFTSM has been applied for various control applications (Al-Ghanimi, Zheng, & Man, 2015; Gudey & Gupta, 2016; Komurcugil, 2011; Mobayen, 2015; Mu, Sun, & Xu, 2015; Van, Mavrovouniotis, & Ge, 2019; S. S. D. Xu, Chen, & Wu, 2015) and has shown not only faster convergence, but also stronger robustness, higher precision and lower chattering compared to conventional SMC. For position control of PMSM, NFTSM was used to reduce the chattering phenomenon and to provide better position tracking and convergence rate compared to a PD controller (Qi & Shi, 2013a)

$$s = x_2 + ax_1 + bx_1^{\frac{q}{p}} \qquad\qquad a,b > 0; p,q > 0 \text{ (odd numbers)}; p > q \qquad (2.6)$$

NFTSM implemented for speed control of PMSM has proven that the singularity problem of TSM is successfully avoided and faster convergence is obtained (Shuo, 2015). Experimental results in W. Xu et al. (2019) proved that the PMSM system with NFTSM has smaller speed fluctuations and better disturbance rejection ability compared to PI controller and conventional SMC.

2.2.5.2 Integer Order Integral SMC

Other than using the terms with fractional power as described above, sliding surface design can also be enhanced with an integral term, as shown in equation (2.7). In conventional sliding mode control, the robustness of the system against parameters variation and external disturbances is achieved in the sliding phase. Prior to that, i.e.,

during the reaching phase, the robustness is not guaranteed. Integral sliding mode control (ISMC) was introduced by V. Utkin and Jingxin (1996) to overcome this problem by eliminating the reaching phase, therefore, the sliding phase is enforced throughout the entire system response. Furthermore, the order of motion equation in integral SMC is not reduced by the control input dimension, but equal to the order of the original system. Control law of ISMC consists of continuous nominal control and discontinuous control, which is responsible for the performance of the nominal system without perturbations and for rejecting perturbations respectively. Therefore, system robustness can be guaranteed from the initial time. In addition, a smaller maximum control magnitude is required for ISMC than conventional SMC since the value is usually bigger during the reaching phase (Castanos & Fridman, 2006; Liang et al., 2012).

$$s = e(t) - \int_0^t (a + bK)e(\tau)d\tau \tag{2.7}$$

In PMSM speed control, constructing a conventional sliding surface requires both speed and acceleration signals. However, acceleration signals are usually immeasurable and difficult to accurately estimate due to noise and parameter uncertainties. Integral sliding mode solves this issue and avoids degradation of the system closed-loop performance (Xia, Wang, Li, & Chen, 2011). ISMC for speed control of PMSM has proven to result in better speed response compared to conventional PI in terms of overshoot, response time and steady-state error. In their simulation, Q. Song and Jia (2016) proved a smaller speed drop by 87.5% under load disturbance when using ISMC, compared to a PI controller. Similarly, an improved speed drop by almost 29% was observed in the experiment executed by Zaky (2012). However, a better result of 4% speed drop was obtained when using a tuned ISMC, concluding that good robustness is only ensured when ISMC gain is carefully tuned. The drawback of ISMC is the difficulty

of parameter tuning of its gain, which is required to ensure a good balance between disturbance rejection property of the controller and the chattering phenomenon. This drawback was overcome using various techniques such as using linear varying gain and extended state observer (Xia et al., 2011) or using gain tuning methods (Zaky, 2012).

2.2.5.3 Fractional Order SMC

Fractional order SMC enhances integral SMC in subsection 2.2.5.2 by replacing its integer order integration term with fractional calculus terms. Fractional calculus emerged theoretically over 300 years ago, but in recent decades it has been applied practically in a wide range of science and engineering disciplines (Efe, 2011). It is a generalization of the traditional integer order integration and differentiation to the non-integer order.

The fundamental operator of fractional calculus, $_aD_t^r$, is defined as in equation (2.8), where a and t are the limits of the operation and r is the order of operation with $0 < |r| < 1$. r is generally $r \in \mathcal{R}$ but r could also be a complex number (Yang Quan, Petras, & Dingyu, 2009).

$$
_aD_t^r = \begin{cases} \dfrac{d^r}{dt^r} & \text{for } r > 0, \\ 1 & \text{for } r = 0, \\ \displaystyle\int_a^t (d\tau)^{-r} & \text{for } r < 0. \end{cases} \tag{2.8}
$$

Three definitions are commonly used for the general fractional differentiation and integration namely the Grunwald-Letnikov (GL) definition in equation (2.9), the Riemann-Liouville (RL) definition in equation (2.10) and the Caputo definition in equation (2.11), where $n - 1 < r < n$ and $\Gamma(.)$ is the Gamma function.

$$_aD_t^r f(t) = \lim_{h \to 0} h^{-r} \sum_{j=0}^{\frac{t-a}{h}} (-1)^j \binom{r}{j} f(t-jh) \tag{2.9}$$

$$_aD_t^r f(t) = \frac{1}{\Gamma(n-r)} \frac{d^n}{dt^n} \int_a^t \frac{f(\tau)}{(t-\tau)^{r-n+1}} d\tau \tag{2.10}$$

$$_aD_t^r f(t) = \frac{1}{\Gamma(r-n)} \int_a^t \frac{f^{(n)}(\tau)}{(t-\tau)^{r-n+1}} d\tau \tag{2.11}$$

RL definition of fractional differentiation and integration is also formulated in the form of Laplace transformation in equation (2.12) with $n-1 < r \leq n$ and $s \equiv j\omega$ denotes the Laplace transform variable. This definition is commonly used in engineering problem solving (Igor Podlubny, 1999; Spanier, 1974).

$$\int_0^\infty e^{-st} {}_0D_t^r f(t) dt = s^r F(s) - \sum_{k=0}^{n-1} s^k {}_0D_t^{r-k-1} f(t) \big| t = 0 \tag{2.12}$$

Fractional order terms have the property of attenuating old data and storing new data, hence they are more stable or at least as stable as their integer order counterparts (Huang, Cui, Shi, Li, & Xiang, 2014; B. Zhang et al., 2012). The extra degree of freedom of integral and differential operators can improve the controller's performance further compared to traditional integer order SMC (IOSMC). Theoretically, fractional order sliding surfaces experience slower energy transfer during switching, hence resulting in smaller chattering compared to integer order sliding surfaces which decay towards zero exponentially, as illustrated in Figure 2.8. Understanding of geometric and physical of fractional differentiation and integration compared to integer order ones are detailed in I. Podlubny (2002) and the main properties of fractional calculus are listed in Yang Quan et al. (2009).
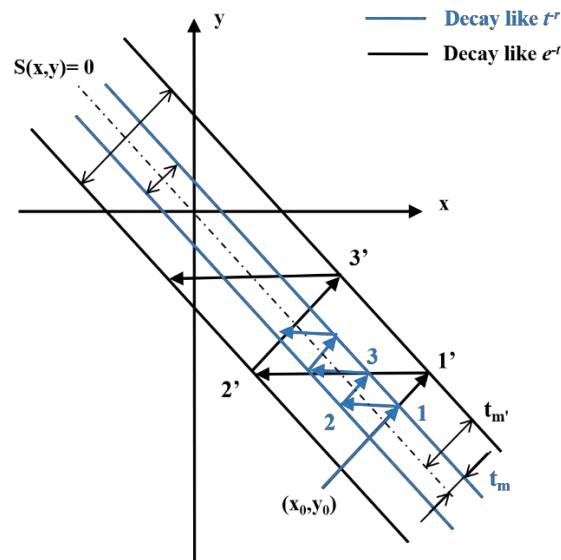
Figure 2.8: Comparison of energy transfer during sliding motion of FOSMC (blue line) and IOSMC (black line) (B. Zhang et al., 2012)

Fractional calculus has been extensively integrated with classical PID control theory to come out with fractional PID controllers indicated as $PI^\lambda D^\mu$ (Chopade, Khubalkar, Junghare, Aware, & Das, 2018; Lanusse, Oustaloup, & Sabatier, 2014; Maddahi, Sepehri, & Kinsner, 2019). Other fractional order controller includes fractional adaptive controllers (Efe, 2008; Ladaci & Charef, 2006), fractional order compensators (Ying Luo, Chen, Ahn, & Pi, 2010; Y. Luo, Chen, Ahn, & Pi, 2012; Salehtavazoei & Tavakoli-Kakhki, 2014; Ying, Yang Quan, Hyo-Sung, & Youguo, 2009) and fractional order observers (K. Chen, Tang, Li, & Wei, 2018; Mujumdar, Tamhane, & Kurode, 2015). The incorporation of fractional calculus in SMC sliding surface design produces a fractional order SMC (FOSMC) and has been applied in S.-Y. Chen and Lee (2017), Davijani, Jahanfarnia, and Abharian (2017), G. Sun, Ma, and Yu (2018) and Zhong, Shao, Li, Ma, and Sun (2018). The superior performance of FOSMC for applications in induction motors was elaborated and compared with a few other SMC controllers in Guanghui Sun, Wu, Kuang, Ma, and Liu (2018).

For PMSM, fractional integration was composited in integer order integral SMC for position control in Huang et al. (2014). The fractional integral term in the control law

ensures timely generation of control output during start-up or load disturbance by eliminating the integral saturation effect without having to increase the switching gain. In addition to the ability to suppress disturbance, the additional term also weakens the chattering phenomenon during the sliding mode. For speed control of PMSM, B. Zhang et al. (2012) has implemented FOSMC with sliding surface in equation (2.13) with $k_p > 0$ and $_0D_t^r(\cdot)$ is fractional order integral. Their experimental results showed that the proposed FOSMC resulted in better control performance with smaller chattering. In addition, the PMSM system with FOSMC is more robust against external load disturbance and parameter variations compared to integer order integral SMC. Similar simulation results were obtained by Huang et al. (2012).

$$s = k_p e(t) + {_0D_t^r} e(t) \qquad (2.13)$$

Both previously stated FOSMC speed control of PMSM differentiate themselves in terms of sliding surface design. B. Zhang et al. (2012) have chosen a fractional integration (PI) surface whereas Huang et al. (2012) have chosen a fractional differentiation (PD) surface. Fractional PID sliding surface has not been implemented for a similar application. In SMC with integer order PID sliding surface, the proportional term drives the system state to the switching surface neighbourhood, whereas the integral term forces the states onto the surface regardless of the bound knowledge of uncertainties and disturbances. With the incorporation of the derivative term, the system will be stabilized by preventing excessive control effect of the integral action (M. Li, Wang, & Gao, 2001). Furthermore, PID sliding surface provides a faster response than a PD sliding surface with less steady-state error (Castillo-Zamora, Camarillo-Gómez, Pérez-Soto, & Rodríguez-Reséndiz, 2018; Jafarov, Parlakci, & Istefanopulos, 2005). Similarly, the performance of FOSMC design depends on PI, PD and PID sliding surface design selection.

Each sliding surface design for SMC proposed in previous literature for speed control of PMSM has its own strength and weaknesses in determining the performance of the controller, as compared in Table 2.3. The terminal sliding surface has a higher tracking speed compared to the conventional linear sliding surface. However, NSFT converges faster to the sliding surface compared to the non-singular terminal sliding surface. Both integral and fractional sliding surface design contributes to higher tracking speed and convergence rate compared to other designs. The integration term is incorporated in the integral and fractional sliding surface to further expedite convergence rate by eliminating the reaching phase of SMC. In terms of anti-disturbance rejection, NSFT, integral and fractional design outperform the other two designs. The linear design does not support chattering reduction. Terminal and integral surface design have low chattering reduction ability. Slow energy transfer properties of fractional calculus in fractional surface design allow better chattering suppression.

Table 2.3: Properties comparison of sliding surface designs

Sliding surface design	Speed of tracking	Convergence rate	Elimination of reaching phase	Anti-disturbance rejection	Chattering reduction ability
Linear (Shihua Li et al., 2011)	Slow	Low	No	Weak	No
Non-singular terminal (X. Liu et al., 2018)	Medium	Medium	No	Weak	Low
Non-singular fast terminal (NSFT) (W. Xu et al., 2019)	Medium	High	No	Strong	Low
Integral (Q. Song & Jia, 2016)	Fast	High	Yes	Strong	Low
Fractional (B. Zhang et al., 2012)	Fast	High	Yes	Strong	High

In conclusion, five categories of SMC enhancement methods based on Figure 2.1 have been discussed. These methods are summarized in Table 2.4, where their remarkable properties and main disadvantages are listed.

Table 2.4: Summary of state-of-the-art implementation of SMC enhancement methods for speed control of PMSM

Method	Remarkable properties	Disadvantages
Reaching law	• Boundary layer around sliding surface • Speed of convergence depends on state variable	• Steady-state error depending on boundary layer selection • Reaching time increases as state approaches sliding surface
Higher order SMC	• Control input acts on higher derivatives of the sliding surface • Sliding order characterizes the system dynamics in the vicinity of the sliding mode	Usage of differentiators, where their practical behaviour requires particular care in real implementation due to measurement noise.
Composite SMC with disturbance compensation	• Allows smaller value of switching gain • Disturbance rejection property is ensured without worsening the chattering effect	Highly dependent on disturbance estimation accuracy
Composite SMC with artificial intelligence	• Control output adapts based on sliding conditions, speed error or deviation from reference model	• Computational load • Requires adjustment of many parameters (neural network) • Requires intensive membership function in fuzzy logic for precision
Sliding surface design modification	• Sliding surface design adjust system's dynamics by modifying behaviour of control law	• Design selection based on application

2.3 Inverter Topologies for PMSM

Apart from the controller, the inverter is also one of the main components of VFD. For PMSM drive systems, several inverter topologies have been employed in previous works, where they can be divided into two main groups namely voltage source inverters (VSI) and current source inverters (CSI). CSI inverters in Figure 2.9 have properties of simple configuration, low differential value of output voltage, high fault-tolerant capability and four quadrant operation. However, CSI fed motor drives suffer from LC

resonance due to the required AC capacitors on the output side to filter harmonics and for current commutation among phases (Z. Wang, Zheng, Zou, & Cheng, 2012).
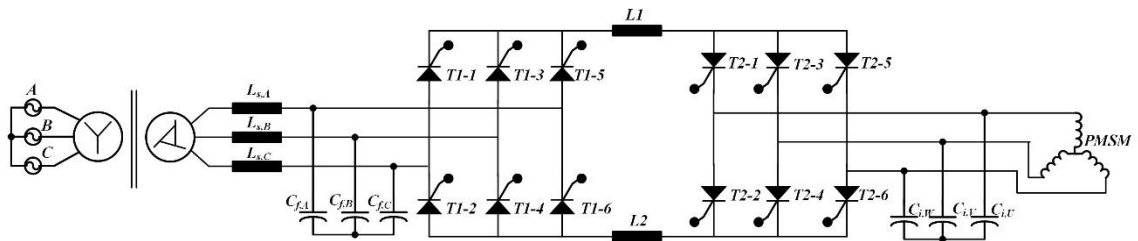
Figure 2.9: Current source inverter (Z. Wang et al., 2012)

Application of three-phase two-level VSI with six switches as shown in Figure 2.10 has been well established in the industries due to its remarkable features such as high efficiency, high power density, low conduction losses, small part count and simple operation principle (Schweizer & Kolar, 2013; Zhu, Zeng, & Zhao, 2017a).
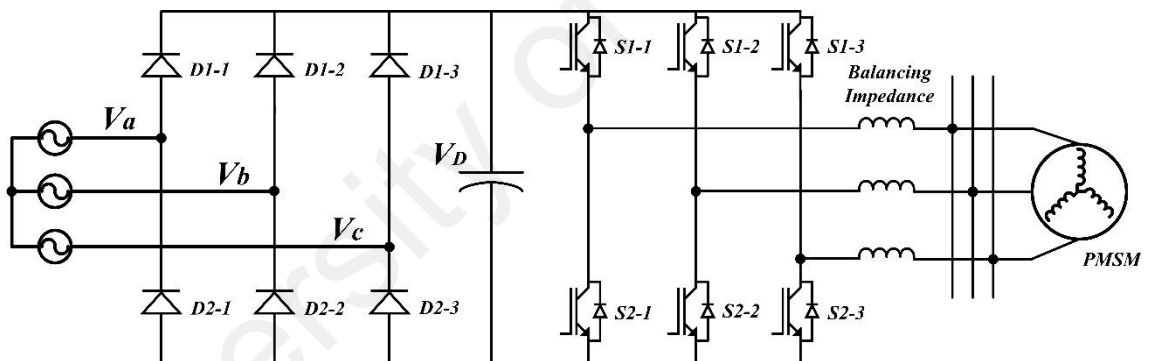
Figure 2.10: Three-phase two-level VSI with six switches (Zaihidee, Mekhilef, & Mubin, 2019)

Low power application of PMSM triggers research on lower cost inverters. For this purpose, three-phase four switches topology is proposed by Gi-Taek and Lipo (1996), where the terminal of one of the three phases is connected to the dc-link capacitor's mid-point. Although this topology can reduce inverter cost, it has disadvantages in terms of reduced dc-link voltage utilization and voltage unbalance between the two capacitors (W. Li, Xuan, Gao, & Luo, 2019). Furthermore, due to its asymmetrical topology, as shown in Figure 2.11, the output voltage drop results in torque ripples which can affect PMSM

drive performance and reliability (Zhu et al., 2017a; Zhu, Zeng, & Zhao, 2017b). Another type of four switches topology in Figure 2.12 has been proposed for PMSM to eliminate dead-time insertion or compensation in the other four switches topologies (W. Li et al., 2019). However, this topology requires appropriate zero-sequence current suppression due to neutral point access of motor.
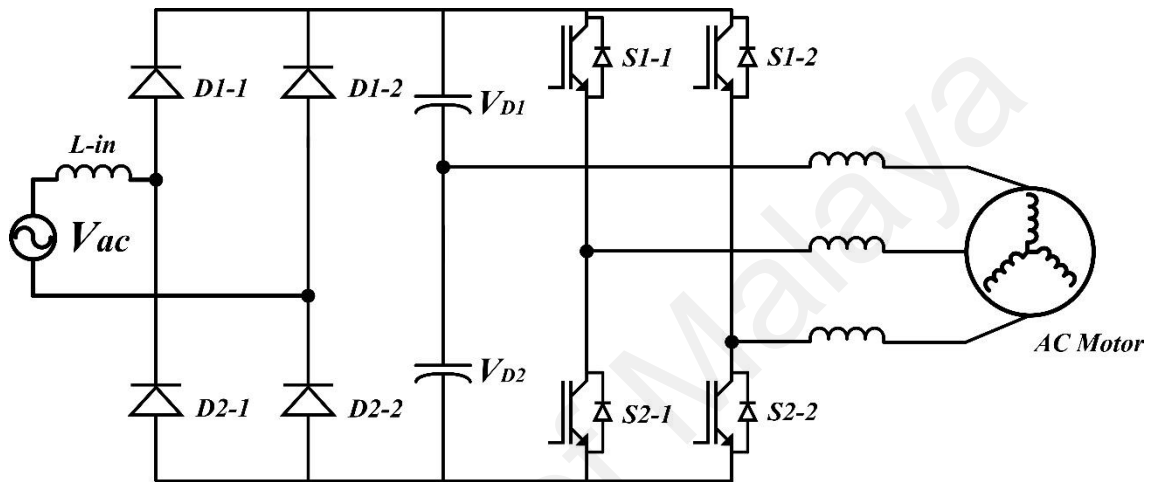
Figure 2.11: Three-phase two-level VSI with four switches (Zhu et al., 2017a)
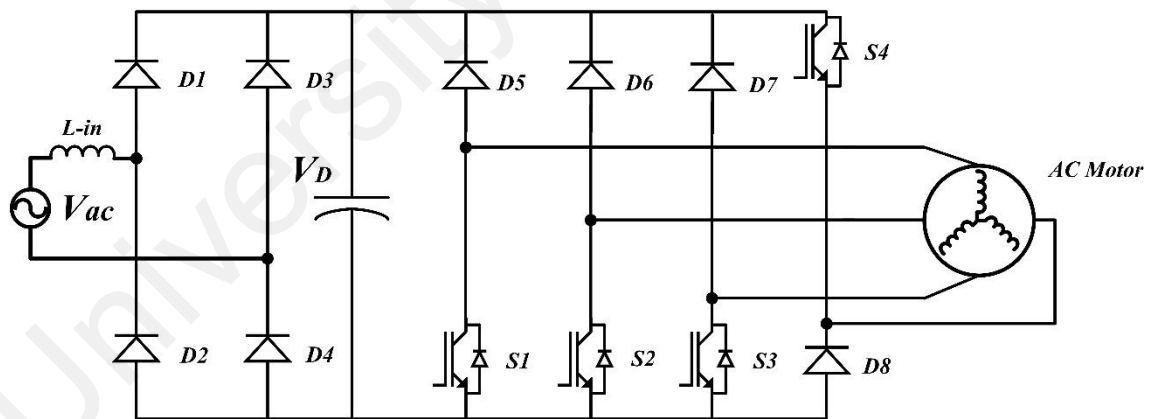
Figure 2.12: Three-phase two-level VSI with four switches (W. Li et al., 2019)

For high power applications, parallel inverters are used, where more than one converter are required to cater to the necessary power. Interleaved operation of parallel VSI as shown in Figure 2.13 can effectively suppress the output current harmonics (Z. Wang, Chen, Cheng, & Zheng, 2015). Parallel CSI inverter as shown in Figure 2.14 is

used to increase power rating under the limitation of the rated current of switches. It is usually used in interleaved operation to suppress LC resonance mentioned previously, which is especially useful to obtain good estimations in sensorless PMSM control (Z. Wang et al., 2012).
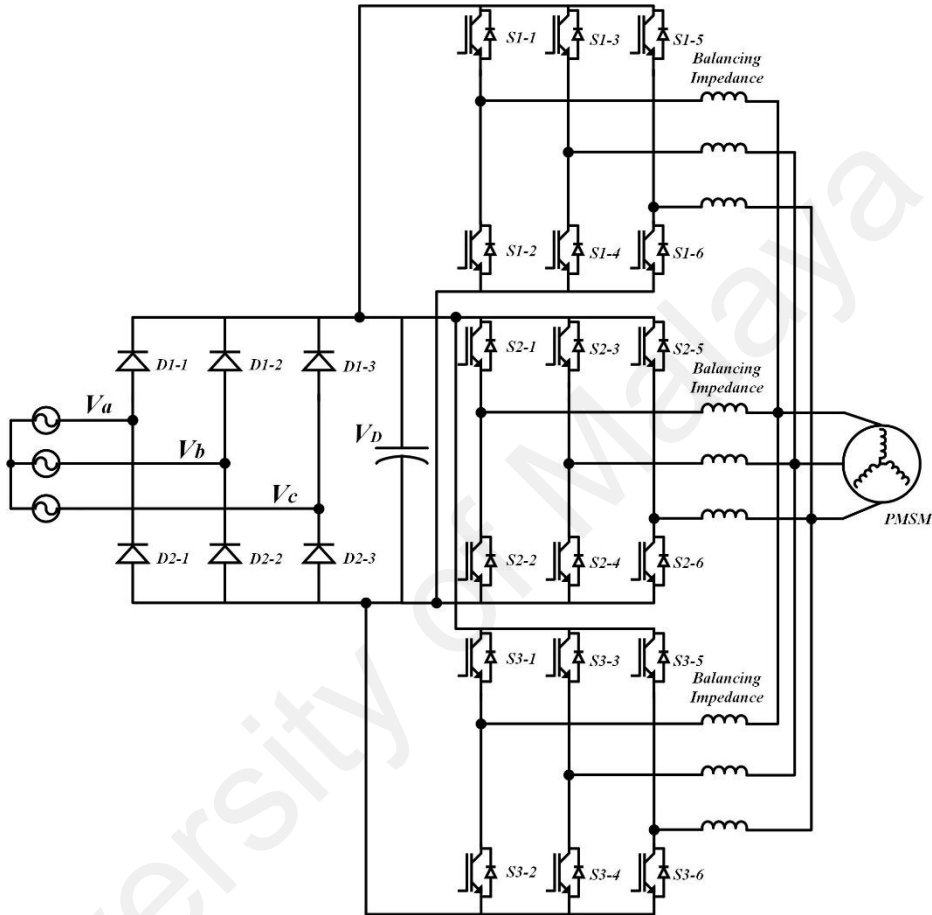
Figure 2.13: Parallel VSI (Z. Wang et al., 2015)
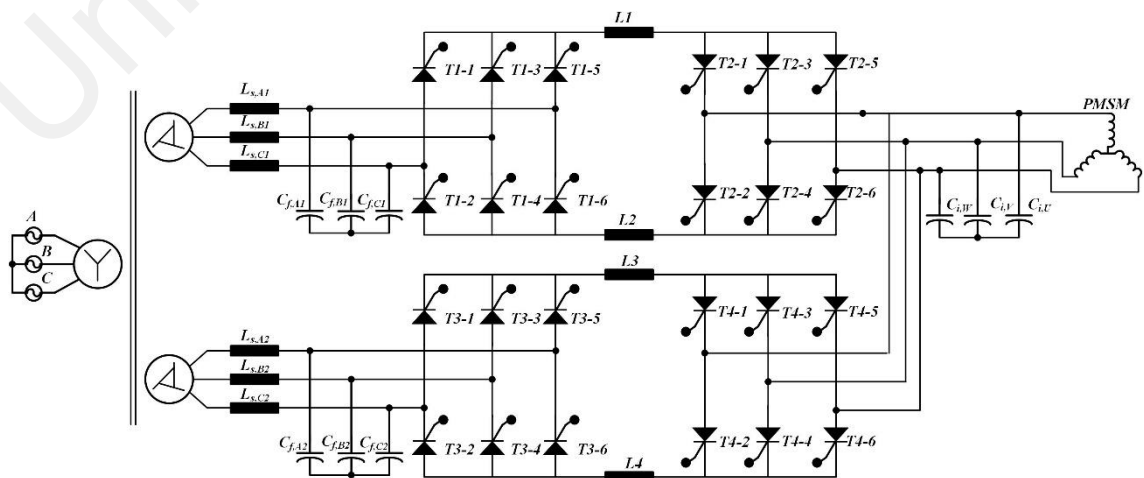
Figure 2.14: Parallel CSI (Z. Wang et al., 2012)

Another type of VSI applied for PMSM is a bidirectional Z-source inverter (ZSI) that allows both switches in upper and lower arms to be turned on simultaneously to boost dc-link voltage, as shown in Figure 2.15. This topology is used to extend the speed range of PMSM and reduce current amplitude during high speed run. It also contributes in preventing inverter damage during shoot-through states (P. Liu & Liu, 2012).
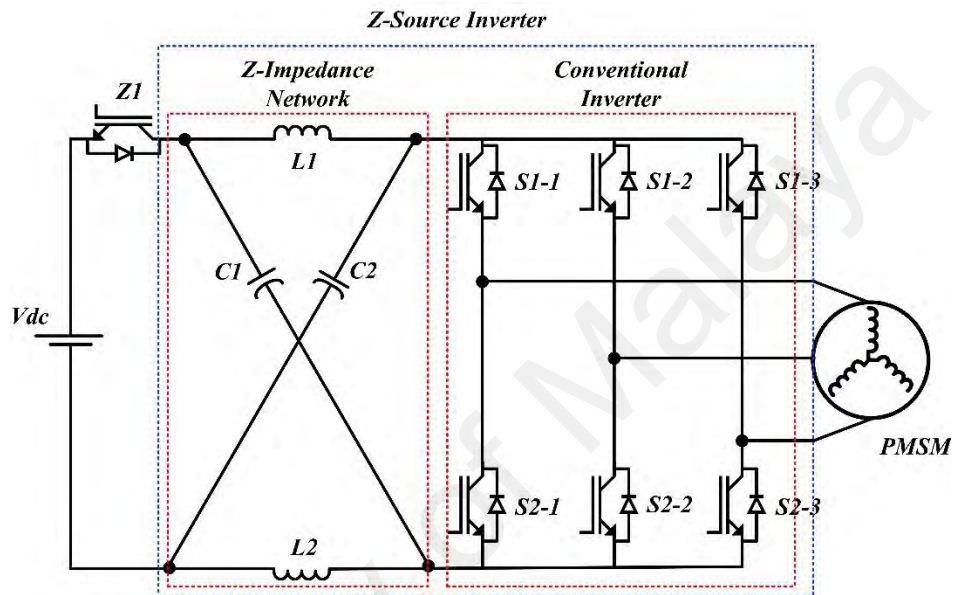
Figure 2.15: Z-source inverter (P. Liu & Liu, 2012)

Multilevel inverters (MLI) increase the rated voltage of the drive system. They provide better output voltage harmonic performance that allows operation with low switching frequency. Several MLIs have been employed for PMSM such as 3-level T-type neutral-point clamped (T-NPC) (Bhattacharya, Mascarella, Joós, Cyr, & Xu, 2016) and 3-level neutral-point clamped (NPC) (Choudhury, Pillay, & Williamson, 2014), as shown in Figure 2.16 (a) and (b) respectively. However, MLIs have a potential drawback of unbalanced dc-link capacitor voltages, which requires an additional voltage balancing scheme or algorithm. Furthermore, the above-stated works aim for application in high power PMSM.

(a)

(b)
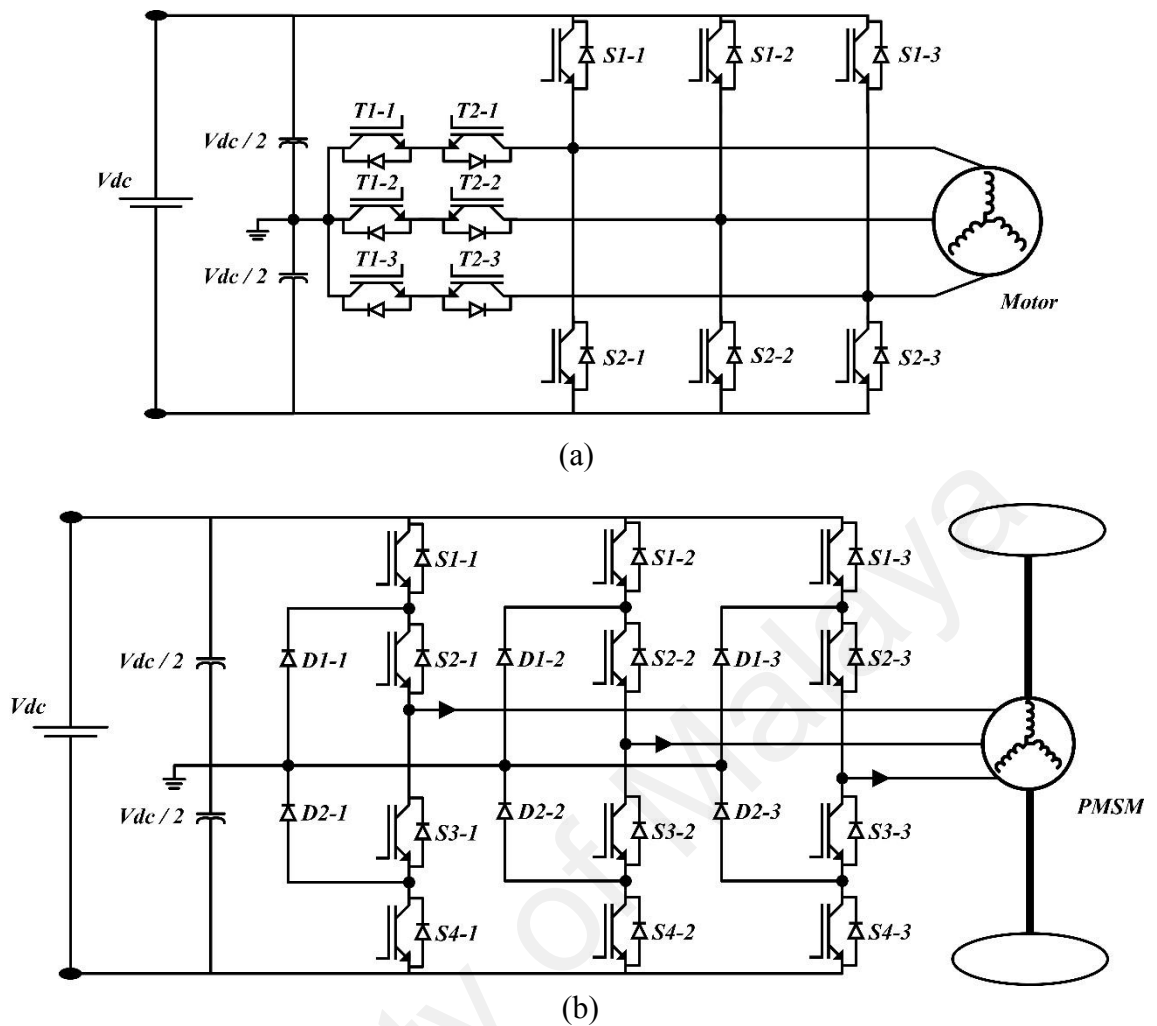
Figure 2.16: Multilevel inverters (a) 3-level T-type neutral-point clamped (T-NPC) (Bhattacharya et al., 2016) (b) 3-level neutral-point clamped (NPC) (Choudhury et al., 2014)

From comparison in Table 2.5, three-phase two-level VSI with six switches is the most suitable inverter topology to be used for medium power application and speed range required in this work, while concurrently utilizing its advantages in terms of cost, simplicity and components availability.

Table 2.5: Comparison of inverter topologies

Topology	Type	No of switches	Cost	PMSM Application
Three-phase six switches (Zaihidee et al., 2019)	VSI	6	Low	Low-Medium power, Below base speed
Three-phase four switches (Zhu et al., 2017a)	VSI	4	Low	Low power
Three-phase six switches (Z. Wang et al., 2012)	CSI	6	Low	Low power
Parallel VSI-fed (Z. Wang et al., 2015)	VSI	≥12	High	High power
Parallel CSI-fed (Z. Wang et al., 2012)	CSI	≥12	High	High power, Sensorless control
Z-source inverter (P. Liu & Liu, 2012)	VSI	7	Medium	High speed
Multilevel inverter (Bhattacharya et al., 2016)	VSI	12	High	High power

2.4 Summary

In this chapter, SMC enhancement methods for speed control of PMSM has been discussed. Different approaches have been proposed in the literature to enhance conventional SMC in terms of speed of response, robustness, anti-disturbance properties and chattering reduction ability. In terms of sliding surface design, nonlinear sliding surfaces can improve the dynamic response of closed-loop systems. Integer order integral SMC has successfully proven to be able to eliminate the reaching phase in sliding mode control and enforces the sliding phase throughout the entire response. However, improving disturbance rejection and fast response properties of the controller easily worsen the chattering phenomenon known in SMC. To tackle this disadvantage, fractional order SMC is presented based on fractional calculus theory, which experiences slower energy transfer during the switching process. This property of FOSMC reduces the chattering phenomenon. Furthermore, the fractional order provides an extra degree of

freedom compared to integer order integral SMC, which enhances disturbance rejection and speed of response properties of the controller. In addition, various inverter topologies utilized for PMSM are compared to show that three-phase six switches two-level inverter is appropriate for the application of medium power PMSM under base speed.

CHAPTER 3: DESIGN OF THE PMSM DRIVE SYSTEM

3.1 Introduction

In this chapter, the design of the proposed PMSM drive system is introduced. Firstly, the complete system of PMSM field-oriented speed control is presented. Then, the proposed fractional order sliding mode speed controller design is explained. The control law is derived from the chosen sliding surface design, reaching law and PMSM mathematical model. The Lyapunov stability theorem is used to analyse and prove the controller's stability. The realisation of the complete PMSM drive system in MATLAB for simulation purpose is also presented. Finally, the developed closed-loop PMSM drive prototype for experimental validation is thoroughly elaborated.

3.2 Field-oriented Speed Control of PMSM

In field-oriented control of PMSM, reference or command values of the decoupled components of stator current in the synchronous rotating reference frame, i_q^* and i_d^*, are calculated by the controller for control of torque and flux respectively. In this study, the indirect FOC of PMSM is used, where motor speed is used as a feedback signal to the controller. This approach is preferred due to simplicity and low in cost compared to direct FOC technique. In direct FOC method, rotor flux is used as feedback for the controller, where flux must be measured directly by means of sensors or must be estimated. Figure 3.1 shows an overview of indirect FOC control of PMSM.
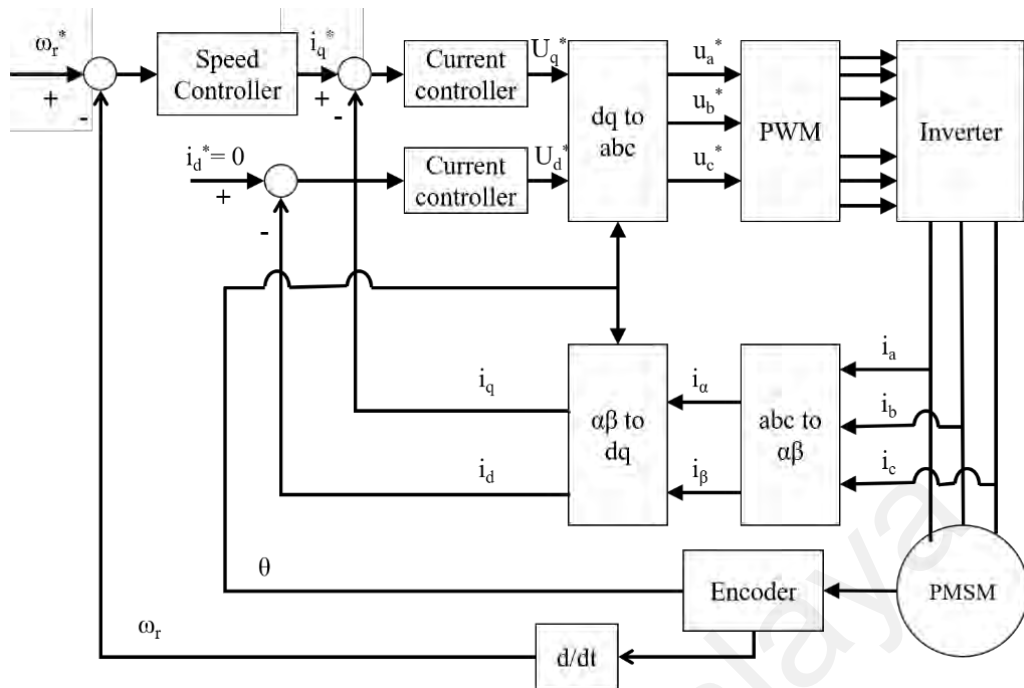
Figure 3.1: Block diagram of indirect field-oriented control of PMSM

This configuration consists of a PMSM with encoder, a pulse width modulation (PWM) voltage source inverter (VSI), a speed controller, two current controllers and coordinate transformers. The speed controller in the outer loop responds to speed error, which is the difference between actual speed and reference speed. Actual speed is obtained from the encoder signal corresponding to rotation of the rotor in PMSM. The output of speed controller provides q-axis current reference value for execution of q-axis current regulation in the inner loop that is responsible of controlling the torque of PMSM. On the other hand, d-axis current controller corresponds to flux control. Current sensors are used to measure the actual current that flows into the motor to be fed into the current controllers as feedback. The output of both current controllers defines reference voltage for PWM in dq-coordinate. Inverse Clarke and Park transformation convert it into abc-coordinate required by PWM to generate appropriate switching signals to the three-phase two-level VSI inverter.

3.2.1 Mathematical Model of PMSM

In field-oriented control of PMSM, stator voltage equations are defined in the rotor reference frame in equation (3.1) until (3.2) with $\omega_f = n_p \omega_r$ (Pillay & Krishnan, 1989) and illustrated in Figure 3.2. It is assumed that the induced EMF is sinusoidal, eddy current and hysteresis losses are negligible and saturation is neglected. Equation (3.3) defines electric torque.

$$u_d^* = R_s i_d^* + \dot{\lambda}_d - \omega_f \lambda_q \tag{3.1}$$

$$u_q^* = R_s i_q^* + \dot{\lambda}_q + \omega_f \lambda_d \tag{3.2}$$

$$Te = 1.5 n_p \left[L_{md} I_{df} i_q^* + \left(L_d - L_q \right) i_d^* i_q^* \right] \tag{3.3}$$
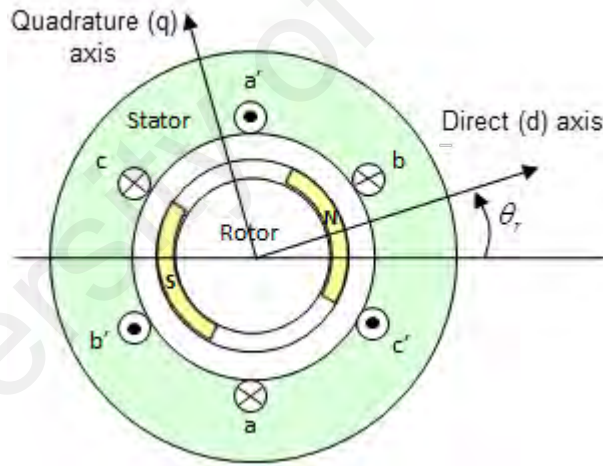
Figure 3.2: Rotor reference frame of a three phase single pole pair PMSM (Mathworks, 2019)

d,q-axis stator flux linkages, λ_d, λ_q are defined in equation (3.4) and (3.5).

$$\lambda_q = L_q i_q^* \tag{3.4}$$

$$\lambda_d = L_d i_d^* + L_{md} I_{df} \tag{3.5}$$

Motor dynamics is described in equation (3.6).

$$T_e = J\dot{\omega}_r + B_m\omega_r + T_L \qquad (3.6)$$

In this study, the constant torque angle (CTA) control strategy is used. This control strategy in commonly used in many drive applications and suitable for speed lower than the base speed (Krishnan, 2001). Furthermore, this strategy can provide sufficiently good control for small saliency ratio machines $(L_d / L_q < 1)$ that is used for this study. Usage of other more complicated control strategies produces insignificant improvement in the control of this kind of motor (Purwadi et al., 2015). In the CTA control strategy $(\delta = 90°)$, d-axis stator current command, i_d^* is set to be zero. Hence, electromagnetic torque in equation (3.3) can be simplified as in equation (3.7) with $K_t = 1.5n_p L_{md} I_{df}$. Equating both equations (3.7) and (3.6), the state equation of the servo drive is obtained as per equation (3.8).

$$T_e = 1.5n_p \left[L_{md} I_{df} i_q^* \right] = K_t i_q^* \qquad (3.7)$$

$$\dot{\omega}_r = -\frac{B_m}{J}\omega_r + \frac{K_t}{J}i_q^* - \frac{T_L}{J} \qquad (3.8)$$

The main control problem is to ensure the motor speed, ω_r to track the desired speed command, ω_r^* asymptotically. For this purpose, the main speed controller i.e. the sliding mode controller provides an output in terms of q-axis stator current command, i_q^* as the control input for the inner q-axis current controller. The speed tracking error, $e(t)$ is defined in (3.9) with its derivative in (3.10), where $a = \frac{B_m}{J}, b = \frac{K_t}{J}, c = \frac{T_L}{J}$.

$$e(t) = \omega_r^*(t) - \omega_r(t) \qquad (3.9)$$

$$\dot{e}(t) = -ae(t) - bi_q^*(t) + \phi(t) + \delta(t) \qquad (3.10)$$

$\phi(t)$ and $\delta(t)$ are defined in equation (3.11) and (3.12) respectively with $\Delta a, \Delta b, \Delta c$ as the time-varying value of the system parameters. Lumped uncertainty, $\delta(t)$ is considered bounded with $|\delta(t)| \leq \Omega$ and $\Omega \in \mathbb{R}^+$.

$$\phi(t) = a\omega_r^*(t) + c(t) + \dot{\omega}_r^*(t) \qquad (3.11)$$

$$\delta(t) = \Delta a\omega_r(t) - \Delta bi_q^*(t) + \Delta c(t) \qquad (3.12)$$

3.2.2 Programming of PMSM model in MATLAB/Simulink

The mathematical model of PMSM elaborated in Subsection 3.2.1 is then programmed as a subsystem in the MATLAB/Simulink environment as shown in Figure 3.3 to simulate actual PMSM behaviour under the proposed control structure.
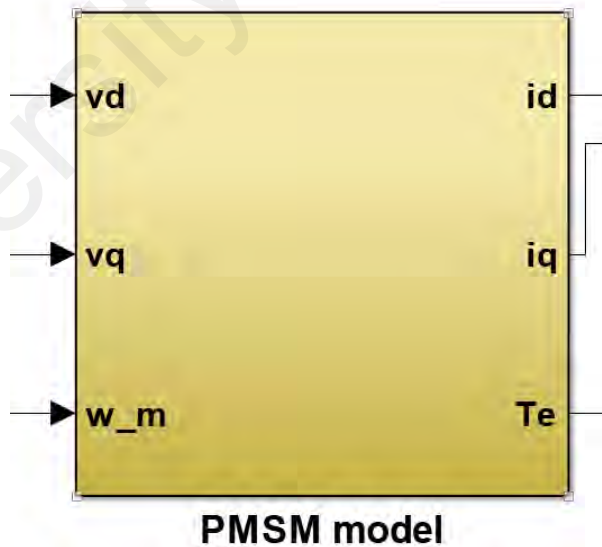
Figure 3.3: PMSM model subsystem in MATLAB/Simulink environment

Standard Simulink blocks are used for this purpose, as shown in Figure 3.4. Apart from mathematical equations mentioned in the previous section, a few additional standard

53

conversion equations are used such as mechanical speed to electrical speed conversion

equation (3.13) and mechanical angle to electrical angle conversion equation (3.14).

$$\omega_e = n_p \omega_m \tag{3.13}$$

$$\theta_e = n_p \theta_m \tag{3.14}$$
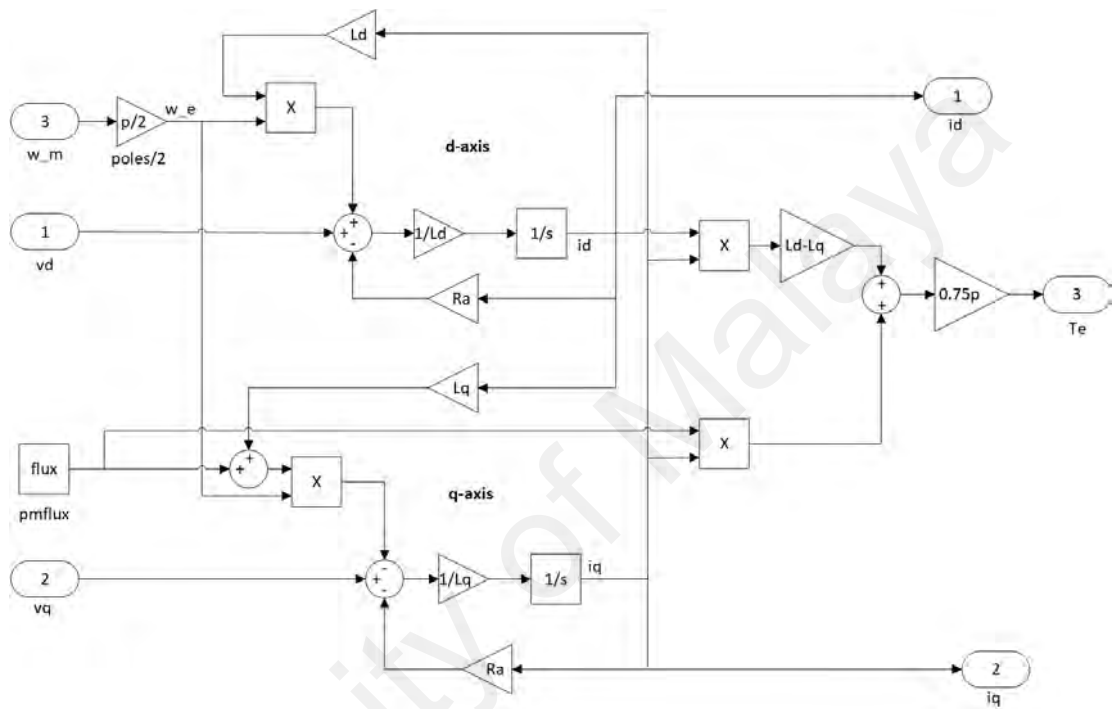
Figure 3.4: PMSM model based on equation (3.1) and (3.2)

The dynamics model of the motor as described in equation (3.6) is realized as in Figure

3.5. Complete PMSM model is also included in Appendix A.
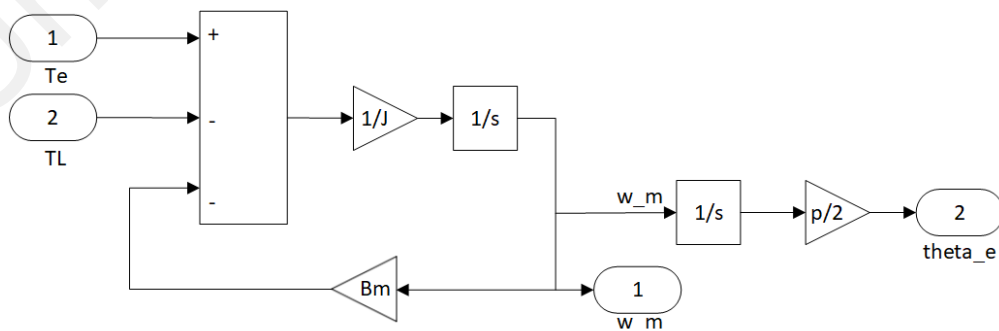
Figure 3.5: Motor dynamics model

3.3 Design of the Proposed FOSMC

Designing a SMC requires two major steps; firstly, to construct the sliding surface ($s(t)$) and secondly, to obtain the equivalent control law that determines the controller's output. In this study, a fractional PID ($PI^\alpha D^\beta$) sliding surface is proposed, which consists of proportional term, fractional integration and fractional differentiation term. The sliding surface is defined in equation (3.15), where ${}_0D_t^{-\alpha}(.)$ is a fractional integration of order α and ${}_0D_t^{\beta}(.)$ is a fractional differentiation of order β. α and β lies between 0 and 1. By selecting $\alpha = \beta = 1$, a classical integer order PID sliding surface is obtained. k_p, k_i and k_d are coefficients of proportional, fractional integration and fractional differentiation respectively.

$$s(t) = k_p e(t) + k_i \, {}_0D_t^{-\alpha} e(t) + k_d \, {}_0D_t^{\beta} e(t) \tag{3.15}$$

Other than sliding surface, reaching law also needs to be defined in sliding mode controllers. This law specifies the dynamics of switching around the sliding surface. In this work, the constant and proportional rate reaching law in equation (3.16) is adopted, where $w, k_s \in \mathbb{R}^+$. The sign function is defined in equation (3.17).

$$\dot{s} = -ws - k_s sign(s) \tag{3.16}$$

$$sign(s) = \begin{cases} 1 \, , \ s > 0 \\ 0 \, , \ s = 0 \\ -1, \ s < 0 \end{cases} \tag{3.17}$$

Sliding mode controllers operate based on its equivalent control law. This law combines plant dynamics with dynamics of the chosen sliding manifold and switching around it. To

obtain the equivalent control law, a derivative of the sliding surface, $\dot{s}(t)$ is constructed first as in equation (3.18).

$$\dot{s} = \frac{ds}{dt} = \frac{d}{dt}\left(k_p e(t) + k_{i\,0}D_t^{-\alpha}e(t) + k_{d\,0}D_t^{\beta}e(t)\right) \tag{3.18}$$

This equation is then extended to equation (3.19) by incorporating motor dynamics and control problem terms specified in equation (3.9) and (3.10).

$$\dot{s} = k_{i\,0}D_t^{1-\alpha}e(t) + k_{d\,0}D_t^{\beta+1}e(t) + k_p\left[-ae(t) - bi_q^*(t) + \phi(t)\right] \tag{3.19}$$

In (3.19), $\dot{s}(t)$ is then replaced with control law in (3.16). At this step, ideal condition is considered, where the lumped uncertainty is ignored $(\delta(t) = 0)$. The equivalent control law is obtained as in equation (3.20). $i_q^*(t)$ is the output of the proposed FOSMC for speed control of PMSM and fed as a reference value for q-axis current controller in the inner loop.

$$i_q^*(t) = \left(bk_p\right)^{-1}\begin{bmatrix}k_{i\,0}D_t^{1-\alpha}e(t) + k_{d\,0}D_t^{\beta+1}e(t) + (w-a)k_p e(t) + k_p\phi(t) \\ + wk_{i\,0}D_t^{-\alpha}e(t) + wk_{d\,0}D_t^{\beta}e(t) + k_s sign(s)\end{bmatrix} \tag{3.20}$$

3.3.1   Stability Analysis of the Proposed FOSMC

In sliding mode control theory, a sliding mode controller is considered stable when two conditions are satisfied namely the reaching condition of the proposed sliding manifold is satisfied and the system stability when sliding mode occurs is satisfied. Stability analysis must be executed for both conditions. Reaching condition of the proposed fractional sliding manifold must be satisfied to ensure convergence of system state to the manifold for any initial condition. For this purpose, the Lyapunov stability theorem is used, where the Lyapunov function candidate is chosen as in equation (3.21)

for system initial states $t_0 \neq 0$. The reaching condition is satisfied when $\dot{V} < 0$ holds or $s\dot{s} < 0$.

$$V = \frac{1}{2}s^2 \tag{3.21}$$

Hence,

$$
\begin{aligned}
\dot{V} \quad &= s \times \dot{s} \\
&= s \times \frac{d}{dt}\Big[k_p e(t) + k_{i\,0}D_t^{-\alpha}e(t) + k_{d\,0}D_t^{\beta}e(t) \Big] \\
&= s \times \Big[k_{i\,0}D_t^{1-\alpha}e(t) + k_{d\,0}D_t^{\beta+1}e(t) + k_p\big(-ae(t) - bi_q^*(t) + \phi(t) + \delta(t)\big) \Big] \\
&= s \times \Big[-ws - k_s sign(s) + k_p\delta(t) \Big] \\
&= -ws^2 - k_s|s| + k_p\delta(t)s
\end{aligned}
\tag{3.22}
$$

From equation (3.22), it shows that $\dot{V} < 0$ holds when $k_s > k_p|\delta(t)|$ is satisfied or $k_s / k_p > |\delta(t)|$ is satisfied. Assumed that $|\delta(t)| \leq \phi \in \mathbb{R}^+$, then, according to Lyapunov stability theorem, the reaching condition of the proposed FOSMC is satisfied if $k_s / k_p > \phi$. In addition, convergence properties of the chosen reaching law are analysed for two initial states, $s(t_0)$ (B. Zhang et al., 2012). For $s(t_0) > 0$, equation (3.16) becomes (3.23).

$$\dot{s} = -ws - k_s \tag{3.23}$$

In this case, the solution for s is as shown in (3.24), which implies that when time, t in (3.25) is satisfied, the system will converge to switching manifold.

$$s = [s(t_0) + w^{-1}k_s]e^{-w(t-t_0)} - w^{-1}k_s \tag{3.24}$$

$$t = t_0 - \frac{1}{w} \ln \frac{k_s}{ws(t_0) + k_s} \tag{3.25}$$

Similarly, reaching law equation becomes (3.26) when $s(t_0) < 0$.

$$\dot{s} = -ws + k_s \tag{3.26}$$

From the solution of s in (3.27), system convergence to switching manifold is guaranteed when time in (3.28)(3.35) is satisfied.

$$s = [s(t_0) - w^{-1}k_s]e^{-w(t-t_0)} + w^{-1}k_s \tag{3.27}$$

$$t = t_0 - \frac{1}{w} \ln \frac{k_s}{k_s - ws(t_0)} \tag{3.28}$$

Above analysis concludes that with the chosen reaching law in equation (3.16), the system will converge to the switching manifold at any initial state when inequality (3.29) is satisfied.

$$t \geq t_0 - \frac{1}{w} \ln \frac{k_s}{w|s(t_0)| + k_s} \tag{3.29}$$

After reaching condition is ensured, the stability of the system during sliding phase must be analysed. For that purpose, Lemma below is presented, followed by its corresponding theorem and proof.

Lemma. (Matignon, 1996) The autonomous fractional order system in (3.30) is considered, where $x \in \mathbb{R}^n$, $A = (a_{ij}) \in \mathbb{R}^{n \times n}$, $0 < r < 1$.

$$_0D_t^r x(t) = A \cdot x(t), \quad x(0) = x_0 \tag{3.30}$$

58

The system is asymptotically stable if and only if the condition in (3.31) is satisfied.

$$\left|\arg(eig(A))\right| > \frac{\pi}{2}r \qquad (3.31)$$

In this case, the components of the state decay towards 0 like t^{-r}.

Theorem. The system in equation (3.15) is stable when below conditions are synchronously satisfied:

$$k_p, k_i, k_d > 0$$

$$0 < \alpha, \beta < 1$$

Proof. When sliding mode occurs, system (3.15) can be represented as follows:

$$k_p e(t) + k_{i\ 0}D_t^{-\alpha}e(t) + k_{d\ 0}D_t^{\beta}e(t) = 0 \qquad (3.32)$$

Performing fractional differentiation on both sides of equation (3.32), equation (3.33) is obtained.

$$k_p D^{\alpha}e(t) + K_i e(t) + K_d D^{\beta+\alpha}e(t) = 0 \qquad (3.33)$$

Hence, from (3.33), the sliding mode dynamics can be represented by the equations (3.34) and (3.35), where $e_1 = e(t)$.

$$_0D_t^{\alpha}\left(e_1\right) = e_2 \qquad (3.34)$$

$$_0D_t^{\beta}\left(e_2\right) = -\frac{k_i}{k_d}(e_1) - \frac{k_p}{k_d}(e_2) \qquad (3.35)$$

Equation (3.34) and (3.35) can be represented in matrix form as:

$$\begin{bmatrix} {}_0 D_t^{\alpha}(e_1) \\ {}_0 D_t^{\beta}(e_2) \end{bmatrix} = \begin{bmatrix} 0 & 1 \\ -\dfrac{k_i}{k_d} & -\dfrac{k_p}{k_d} \end{bmatrix} \begin{bmatrix} e_1 \\ e_2 \end{bmatrix} \tag{3.36}$$

$$\begin{bmatrix} {}_0 D_t^{\alpha}(e_1) \\ {}_0 D_t^{\beta}(e_2) \end{bmatrix} = A \begin{bmatrix} e_1 \\ e_2 \end{bmatrix} \tag{3.37}$$

By Lemma, system (3.15) is stable if the condition in (3.31) is satisfied. Since $0 < \alpha, \beta < 1$ is satisfied, hence, $0 < \alpha\pi/2 < \pi/2$ and $0 < \beta\pi/2 < \pi/2$. The stability region is depicted in Figure 3.6.
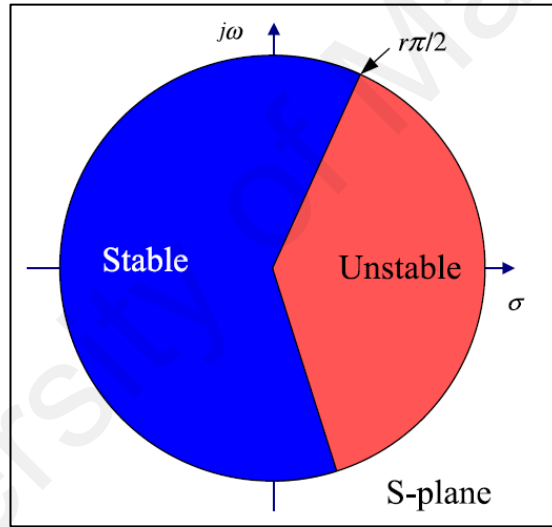
Figure 3.6: Stability region of fractional order system in S-plane (B. Zhang et al., 2012)

From equations (3.31) and (3.36), for $0 < r < 1$, inequality in equation (3.38) is obtained.

$$0 < \frac{k_p}{\sqrt{k_p^2 - 4k_i k_d}} < \frac{\pi}{2} \tag{3.38}$$

Hence, from equation (3.38), stability condition in Lemma is satisfied if $0 < k_p < 2.593\sqrt{k_i k_d}$ and $k_p \neq 2\sqrt{k_i k_d}$.

3.3.2 Programming of FOSMC in MATLAB/Simulink

In this work, fractional calculus is realized in MATLAB/Simulink environment using the Ninteger toolbox developed by Valerio and Da Costa (2004). This toolbox is also used in many other works of literature (Azar, Radwan, & Vaidyanathan, 2018; Petráš, 2011; Szewczyk, Zieliński, & Kaliczyńska, 2015). Compared to other fractional calculus toolboxes such as CRONE (Oustaloup, Melchior, Lanusse, Cois, & Dancla, 2000) and FOMCON (Tepljakov, Petlenkov, & Belikov, 2011), Ninteger toolbox is chosen due to its easy availability, systematic and user-friendly parameter window and multiple options of approximation algorithm parameters to suit various applications. This toolbox also allows the implementation of fractional calculus in both time and frequency domain.

Ninteger toolbox consists of two main blocks (*nintblocks*) namely *nid* block and *nipid* block. *nid* block is used to incorporate fractional calculus as part of a controller or system, whereas *nipid* block is a pre-programmed fractional PID controller with user-defined parameters. In this work, *nid* block is used among other standard Simulink blocks to construct equivalent control law as obtained in equation (3.20).

Figure 3.7 shows the default parameter window of *nid* block when added to a Simulink model. *nid* block provides integer approximations of equation $k*s^v$, where parameter k is a constant and parameter v is the selected order of fractional calculus. For $0<v<1$, fractional derivative is performed and for $-1<v<0$, fractional integration is performed. Parameter *bandwidth* and *n* have a different definition in continuous approximation and digital approximation application.
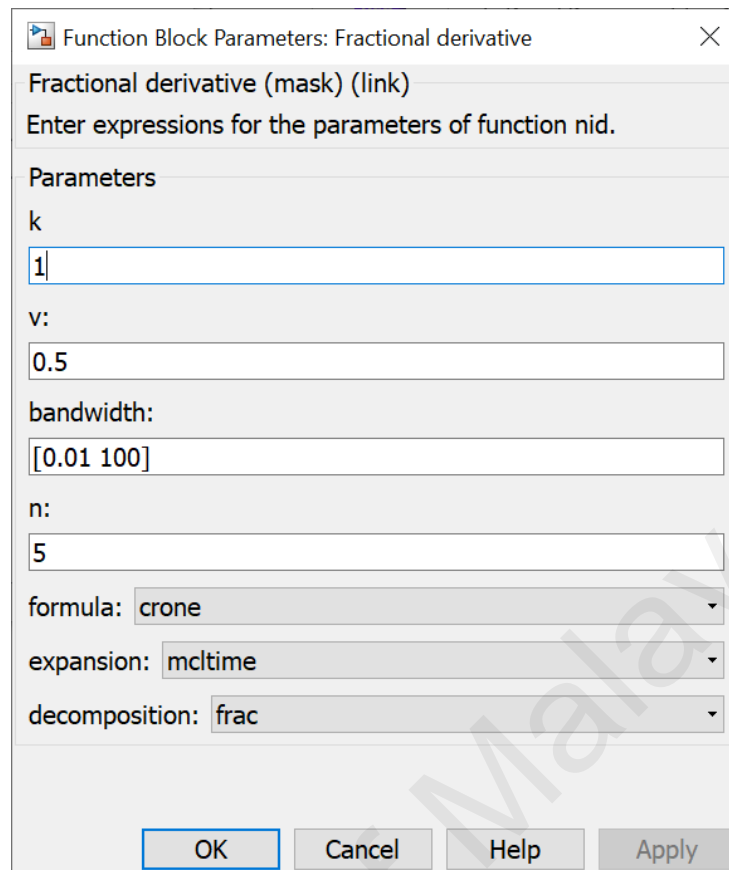
Figure 3.7: Default parameter window of *nid* block

Details on parameters setting for *nid* block is presented in Table 3.1.

Table 3.1: Parameters setting in *nid* block

Parameter in *nid* block	Item	Application type	
		Continuous approximation	Digital approximation
k	Definition	constant	
	Value restriction	$k > 0$	
	Unit	nil	
v	Definition	order of fractional calculus	
	Value restriction	$-1 < v < 1$	
	Unit	nil	
bandwidth	Definition	frequency range of validity	sampling time
	Value restriction	nil	nil
	Unit	rad/s	s

Parameter in *nid* block	Item	Application type	
		Continuous approximation	Digital approximation
n	Definition	number of zeros and poles	maximum number of delays
	Value restriction	Integer, $n > 0$	
	Unit	nil	nil
formula	Definition	Approximation formula of fractional calculus	
	Selection	5 out of 13 formulas	8 out of 13 formulas
expansion	Definition	Variable expansion method	
	Selection	neglected	McLaurin series expansion, continued fraction expansion
decomposition (optional)	Definition	Approximation of order, *v* during variable decomposition	
	Selection	• 'frac' - (default) order v - floor(v) is approximated and added to the integer part floor(v) • 'all' - order v is approximated	

Approximation formula for $k*s^v$ is chosen by selecting one formula from 13 available formulas provided by this toolbox as listed in its dropdown menu, as detailed in Table 3.2.

Table 3.2: Approximation formula of fractional calculus

	No	Approximation formula	Details
Application type: Continuous approximation	1	crone	first generation Crone approximation with n zeros and n poles, valid in frequency range [bandwidth(1); bandwidth(2)] rad/s (Oustaloup, 1991)
	2	carlson	Carlson approximation with at least n zeros and n poles, valid around frequency bandwidth rad/s or sqrt(bandwidth(1)*bandwidth(2)) rad/s
	3	matsuda	Matsuda approximation with n zeros and poles, valid in frequency range [bandwidth(1); bandwidth(2)] rad/s

No	Approximation formula	Details
4	cfehigh	approximation based upon the continued fraction expansion of $(1+s)^v$ with about n zeros and n poles, valid from bandwidth rad/s up
5	cfelow	approximation based upon the continued fraction expansion of $(1+1/s)^{(-v)}$ with about n zeros and n poles, valid until bandwidth rad/s
6	tustin	Tustin approximation formula
7	simpson	Simpson approximation formula
8	1ofd	first order backwards finite difference approximation
9	2ofd	second order backwards finite difference approximation
10	3ofd	third order backwards finite difference approximation
11	delta	delta transform approximation
12	impulse	impulse response approximation
13	step	Step response approximation

The left column for rows 4–5 and 6–13 contains: "Application type: Digital approximation"

In this simulation work, crone approximation is selected with McLaurin expansion method. Parameters *v* and *bandwidth* are given by variables "order" and the range between "b1" and "b2" respectively, which are pre-defined in Callback function "InitFcn" under "Model Properties" menu of the Simulink model. Table 3.3 summarizes the parameter setting of *nid* block used in this work.

Table 3.3: Chosen parameters setting of *nid* block

Parameter	Values/Option	Fixed/Variable
k	1	Fixed
v	"-order" for fractional integration, "order2" for fractional differentiation	Variable
bandwidth	[0.001 1000]	Fixed
n	5	Fixed
formula	crone	Fixed
expansion	mcltime	Fixed
decomposition	frac	Fixed

Crone formula is chosen since it is a well-known formula as far as fractional calculus is concerned and it was developed by pioneers of fractional calculus namely Oustaloup (1991). This formula uses the recursive distribution of N poles and N zeros, as presented by equation (3.39).

$$C(s) = k \prod_{n=1}^{N} \frac{1 + s / \omega_{zn}}{1 + s / \omega_{pn}} \tag{3.39}$$

As shown in Figure 3.8, parameter k is chosen to be 1, so that $|C(s)| = 0 dB$ at 1 rad/s. Zeros and poles are found inside the defined bandwidth or frequency interval. For positive v, equations (3.40)-(3.42) are used, whereas for negative v, the role of zeros and poles is interchanged (Valerio & Da Costa, 2004).

$$\alpha = \left(\omega_h / \omega_l \right)^{\frac{v}{N}}, \quad \eta = \left(\omega_h / \omega_l \right)^{\frac{1-v}{N}} \tag{3.40}$$

$$\omega_{z1} = \omega_l \sqrt{\eta}, \quad \omega_{zn} = \omega_{p,n-1} \eta, \quad n = 2....N \tag{3.41}$$

$$\omega_{pn} = \omega_{z,n-1} \alpha, \quad n = 1....N \tag{3.42}$$

Six *nid* blocks with different parameter selection are used to realize fractional order sliding mode speed control used in this research, among other standard blocks in Simulink. This speed controller is programmed in subsystem "FOSMC", as shown in Figure 3.9 and detailed in Appendix B. It acquires speed error and reference speed as its input and gives reference q-axis current value as its output.

Figure 3.8: Chosen parameters for *nid* block

Figure 3.9: Subsystem "FOSMC" as part of the motor drive program

3.4   Design of the Current Controllers

The indirect FOC method used in this research requires current control to be decoupled into d- and q-axis components, which are responsible for flux and torque control respectively. Conventional PI controller is chosen for both current controllers in the inner loop to ensure their execution is fast enough to support the outer speed control in providing excellent speed tracking. Similar recent previous works also use the PI controller in the inner loop (Y. Wang, Feng, Zhang, & Liang, 2019; W. Xu et al., 2019).

Current controllers are designed from voltage equations of the PMSM mathematical model defined in Subsection 3.2.1. By putting equation (3.4) and (3.5) as well as derivatives of d,q-axis stator flux linkages in equation (3.1) and (3.2), equation for d-axis (3.43) and q-axis (3.44) current controllers are obtained.

$$u_d^* = R_s i_d^* + L_d \dot{i}_d^* - \omega_f L_q i_q^* \tag{3.43}$$

$$u_q^* = R_s i_q^* + L_d \dot{i}_q^* + \omega_f L_d i_d^* + \omega_f L_{md} I_{df} \tag{3.44}$$

As shown in the indirect FOC block diagram in Figure 3.1, the output of the fractional order sliding mode speed controller designed in Subsection 3.3 is fed as a reference value of q-axis current controller. For d-axis current controller, the reference value is set to be zero since CTA control strategy is used. Actual currents, $i_{a,b,c}$ are obtained either from the PMSM model as detailed in Subsection 3.2.2 during simulation run or measured using current sensors during the actual experimental run, which is detailed in Subsection 3.7.4.1. The current values are then transformed to αβ0-coordinates using Clarke transformation (equation (3.45)), prior to being transformed to dq0-coordinates using Park transformation (equation (3.46)).

$$\begin{bmatrix} I_\alpha \\ I_\beta \\ I_0 \end{bmatrix} = \begin{bmatrix} 1 & -\dfrac{1}{2} & -\dfrac{1}{2} \\ 0 & \dfrac{\sqrt{3}}{2} & -\dfrac{\sqrt{3}}{2} \\ \dfrac{1}{2} & \dfrac{1}{2} & \dfrac{1}{2} \end{bmatrix} \begin{bmatrix} I_a \\ I_b \\ I_c \end{bmatrix} \tag{3.45}$$

$$\begin{bmatrix} I_d \\ I_q \end{bmatrix} = \begin{bmatrix} \cos\theta & \sin\theta \\ -\sin\theta & \cos\theta \end{bmatrix} \begin{bmatrix} I_\alpha \\ I_\beta \end{bmatrix} \tag{3.46}$$

Other than actual currents, the current controllers also acquire actual electrical speed of the motor to perform its operation. During simulation, this information is obtained from PMSM model as detailed in Subsection 3.2.2, whereas during experiment, it is calculated using incremental encoder position data detailed in Subsection 3.7.4.3. The output of both current controllers are voltage references in dq-coordinates, which are then transformed back to abc-coordinates using inverse Clarke and Park transformations as defined in equation (3.47) and (3.48) respectively. These voltage references will determine operation of succeeding pulse width modulation (PWM) block.

$$\begin{bmatrix} I_a \\ I_b \\ I_c \end{bmatrix} = \begin{bmatrix} 1 & 0 & 1 \\ -\dfrac{1}{2} & \dfrac{\sqrt{3}}{2} & 1 \\ -\dfrac{1}{2} & -\dfrac{\sqrt{3}}{2} & 1 \end{bmatrix} \begin{bmatrix} I_\alpha \\ I_\beta \\ I_0 \end{bmatrix} \tag{3.47}$$

$$\begin{bmatrix} I_\alpha \\ I_\beta \end{bmatrix} = \begin{bmatrix} \cos\theta & -\sin\theta \\ \sin\theta & \cos\theta \end{bmatrix} \begin{bmatrix} I_d \\ I_q \end{bmatrix} \tag{3.48}$$

3.4.1 Calculation of current controller's parameters

The first two terms of equations (3.43) and (3.44) are used to construct PI current controller, whereas other remaining terms are added and/or subtracted to the PI controller's output. The proportional coefficient, K_p and integral coefficient, K_i are calculated using equations (3.49)-(3.52) (Capitan, 2009), where d-axis electrical time constant, $\tau_d = L_d / R_s$, q-axis electrical time constant, $\tau_q = L_q / R_s$ and delay time constant, $T_{si} = 2.5 * T_{sw}$.

$$PI\_Kp\_d = \frac{R_s * \tau_d}{2T_{si}} \tag{3.49}$$

$$PI\_Kp\_q = \frac{R_s * \tau_q}{2T_{si}} \tag{3.50}$$

$$PI\_Ki\_d = \frac{PI\_Kp\_d}{\tau_d} \tag{3.51}$$

$$PI\_Ki\_q = \frac{PI\_Kp\_q}{\tau_q} \tag{3.52}$$

Hence, based on parameters of PMSM used in this work, parameters of d-axis and q-axis PI current controllers are chosen to be as listed in Table 3.4.

Table 3.4: Parameters of current controllers

Parameter	Parameter name	Value
Proportional coefficient of d-axis PI current controller	*PI_Kp_d*	4.8
Integral coefficient of d-axis PI current controller	*PI_Ki_d*	960
Proportional coefficient of q-axis PI current controller	*PI_Kp_q*	5.4
Integral coefficient of q-axis PI current controller	*PI_Ki_q*	960

3.4.2 Programming of Current Controllers in MATLAB/Simulink

d-axis and q-axis current controllers designed in the previous section are programmed separately in their own subsystem in MATLAB/Simulink environment, as shown in Figure 3.10.
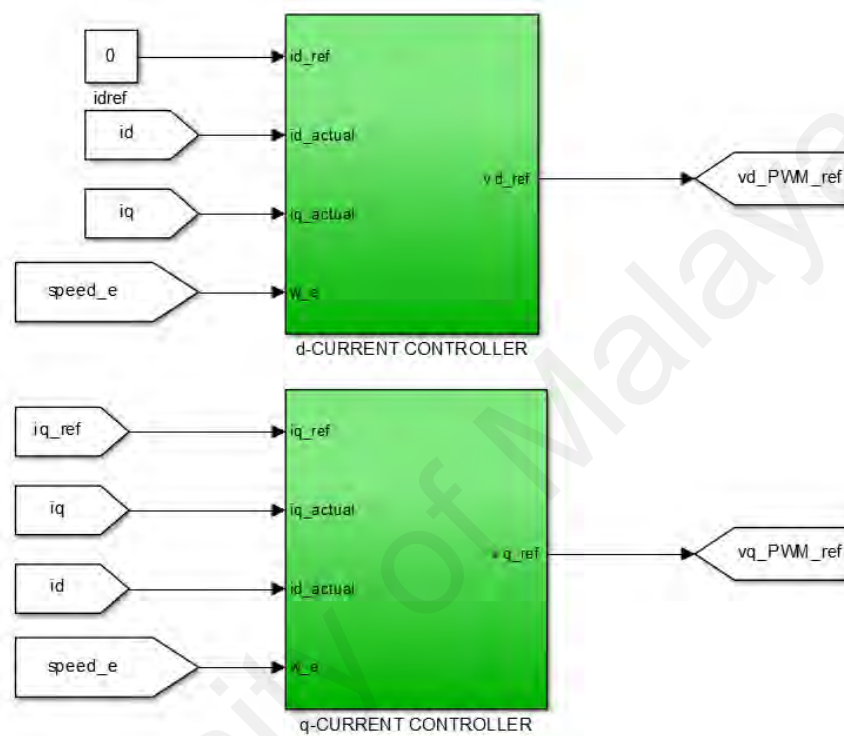
Figure 3.10: d-axis and q-axis current controller subsystems

As shown in Figure 3.11 and Figure 3.12, standard PID block is used to realize the PI current controllers in MATLAB/Simulink environment.
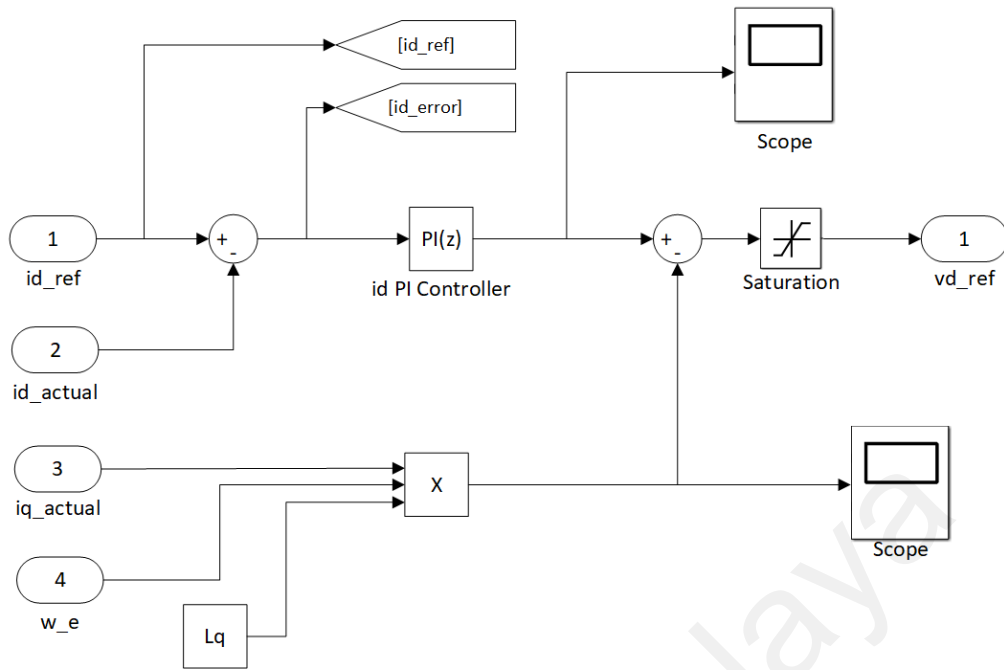
Figure 3.11: d-axis current controller
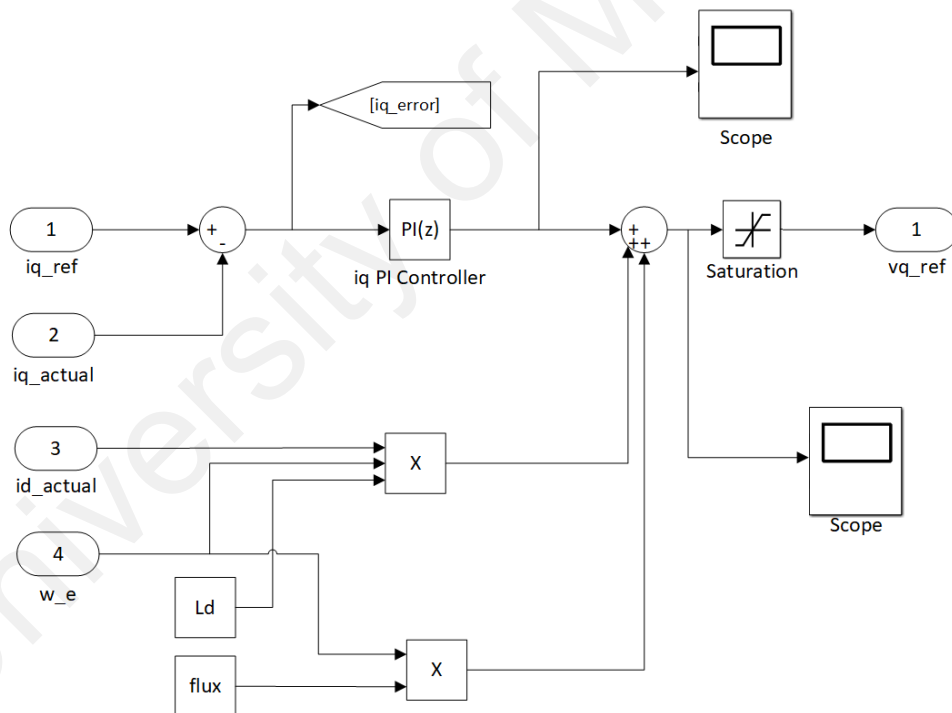
Figure 3.12: q-axis current controller

Among other required settings, calculated coefficients are fixed values used in the function block settings, as shown in Appendix E. The coefficient values are pre-defined in the Callback function "InitFcn" under the "Model Properties" menu of the Simulink model with values in Table 3.4.

3.5   Sinusoidal Pulse Width Modulation

The output of d-axis and q-axis current controllers described in Subsection 3.4 provides reference voltages for the operation of pulse width modulation (PWM). Interception points of the reference voltage waveform and a triangular waveform result in a rectangular pulse with modulated pulse width, which varies its average value. There are several PWM techniques proposed in previous literature such as single-pulse width modulation, multiple-pulse width modulation, hysteresis band pulse width modulation and sinusoidal pulse width modulation (SPWM). In this work, the latter technique of PWM is used namely the sinusoidal PWM.

Sinusoidal PWM technique is widely used in industrial applications. In SPWM, the output is generated by comparing a reference sinusoidal wave (in this work, reference sinusoidal voltage) with a high-frequency triangular carrier wave, as illustrated in Figure 3.13. The frequency of the modulating wave decides the frequency of the output voltage. The peak amplitude of the modulating wave decides the modulation index and controls the RMS value of output voltage. Compared to other multi-phase modulation techniques, SPWM is proven to improve the distortion factor more significantly. Furthermore, it also eliminates all harmonics less than or equal to $2p-1$, where p is defined as the number of pulses per half cycle of the sine wave. The higher order harmonics can be easily removed using filter (Hardik Shahane, 2018).
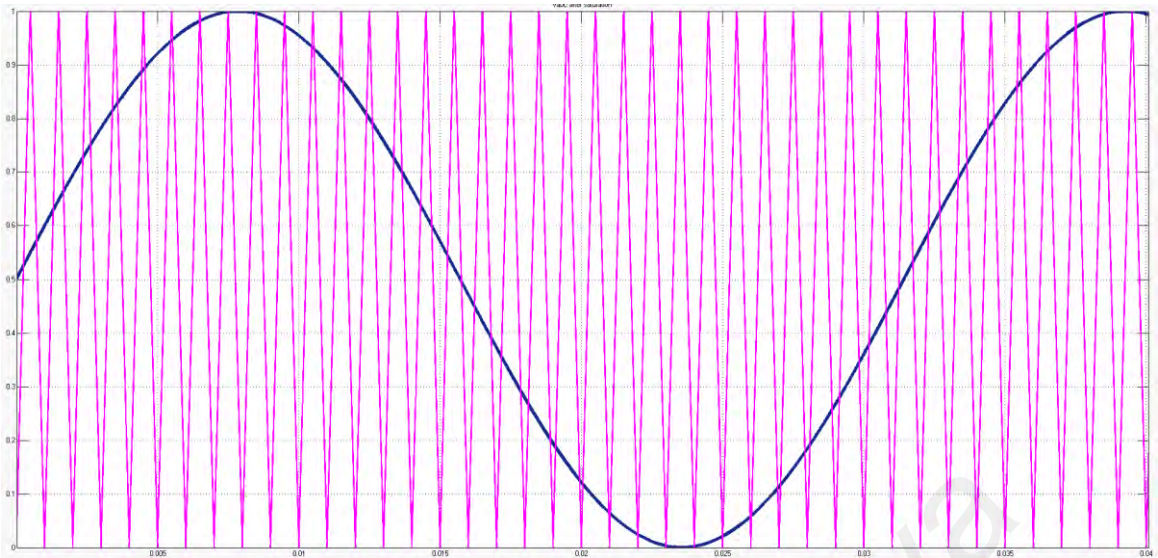
Figure 3.13: Sinusoidal PWM with reference signal (blue) and triangular carrier signal (magenta)

In common practice, carrier wave usually is programmed to have an amplitude of between -0.5 and 0.5. However, in the experimental approach of this research, PWM is executed using a standard built-in dSpace DS1104SL_DSP_PWM block. This block utilizes a triangular carrier wave of amplitude between 0 to 1. Hence, the reference voltages are scaled within this range prior to being fed into the PWM block as reference input. A similar approach is used in simulation work for simplicity purpose, as detailed in Appendix C. The carrier wave frequency can also be user-defined, based on required switching frequency, as shown in Appendix E. In this work, the selected switching frequency is 4kHz. This is due to the limitation of the developed prototype in terms of sampling time of dSpace DS1104 controller, when advanced controllers are used. With the proposed FOSMC, the sampling time is limited up to $5e^{-4}$ seconds only. An overrun error will occur if the controller is run with higher sampling time. Hence, this limitation also affects the switching frequency of PWM generation, where the maximum frequency of only 4kHz can be set. Three SPWM are required for three phase reference voltages on the input side. These PWMs provide output in the form of six switching signals for the succeeding three phase six switches two-level inverter described in Subsection 3.6.

73

3.6   Three Phase Six Switches Two-level Voltage Source Inverter

Sinusoidal PWM detailed in the preceding subsection produces three sets of switching signals for three phases operation of the PMSM with two complementary signals (0 or 1) in each set. This work implements a three phase six switches two-level voltage source inverter topology, which is suitable for low to medium power motor and for operation below motor's base speed compared to other topologies in comparison, as shown in Table 2.5. Figure 3.14 as well as Appendix D shows the inverter circuit developed in MATLAB/Simulink environment using six standard IGBT blocks for simulation purposes. However, in experimental verification, this circuit is omitted and replaced with an actual inverter hardware, which will be described in detail in Subsection 3.7.3.
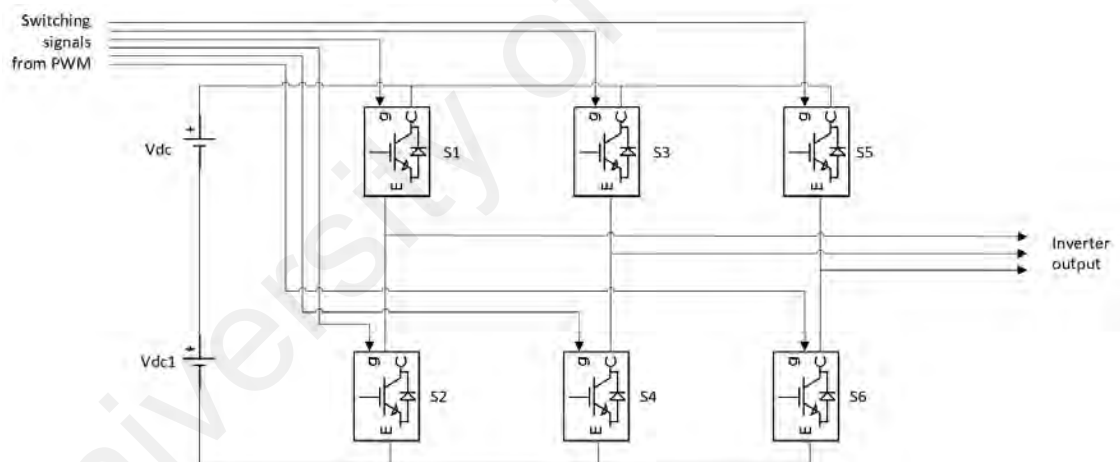
Figure 3.14: Inverter circuit from simulation

3.7   Development of Closed-Loop PMSM Drive System Prototype

In addition to simulation, the robustness and stability of the proposed control scheme are also verified through the actual experiment. The experimental setup is a closed-loop PMSM drive system prototype, which consists of an interior PMSM with built-in encoder, three phase voltage source inverter, AC source, two programming PC,

dSpace DS1104 controller, hysteresis brake, dynamometer controller, power analyser, speed/torque transducer, DC supplies and oscilloscope, as illustrated in Figure 3.15.
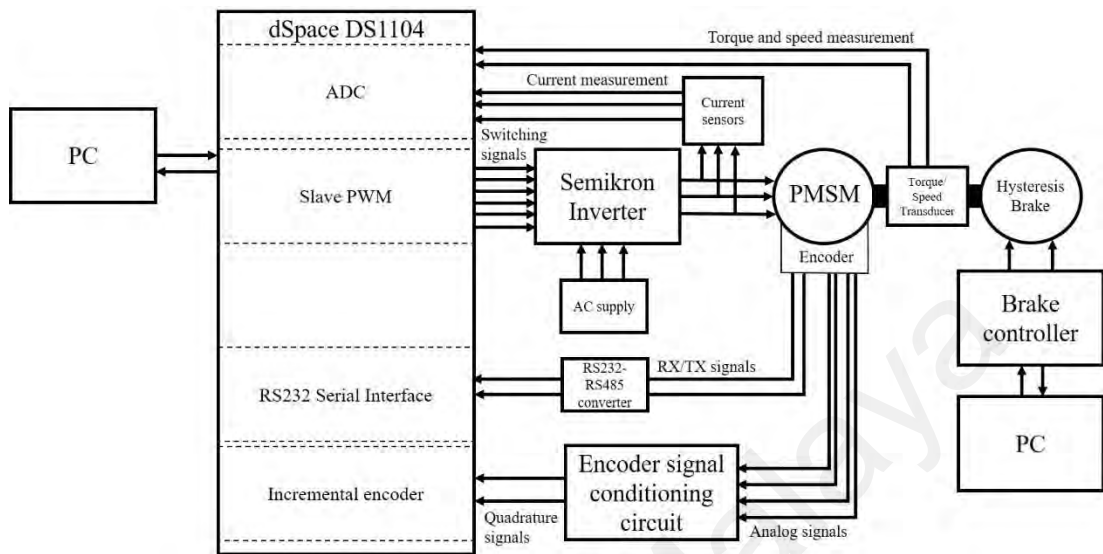
Figure 3.15: Closed-loop PMSM drive prototype architecture

C code of the designed controller, coordinate transformations and PWM is generated in MATLAB/Simulink and is uploaded to the DS1104 controller board. Inputs and outputs to and from the controller are obtained and distributed respectively using the CP1104 connector panel. Switching signals produced by the PWM are fed to the inverter. The inverter produces the appropriate output voltages for the motor. Encoder data is fed to the controller as feedback. From these data, the position of the rotor and the motor speed can be extracted. Other than that, output currents to the motor are measured using AC current sensor circuitries and are also fed back to the controller as feedback to the current controllers. Input signals monitoring and output signals monitoring/manipulation are executed within the ControlDesk software environment. Hysteresis brake AHB-3 was used to produce the required load torque for evaluation of the controller's performance in various load conditions. The development of the complete prototype is detailed further in the following subsections.

3.7.1   dSpace DS1104 Controller Board

The DS1104 R&D Controller Board is a real-time hardware based on the PowerPC 603e microprocessor and equipped with various I/O interfaces, as shown in Figure 3.16. In this work, external devices are connected to the controller board using connector panel CP1104 and LED panel CLP1104, which provides an additional array of LEDs indicating the states of the digital signals, as shown in Figure 3.17. The DS1104's main processing unit, MPC8240, consists of the master PPC that runs at 250 MHz (CPU clock), an interrupt controller, a synchronous DRAM controller, timers and a PCI interface. The master PPC controls the I/O features such as ADC unit, DAC unit, bit I/O, incremental encoder interface and serial interface.
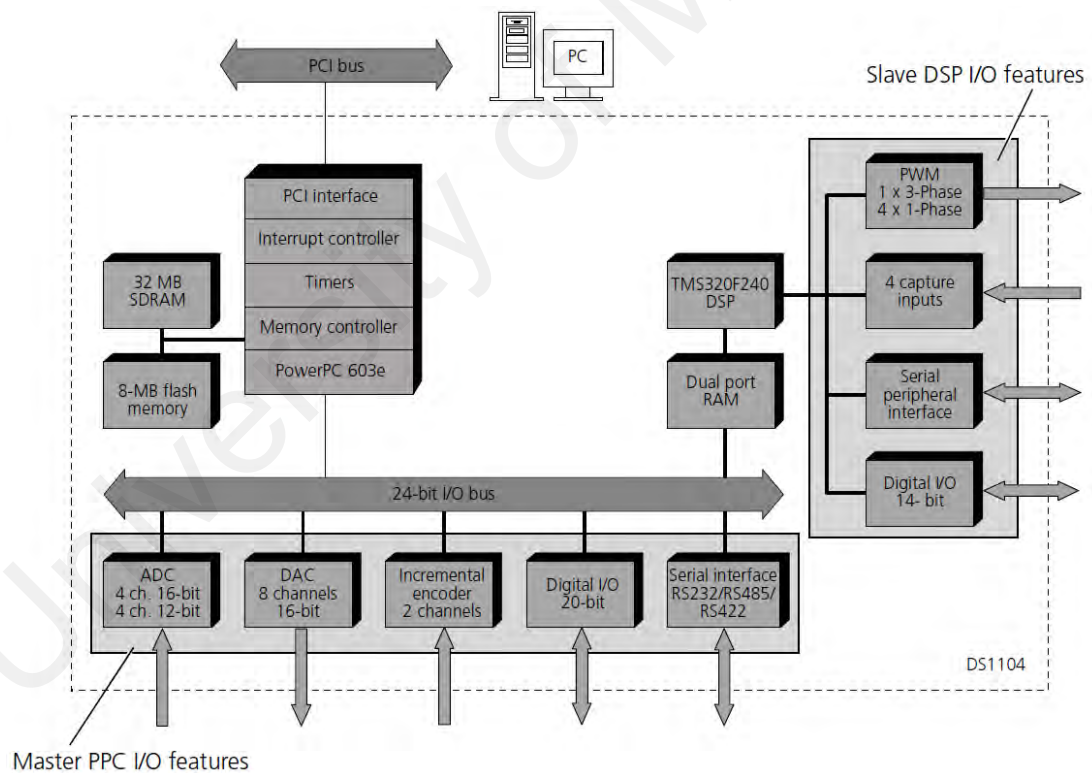
Figure 3.16: DS1104 Controller Board architecture
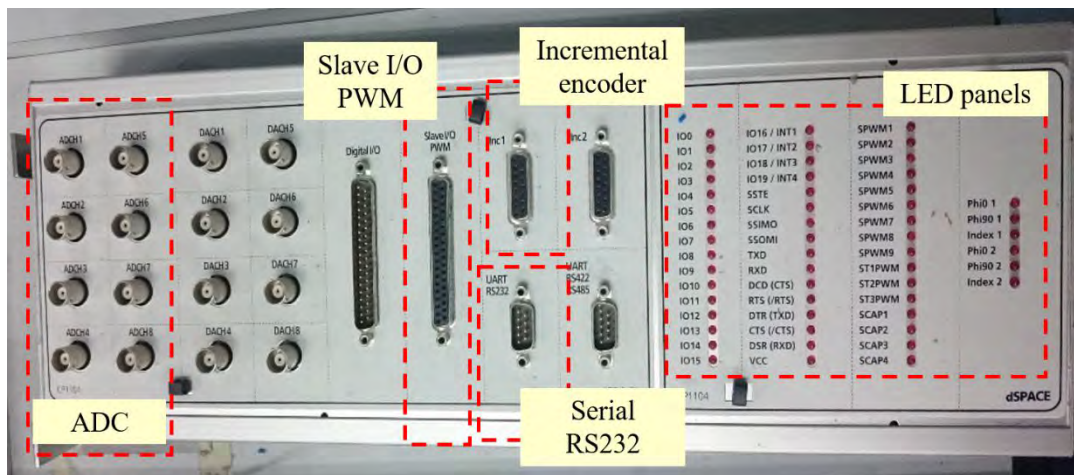
Figure 3.17: Connector panel CP1104 and LED panel CLP1104

The DS1104 contains two different types of ADC for the analog input channels namely one 16-bit ADC with four multiplexed input signals (ADCH1 - ADCH4) and four 12-bit parallel ADCs with one input signal each (ADCH5 - ADCH8). The analog inputs are single-ended bipolar inputs with an input voltage range between -10V and +10V.

In addition, the DS1104 is also equipped with a universal asynchronous receiver and transmitter (UART) to perform serial asynchronous communication with external devices. The UART interface is based on a 16C550C-compatible communication element (TL16C550C from Texas Instruments) and is driven by a 16 MHz oscillator. The UART can be used in the RS232, RS422 or RS485 transceiver mode with selectable baud rates up to 115.2 kBd (for RS232) or 1 MBd (for RS422/ RS485), selectable number of data bits, parity bit and stop bits and selectable software FIFO buffer size.

The master PPC on DS1104 also controls an incremental encoder interface, which is available through two digital incremental encoder input channels (INC1, INC2). These channels support single-ended TTL signals with 1.65 MHz maximum encoder line count frequency, hence, with internal 4-fold subdivision of each encoder line, the DS1104 can therefore handle count frequencies of up to 6.6 MHz. The position counter has 24-bit

resolution, with count direction depending on the encoder's rotation direction and can be reset by the encoder's index pulse.

The slave DSP on the DS1104 provides a timing I/O unit that can be used to generate and measure various pulse-width modulated (PWM) signals. In this work, 3-phase PWM signal (PWM3) is generated with non-inverted and inverted outputs with variable duty cycles, PWM frequencies (1.25 Hz - 5 MHz) and dead band. In PWM3 generation mode, the pulse pattern for the three non-inverted PWM signals SPWM1, SPWM3 and SPWM5 is as shown in Figure 3.18, where T_P is the PWM period.

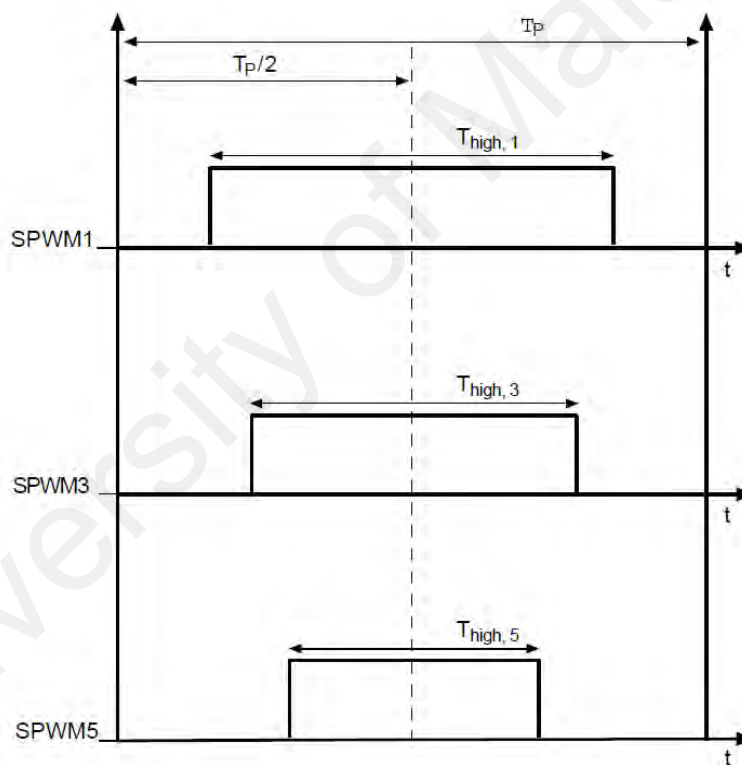Figure 3.18: Pulse pattern of three non-inverted PWM signals of a 3-phase PWM signals

Last but not least, the DS1104 provides access to various hardware interrupts, originating either from on-board devices such as timers or from external devices connected to the board, as summarized in Table 3.5. In the latter case, the interrupts are sampled at a frequency of bus clock (BCLK)/64. Interrupt-driven subsystems can be

78

implemented in MATLAB/Simulink environment by using specific interrupt blocks provided by RTI1104.

Table 3.5: Hardware interrupts provided by DS1104

Interrupt type	Description
ADC1-5 end of conversion	Interrupt on end of A/D conversion
Encoder index channels 1-2	Interrupt on index found
Host interrupt	Interrupt from the host PC
User interrupt 1-4	Interrupt from external device
Timer 0-3 and decrementer interrupt	Interrupt when timers reach 0
UART interrupt	Interrupt of the serial interface
Slave DSP Interrupt	Interrupt of the slave DSP to the master
Slave DSP PWM interrupt	PWM interrupt of the slave DSP

In this work, timer interrupt and Slave DSP PWM interrupt are used. Timer interrupts in DS1104 are obtained using 32-bit down counters driven by BCLK/8. The period of each timer can be selected. An interrupt is generated when the counter reaches zero. After that, the counter will be reloaded automatically which makes this type of interrupt suitable for triggering periodic tasks.

In this work, usage of dSpace DS1104 controller board is extended with the usage of ControlDesk, which is a real-time experiment and visualisation software that functions as a user interface between programming tool and test equipment controlled by dSpace controller boards, as shown in Figure 3.19. Users can select appropriate instruments based on desired application such as plotter to plot analog data, on/off button to activate/deactivate a switch, numeric input to assign any numeric data to a variable. Each instrument has at least one variable assigned to it. These variables are variables that are programmed in MATLAB environment, built and loaded into connected dSpace controller.

Figure 3.19: ControlDesk software panels

3.7.2 Permanent Magnet Synchronous Motor

In this work, the PMSM drive prototype is realized using Schneider Electric BSH1002P12A1A three-phase AC servo motor, an interior 1.93kW permanent magnet synchronous motor, as shown in Figure 3.20.
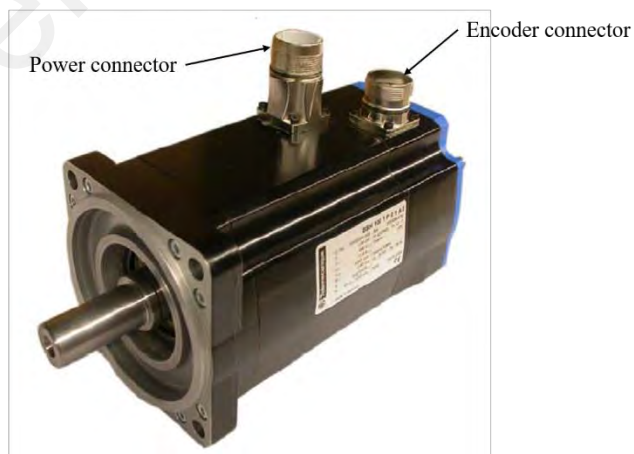

Figure 3.20: BSH1002P12A1A three-phase AC servo motor

Conforming IEC standard, the motor is labelled with its own nameplate, where among others, maximum voltage, maximum current and maximum mechanical speed of the

motor are given. The motor's nameplate is shown in Figure 3.21 and the important data is tabulated in Table 3.6.

Figure 3.21: Motor nameplate

Table 3.6: Motor name plate data

Motor parameter	Symbol	Motor data
Nominal output power	P_N	1.93kW
Maximum voltage	U_{max}	480V_{rms}
Maximum current	I_{max}	17.1A_{rms}
Maximum mechanical speed	n_{max}	6000min^{-1}
Continuous stall torque	M_0	5.8Nm

BSH1002P12A1A motor is compact in size with a length of only 204.5mm, 100mm in width and 138.4mm in height, as shown in Appendix F. This interior PMSM has 4 pole pairs of permanent magnets buried in the rotor, hence, it has a small effective air gap and a more robust construction compared to surface PMSMs. One remarkable parameter feature of IPMSM is unidentical value of d-axis and q-axis inductance, as shown in the motor's parameter list in Table 3.7. The complete technical data of the motor is attached in Appendix F. In simulation works, parameters listed in Table 3.7 are pre-defined in Callback function "InitFcn" under "Model Properties" menu of the Simulink model.

Table 3.7: PMSM parameters

Motor parameter name	Symbol	Motor parameter value
Stator resistance	R_s	1.2Ω
d-axis stator inductance	L_d	6mH
q-axis stator inductance	L_q	6.75mH
Number of poles	p	8
Inertia	J	2.31 kgcm^2
Back emf constant	K_e	77 V$_{rms}$/krpm
Torque constant	K_t	0.9Nm/A

As seen from Figure 3.20, BSH1002P12A1A PMSM has two connectors namely power connector and encoder connector. Schneider Electric VW3M5101R30 power cable is used to supply power to the motor through its industrial M23 power connector on the motor side. The cable core consists of 4 units of 1.5 mm² cables and 2 units of 1 mm² cables, as shown in Figure 3.22. Table 3.8 shows the pin assignment of the power cable.

Figure 3.22: Power cable core

Table 3.8: Pin assignment of M23 power connector

Pin	Designation	Meaning	Range
1	U	Power	3 AC 0 - 480V
2	PE	Shield	
3	W	Power	3 AC 0 - 480V
4	V	Power	3 AC 0 - 480V
A	Brake + (if any)	Brake	DC 24V
B	Brake - (if any)	Brake	DC 0V
C	-	Not assigned	
D	-	Not assigned	

The other M23 industrial connector namely the encoder connector is used for motor feedback system. The motor used in this work is equipped with a built-in absolute multiturn SinCos Hiperface SICK SKM36-HFA0-K02 encoder. It provides both absolute and incremental position of the rotor from its binary code digital signal and its differential analog sin cos signals respectively, as summarized in Figure 3.23. These signals are fed to the controller either directly or through a signal conditioning circuit through encoder cable VW3M8101R30 as shown in Figure 3.24. Its corresponding pin assignment is tabulated in Table 3.9. Pin 10 and 11 are used to supply the encoder with 10V DC for power.
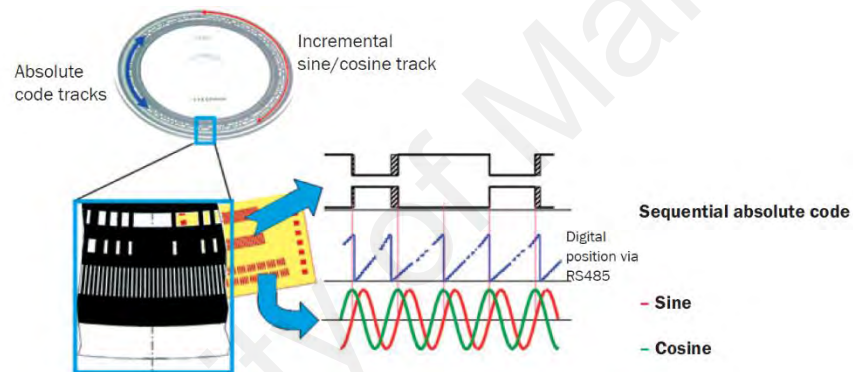

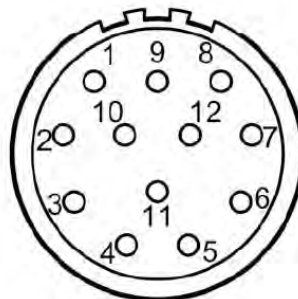Figure 3.23: Hiperface SICK SKM36-HFA0-K02 encoder data

Figure 3.24: Encoder cable core

Table 3.9: Pin assignment of M23 encoder connector

Pin	Designation	Meaning	Range
1	Sensor PTC	Temperature	
2	Sensor PTC	Temperature	
3	-	Not assigned	
4	REF SIN	REF signal	
5	REF COS	REF signal	
6	Data +	RS 485	
7	Data -	RS 485	
8	SIN +		
9	COS +		
10	U	Power	DC 7 – 12V
11	GND	Ground	DC 0V
12	-	Not assigned	

Details on the working principle of this encoder as a feedback system in the developed closed-loop PMSM drive prototype will be detailed in Subsection 3.7.4.2 and 3.7.4.3.

Figure 3.25 shows the motor in use is securely fixed to a T-slot base plate using Magtrol Adjustable Motor Fixtures AMF-3, which is individually shown in Figure 3.26. The motor fixture not only secures the motor in place while running any test, but also versatile enough to enable easy motor centering for optimum coupling to other components such as transducer and dynamometer in this work. Furthermore, this type of fixture is chosen due to its two adjustable bridges feature that allows clamping position variation. In addition, its locking thumb screw feature provides better protection against vibration. Lastly, all motor-to-fixture contact surfaces on Magtrol AMF-3 are nylon padded for scratch-free clamping.

Figure 3.25: PMSM with fixture

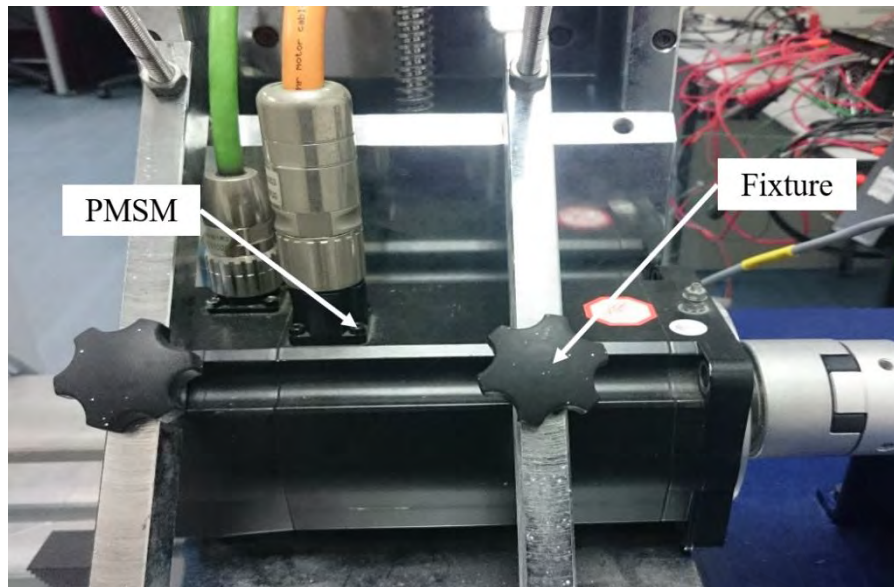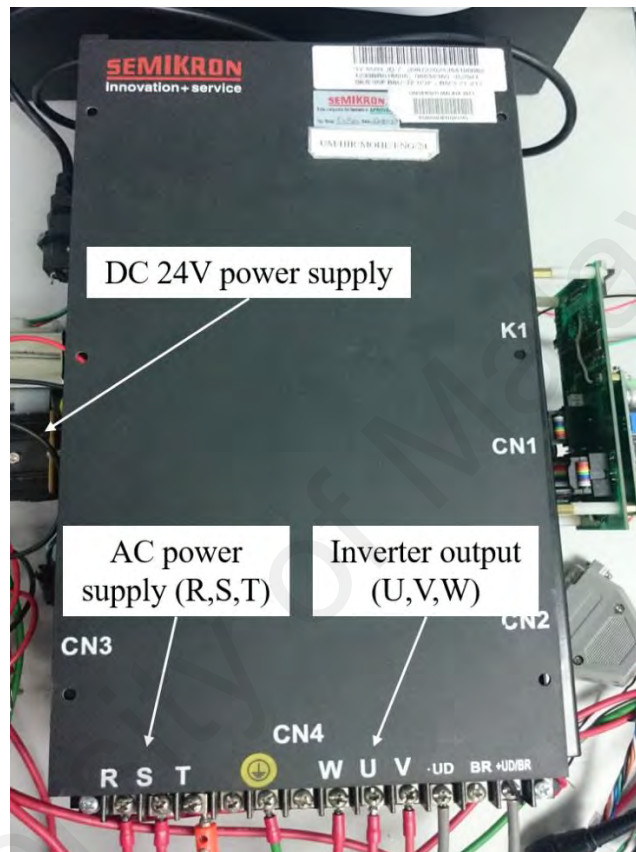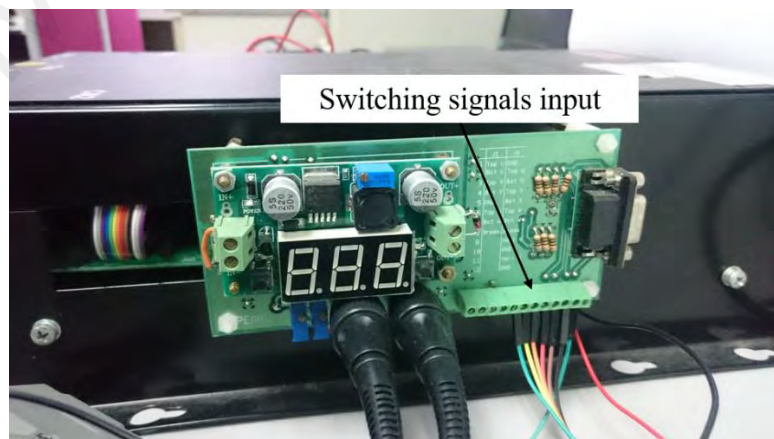Figure 3.26: Magtrol Adjustable Motor Fixtures AMF-3

3.7.3 Semikron Three Phase Six Switches Two-level VSI

PMSM drive prototype developed in this work uses Semikron three phase six switches two-level VSI Semikron SKS 13F B6U+B6CI+E1CIF*2 09 V12, as shown in Figure 3.27.

(a)

(b)

Figure 3.27: Semikron SKS 13F B6U+B6CI+E1CIF*2 09 V12 voltage source inverter
(a) top view   (b) side view

Figure 3.28 shows the complete circuit inside Semikron VSI that consists of a rectifier that converts input AC supply to DC link, with which the succeeding inverter circuit operates. The maximum output voltage and current of the inverter is 380V AC and 13A respectively. The inverter's absolute maximum switching frequency is 20kHz, but it operates optimally at maximum 10kHz. A DC 24V is also supplied separately to the inverter to power up additional internal submodules such as cooling fan and LED display.
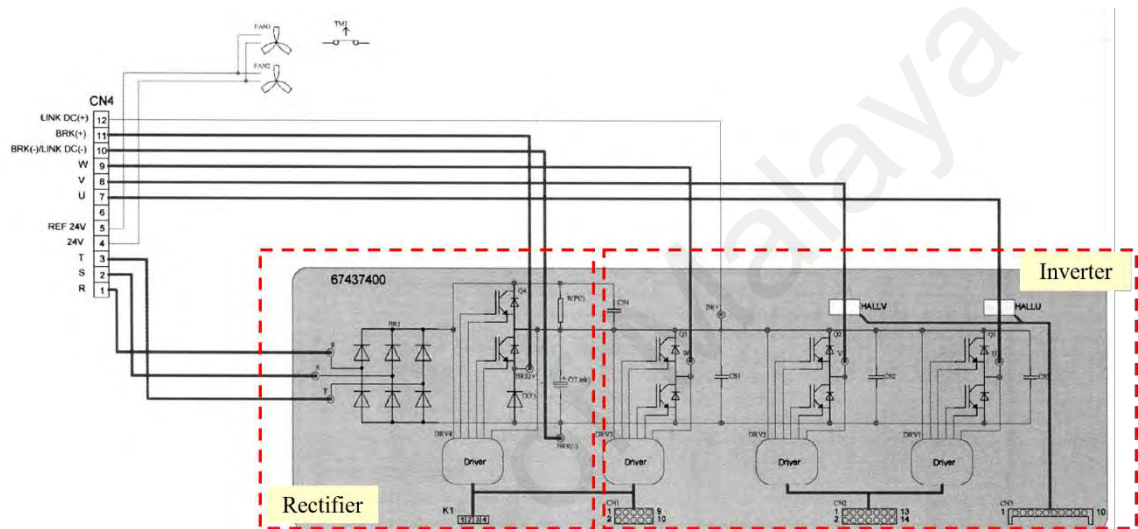
Figure 3.28: Semikron SKS 13F VSI circuit

The switching sequence of six switches in the inverter circuit depends on switching signals, which are externally fed from the controller as CMOS signal between 0 to 15V. The Semikron inverter was powered by Chroma 61511 programmable AC supply, as shown in Figure 3.29, which can deliver a clean and balanced AC supply to the system. With a power rating of 12KVA, it can supply a single phase or three phase supply with maximum output voltage up to 300V AC and output frequency from 15Hz to 1500Hz. In this work, the supply was tuned at 100V with a frequency of 50Hz.

Figure 3.29: Chroma 61511 programmable AC power source

3.7.4   Feedback for Closed Loop PMSM Drive Prototype

For closed-loop operation of PMSM drive, several feedback signals are required to be fed to the main controller. These include motor phase currents as feedback to current controllers, rotor absolute position data for initial motor start-up and incremental position data for speed calculation and coordinate transformations.

3.7.4.1   Motor Phase Current

PMSM phase currents are measured using a developed current sensor circuit, as shown in Figure 3.30 and fed to the dSpace DS1104 controller through ADC input of dSpace CP1104 connector panels.
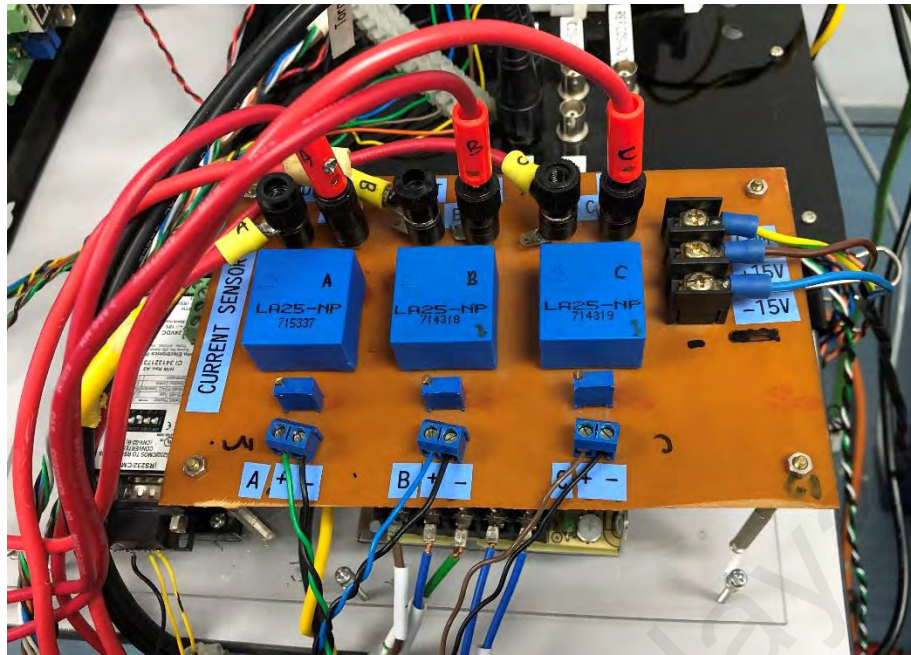
Figure 3.30: Current sensors

The current measurement is executed using current transducer LEM LA25-NP, which has excellent accuracy ($\pm 0.5\%$) and very good linearity of measurement (<0.2% linearity error), as well as highly suited for application in variable speed drives. The transducer requires ± 15 V power supply and can measure current between 0 and ± 36 A. In this work, turns ratio of 1:1000 is selected. A variable resistor is placed in series to 0V connection for transducer's calibration, which is executed prior to taking the actual current measurement. Figure 3.31 shows the schematic of the current sensor circuit developed for this prototype.

Figure 3.31: Schematic of current sensor circuit

Three-phase current readings are fed to the controller through analog input channels ADCH2, ADCH3 and ADCH4. These channels have 16-bit resolution for ± 10 V input, whereas the current transducers have 0.1 mV/mA resolution. H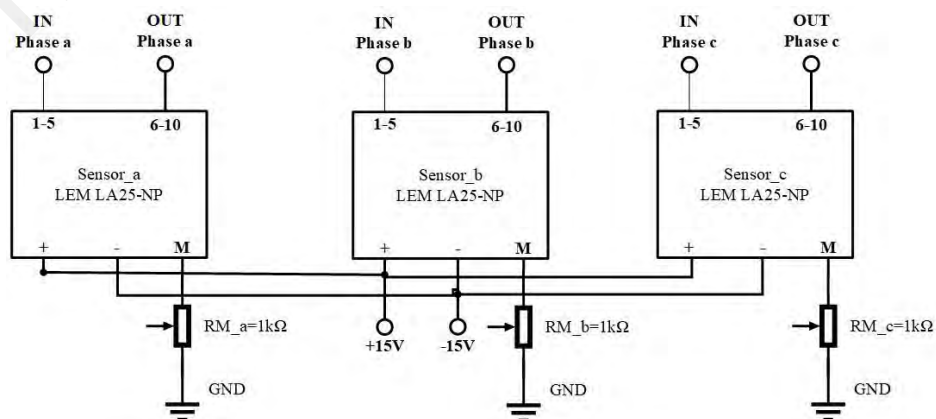ence, the overall current feedback resolution achieved in this prototype is around 3 mA. MATLAB/Simulink DS1104 ADC_Cx blocks are used to capture the measurement values in the controller.

Drives control application in this work requires accurate timing for the control of analog inputs and incremental encoder position readouts. Hence, these actions are synchronized with the PWM signal i.e. using the interrupt provided by the ST1PWM signal line of the DS1104. PWM generation performed in this work, enable interrupt generation by the slave DSP at the beginning or in the middle of each PWM period. The I/O components are triggered synchronously with the PWM interrupt. Figure 3.32 shows the parameter window of the DS1104SLAVE_PWMINT block, where A/D conversion is triggered in the middle of the PWM period (0.5).
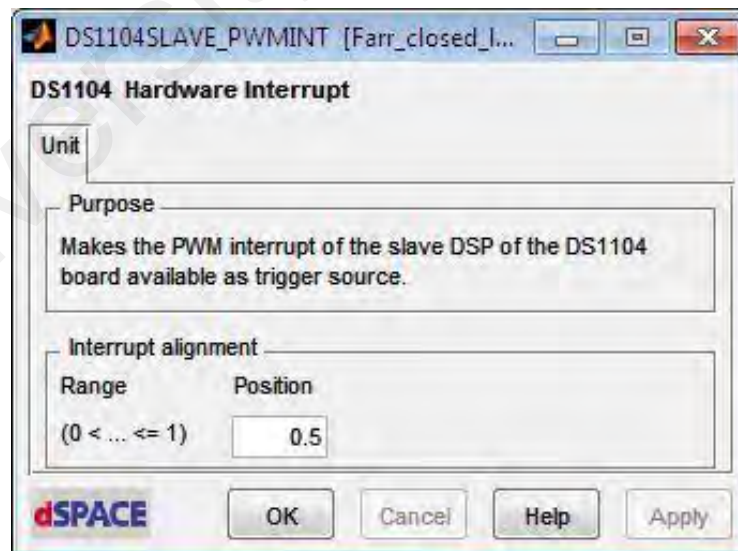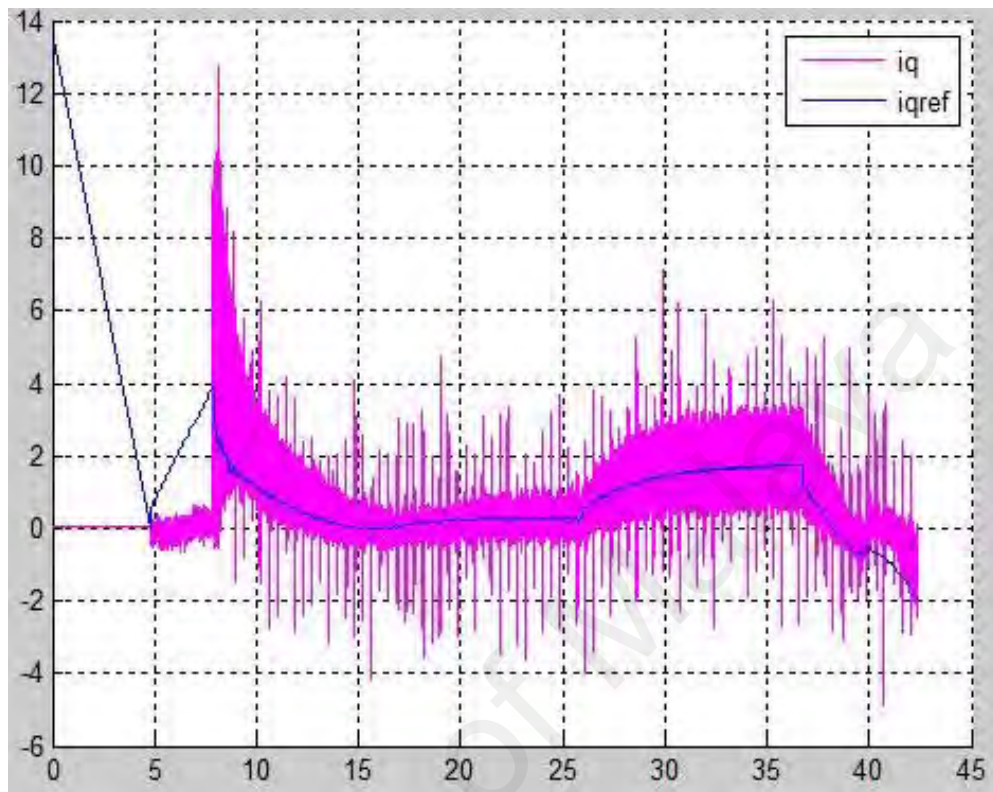

Figure 3.32: DS1104SLAVE_PWMINT Interrupt block parameter for conversion synchronisation with PWM signal

An example of current measurement before and after implementation of soft-synchronisation with PWM signals are shown in Figure 3.33(a) and (b) respectively.

(a)

(b)

Figure 3.33: Current measurement   (a) before synchronisation   (b) after synchronisation

3.7.4.2 RS232 rotor absolute position

Apart from current feedback, the designed PMSM speed controller also requires rotor absolute position information for motor start-up. This is due to the dependency of PMSM operation on the rotor position or angle. Several studies proposed sensorless PMSM control, in which rotor position is estimated (Z. Song, Hou, Jiang, & Wei, 2006; Z. Wang et al., 2012). However, that option is not considered in this work, due to high reliability of speed controller performance on the accuracy of the designed estimation algorithm. Built-in absolute multiturn SinCos Hiperface SICK SKM36-HFA0-K02 encoder in the motor can provide an absolute position with a resolution of 4,096 increments per revolution and 4,096 revolutions with the multiturn system. The data is obtained through RS485 serial communication using Data+ and Data- digital signals supplied through pin 6 and 7 of the encoder cable respectively. Hiperface encoder uses half-duplex two-line connection for the serial communication. Serial communication data of the encoder follows asynchronous half-duplex UART protocol with binary data format. Parameter settings for communication is fixed according to encoder specification prior to command sending to ensure successful communication and correct data is received. UART parameter settings for Hiperface encoder in use is listed in Table 3.10.

Table 3.10: UART parameter settings for SKM36-HFA0-K02 encoder

Parameter	Setting
Data rate	9600 Baud
Data bits	8, LSB first
Start bit	1
Stop bit	1
Parity	Even

On the controller side, parameters are set in dSpace DS1104SER_SETUP block, as shown in Figure 3.34. This block is compulsory to be put in Simulink model if any other serial blocks are in use.

Figure 3.34: UART parameter settings in DS1104SER_SETUP block

Each data transmission consists of a master request frame followed by a slave response frame. In this work, dSpace DS1104 is the master and the encoder is the slave. The master transmission must be terminated through a timeout condition after the last byte is transmitted. Then, the slave transmission will initiate within a specified response time. Data transmission uses bus topology and addressing scheme. Each frame in the data bus contains an address byte, command bytes and optionally data bytes of varying length and a trailing checksum to detect transmission errors. The default address for encoder used in this work is 40h. Checksum byte is defined through an XOR operation on all frame bytes including the address.

The absolute position value is obtained by using command identifier 42h. Command identifier is used to construct command bytes to be sent to the encoder,

together with other corresponding bytes according to data frame format. Figure 3.35(a) and (b) show the data bus that are sent and received by the master (controller) respectively in one cycle of "Read position" command. The position data consists of 32-bit value with most significant bits sent first from 0x0 to 0xFFFFFF80 that represents from 0 to 360 degrees or 2π rad. Checksum for the data from encoder to controller changes according to the current position data.
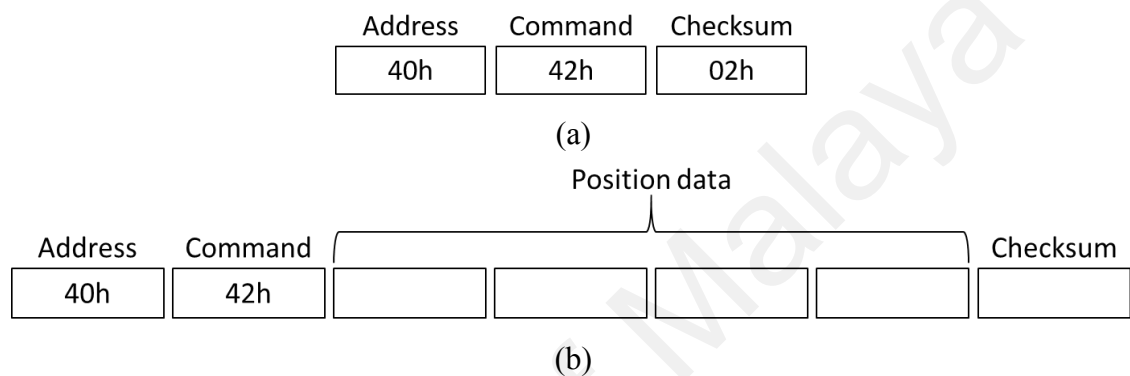

(a)

(b)

Figure 3.35: Data bus structure for serial communication (a) from master to slave to enquire to read position data (b) from slave to master with current absolute position data

To ensure successful absolute position reading communication, a few other supporting commands are also used. Command 50h is used to read the encoder status. This command returns active warning and error codes of the encoder, if any. Else, the encoder will return status code 00h. After all active warnings and errors have been solved, encoder software reset can be executed. To do so, command 53h is used. This command initializes the encoder with power-on initialization process. Unlike other commands, the slave does not send any data to the master as a response in this case.

Serial communication is initiated by the controller using one of DS1104 timer interrupts. The timer is set at 0.08 seconds period or 12.5 Hz frequency, considering the response time required for each cycle and time-out time. This interrupt triggers data sending from the controller to the slave (encoder), which is executed inside a Function-Call subsystem. Figure 3.36 shows a multi-port switch block used to enable four options

of commands to be chosen and sent to the encoder, depending on the user-defined "Command" value, as listed in Table 3.11.

Table 3.11: User-defined serial communication command selection

"Command" value	Serial communication command
1	Read encoder status
2	Read absolute position
3	Encoder reset

Command sending is executed using DS1104SER_TX block, as shown in Figure 3.36 with block's parameters as shown in Figure 3.37.

Figure 3.36: Serial communication data transmission in MATLAB/Simulink environment
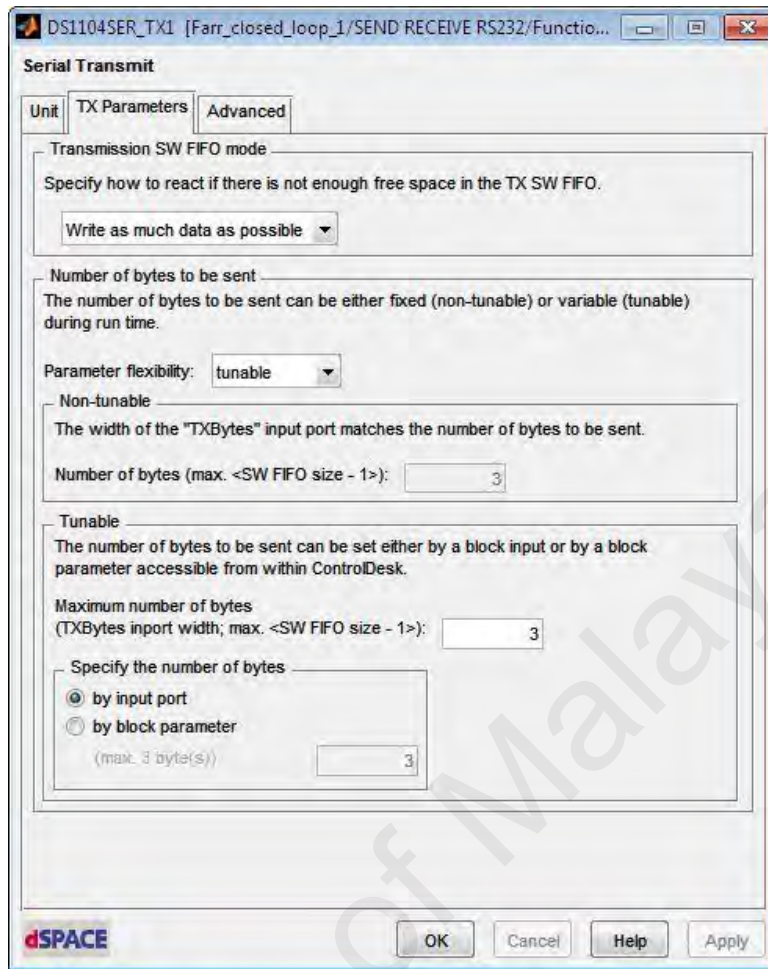
Figure 3.37: DS1104SER_TX block parameters

On the other hand, the DS1104SER_RX block shown in Figure 3.38 is used for data reception from the slave. Similar to the command sending procedure, the length of data expected from the slave is also individually configured, according to selected command in Table 3.11. Figure 3.39 shows the data reception block's parameters.
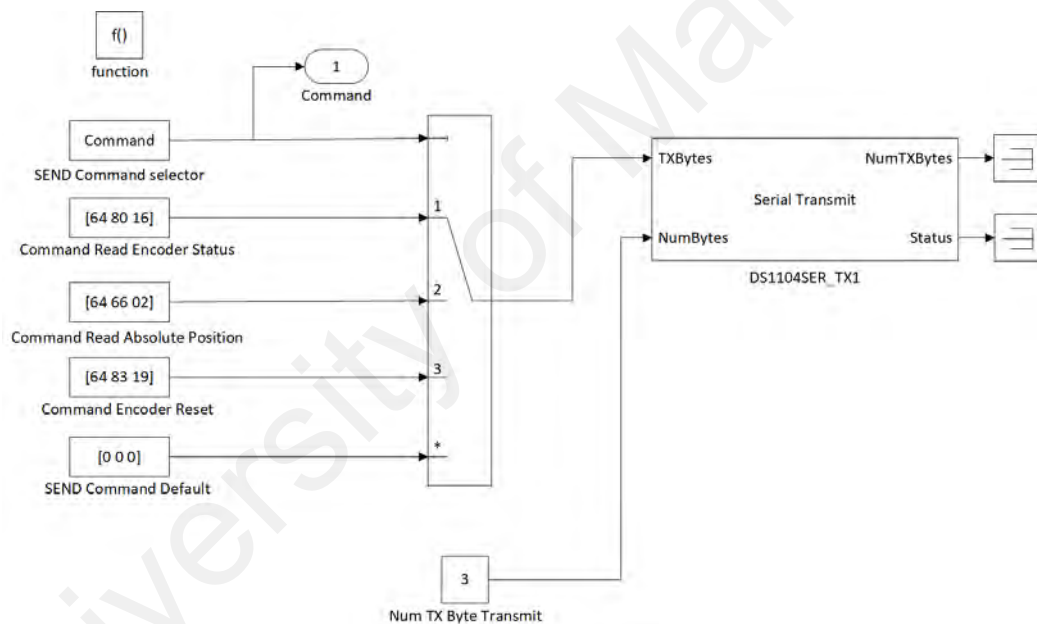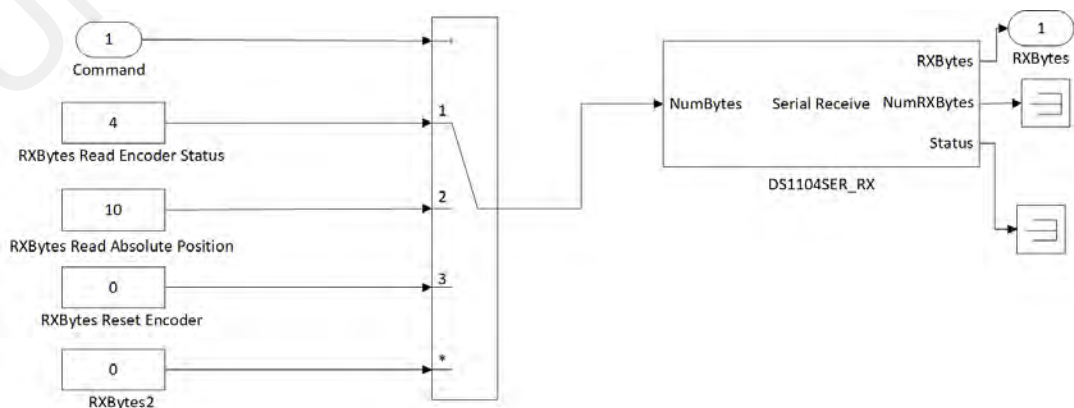

Figure 3.38: Serial communication data reception in MATLAB/Simulink environment
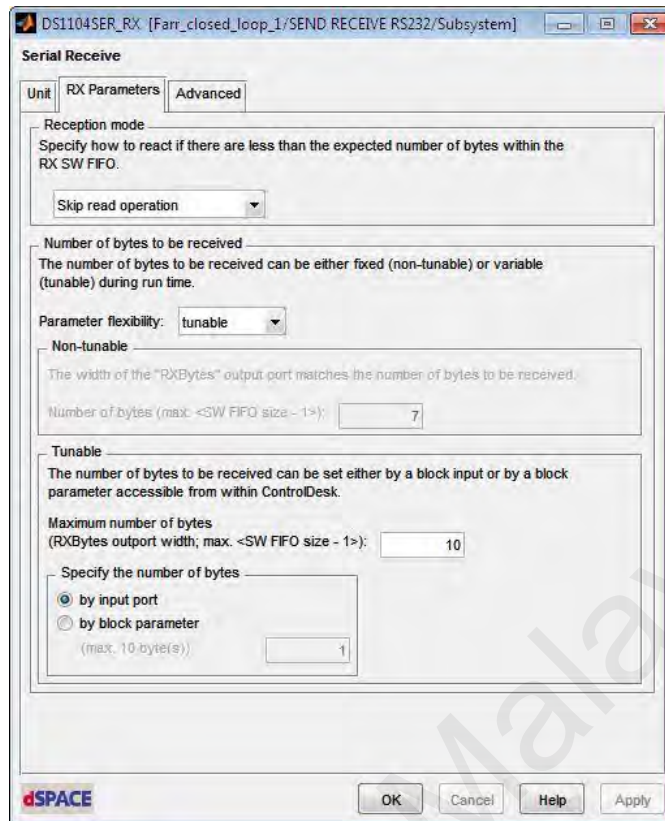
Figure 3.39: DS1104SER_RX block parameters

In this work, due to the limitation of RS485 serial communication of dSpace DS1104 controller in terms of speed, RS232 interface has to be used instead. Hence, a Toshiba RS232-RS485 converter CNV-02-B, as shown in Figure 3.40, is connected between dSpace CP1104 RS232 port and the encoder to ensure correct and fast absolute position data acquisition, as detailed in Figure 3.41.

Figure 3.40: RS232-RS485 converter CNV-02-B

Figure 3.41: Connection of CNV-02-B RS232-RS485 converter

The converter must be configured according to hardware communication specifications. For correct half-duplex data transfer between encoder and CP1104, converter configuration in Table 3.12 is chosen.

Table 3.12: Configuration of CNV-02-B RS232-RS485 converter

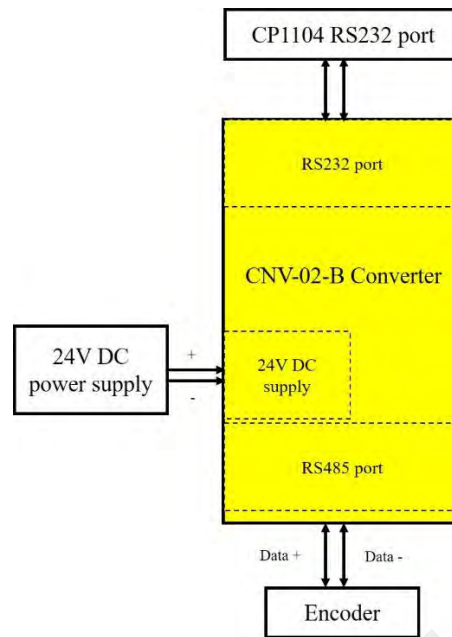| Parameter	Switch position	Description
RS485 type	ON	2-wire half-duplex network
RS485/RS422 selection	ON	To/from RS485 conversion
Direction control	OFF	Auto-direction control with termination
Termination	ON	

Although the speed limitation of serial communication has been solved with the converter, rotor absolute position data acquisition in this prototype still suffers from the limitation of sampling time by DS1104 controller. Hence, position data accuracy is only guaranteed for very low speed operation of the motor e.g. up to 100 rpm. However, this issue is not crucial since absolute position data is only used during motor start-up in this work i.e. when the rotor is in a standstill. When the rotor already rotates, absolute position data is not required by the controller anymore, since the position data is provided by a

high-resolution incremental position data, as detailed in subsection 3.7.4.3. Figure 3.42 shows rotor absolute position data from 0 to 6.28 rad, extracted from received serial communication data using "Read Absolute Position" command repeatedly.
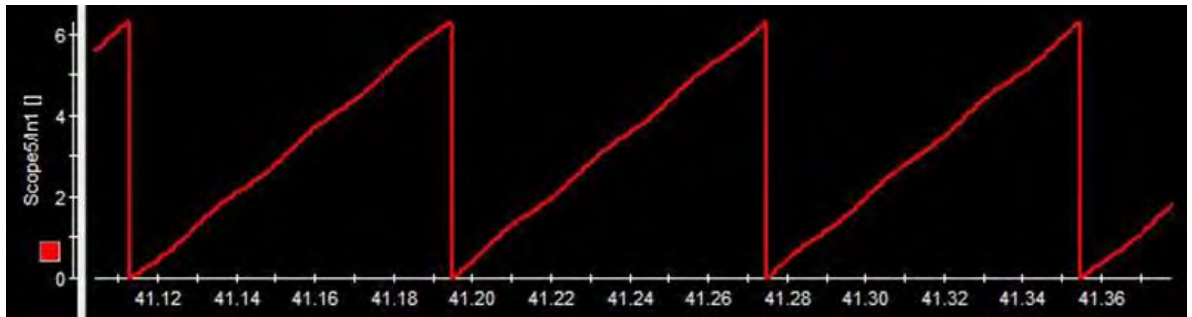
Figure 3.42: Rotor absolute position curve from serial communication

3.7.4.3 Incremental position data

Incremental position data is obtained from Hiperface SICK SKM36-HFA0-K02 encoder via its analog differential sin and cos signals, as shown in Figure 3.43. Reference sin/cos voltage level (REFSIN, REFCOS) is constant at DC 2.5V, resulting in differential sin/cos (SIN, COS) voltages of between 2.0V and 3.0V or peak-peak voltage of 1.0V.
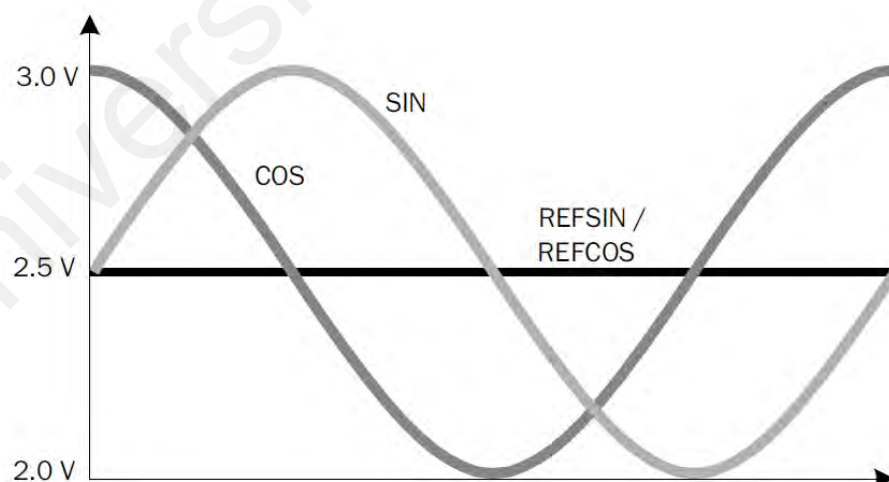
Figure 3.43: Analog differential sin/cos signals of Hiperface SICK SKM36-HFA0-K02 encoder (clockwise rotation)

These analog differential signals are fed to a signal conditioning circuit in order to generate square pulses (A and B) or quadrature signals for quadrature counting inside

DS1104 controller. Figure 3.44 shows the actual signal conditioning circuit with its schematics and the complete circuit shown in Figure 3.45 and in Appendix G respectively. Each analog signal is amplified and fed to a comparator to obtain a quadrature signal. The amplifier used in this work is AD8044AR quad amplifier from Analog Devices Inc., whereas the comparator is the LM339N quad comparator by Texas Instruments.
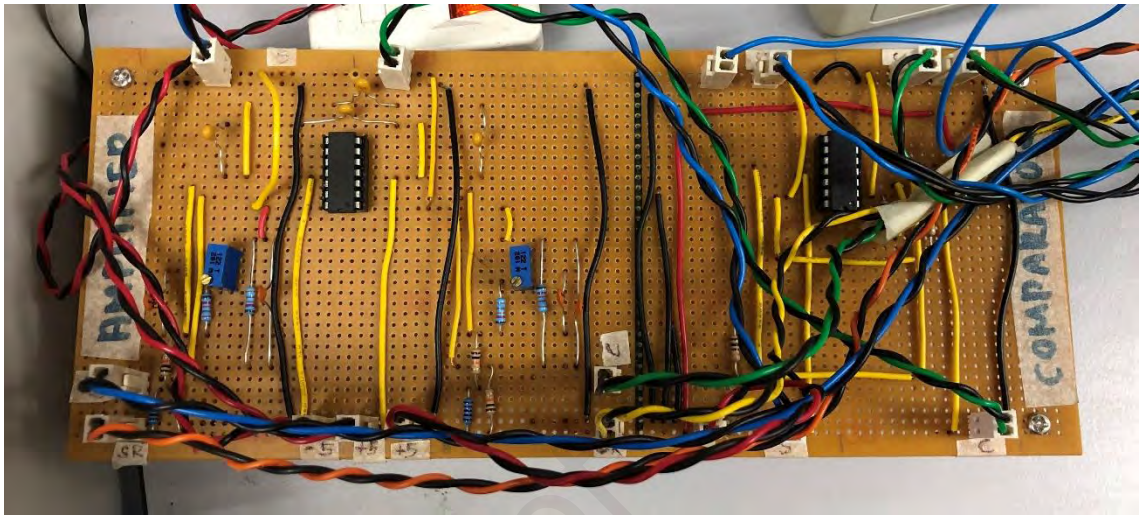
Figure 3.44: Actual encoder signal conditioning circuit
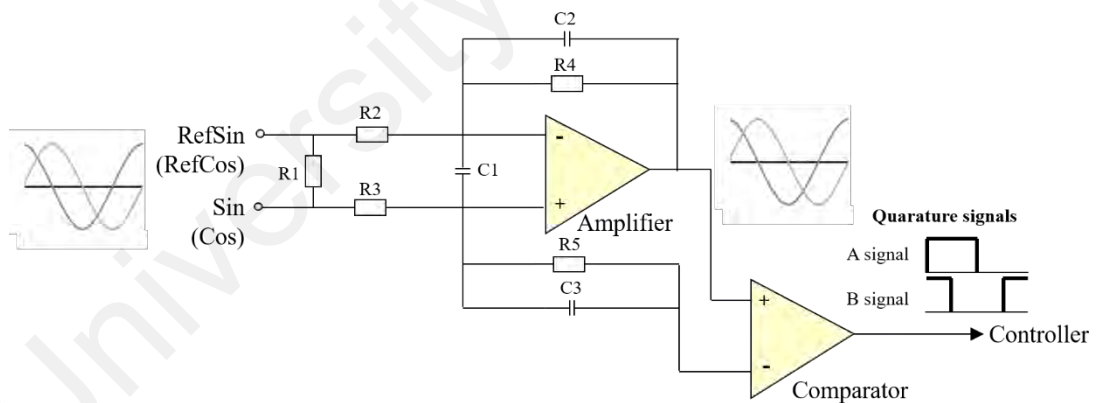
Figure 3.45: Encoder signal conditioning circuit schematics

Figure 3.46 shows an example of an analog sin signal and its corresponding square pulses after being fed through the signal conditioning circuit when the motor is moving at 75 rpm.
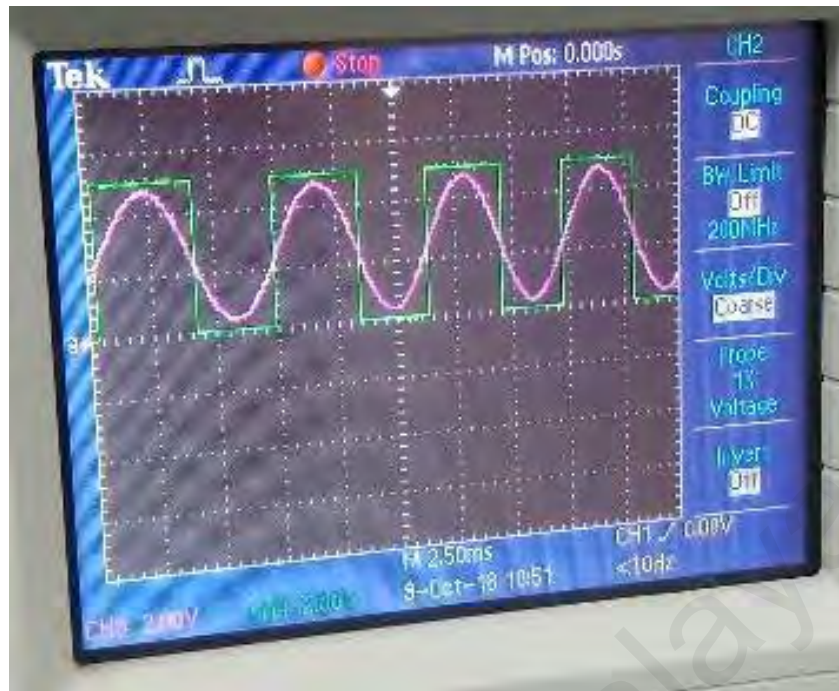
Figure 3.46: Analog sin signal from encoder (purple) and its resulting square pulses (green)

From each SKM36-HFA0-K02 encoder, one set of quadrature signals can be obtained, which consists of two square pulses with 90 degrees phase shift between each other, as shown in Figure 3.47. These pulses are fed to dSpace DS1104 controller through an incremental encoder input connector (INC1).
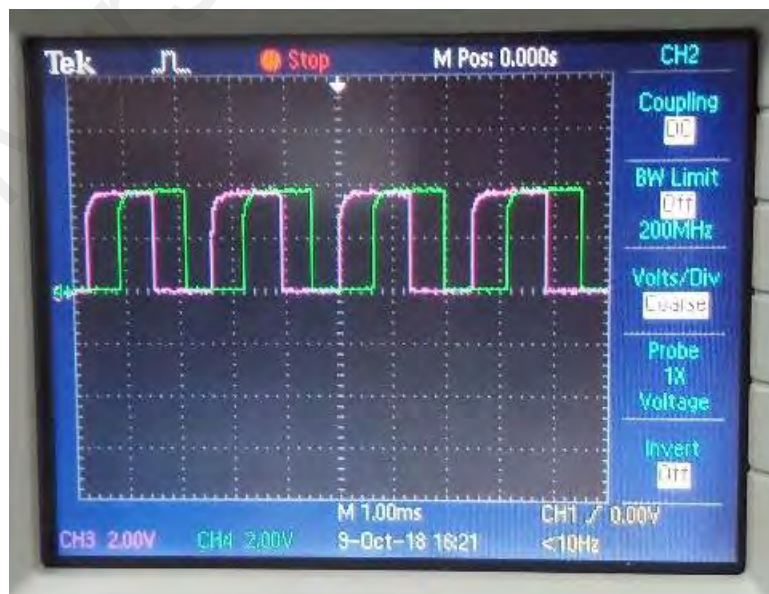
Figure 3.47: Resulting square pulses from sin signal (green) and cos signal (purple) when the motor is moving in forward direction

The combination of A and B signals in a quadrature counter logic allows determination of the incremental position with 4 steps per sin/cos signal period. This type of encoding is referred to as quadrature encoding because there are four output states: signal A rising, signal A falling, signal B rising, and signal B falling. By counting the generated pulse, the amount of rotation can be determined. For this purpose, one signal (A or B) is sufficient. However, the second pulse is required for determining the direction of rotation, by reading which signal is leading and which is following.

In MATLAB/Simulink environment, firstly, DS1104ENC_SETUP block is used to set the global parameters for the 2 encoder channels. In this work, the parameters are set as shown in Figure 3.48.
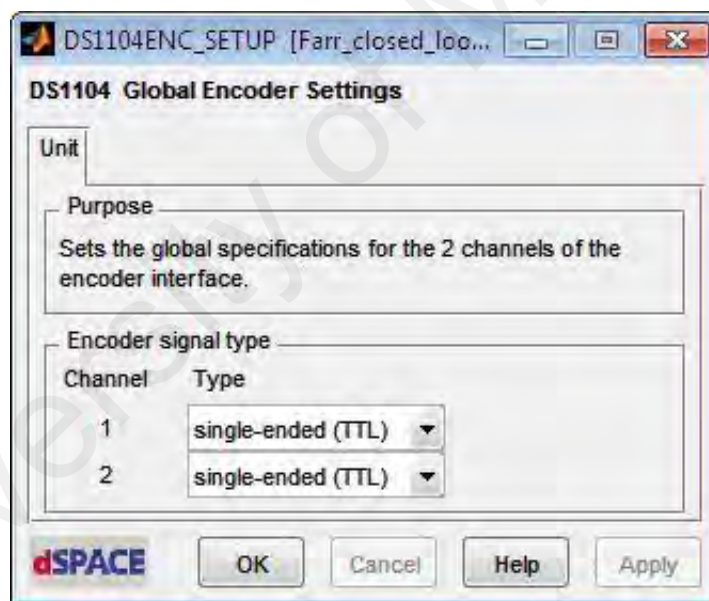
Figure 3.48: Parameter settings in DS1104ENC_SETUP block

Quadrature counting is performed using pre-programmed DS1104ENC_POS_C1 block, with parameters shown in Figure 3.50.
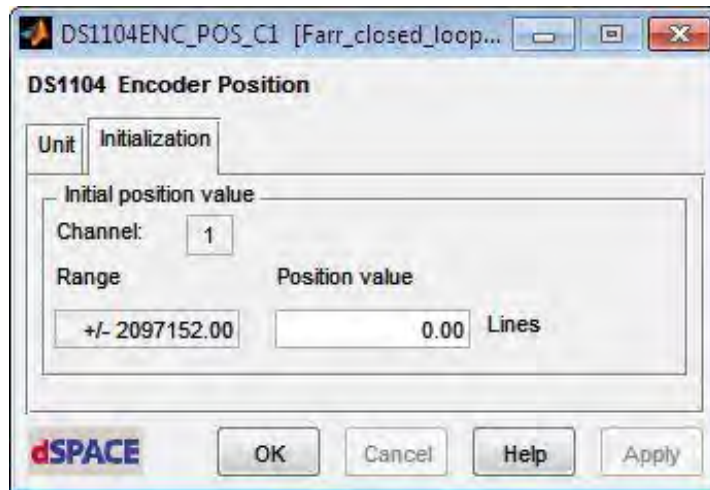
Figure 3.49: Parameter settings in DS1104ENC_POS_C1 block

The complete subsystem to extract incremental position data from quadrature signals are shown in Figure 3.50.
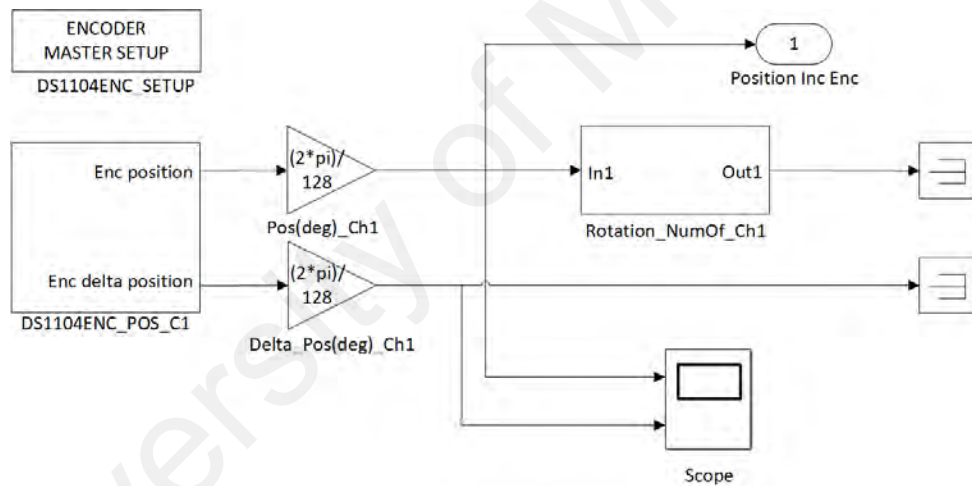
Figure 3.50: Extraction of incremental position data from quadrature signals

Table 3.13 shows counter operations performed is DS1104 controller based on A and B signals sampled currently (A_n , B_n) and the previous signals (A_{n-1} , B_{n-1}).

Table 3.13: Quadrature counter operation algorithm

A_{n-1}	B_{n-1}	A_n	B_n	Counter operation
0	0	0	0	No action
0	0	0	1	+1
0	0	1	0	-1
0	0	1	1	Invalid
0	1	0	0	-1
0	1	0	1	No action
0	1	1	0	Invalid
0	1	1	1	+1
1	0	0	0	+1
1	0	0	1	Invalid
1	0	1	0	No action
1	0	1	1	-1
1	1	0	0	Invalid
1	1	0	1	-1
1	1	1	0	+1
1	1	1	1	No action

SKM36-HFA0-K02 encoder has a resolution of 128 sin/cos periods per revolution, i.e. up to 512 states per revolution, resulting in 0.7 degrees incremental position data maximum resolution. From the obtained incremental position data, the speed of rotation can be calculated using equation (3.53). Appendix E shows the complete Simulink subsystem to obtain the rotor's mechanical speed.

$$\omega_m = \frac{\theta_{m,n-1} - \theta_{m,n}}{T_s} \qquad (3.53)$$

Figure 3.51 (a) and (b) show an example of incremental position data extracted and the corresponding calculated speed respectively.
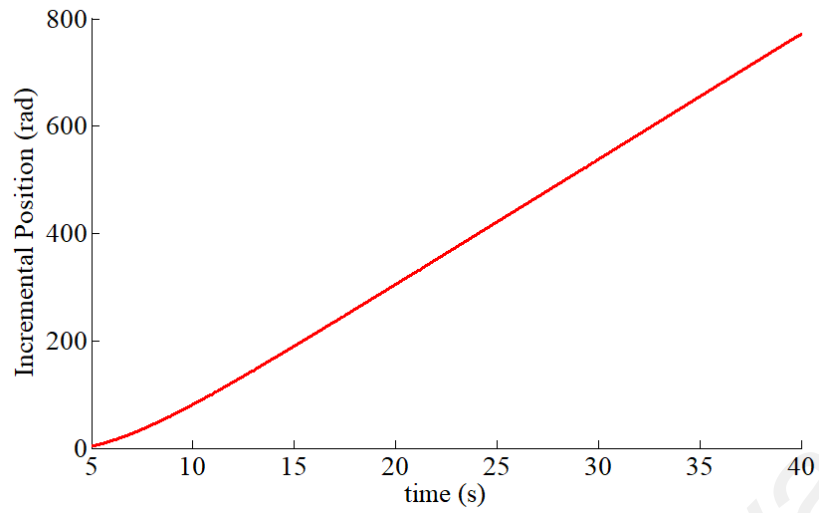
(a)
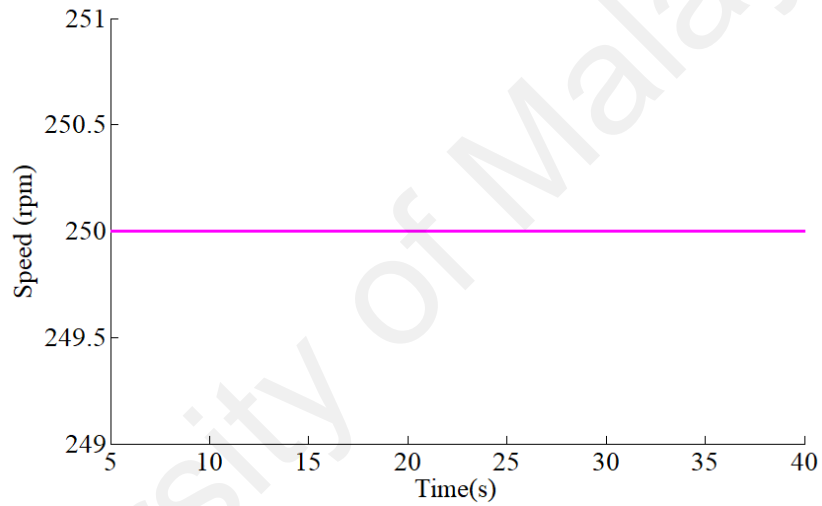
(b)

Figure 3.51: (a) Extracted incremental position and (b) its corresponding calculated speed curve.

3.7.5   Testing Load

In this prototype, hysteresis brake AHB-3, as shown in Figure 3.52, is used to produce the required load torque for evaluation of controller's performance in various load conditions. This model can provide load torque between 0.7 and 3.6 Nm for speed up to 20000rpm and power up to 1800W. Torque is produced strictly through a magnetic air gap between the rotor and the pole structure, resulting in smooth, infinitely controllable, speed independent and quiet torque loads. Complete torque control is

obtained by adjusting DC current supplied to the field coil. The amount of braking torque transmitted by the brake is proportional to the amount of current flowing through the field coil, regardless of the direction of current flow (polarity). In addition, the brake's compressed-air cooling system offers excellent heat dissipation.
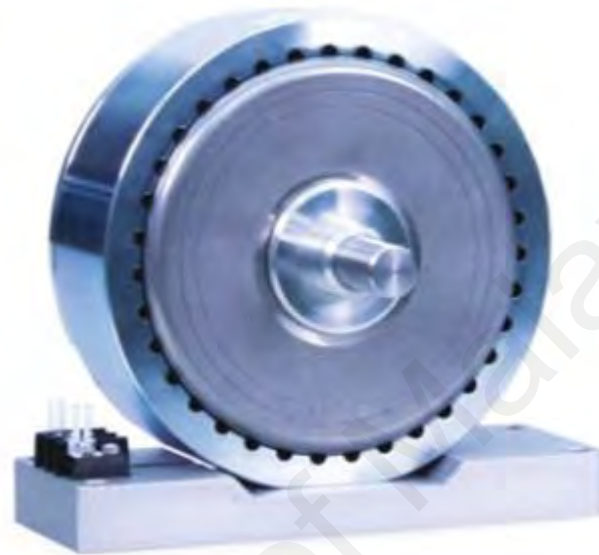
(a)
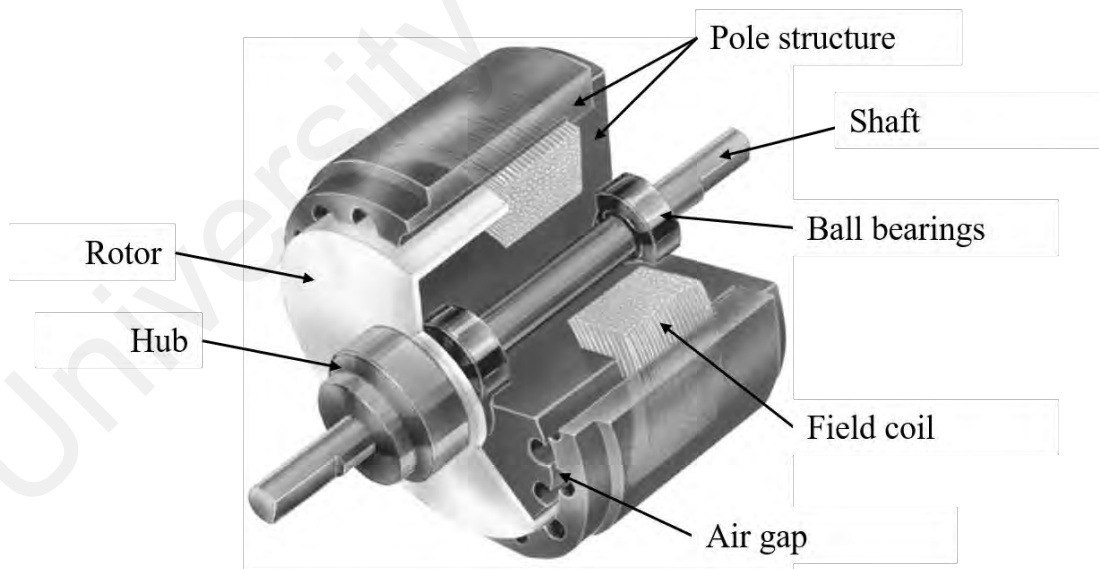
(b)

Figure 3.52: Magtrol AHB-3 hysteresis brake (a) exterior   (b) interior

The hysteresis brake is controlled through Magtrol Dynamometer Controller DSP6001, which can be programmed using Magtrol M-TEST 5.0 Motor Testing

software. Prior to any test, the connected motor test equipment must first be set up within M-TEST environment, as shown in Figure 3.53.

Figure 3.53: "Configure Hardware" window

The output load torque produced is controlled by a PID controller embedded inside the DSP6001 controller. Initially, the proportional, integral and derivative gains of this PID controller is tuned to suit its usage to the motor in use. Magtrol M-TEST 5.0 software is also a visualisation software, where among others, the motor torque and speed can be displayed. These data were provided by TMB 307/411 in-line torque and speed transducer via IEEE bus with acquisition speed of 120 torque and speed points per second. The transducer is equipped with an integrated conditioning electronic module providing 0 to ±10 V DC torque output and an open collector speed output. By employing non-contact differential transformer torque measuring technology, this transducer has remarkable properties such as high reliability, high overload protection, excellent long-term stability and high noise immunity.

Other than that, power measurement data of the motor in the test is obtained using Magtrol 6350 Power Analyzer connected to the prototype. It provides voltage, current, power etc. data through IEEE bus at up to 100 data per second for display in M-TEST environment and on its front panel display.

3.8 Summary

In this chapter, a fractional order sliding mode speed control of a PMSM has been designed. A control law has been obtained as the basis of the controller. Using Lyapunov stability theorem, the proposed controller has satisfied both stability conditions required according to SMC theory namely the reaching condition where the system should converge to the sliding surface and the stability condition in the sliding phase. Firstly, the proposed controller is simulated using simulation program in MATLAB/Simulink environment that comprises all required components in a complete PMSM drive system. The parameters in the program are carefully chosen to closely represent the experimental setup used for experimental verification. A closed-loop PMSM drive system prototype is developed to replicate the real implementation of PMSM in industries. Using this prototype, the performance of the proposed controller in real applications can be verified. Appropriate signal acquisition procedures of the feedback signals are crucial to ensure the accuracy of closed-loop performance of the developed drive system.

CHAPTER 4: SIMULATION AND EXPERIMENTAL RESULTS

4.1 Introduction

The performance of the PMSM drive system designed in Chapter 3 is evaluated using simulation in MATLAB/Simulink environment and then validated by experimental results using a PMSM drive prototype. In this chapter, first, the performance of the proposed FOSMC as a robust anti-disturbance speed control of PMSM is presented. Then, its performance is compared with a conventional integral SMC to show the advantages of incorporating fractional calculus in SMC. In addition, comparisons are made between the proposed FOSMC and other similar controller design in fractional order SMC family. Finally, effects of fractional order selection on drive performance are presented. Results are also analysed and discussed in this chapter.

4.2 Proposed FOSMC for speed control of PMSM

Performance of the proposed FOSMC for speed control of PMSM is evaluated by simulation in MATLAB/Simulink environment and then is further verified through hardware implementation using the developed closed-loop PMSM drive prototype, as shown in Figure 4.1 and as detailed in subsection 3.7. The parameters of FOSMC are chosen as in Table 4.1.
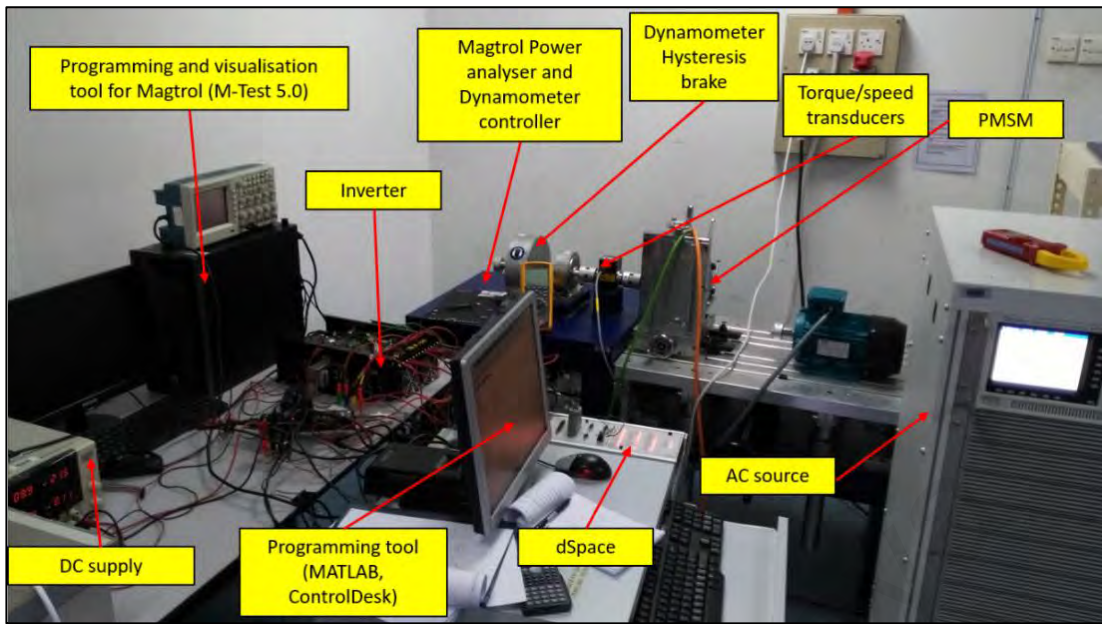
Figure 4.1: Actual closed-loop PMSM drive prototype

Table 4.1: FOSMC controller parameter values

Parameter name	Parameter value
Order of fractional order integration, α	0.35
Order of fractional order differentiation, β	0.3
k_p	0.08
k_i	0.6
k_d	0.01
w	80
k_s	0.08

4.2.1   No load condition

Initially, a reference speed of 500 rpm is given to the system without any load torque to obtain the step response of the controller. Simulation results in Figure 4.22(a) show that the speed output of the system controlled with FOSMC has a very small overshoot (1.96%) with a rise time of 0.006181 seconds and settling time of 0.096 seconds. A steady state error of 0.1 rpm was recorded, which is equivalent to only 0.02%. Similar results are obtained in experimental validation, where recorded overshoot, rise

time and settling time are 8.18%, 0.7778 seconds and 7.007 seconds respectively, as shown in Figure 4.2(b). No steady state error is recorded during the experimental run.
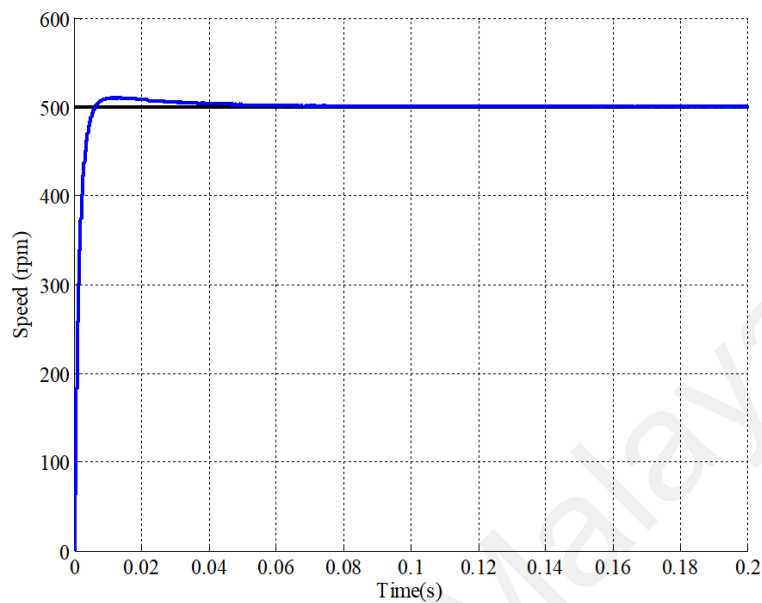
(a)
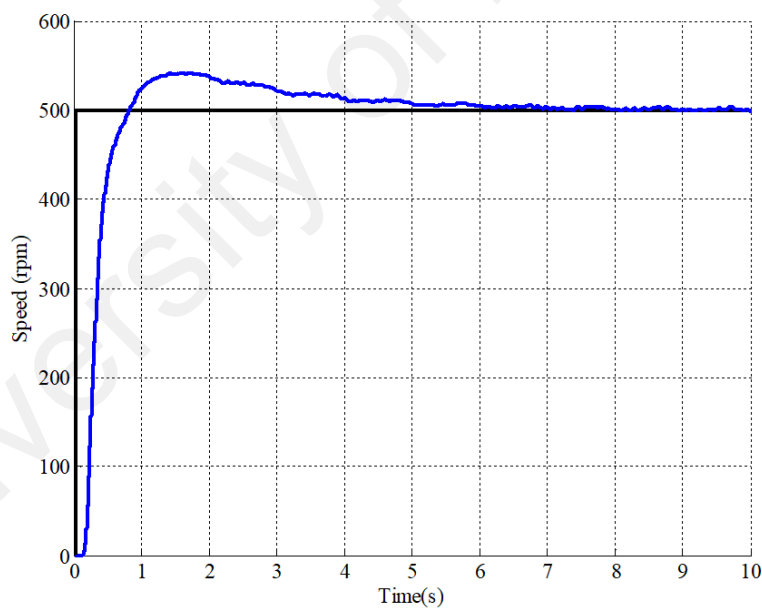
(b)

Figure 4.2: Speed response for reference speed 500rpm at no load (a) simulation (b) experiment

From Figure 4.3(a), it is shown that torque converges to zero at steady state since no load is applied to the system, with maximum torque spike of 9.087 Nm during transient mode and torque ripple of around 0.2 Nm in simulation case. A similar convergence trend

is observed in the experiment, where torque rises to 0.219 Nm during transient mode and experiences a lower torque ripple of only 0.0115 Nm during steady state, as shown in Figure 4.3(b).

A similar convergence pattern is obtained with current measurement, where the value converges to zero after the initial spike during the transient mode. The CTA control approach used in this work fixes d-axis current reference value at zero. In the case of simulation, the maximum value of d-axis current during transient is 0.4421A (Figure 4.4(a)), whereas the current ripple during steady state is recorded at around 0.27A. Figure 4.4(b) shows that a slightly higher current spike is measured during transient mode in the actual experiment, namely 0.7118A. A higher current ripple of 0.434A is also obtained during steady state.
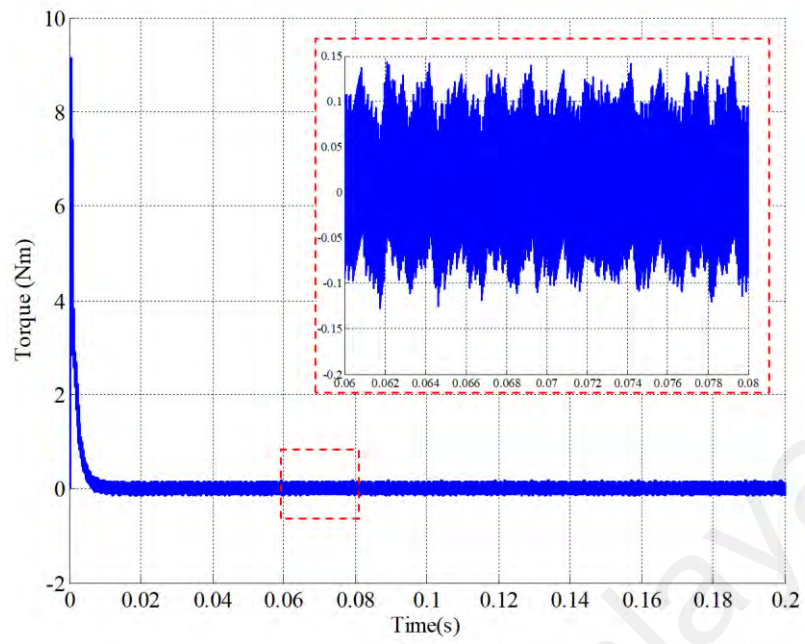
(a)
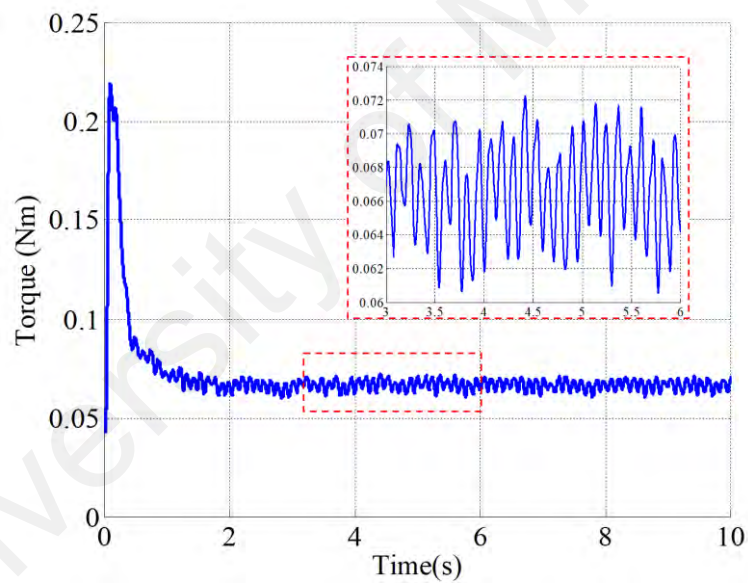
(b)

Figure 4.3: Torque response for reference speed 500rpm at no load   (a) simulation
(b) experiment
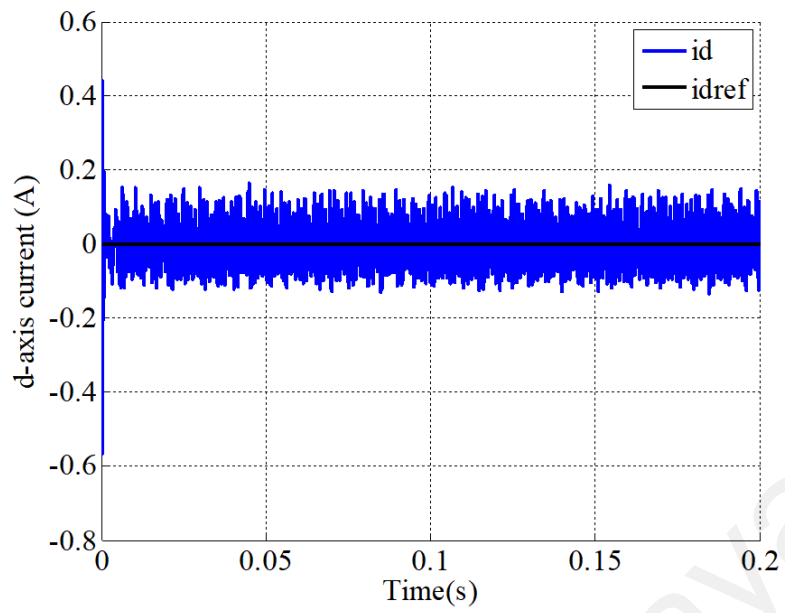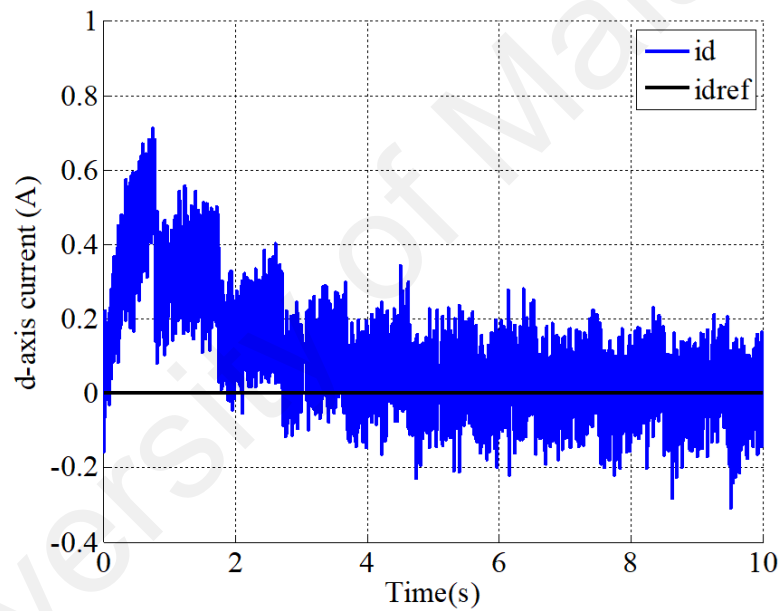
Figure 4.4: d-axis current response for reference speed 500rpm at no load
(a) simulation (b) experiment

On the other hand, for the q-axis current, the reference value is determined by the output of the speed controller in the outer loop. Since no load is applied to the machine, q-axis current reference value is zero. During the simulation, actual i_q rises to 10.05A at transient mode and then converges to zero at steady state with 0.1863A ripple, as shown in Figure 4.5(a). However, Figure 4.5(b) shows that a much lower transient q-axis current is recorded during the experiment namely only 0.7123A. Steady state current does not converge exactly to zero in the actual experimental run since the motor experiences friction, which acts as a small load compared to the ideal frictionless model in the simulation. q-axis current ripple is 0.34A in this case. Like d-axis and q-axis currents, phase currents also converge to zero. In addition, d-axis and q-axis current ripples obtained are also reflected in *a, b, c* phase currents waveforms, as shown in Figure 4.6(a) and (b) for simulation and experiment respectively.
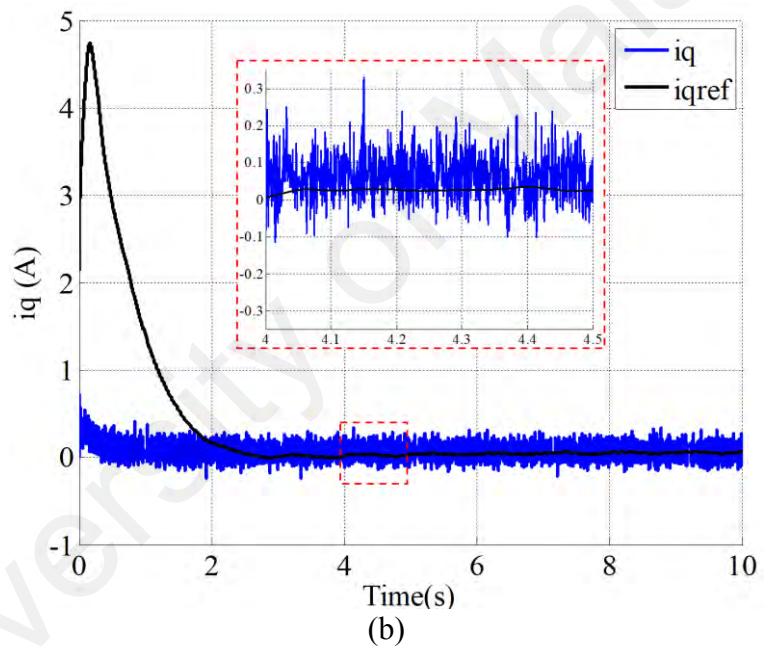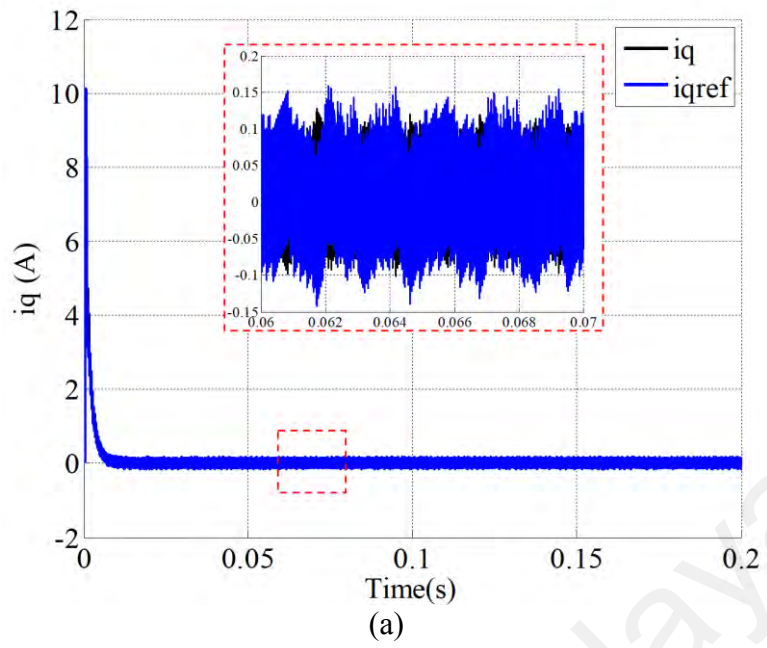
Figure 4.5: q-axis current response for reference speed 500rpm at no load
(a) simulation (b) experiment
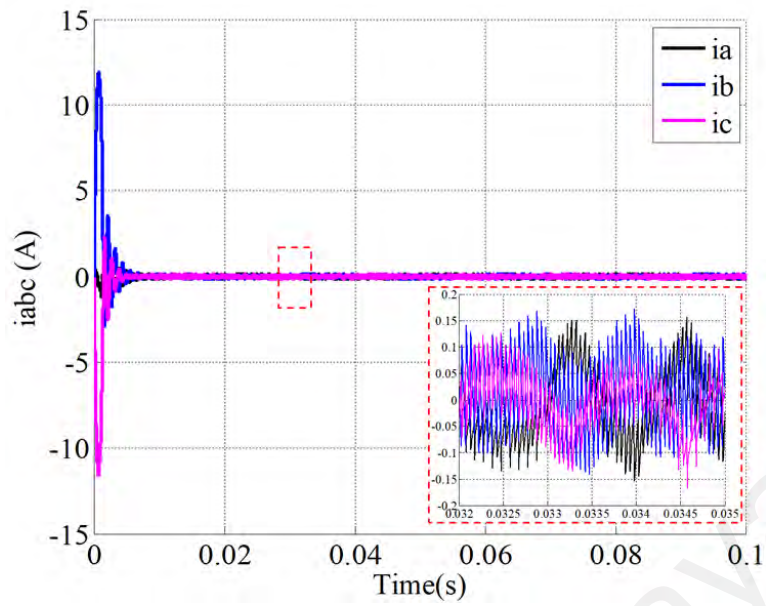
(a)
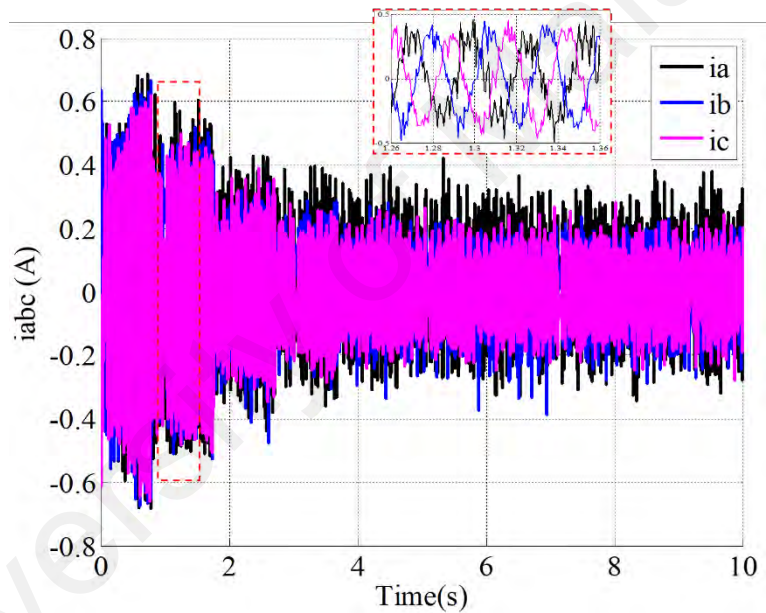
(b)

Figure 4.6: abc phase current for reference speed 500rpm at no load (a) simulation (b) experiment

The output of current controllers provides reference voltages, from which three phase duty cycles are generated to determine PWM operation. In the simulation, during the transient mode, maximum duty cycle is fed to the PWM, then reduced to between 0.4 and 0.6 when reference speed is reached, as shown in Figure 4.7(a). However, experimental results in Figure 4.7(b) show that the duty cycle throughout the whole speed tracking is almost similar namely between 0.3 and 0.7 without apparent hike during the

transient mode. Equation (4.1) is used to prove that the frequency of the obtained duty cycle in both cases (f = 33.33Hz) corresponds to mechanical speed of 500 rpm, which is the reference speed.

$$n_s = \frac{120 * f}{p} \qquad (4.1)$$

(a)

(b)
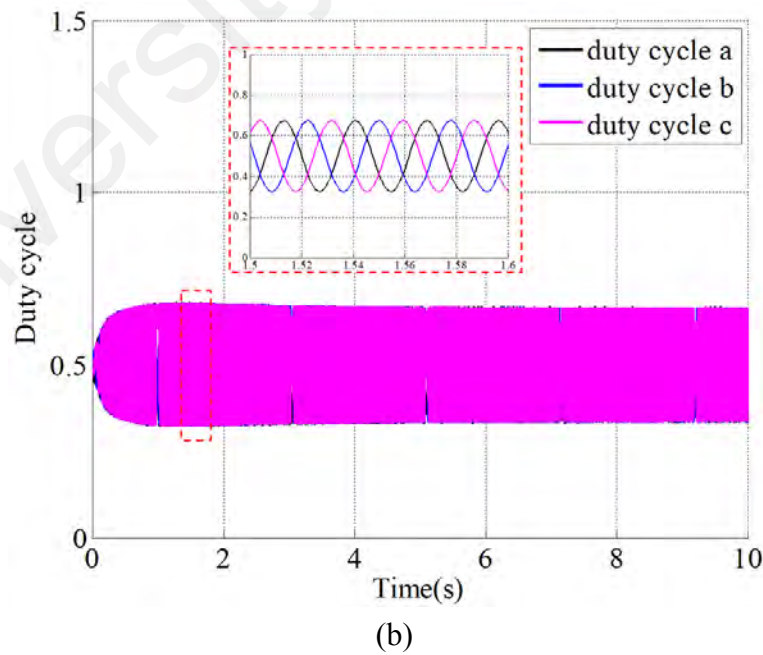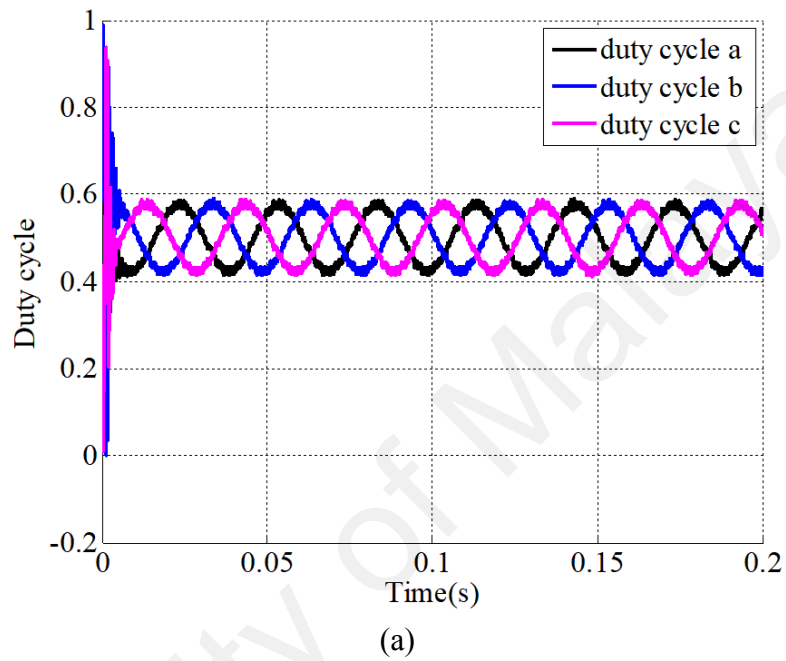
Figure 4.7: abc phase duty cycle for reference speed 500rpm at no load (a) simulation (b) experiment

Figure 4.8 shows line to line voltage obtained in simulation, which is square signals with an amplitude of V_{dc} value, 400V, and with a period of 0.03 seconds. Unfortunately, the experimental line to line voltage high frequency signals cannot be captured in ControlDesk environment due to sampling time limitation of dSpace DS1104. However, similar signal patterns are expected.
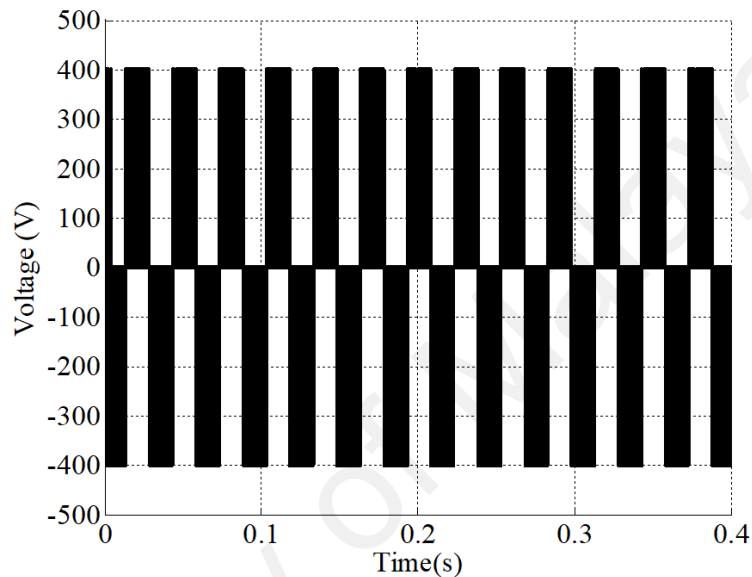
Figure 4.8: Line to line voltage for reference speed 500rpm at no load (simulation)

The results above show that the proposed FOSMC performs as a fast and stable speed controller. In the simulation, d-axis and q-axis reference currents are tracked excellently. However, poor tracking during the transient stage is recorded in actual hardware implementation. This is due to the limitation of the developed prototype in terms of sampling time of dSpace DS1104 controller, where the sampling time is limited up to $5e^{-4}$ seconds only, compared to $1e^{-6}$ seconds in simulation works. Lower sampling time resulted in slower response of the controller to the measured speed and current error. Sampling time of simulation works were purposely not reduced to adapt to the hardware limitation in order to show the best performance that the proposed controller can achieve in terms of tracking properties and anti-disturbance properties. Despite the above-

mentioned limitation, experimental results sufficiently validate simulation results to prove that the proposed FOSMC can track the reference speed.

To further investigate its transient performance, the controller is tested with various reference speeds between 200 to 600 rpm with 100 rpm increment. This speed range is chosen since the focus of this work is to investigate the chattering effect, which is more obvious at low speeds, namely below the base speed of the motor in use. Results in Figure 4.9(a) and (b) verify that fast speed tracking is obtained for all cases in study, with a maximum overshoot of only 2.1% and 9.52% for speed reference of 600 rpm in simulation and experimental run respectively. In the simulation, reference speed is reached at around 0.06 seconds for all cases, whereas in the experiment, the settling time is higher namely at 6 seconds. Small and acceptable steady state error is recorded at a higher speed with around 0.18% in both simulation and experiment for reference speed of 600 rpm.
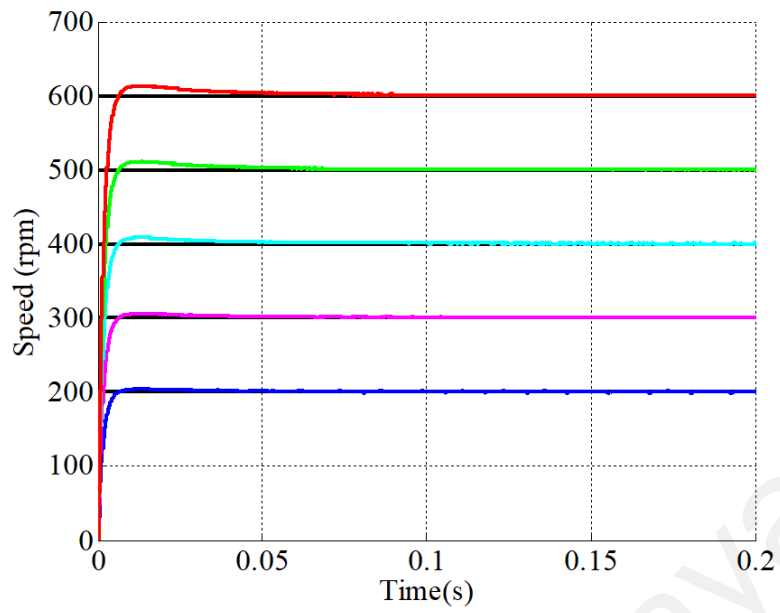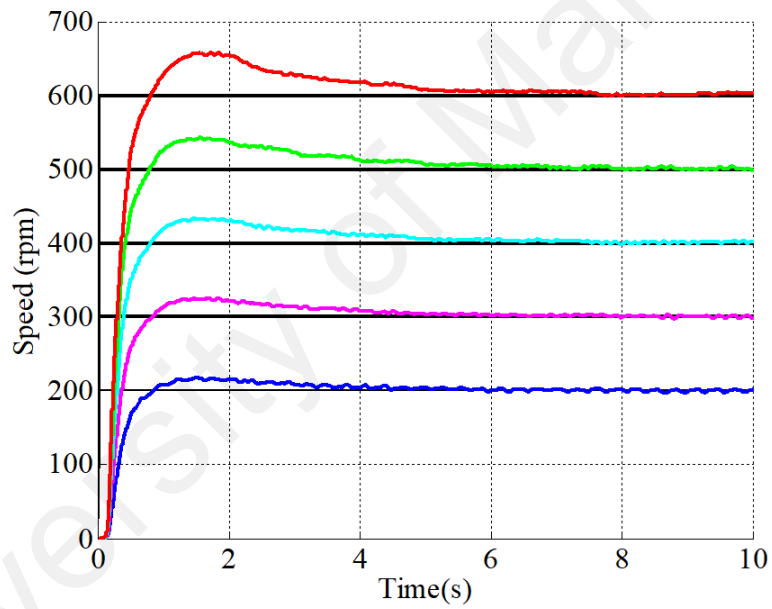
Figure 4.9: Speed response for various reference speeds between 200 to 600 rpm at no load (a) simulation   (b) experiment

Rise time, overshoot, settling time and steady state error recorded for different reference speeds in both simulation and experiment are listed in Table 4.2.

Table 4.2: Comparison of speed tracking properties for different reference speeds at no load condition

Reference speed (rpm)	Rise time (s)		Overshoot (%)		Steady state error (%)	
	Simulation	Experiment	Simulation	Experiment	Simulation	Experiment
200	0.006124	0.8658	2.45	8.35	0	0
300	0.006095	0.8073	2.00	8.00	0	0
400	0.006153	0.8159	1.95	8.32	0.17	0.1
500	0.006181	0.7778	1.96	8.18	0.18	0.12
600	0.006180	0.8059	2.10	9.52	0.18	0.18

4.2.2 Under load torque

Excellent transient properties in no load condition do not guarantee the robustness of the tested controller. Hence, load torque is applied to the PMSM drive system after a certain time to evaluate the proposed FOSMC speed controller's performance under load. First, the reference speed is fixed at 500 rpm. Initially, a load torque of 0.5Nm is applied to the drive system at $t = 0.5s$ and $t = 14s$ in simulation and experiment respectively. In the simulation, the motor experiences a speed drop of 3.34% and manages to track back the reference speed after around 0.5 seconds but with a small steady error of 0.68%, as shown in Figure 4.10(a). Experimental results show a higher speed drop (9.36%) and a longer recovery time (3.36 seconds) compared to those obtained in simulation, as shown in Figure 4.10(b). 1.14% steady state error is obtained in this case. Speed ripple in the experimental run is recorded at 1.08%, which is almost 10 times higher than the speed ripple in the simulation run.
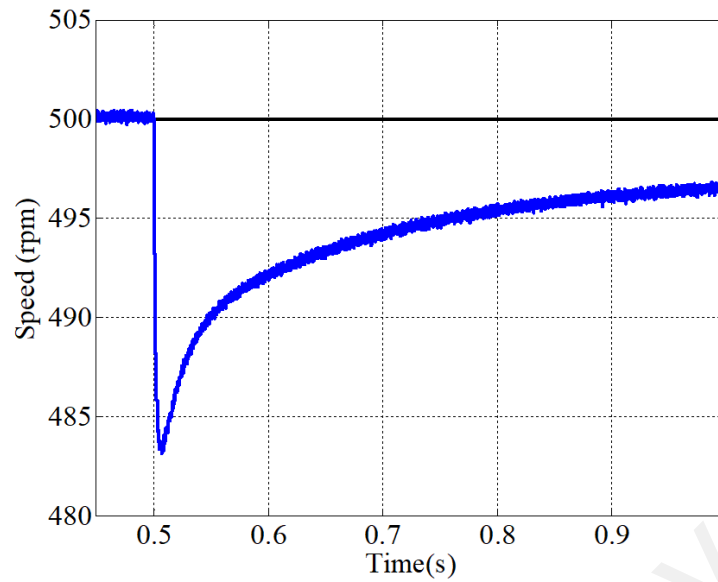
(a)
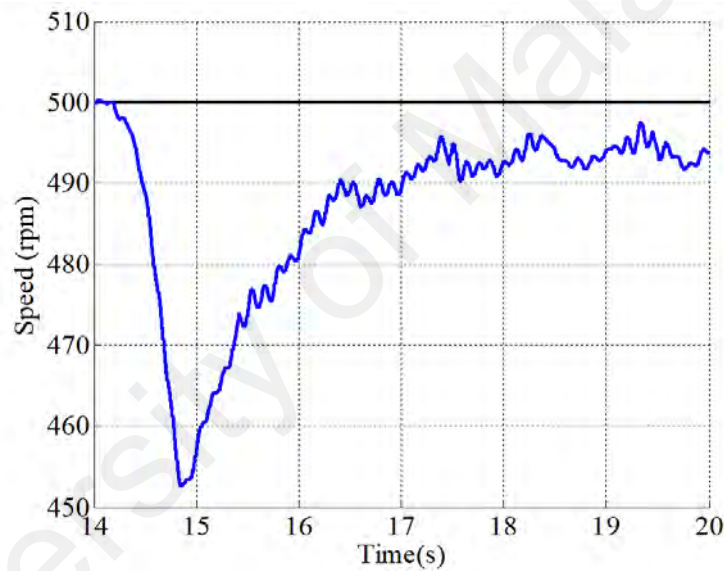
(b)

Figure 4.10: Speed response for reference speed 500rpm with applied load of 0.5Nm
(a) simulation (b) experiment

On the other hand, Figure 4.11(a) and (b) show that torque ripple in the experiment is only at 3.88% compared to those in simulation, which is more than 10 times higher. With applied load, d-axis current reference value remains unchanged at zero. On the contrary, q-axis current reference value changes following equation (4.2) as torque controlling part of field-oriented control of PMSM.

$$T_e = K_t * i_q \tag{4.2}$$
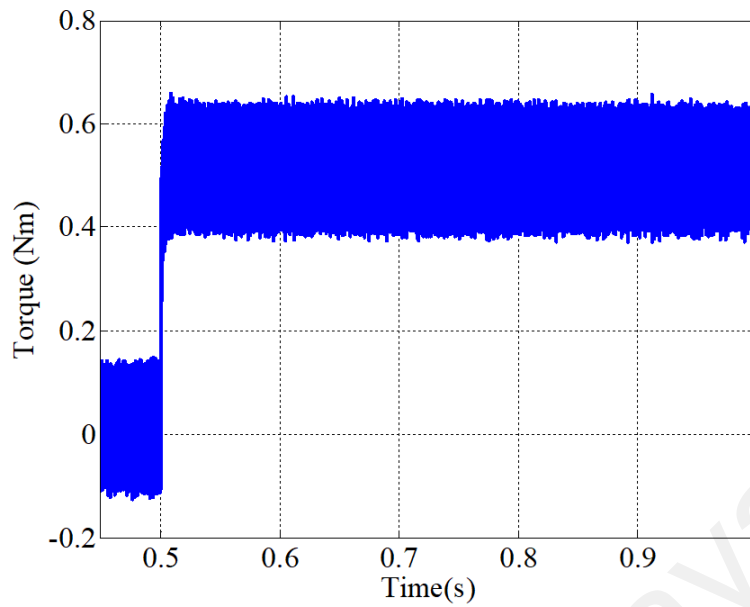
(a)
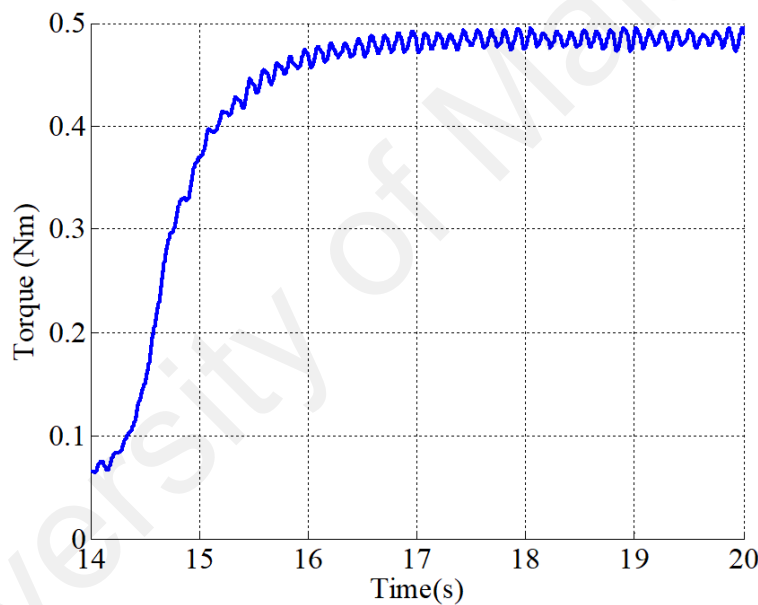
(b)

Figure 4.11: Torque response for reference speed 500rpm with applied load of 0.5Nm
(a) simulation (b) experiment

Both d-axis and q-axis current measurement experience higher ripples in the experimental case compared to in the simulation case, as shown in Figure 4.12 and Figure 4.13. However, q-axis current reference value itself has a significant ripple of 0.1947A in simulation, reflecting the insufficient performance of q-axis current PI controller in the inner loop.
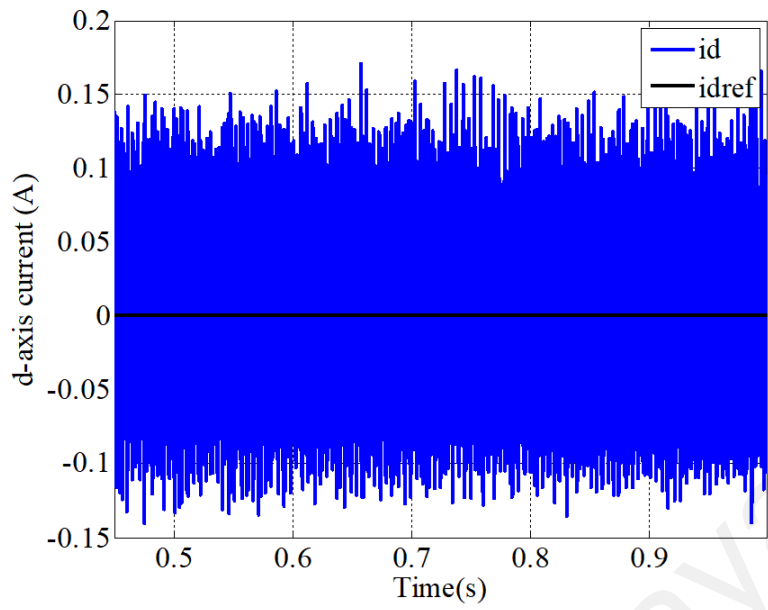
(a)
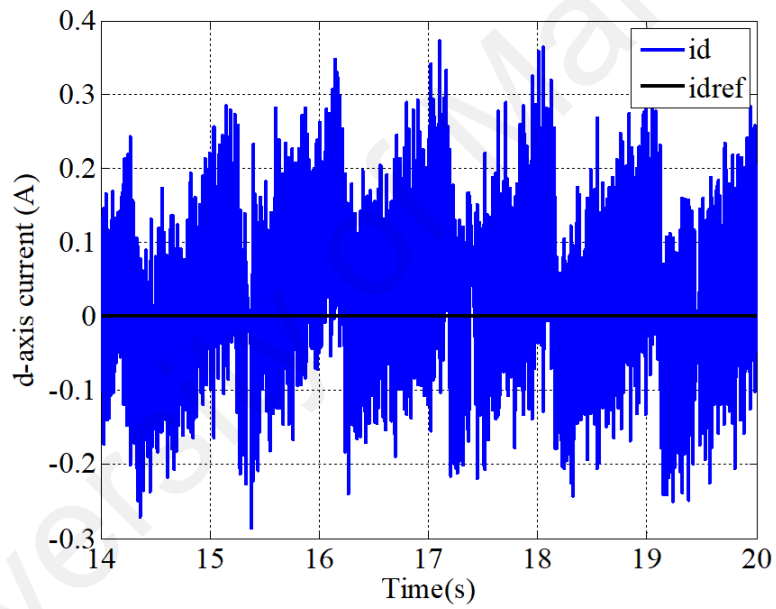
(b)

Figure 4.12: d-axis current response for reference speed 500rpm with applied load of 0.5Nm (a) simulation (b) experiment
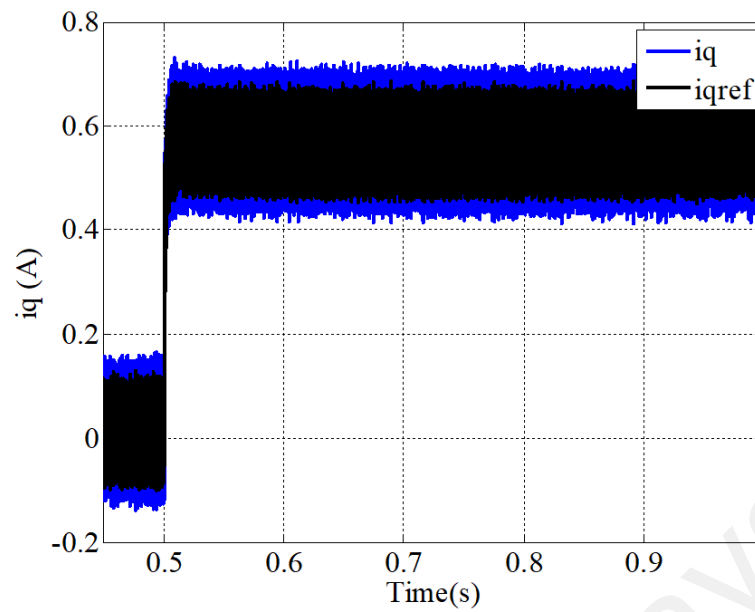
(a)
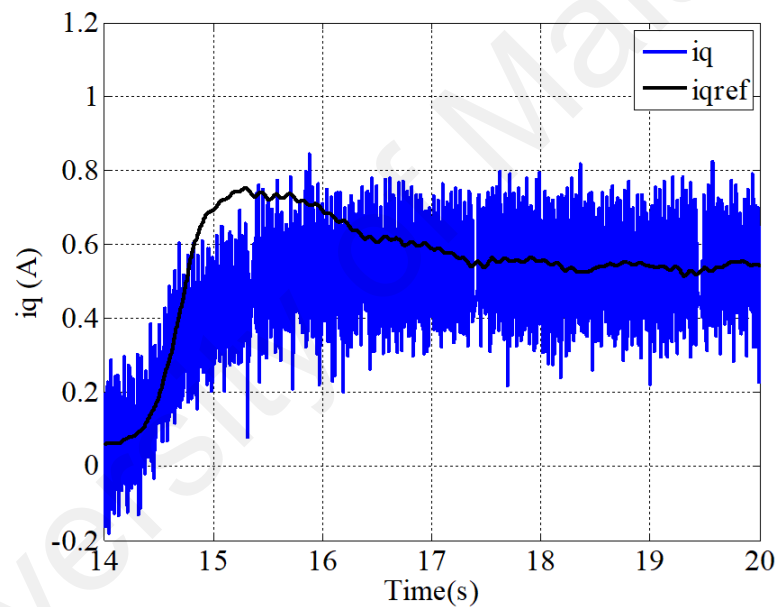
(b)

Figure 4.13: q-axis current response for reference speed 500rpm with applied load of 0.5Nm (a) simulation (b) experiment

Although the machine in test suffers from speed drop when load torque is suddenly applied, no significant change can be seen in the duty cycle in both simulation and experiment due to fast speed recovery, as shown in Figure 4.14(a) and (b) respectively. The period of duty cycle remains unchanged at 0.03 seconds which corresponds to 500rpm.

(a)

(b)
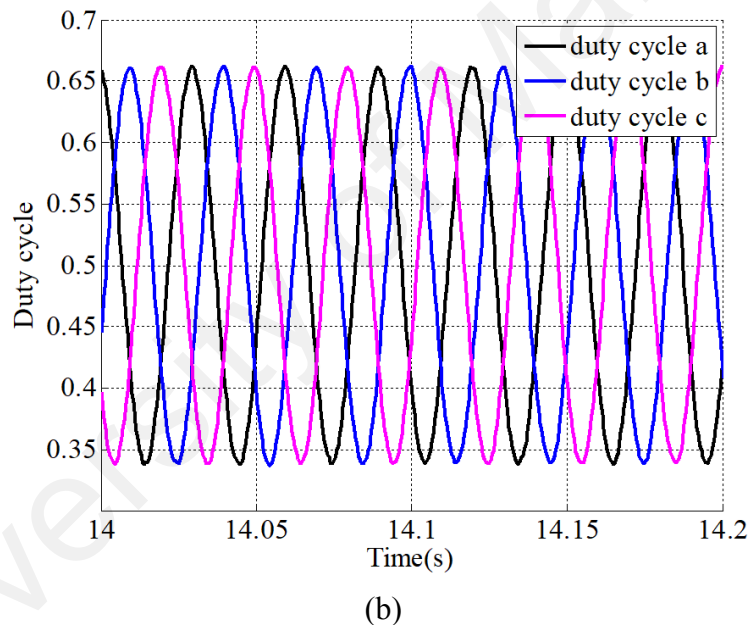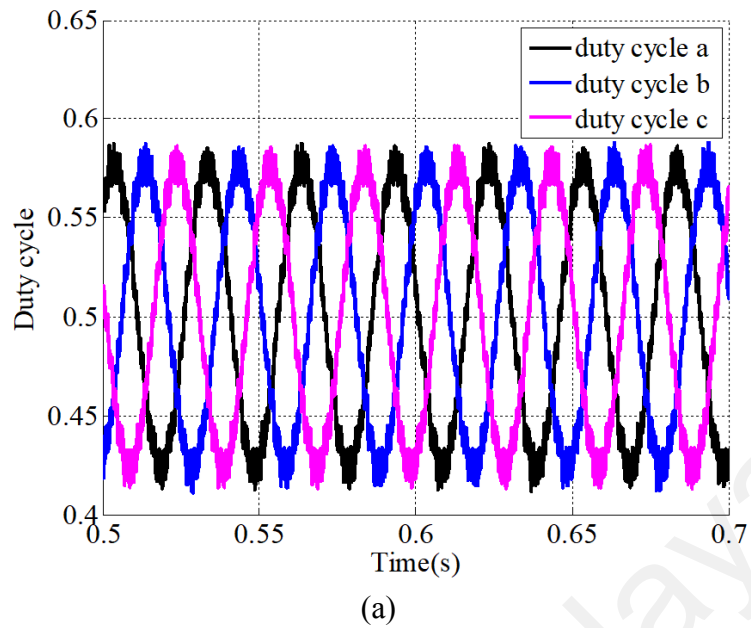
Figure 4.14: abc phase duty cycle for reference speed 500rpm with applied load of 0.5Nm (a) simulation (b) experiment

Results above prove that the designed FOSMC is a robust speed controller that can successfully reject load disturbance applied to the machine. Further verification of the controller's robustness is executed by applying higher load torques. Load of 1.0 Nm is applied at $t = 1.0s$ in simulation and at around $t = 31s$ in experiment. Figure 4.15(a) shows that the PMSM suffers a speed drop of 4.06% in simulation but recovers to steady state after around 0.5 seconds with 1.22% speed error. Similar to the test with 0.5Nm load

torque, a slightly poorer performance of speed controller is obtained in experiment with 13.92% speed drop, 5.18 seconds recovery time and 2.12% steady state error, as shown in Figure 4.15(b).
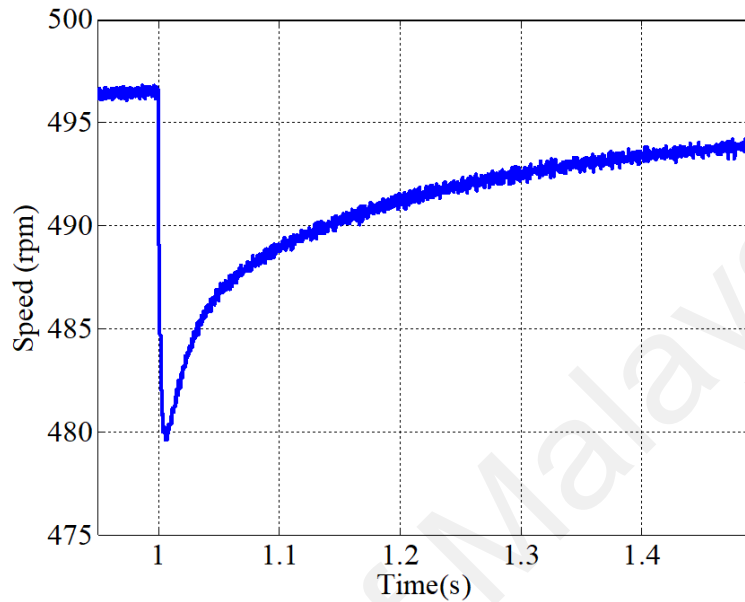
(a)
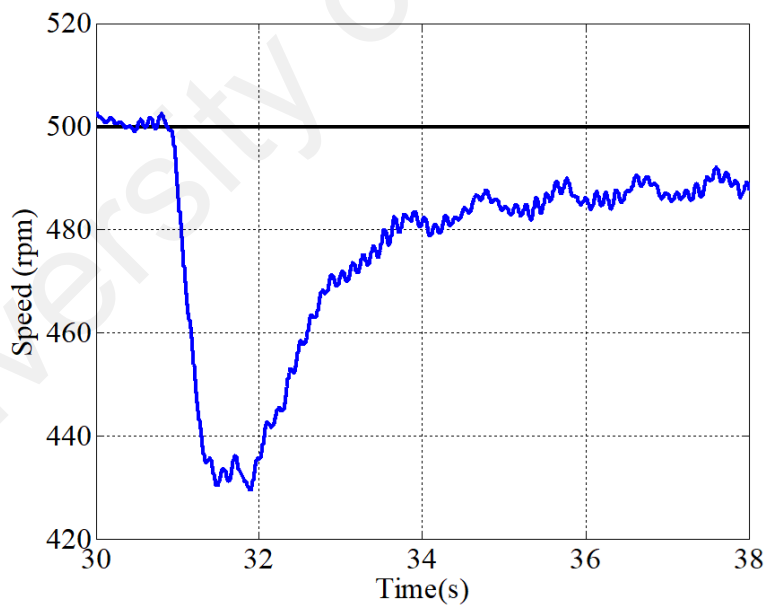
(b)

Figure 4.15: Speed response for reference speed 500rpm with applied load of 1.0Nm
(a) simulation   (b) experiment

In terms of torque, almost 6 times smaller ripple is obtained in the experiment compared to simulation, namely only at 3.19%, as can be seen in Figure 4.16(a) and (b).
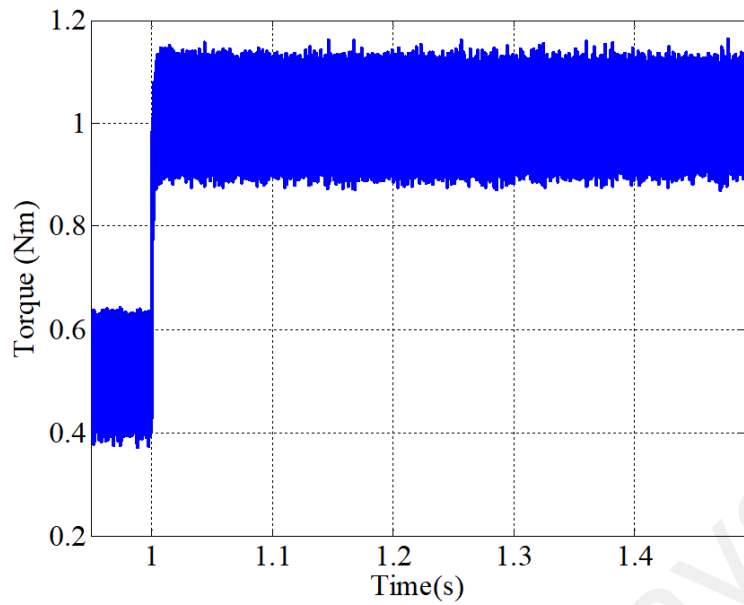
(a)
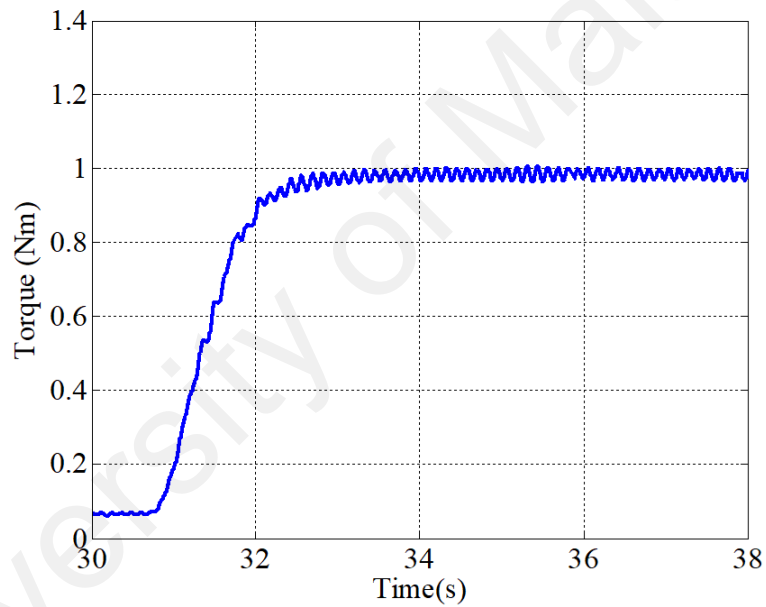

(b)

Figure 4.16: Torque response for reference speed 500rpm with applied load of 1.0Nm
(a) simulation   (b) experiment

Figure 4.17(a) shows the speed response during simulation when a load torque of 1.5Nm is applied to the system at $t = 1.5s$. After a speed reduction of 4.58%, a steady state is reached with 1.66% error. Experimental results in Figure 4.17(b) show that the motor slows down to 390 rpm and then recovers back to 13.7 rpm below reference speed when the load is applied at around $t = 48s$.
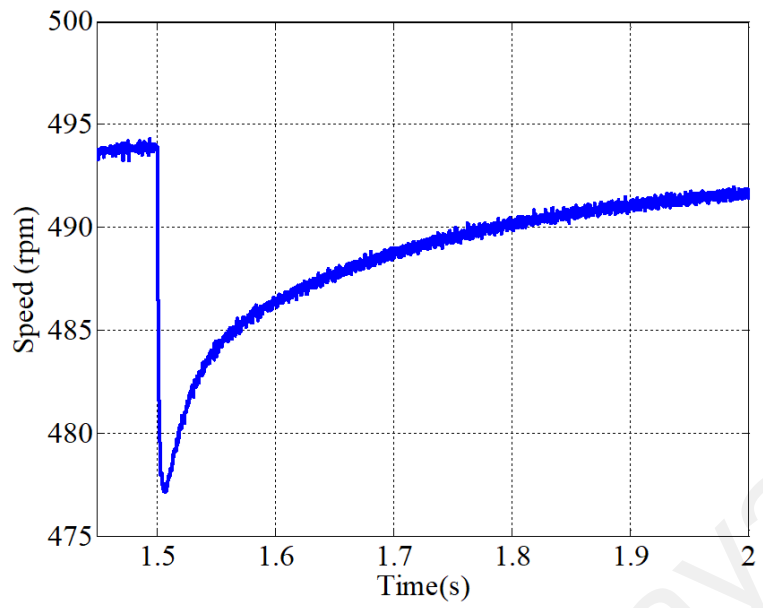
(a)
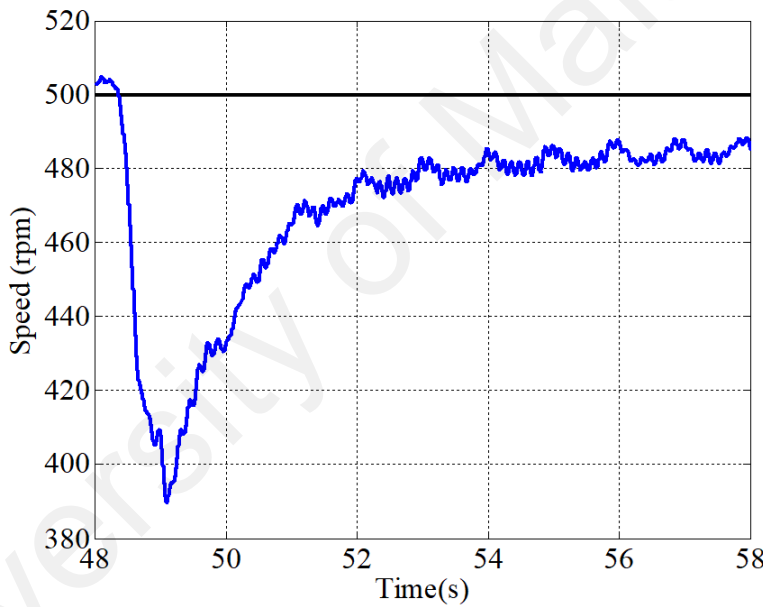
(b)

Figure 4.17: Speed response for reference speed 500rpm with applied load of 1.5Nm
(a) simulation   (b) experiment

In this case, torque ripple of 12.53% and 2.47% is recorded in simulation and experiment

respectively, as shown in Figure 4.18.
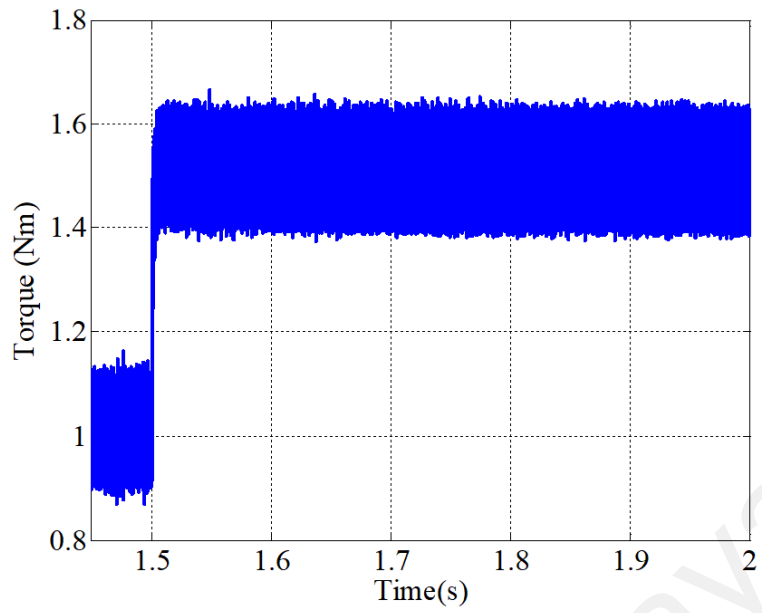
(a)
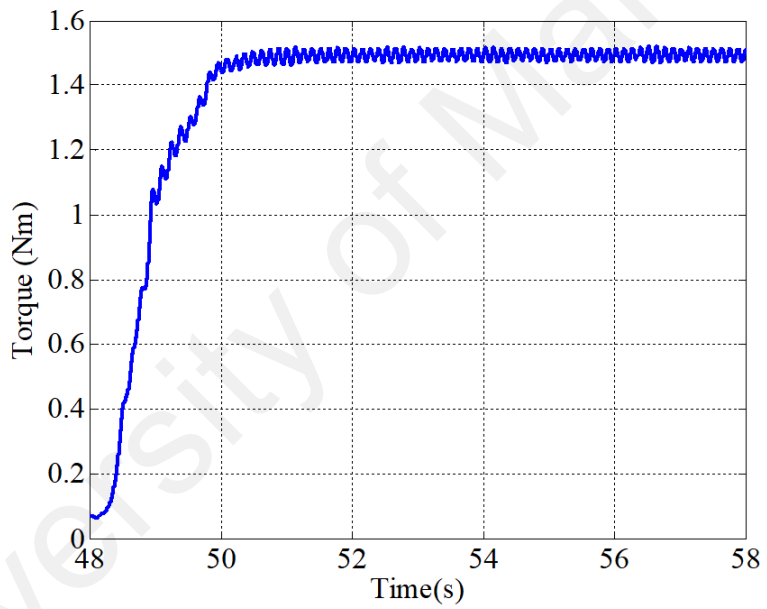

(b)

Figure 4.18: Torque response for reference speed 500rpm with applied load of 1.5Nm
(a) simulation   (b) experiment

Table 4.3 summarizes the speed tracking properties of the PMSM drive system with the FOSMC speed controller under various applied load torques ranging from 0.5Nm to 1.5Nm.

Table 4.3: Comparison of speed tracking properties for reference speed 500 rpm with different applied load torques

Load torque (Nm)	Speed drop (%)		Recovery time (s)		Steady state error (%)		Torque ripple (%)	
	Simulation	Experiment	Simulation	Experiment	Simulation	Experiment	Simulation	Experiment
0.5	3.34	9.36	0.5	3.36	0.68	1.14	40.98	3.88
1.0	4.06	13.92	0.5	5.18	1.22	2.12	18.43	3.19
1.5	4.58	22	0.5	6.03	1.66	2.74	12.53	2.47

Other than 500 rpm, the performance of the proposed controller is also evaluated with a range of different reference speeds between 200 rpm and 600 rpm. During the simulation run, when load torque of 0.5 Nm is applied, speed drop experienced by the motor decreases from 8.75% to 2.62% as reference speed increases, as shown in Figure 4.19(a). Figure 4.19(b) shows that a similar speed tracking trend is also recorded experimentally, where the speed drop ranges from 6.97% to 46.4%.
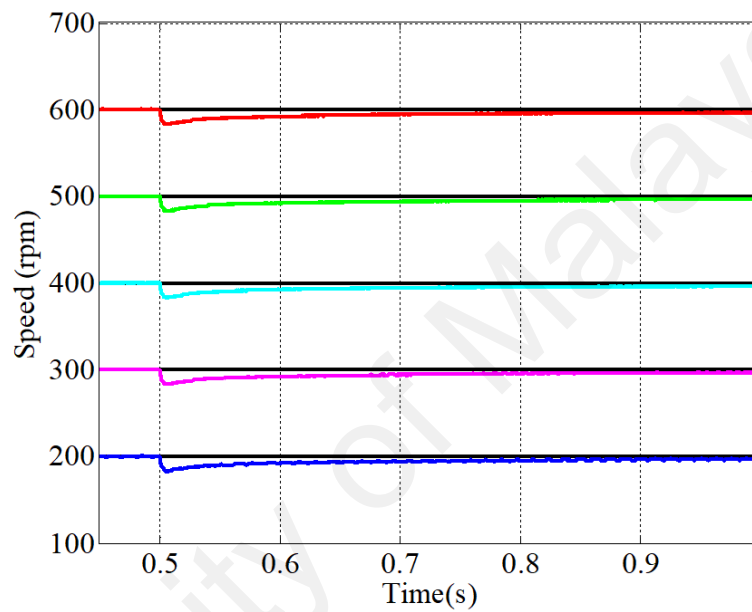
(a)
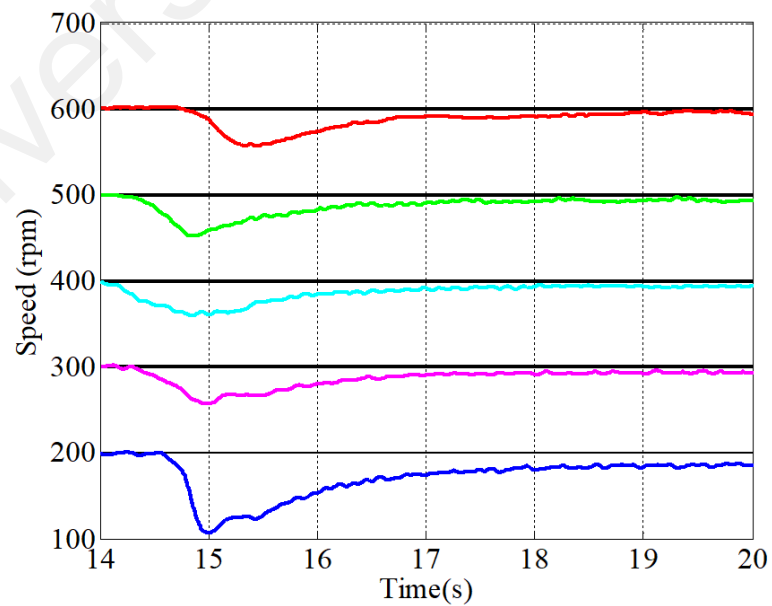
(b)

Figure 4.19: Speed response for various reference speeds between 200 to 600 rpm with applied load of 0.5Nm (a) simulation (b) experiment

Results in Figure 4.20(a) and (b) are obtained when the system is loaded with 1.0 Nm torque. Motor speed reduces more significantly in this case compared to the previous case due to higher applied load. In addition, speed loss is not fully recovered, where steady state error lies in the range of 1.08–3.1% and 1.58–8.6% for simulation and experiment respectively.
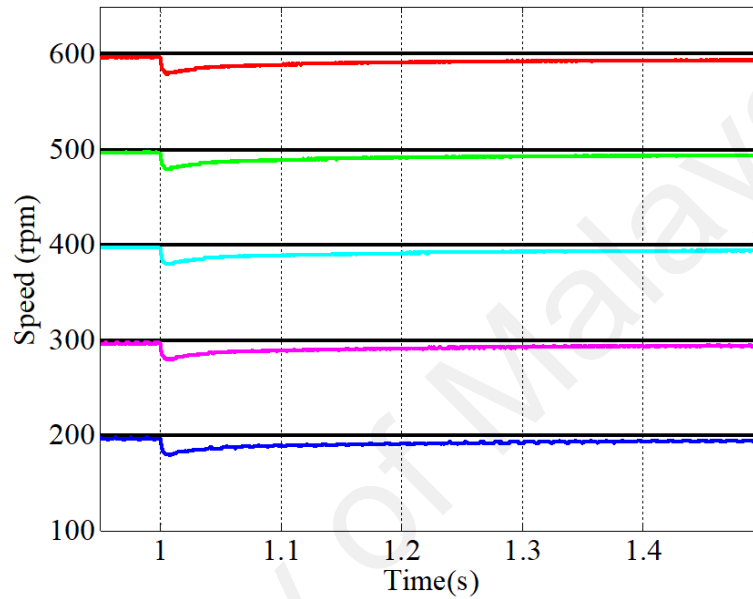
(a)
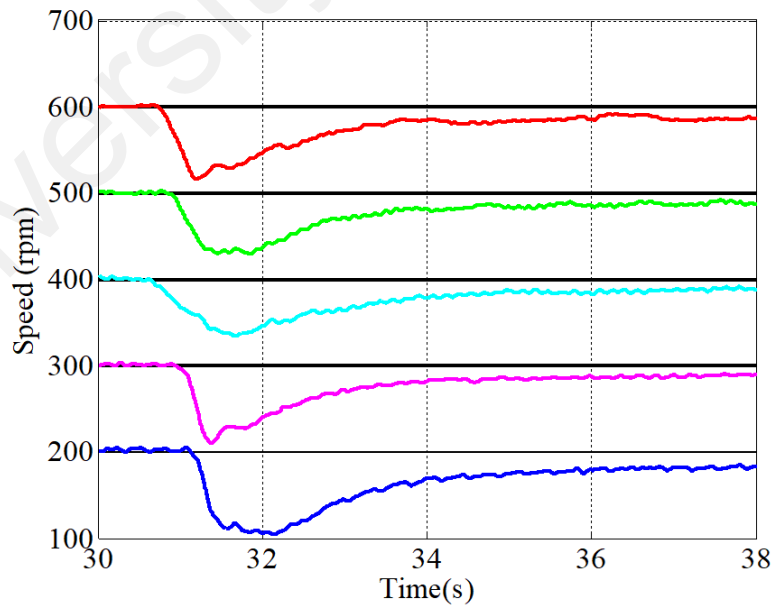
(b)

Figure 4.20: Speed response for various reference speeds between 200 to 600 rpm with applied load of 1.0Nm (a) simulation (b) experiment

Load torque of 1.5 Nm results in higher speed drop and steady state error, as shown in Figure 4.21(a) and (b). In addition, in the case of 200 rpm speed reference during the actual experiment, the applied load brings the motor to a complete halt.
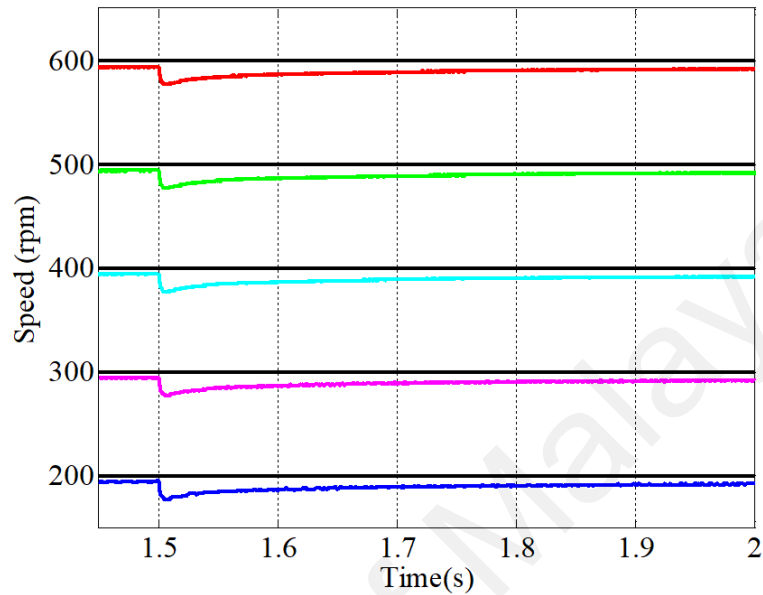
(a)
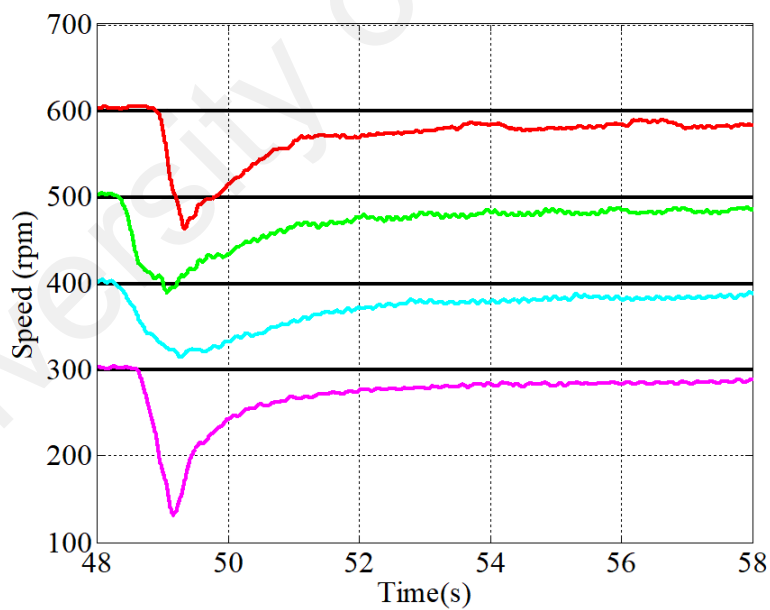
(b)

Figure 4.21: Speed response for various reference speeds between 200 to 600 rpm with applied load of 1.5Nm (a) simulation (b) experiment

Speed drop and steady state error for various reference speeds and applied load torques are summarized in Table 4.4. Among all the chosen reference speeds, the best speed

tracking properties are obtained at the reference speed of 600 rpm. At 200 rpm reference speed, the highest speed drop and steady state error are recorded. Difference in quantitative values of speed drops and steady state errors between simulation and experimental values are expected, similar to other tracking properties values in no load condition. This is due to slower controller's response in experimental validation compared to those in simulation when load is applied, resulting from sampling time limitation, as elaborated in the previous section.

Table 4.4: Comparison of speed tracking properties for reference speeds 200 - 600 rpm with different applied load torques

Load torque (Nm)	Speed reference (rpm)	Speed drop (%)		Steady state error (%)	
		Simulation	Experiment	Simulation	Experiment
0.5	200	8.75	46.4	1.7	6.75
	300	5.33	14.23	1.17	2.33
	400	4.05	10.07	0.93	1.85
	500	3.34	9.36	0.68	1.14
	600	2.62	6.97	0.57	0.62
1.0	200	10.05	48	3.1	8.6
	300	6.4	30	2.13	3.7
	400	5.05	16.42	1.63	3.08
	500	4.06	13.92	1.22	2.12
	600	3.42	13.85	1.08	1.58
1.5	200	11.65	-	4.3	-
	300	7.47	55.9	3.07	4.7
	400	5.68	21.28	2.23	3.8
	500	4.58	22	1.66	2.74
	600	3.78	22.57	1.45	1.77

The presented data prove that the proposed FOSMC performs as a fast and accurate speed tracking for the chosen wide range of speed references in both no load and under load torque conditions.

4.3   Comparison of proposed FOSMC with conventional integer order SMC

In this work, the fractional order sliding surface is proposed to replace the conventional integer order sliding surface in designing PMSM sliding mode speed controller. Hence, it is relevant to compare the performance of the proposed FOSMC and the integer order SMC (IOSMC), as used by Zaky (2012) in their work.

4.3.1   No load condition

Initially, no load condition is considered. For this purpose, reference speed of 500 rpm is selected. Speed responses in Figure 4.22 show that FOSMC results in faster speed tracking with less overshoot compared to IOSMC for both simulation and experimental case. Experimentally, motor controlled with SMC exhibits some speed oscillation in transient mode, as shown in Figure 4.22(b).

Fast transient speed response is obtained due to higher transient torque experienced by the motor. In the simulation, initial torque of about 9.106 Nm is recorded for the FOSMC system, as shown in Figure 4.23(a), compared to only 0.8077 Nm for IOSMC system. Similarly, in the experimental case shown in Figure 4.23(b), the initial torque of the FOSMC system is almost twice as much as the initial torque of IOSMC system. In addition, in terms of torque ripple, FOSMC system slightly outperforms IOSMC system with only 0.2 Nm and 0.01 Nm ripple in simulation and experiment respectively, compared to 0.2143 Nm and 0.01 Nm for IOSMC system.
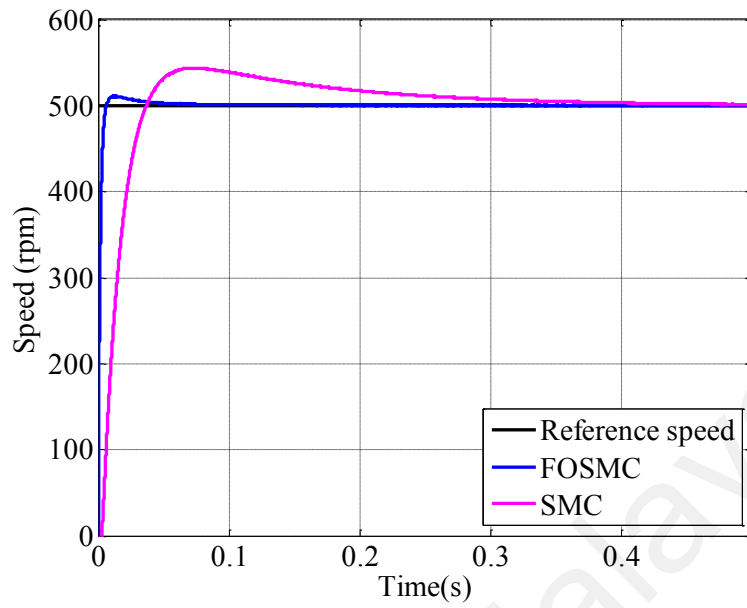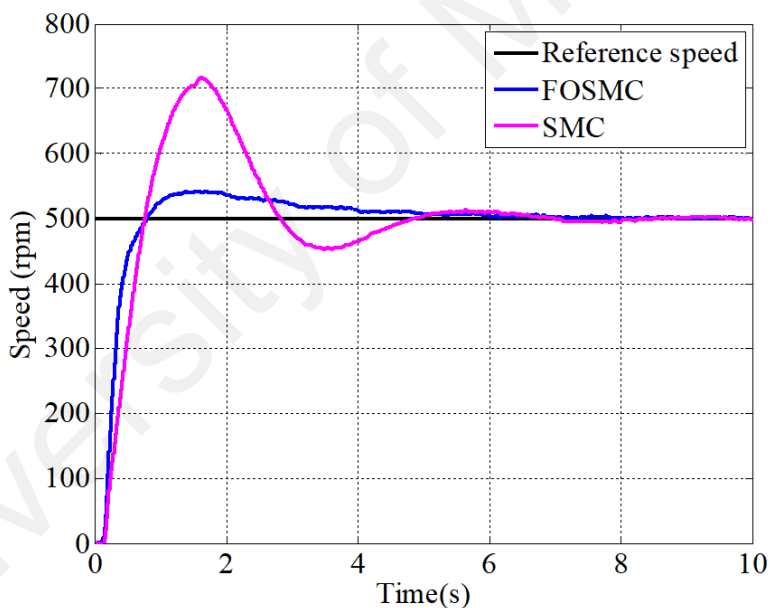
Figure 4.22: Speed response comparison between FOSMC and SMC for speed reference of 500 rpm at no load (a) simulation (b) experiment

(a)

(b)

Figure 4.23: Torque response comparison between FOSMC and SMC for speed reference of 500 rpm at no load (a) simulation (b) experiment

The difference in performance of both controllers in comparison is more significant when q-axis reference current response is analysed. Figure 4.24(a) shows that $i_{q,ref}$ ripple produced in FOSMC simulation is only 0.16A, which is more than 10 times smaller than the ripple in IOSMC. In experiment, $i_{q,ref}$ ripple produces in FOSMC is only 0.0136A compared to 0.02198A in IOSMC, as shown in Figure 4.24(b).

Figure 4.24: q-axis reference current response comparison between FOSMC and SMC
for speed reference of 500 rpm at no load (a) simulation (b) experiment

In addition, actual i_q ripple in FOSMC drive system is also recorded to be smaller
compared to in IOSMC drive system in both simulation and experiment, as shown in
Figure 4.25(a) and (b) respectively.
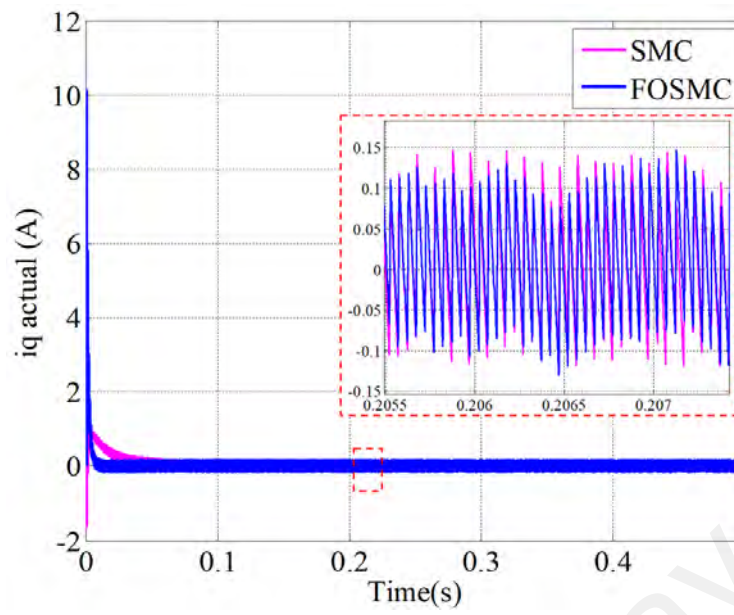
(a)
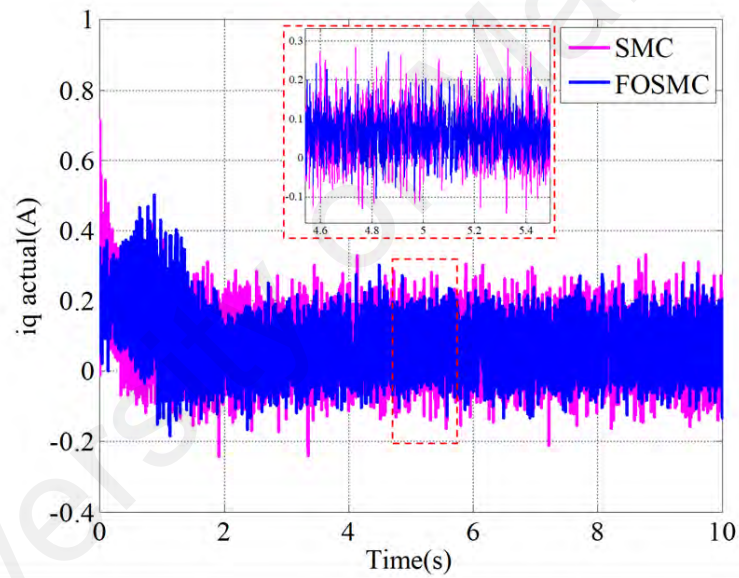
(b)

Figure 4.25: q-axis actual current response comparison between FOSMC and SMC for speed reference of 500 rpm at no load (a) simulation (b) experiment

Table 4.5 compares simulation and experimental results of FOSMC and IOSMC systems in terms of various speed tracking properties when no load is applied to the systems.

Table 4.5: Comparison of speed tracking properties for the proposed FOSMC and conventional integer order SMC with reference speed 500 rpm at no load condition

Properties	FOSMC		SMC (Zaky, 2012)	
	Simulation	Experiment	Simulation	Experiment
Rise time (s)	0.0062	0.7778	0.0361	0.7627
Settling time (s)	0.0096	7.007	0.35	9.017
Steady state error (%)	0.02	0	0.28	0.18
Overshoot (%)	1.96	8.18	8.66	43.2
Torque ripple (Nm)	0.2	0.01	0.2143	0.01
$i_{q,ref}$ ripple (A)	0.16	0.0136	1.8948	0.02198
$i_{q,actual}$ ripple (A)	0.186	0.34	0.2597	0.3653

4.3.2 Under load torque

Other than performance in no load condition, a comparison is also made when load torque is applied to both drive systems. When a load torque of 0.5 Nm is applied to an IOSMC system at $t = 0.5s$ in simulation, the system experiences almost 66% higher speed drop than FOSMC system, as shown in Figure 4.26(a). However, experimental results in Figure 4.26(b) show that the speed drop is almost equal in both systems. On the contrary, the IOSMC system outperforms the FOSMC system in terms of steady state error. Experimentally, no steady state error is recorded when the integer order speed controller is used, however, the motor suffers under steady state speed oscillation of about 2.2%.
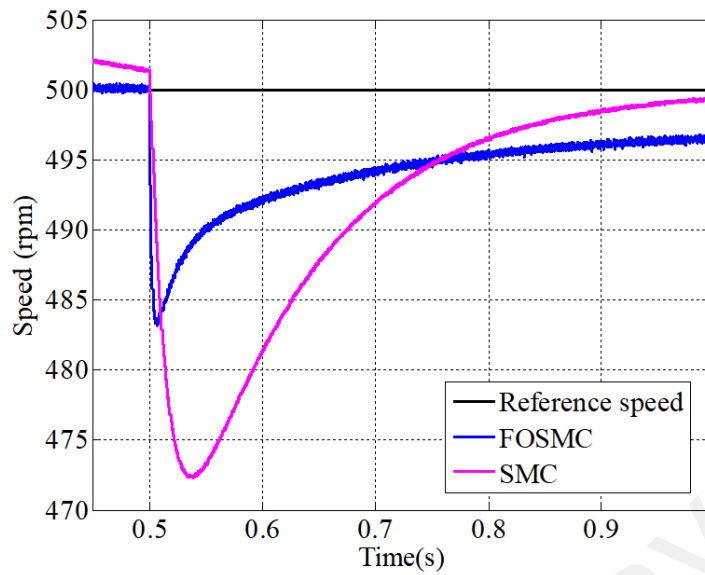
(a)
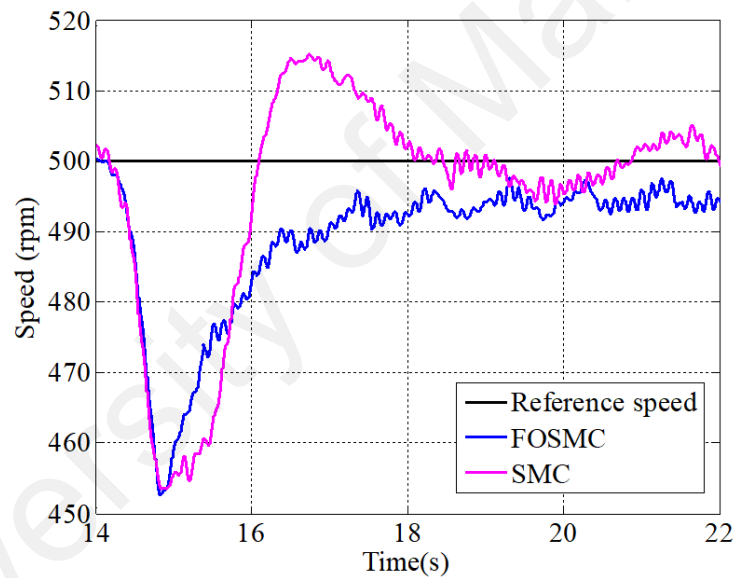
(b)

Figure 4.26: Speed response comparison between FOSMC and SMC for speed reference of 500 rpm with applied load of 0.5Nm (a) simulation (b) experiment

With the application of 1.0 Nm load torque, speed of the motor in the IOSMC system is more significantly reduced namely by 5.86% and 27.54% in simulation and experiment respectively, as shown in Figure 4.27. Similar to the previous case, its speed error at steady state is smaller than the FOSMC system. Speed oscillation of around 2.06% is recorded experimentally in this case.

(a)

(b)

Figure 4.27: Speed response comparison between FOSMC and SMC for speed reference of 500 rpm with applied load of 1.0Nm (a) simulation (b) experiment

Figure 4.28 shows how an applied load of 1.5 Nm affects speed tracking of the drive system. FOSMC system outperforms IOSMC in terms of speed drop but shows its disadvantage in terms of steady state error.
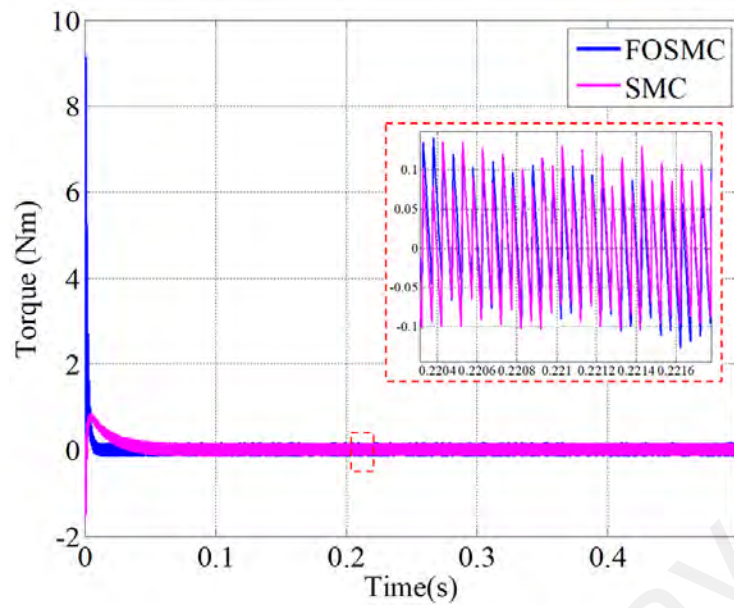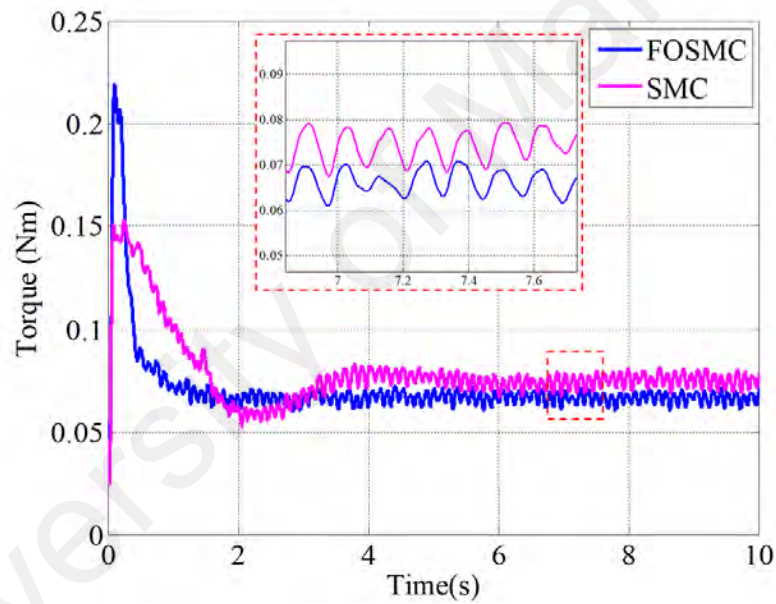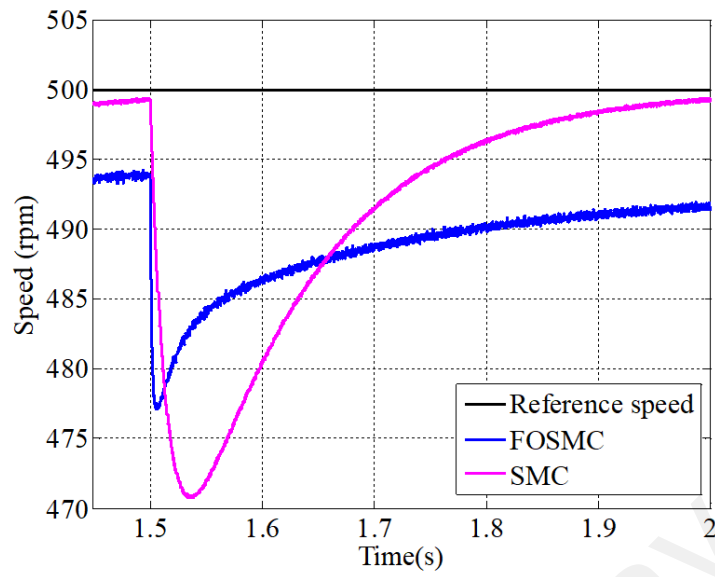
(a)
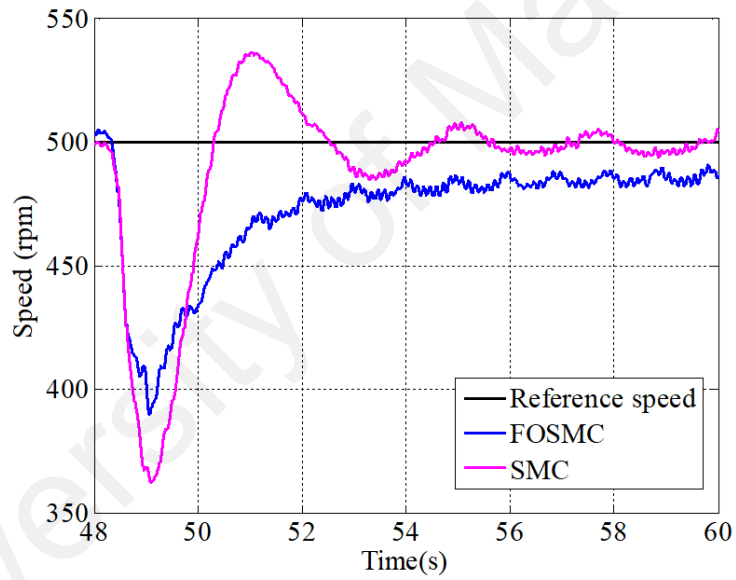
(b)

Figure 4.28: Speed response comparison between FOSMC and SMC for speed
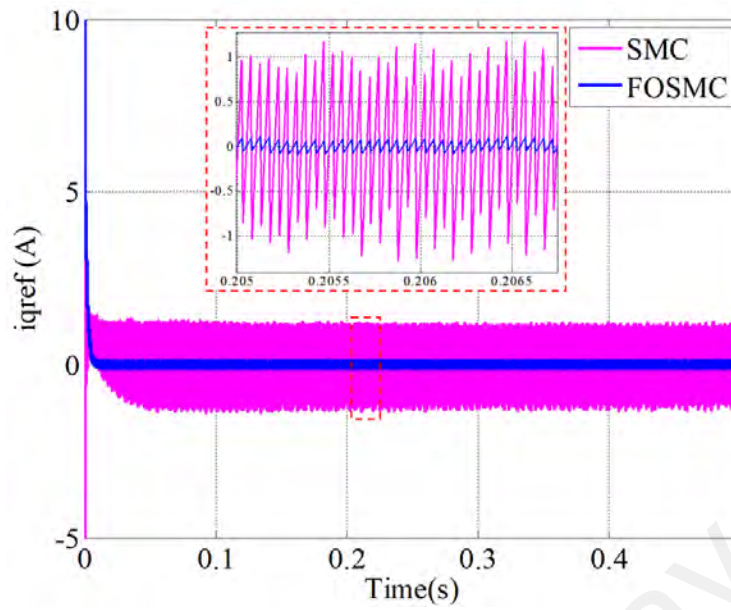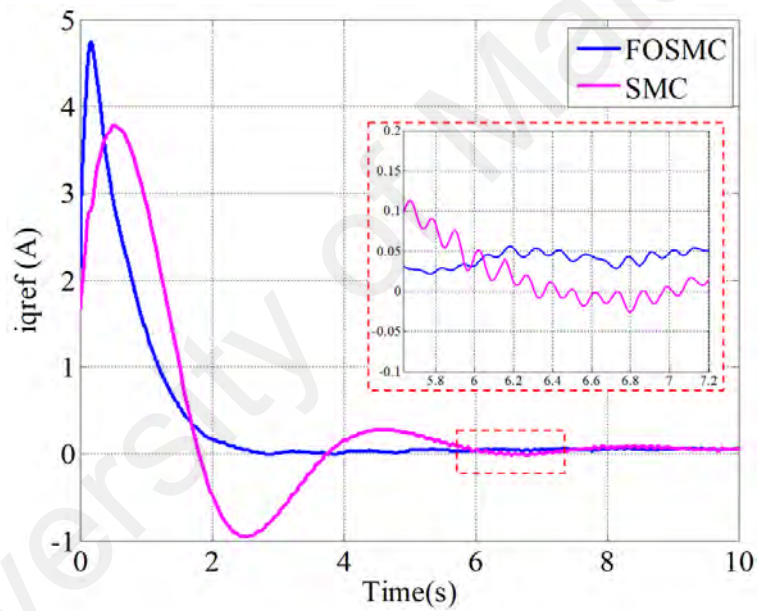reference of 500 rpm with applied load of 1.5Nm (a) simulation (b) experiment

Table 4.6 compares the performance of PMSM driven with FOSMC and IOSMC with applied external loads.

Table 4.6: Comparison of speed tracking properties for the proposed FOSMC and conventional integer order SMC with reference speed 500 rpm under various applied load torques

Properties	Load torque (Nm)	FOSMC		SMC (Deng, Wang, Li, Liu, & Tian, 2019; Y. Wang et al., 2019; Zaky, 2012)	
		Simulation	Experiment	Simulation	Experiment
Speed drop (%)	0.5	3.34	9.36	5.54	9.26
	1.0	4.06	13.92	5.86	22.3
	1.5	4.58	22	5.84	27.54
Steady state error (%)	0.5	0.68	1.14	0.14	0
	1.0	1.22	2.12	0.14	0
	1.5	1.66	2.74	0.14	0

From a detailed comparison in Table 4.5 and Table 4.6, it is clear that the incorporation of fractional calculus in SMC design improves the PMSM drive speed tracking performance. SMC with fractional order sliding surface also makes the system more insensitive to external load disturbances. Furthermore, the proposed controller ensures more stable steady state motor rotation without oscillation, as experienced by the motor in IOSMC system. Although speed error is recorded during steady state, the values are relatively small. In addition, the presented results prove that replacing integer order calculus with fractional order ones in sliding surface design reduces SMC's chattering effects, which are originated from current, torque and speed ripples and/or oscillations.

4.4 Comparison of proposed FOSMC with FOSMC-PI and FOSMC-PD speed controllers

In this work, a fractional PID sliding surface is proposed to construct the sliding mode speed controller. Other similar sliding surface designs that fall under fractional order SMC category are fractional PI sliding surface as proposed by B. Zhang et al. (2012) (FOSMC-PI) and fractional PD sliding surface as proposed by Huang et al. (2012) (FOSMC-PD). Hence, it is relevant to compare the performance of the proposed FOSMC with the other two types of FOSMC.

4.4.1 No load condition

With speed reference of 250 rpm, initially, all tests are executed without any applied load. As seen in Figure 4.29(a) and (b), FOSMC with PID sliding surface design has advantages against FOSMC-PI and FOSMC-PD in terms of overshoot and rise time respectively, in both simulation and experiment.
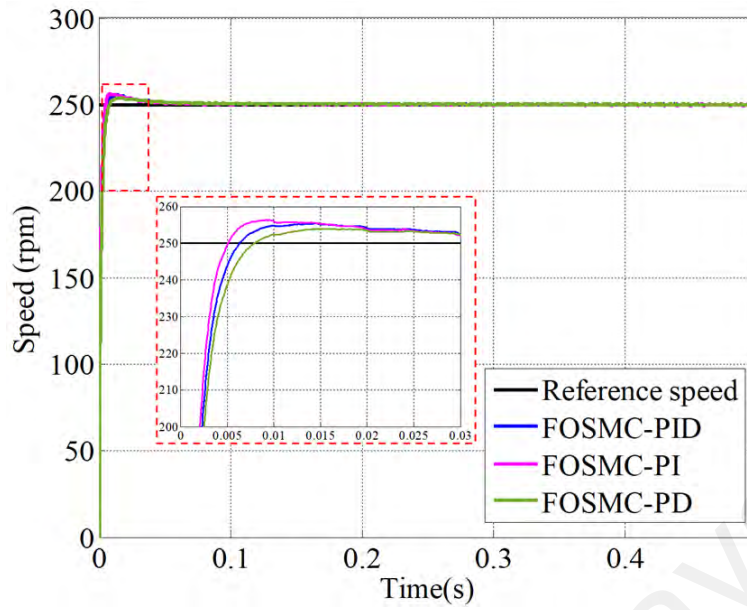
(a)
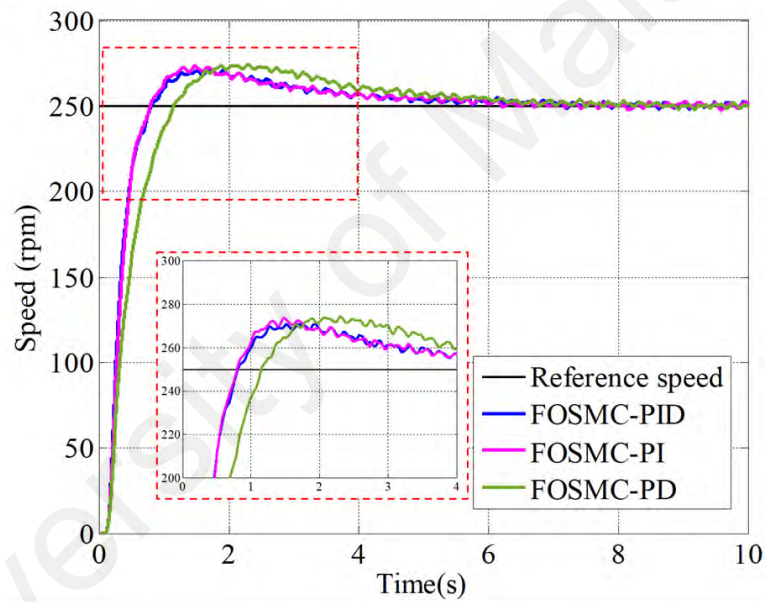
(b)

Figure 4.29: Speed response comparison between FOSMC-PID, FOSMC-PI and FOSMC-PD for speed reference of 250 rpm at no load condition (a) simulation (b) experiment

In terms of torque response, the FOSMC-PID system exhibits a slightly lower torque ripple in experimental validation, as shown in Figure 4.30(b). This advantage is however not clearly portrayed in simulation results in Figure 4.30(a).
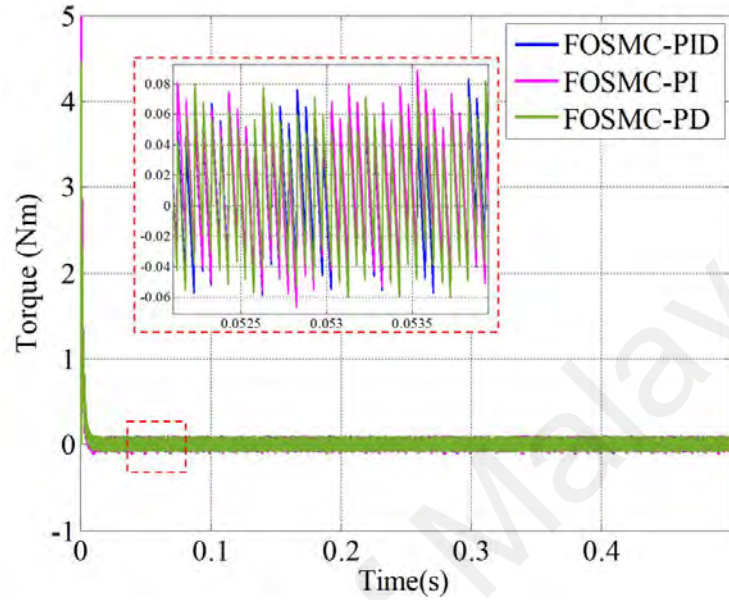
(a)
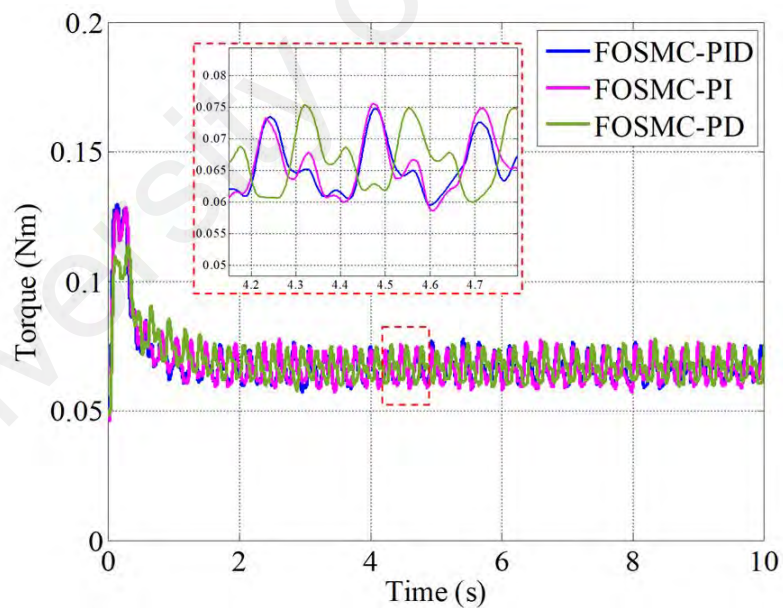
(b)

Figure 4.30: Torque response comparison between FOSMC-PID, FOSMC-PI and FOSMC-PD for speed reference of 250 rpm at no load condition (a) simulation (b) experiment

q-axis reference current simulation results in Figure 4.31(a) show that FOSMC-PI outperforms the other two FOSMC in comparison with around 50% smaller ripple. In the contrary, experimental results indicate that FOSMC-PID system has lower $i_{q,ref}$ ripple i.e. only 0.001A compared to the other three systems, as shown in Figure 4.31(b).

(a)

(b)
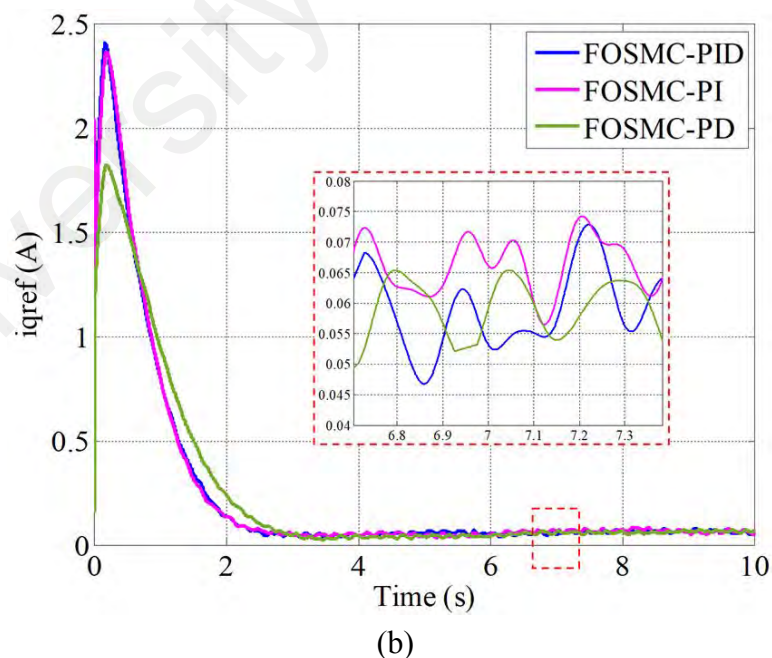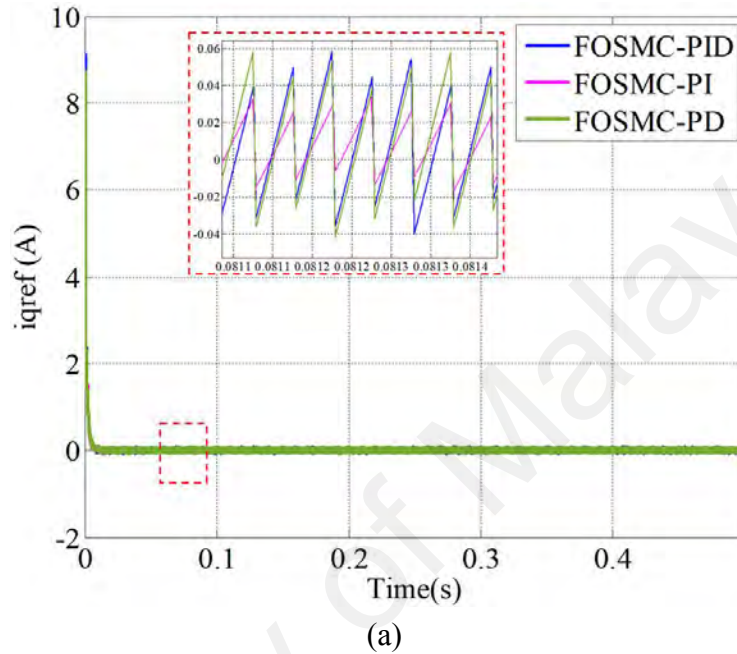
Figure 4.31: q-axis current reference value comparison between FOSMC-PID, FOSMC-PI and FOSMC-PD for speed reference of 250 rpm at no load condition (a) simulation (b) experiment

The actual q-axis current measurement in simulation and experiment is shown in Figure 4.32(a) and (b) respectively. Around 0.107A ripple is recorded in simulation, whereas in the experiment, a slightly higher ripple is obtained for all systems.
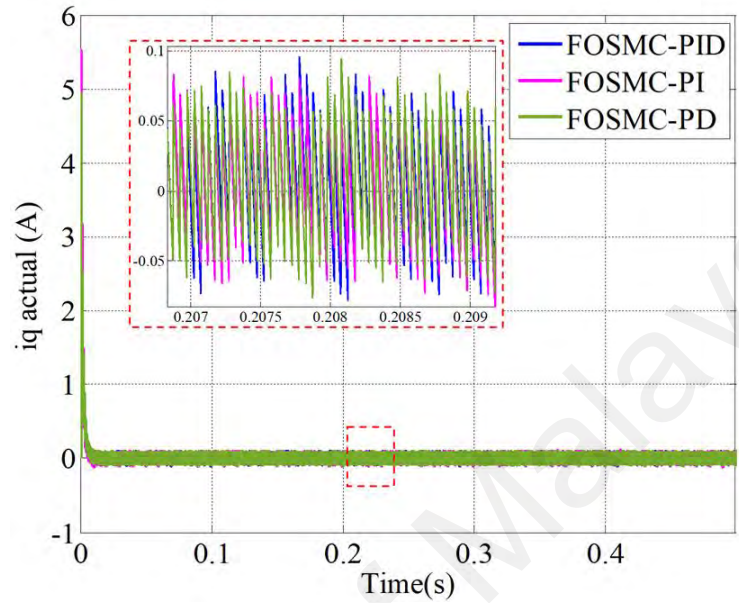
(a)
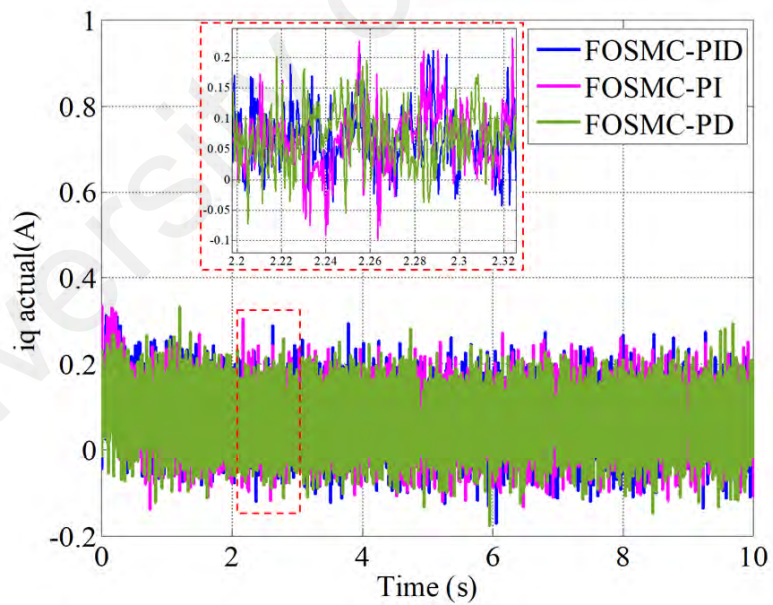
(b)

Figure 4.32: actual q-axis current comparison between FOSMC-PID, FOSMC-PI and FOSMC-PD for speed reference of 250 rpm at no load condition (a) simulation (b) experiment

4.4.2 Under load torque

A load torque of 0.5 Nm is then applied to all three systems in comparison to investigate their performances under load disturbance. In this case, the proposed FOSMC-PID shows its superiorities against other FOSMC types in terms of robustness. The speed of motor in the FOSMC-PID system is less affected by the external load applied namely with only 6.64% speed drop in simulation, compared to 7.64% for FOSMC-PI and 7.44% for FOSMC-PD, as shown in Figure 4.33(a). Experimental results in Figure 4.33(b) show a similar prominent advantage with only 16.88% speed drop for FOSMC-PID, which is around 20% less than the speed drop of FOSMC-PD. In addition, high steady state error and slow speed recovery issues of FOSMC-PD system are easily omitted using FOSMC-PID controller.
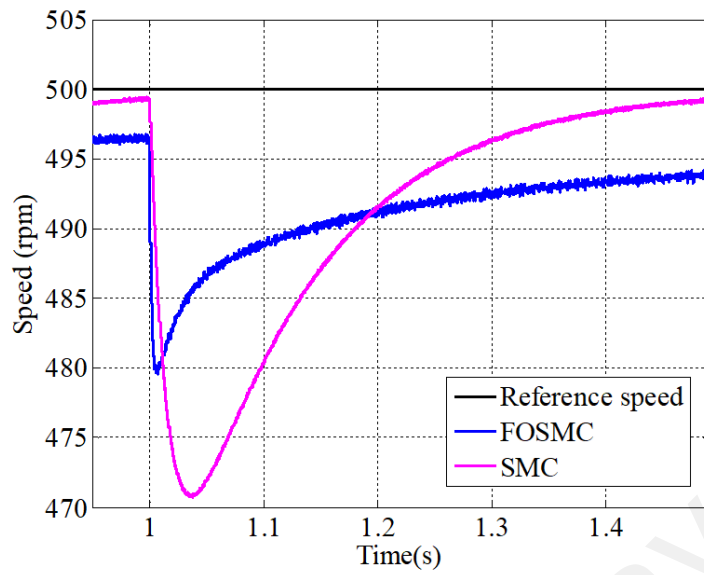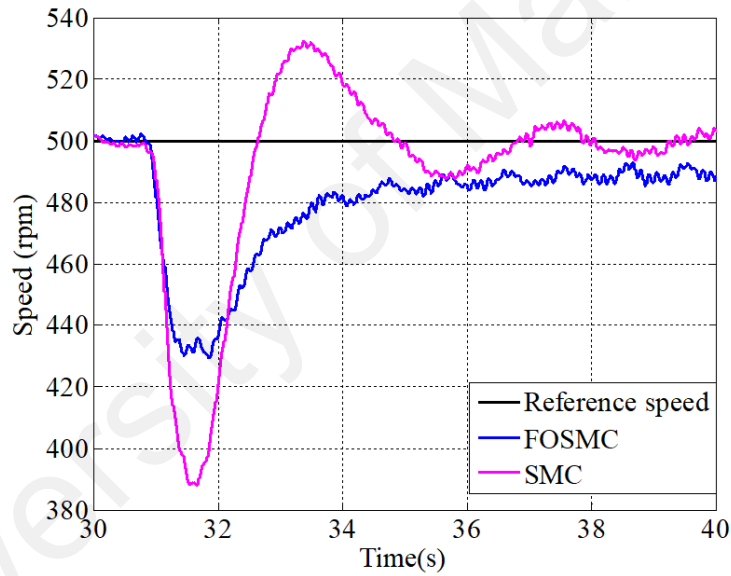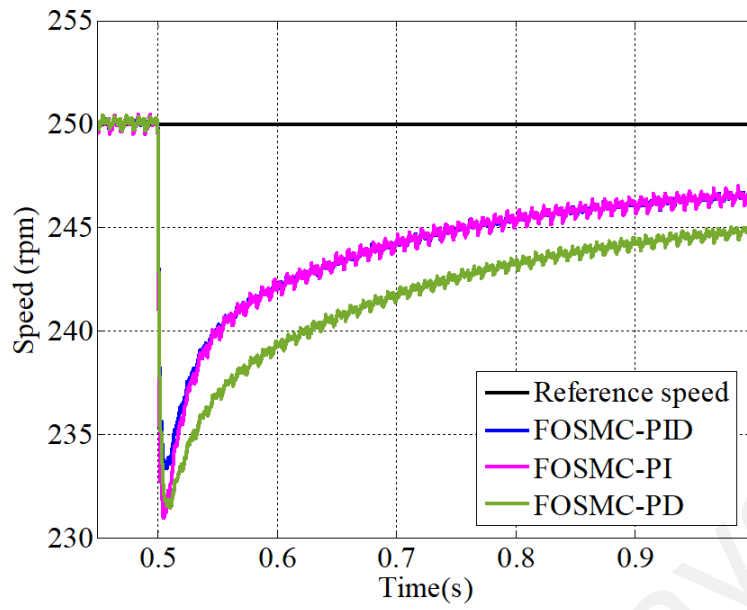
(a)
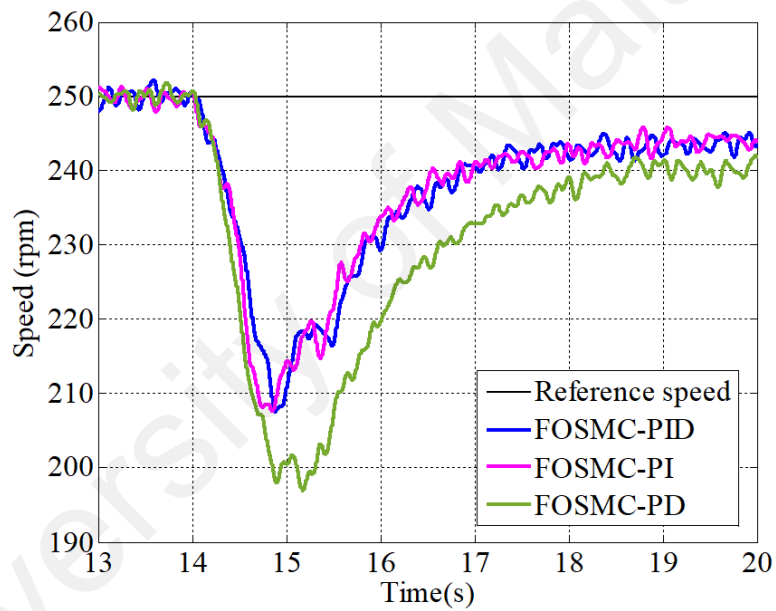
(b)

Figure 4.33: Speed response comparison between FOSMC-PID, FOSMC-PI and FOSMC-PD for speed reference of 250 rpm with applied load of 0.5 Nm (a) simulation (b) experiment

Table 4.7 compares the speed tracking properties of FOSMC-PID, FOSMC-PI and FOSMC-PD recorded in both simulation and experimental work, with and without applied external load disturbances.

Table 4.7: Comparison of speed tracking properties for the proposed FOSMC-PID with FOSMC-PI and FOSMC-PD with reference speed 250 rpm

Properties		FOSMC-PID (proposed)		FOSMC-PI (B. Zhang et al., 2012)		FOSMC-PD (Huang et al., 2012)	
		Simulation	Experiment	Simulation	Experiment	Simulation	Experiment
No load torque	Rise time (s)	0.006	0.81	0.005	0.8	0.008	1.15
	Settling time (s)	0.07	5.8	0.07	5.8	0.07	6.6
	Steady state error (%)	0.04	0	0.04	0	0.04	0
	Overshoot (%)	2.16	8.28	2.52	9.4	1.6	9.64
	Torque ripple (Nm)	0.1	0.013	0.1	0.017	0.1	0.015
	$i_{q,ref}$ ripple (A)	0.08	0.001	0.041	0.014	0.08	0.011
	$i_{q,actual}$ ripple (A)	0.107	0.17	0.107	0.17	0.107	0.19
Load torque 0.5 Nm	Speed drop (%)	6.64	16.88	7.64	16.92	7.44	21.2
	Steady state error (%)	1.32	2.88	1.32	2.88	2.04	4.4

As a conclusion, when both fractional integration and fractional differentiation terms are combined in sliding surface design, the resulting FOSMC balances the advantages and disadvantages of FOSMC-PI and FOSMC-PD individually. Hence, optimum performance during transient mode as well as under external load disturbances is guaranteed.

154

4.5 Effects of fractional order selection on the proposed FOSMC speed controller performance

The sliding surface design proposed in this research as shown in equation (3.15) consists of two fractional order terms namely fractional integration and fractional differentiation. Both terms are identified by the order assigned to them, which can hold any real values between 0 to 1. Previously presented results are executed using order of fractional order integration, α of 0.35 and order of fractional order differentiation, β of 0.3, as listed in Table 4.1. This section investigates changes in speed response that occur when values of α and β are manipulated.

4.5.1 Various order of fractional order differentiation, β

Initially, the order of fractional order differentiation, β is varied with fixed value of α at 0.5 (middle value between 0 and 1). 250 rpm of speed reference is given to the drive system. Simulation results in Figure 4.34(a) show that time taken for the motor to reach reference speed increases as β increases. On the contrary, speed transient overshoot reduces as β increases. Unfortunately, these relations cannot be clearly identified in experimental validation, as shown in Figure 4.34(b). In addition, a peculiar transient reverse motor rotation is recorded for $\beta > 0.5$.
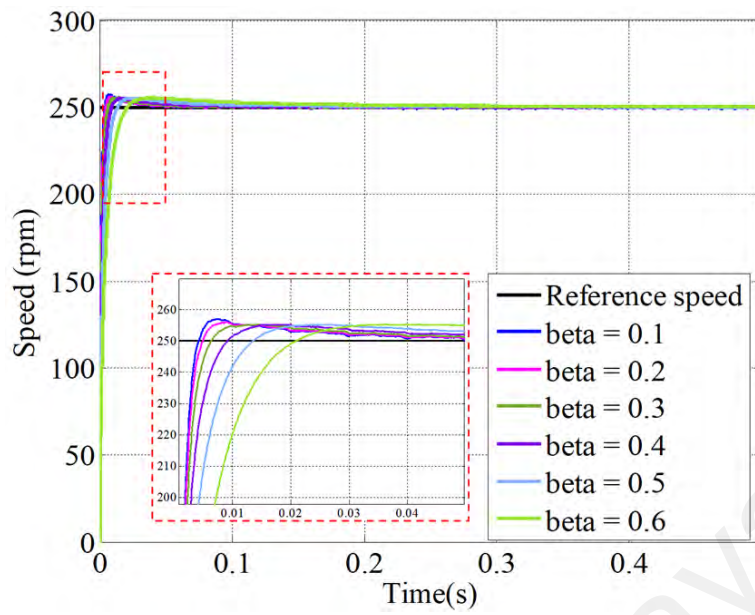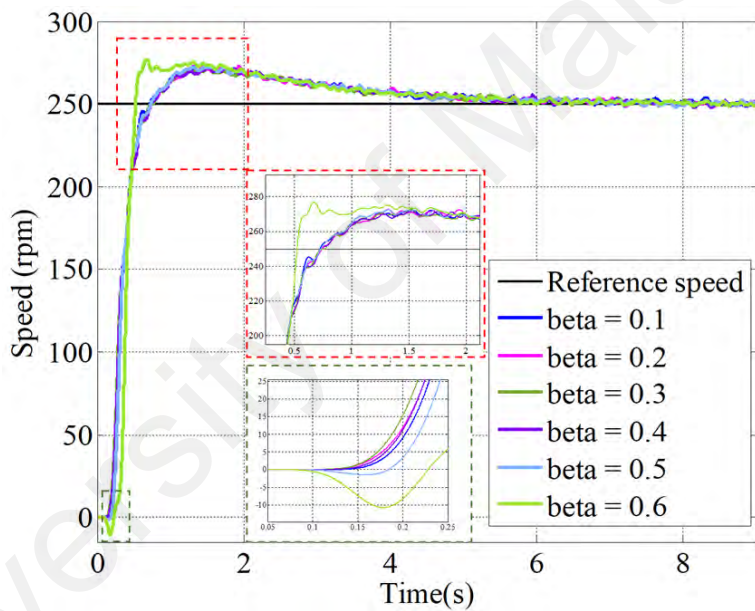
Figure 4.34: Speed response comparison of FOSMC with various order of fractional order differentiation, β at no load   (a) simulation (b) experiment

Speed tracking properties are then analysed when the system is burdened with load torque of 0.5Nm. Higher β values result in lower speed drop and lower speed ripple during simulation run, as indicated in Figure 4.35(a). On the other hand, although small differences can be identified from experimental results in Figure 4.35(b), relation between β values and speed drop or speed ripple cannot be concluded.
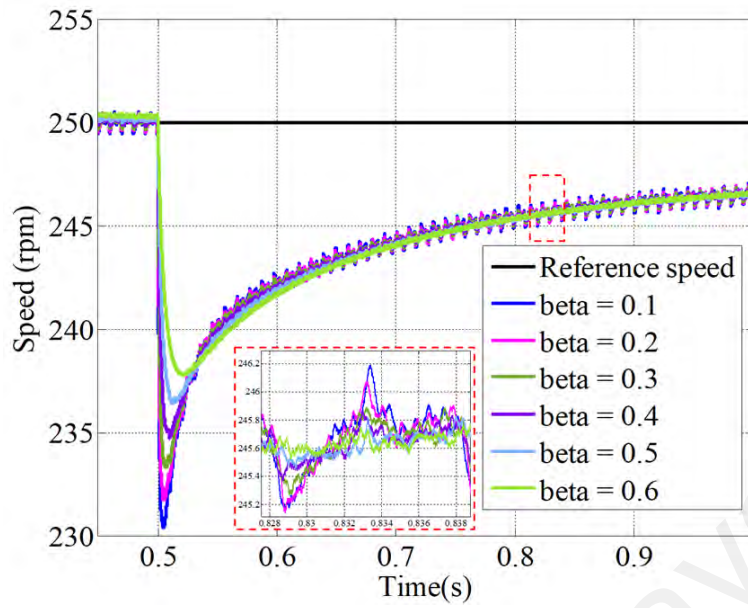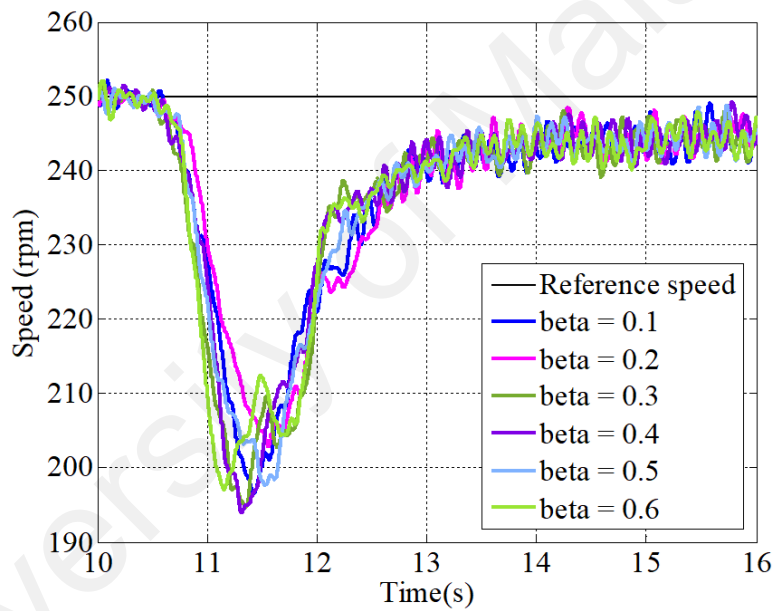
Figure 4.35: Speed response comparison of FOSMC with various order of fractional order differentiation, β with applied load of 0.5 Nm   (a) simulation (b) experiment

4.5.2   Various order of fractional order integration, α

Secondly, the order of fractional order integration, α is varied with a fixed value of β at 0.5 (middle value between 0 and 1). The same speed reference of 250 rpm is given to the drive system. Increasing α values causes an increment in rise time, as shown in simulation results in Figure 4.36(a). In the contrary, experimental results in Figure 4.36(b)

show that as α increases, rise time decreases. However, similar to the previous case, reverse motor rotation during transient mode is recorded for $\alpha > 0.4$. In terms of overshoot, the value increases for α between 0.1 and 0.4, then decreases for $\alpha > 0.4$ in simulation case. In the experimental case, gradual overshoot increment is experienced by the system as α increases.
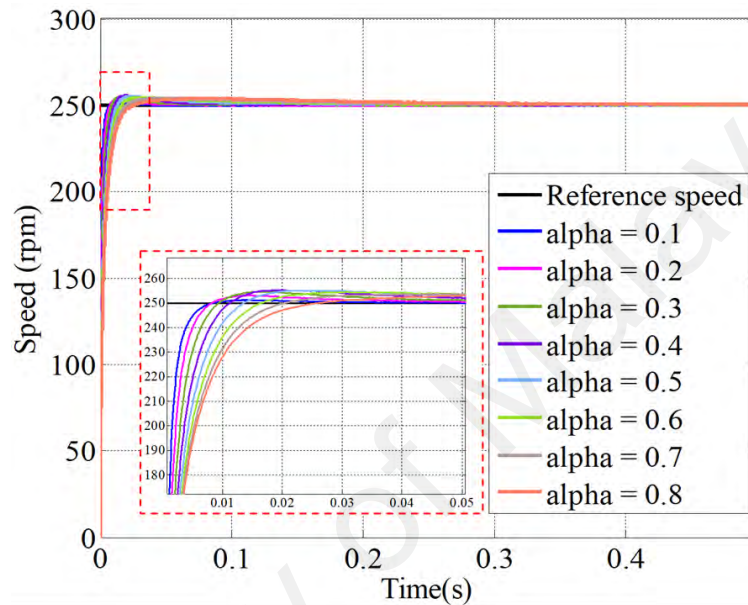
(a)
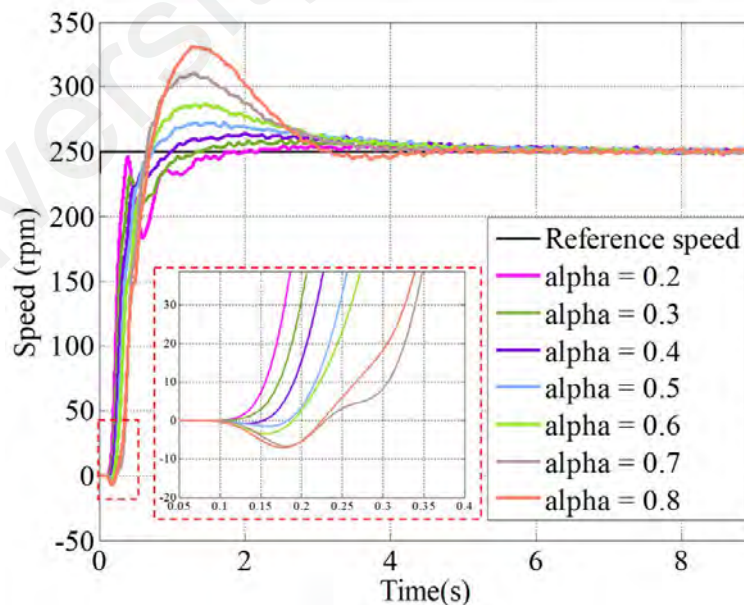
(b)

Figure 4.36: Speed response comparison of FOSMC with various order of fractional order integration, α at no load   (a) simulation (b) experiment

Under load torque of 0.5Nm, higher values of α causes higher speed drop in simulation, as shown in Figure 4.37(a). A similar trend is also recorded during the experiment. During steady state, systems with higher α values experience lower steady state speed error in both simulation and experimental run. In addition, experimental results in Figure 4.37(b) show that a significant speed oscillation occurs in steady state for $\alpha > 0.7$.
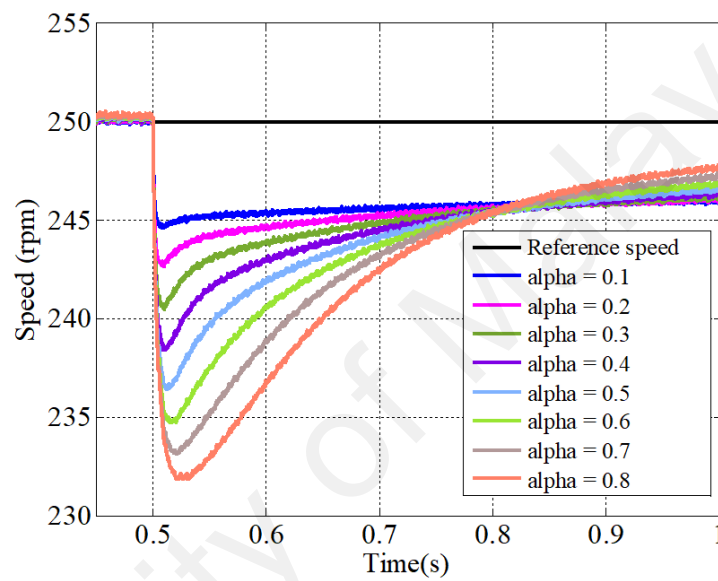
(a)
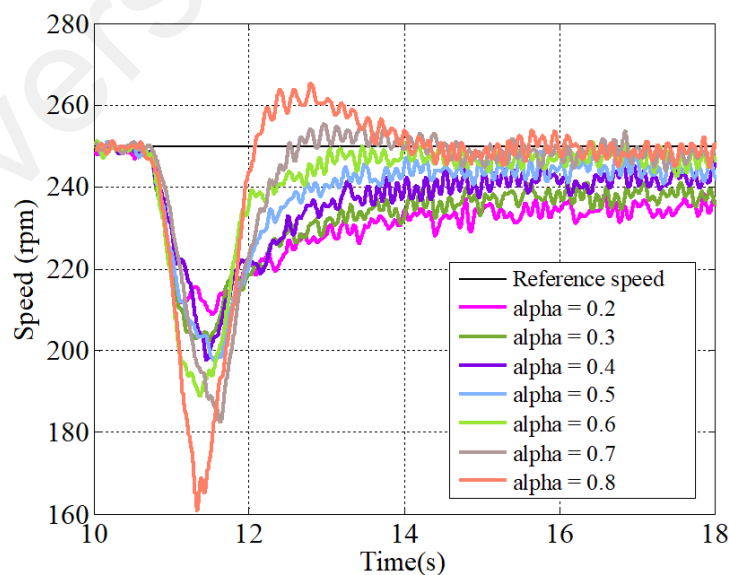
(b)

Figure 4.37: Speed response comparison of FOSMC with various order of fractional order integration, α with applied load of 0.5 Nm   (a) simulation (b) experiment

Variation of the order of fractional order integration, α and order of fractional order differentiation, β can affect the performance of the proposed FOSMC controller. Results presented in this section show that proper selection of both values i.e. with appropriate optimization algorithm can produce optimum speed tracking in all conditions e.g. transient, under external load disturbances and steady state.

4.6   Discussion

Experimental results presented in subsections 4.2 - 4.5 describe the performance of the proposed FOSMC as well as other controllers in comparison when applied to the developed closed-loop PMSM drive prototype in this work. Behaviour of all controllers are tested in a system under same parameter variations and external load disturbances pattern. However, apart from this fair comparison, it is also relevant to analyse the performance of the proposed method with respect to other methods in previous literature. Table 4.8 summarizes quantitative values of various PMSM sliding mode speed controller designs according to several important indicators in terms of tracking, disturbance rejection and chattering suppression properties.

From the presented table, it can be seen that composite sliding mode controllers with observer for disturbance compensation resulted in low overshoot and low speed drop, but do not guarantee low current ripple value. In cases where overshoot is reduced, speed ripple is compromised. The proposed controller resulted in a comparatively poor performance in terms of tracking properties. However, its current, torque and speed ripple values are low, compared to the other methods. Furthermore, the reference speed used in this work is low, which is supposed to result in higher ripple values compared to other works with higher speed references. In addition, in terms of speed ripple, the obtained result (1.08%) corresponds to 0.09Hz vibration frequency. This value falls in a good range

of acceptable Class I motor vibration according to ISO 10816 standard. These analyses show that the proposed FOSMC contributes significantly to chattering suppression of SMC. In addition, tracking and disturbance rejection properties can be further improved by combining the designed controller with a disturbance compensation mechanism.

Quantitative comparison as presented in Table 4.8 cannot directly conclude the performance of one controller compared to the others since different load conditions and reference values are given to the system. Furthermore, a few variables are not considered in the comparison such as PMSM type and rating as well as the control architecture. In addition, some indicator values cannot be extracted from previous literature. However, the presented summary can provide relevant orientation of future works resulting from this research findings.

Table 4.8: Performance comparison of various PMSM sliding mode speed controller designs

Reference	SMC design	Reference speed (rpm)	Overshoot	Load torque	Speed drop	Recovery time	Steady state error	i_q ripple	Torque ripple	Speed ripple
Xiaoguang et al. (2013)	Adaptive reaching law + Extended sliding mode observer	1000	7.5%	4 Nm	0.9%	0.08 s	2.5%	-	10%	-
Xudong Liu and Li (2018)	Speed and current in single loop + Disturbance observer	1000	1%	1.5 Nm	4.375%	1.5 s	0	0.5 A	-	-
Junejo et al. (2020)	Adaptive reaching law + NFTSM + ESMDO	1600	-	10 Nm	24.38%	0.4 s	-	0.75 A	-	5%
Shihua Li et al. (2011)	SMC + Extended state observer	1000	3.28%	2 Nm	11.1%	0.45 s	0	1.09 A	-	0.39%
Shihua et al. (2013)	Terminal SMC + Disturbance observer	1500	0.67%	2.4 Nm	1.34%	0.2 s	0	0.29 A	-	0.67%
W. Xu et al. (2019)	Terminal SMC + Extended state observer	1000	5%	5 Nm	2.5%	0.1 s	0	0.7 A	-	7.5%
En Lu et al. (2019)	SMC + Second-order non-singular terminal sliding mode observer	150	3.33%	400 Nm	9.33%	0.8 s	2.22%	1.25 A	3.75%	2%
Y. Wang et al. (2019)	Integral SMC + Novel reaching law + Extended state observer	1000	0	1.27 Nm	7.14%	0.06 s	0	-	-	8.3%
Proposed controller in this work	Fractional order SMC	500	8.18%	0.5 Nm	9.36%	3.36 s	0.12%	0.34 A	3.88%	1.08%

162

4.7 Summary

Evaluation of the proposed FOSMC controller through MATLAB/Simulink simulation and experimental validation using the PMSM closed-loop drive system prototype is presented in this chapter. Fast and accurate speed tracking is obtained in both no load and under load torque conditions, regardless of speed reference given to the system. Compared to conventional integer order SMC, SMC with fractional order sliding surface design does not only improve speed tracking properties during the transient, but also is proven to increase the system's robustness to reject external load disturbances. In addition, presented current, torque and speed ripples results prove the ability of the proposed speed controller to reduce SMC's chattering effects. Within its own fractional order SMC group, the proposed FOSMC with PID sliding surface has shown its advantages in balancing the individual strength and weaknesses of FOSMC-PI and FOSMC-PD. The proposed FOSMC reduces overshoot contributed by the integral portion and at the same time reduces steady state error contributed by the differential portion. The combination of PID also improves speed loss when the load torque is applied, compared to speed loss of the FOSMC-PI and FOSMC-PD individually. Hence, optimum performance during transient mode as well as under external load disturbances is guaranteed. Then, results are presented to show how additional variables of fractional calculus incorporated in the SMC design provides an extra degree of freedom for the SMC. Proper selection of these variables can further contribute to obtain optimum speed tracking, disturbance rejection and chattering reduction abilities. Finally, the last section analyses the findings of this research with respect to the performance of the other control methods extracted from previous literature.

CHAPTER 5: CONCLUSION AND FUTURE WORKS

Permanent magnet synchronous motors are widely used in industries and slowly replacing induction motors due to their advantages especially in terms of efficiency, compactness and maintenance. One of the research areas of PMSMs focuses on speed controller designs to enhance energy saving as well as to obtain precise tracking for high performance application, regardless of speed command and load disturbances. The sliding mode speed controller of PMSM has been widely used due to its robustness, high accuracy and simplicity. However, the high frequency switching properties of SMC causes chattering phenomenon to the system. Chattering can affect the system in terms of reducing control accuracy, resulting in high heat losses in electrical power circuits, high wear of moving mechanical parts and unwanted vibrations in the rotor movement.

A fractional order sliding mode speed control of PMSM has been proposed in this research to overcome the above-stated problem. The FOSMC has been designed by incorporating fractional calculus into SMC. This speed control provides a q-axis reference current for the PI current controller in the inner loop. The outputs of the current controllers construct the reference voltage for switching signal generation of PWM, which will be fed to the inverter. The inverter output runs the motor where the speed is regulated to the given command speed.

The proposed fractional order sliding mode speed controller is designed with a sliding surface that consists of both fractional differentiation and integration. Fractional order term provides an extra degree of freedom for the SMC which hypothetically not only can improve its robustness and accuracy, but also can contribute to chattering reduction with slower energy transfer properties of fractional calculus. The stability of the designed controller is then analysed using Lyapunov stability theorem. Performance

evaluation of the proposed control system is executed by simulation in MATLAB/Simulink environment. Then, a closed-loop PMSM drive prototype is developed to run experimental verification of the control system.

Simulation and experimental results show that the proposed FOSMC speed controller performs as a robust and fast anti-disturbance controller to regulate the speed of a PMSM. With the proposed controller, the PMSM managed to reach the command speed from a standstill with a little overshoot. When load torque is applied, motor speed settles back to the command speed with negligible steady state error after a small speed drop. Good speed tracking is also obtained for all tested range of speed reference.

Relevant performance comparison is also executed in this work. The proposed FOSMC shows remarkable performance in terms of transient response and anti-disturbance properties compared to conventional integer order SMC. Chattering suppression ability of SMC with fractional order sliding surface is proven by the presented results indicating lower current, torque and speed ripples and/or oscillations, compared to those in IOSMC system. On top of that, a comparison is made between the proposed FOSMC, which has a PID type sliding surface, with other controllers in its own FOSMC group. The proposed controller has shown its advantages by balancing the individual strength and weaknesses of FOSMC-PI and FOSMC-PD in speed tracking, robustness against external load disturbances and chattering reduction ability.

Finally, simulation and experiment are executed where the order of fractional integration and order of fractional differentiation are changed within their allowable range. Comparison of transient response, anti-disturbance and steady state properties show that the fractional order terms add an extra degree of freedom, which allows further optimization of the controller's speed tracking performance.

This research provides valuable insight of fractional calculus incorporation for enhancement of PMSM sliding mode speed controller. The proposed controller has a good potential for application in high performance PMSM systems in industries that require fast response, precise tracking, small overshoot, suppressed chattering effect and strong disturbance rejection ability. In addition, the improved control method can significantly contribute to energy saving in permanent magnet machines. With the increasing trend of PMSM usage, development of this efficient controller can be very influential to facilitate sustainability initiatives in industrial sector. Furthermore, this proposed method can adjust the PMSM system's dynamics by modifying the behaviour of the control law with modification in the sliding surface design itself. Hence, compared to other SMC enhancement methods, the proposed method does not require complicated extension in the control structure and still maintains the remarkable property of SMC, namely its design simplicity.

As future work, the author would like to suggest implementation of the proposed FOSMC with disturbance compensation mechanism to further improve the tracking and disturbance rejection properties of the controller. In addition, optimization algorithm can be applied to systematically determine the values of fractional integration and fractional differentiation orders such as using particle swarm optimization (PSO) algorithm or genetic algorithm (GA). Finally, the performance of the proposed controller can be further validated in a sensorless application of PMSM.

References

Abu-Rub, H., Iqbal, A., & Guzinski, J. (2012). *High Performance Control of AC Drives with Matlab/Simulink Models.* Wiley.

Al-Ghanimi, A., Zheng, J., & Man, Z. (2015). Robust and fast non-singular terminal sliding mode control for piezoelectric actuators. *IET Control Theory & Applications, 9*(18), 2678-2687.

Azar, A. T., Radwan, A. G., & Vaidyanathan, S. (2018). *Mathematical Techniques of Fractional Order Systems.* Elsevier Science.

Bao-Lin, Z., Qing-Long, H., Xian-Ming, Z., & Xinghuo, Y. (2014). Sliding Mode Control With Mixed Current and Delayed States for Offshore Steel Jacket Platforms. *IEEE Transactions on Control Systems Technology, 22*(5), 1769-1783.

Bartolini, G., Ferrara, A., Levant, A., & Usai, E. (1999). On second order sliding mode controllers. In K. D. Young & Ü. Özgüner (Eds.), *Variable structure systems, sliding mode and nonlinear control* (329-350). London: Springer London.

Bartolini, G., Pisano, A., Punta, E., & Usai, E. (2003). A survey of applications of second-order sliding mode control to mechanical systems. *International Journal of Control, 76*(9), 875-892.

Bartolini, G., Pisano, A., & Usai, E. (2002). Second-order sliding-mode control of container cranes. *Automatica, 38*(10), 1783-1790.

Beltran, B., Benbouzid, M. E. H., & Ahmed-Ali, T. (2012). Second-Order Sliding Mode Control of a Doubly Fed Induction Generator Driven Wind Turbine. *IEEE Transactions on Energy Conversion, 27*(2), 261-269.

Bhattacharya, S., Mascarella, D., Joós, G., Cyr, J., & Xu, J. (2016). A Dual Three-Level T-NPC Inverter for High-Power Traction Applications. *IEEE Journal of Emerging and Selected Topics in Power Electronics, 4*(2), 668-678.

Bitao, Z., & Youguo, P. (2010). *Velocity Control of Permanent Magnet Synchronous Motor Based on Second-Order Sliding-Mode Technology.* Paper presented at the International Conference on Digital Manufacturing and Automation (ICDMA).

Boiko, I., Fridman, L., Pisano, A., & Usai, E. (2007). Analysis of Chattering in Systems With Second-Order Sliding Modes. *IEEE Transactions on Automatic Control, 52*(11), 2085-2102.

Bounasla, N., & Hemsas, K. E. (2013). *Second order sliding mode control of a permanent magnet synchronous motor.* Paper presented at the 14th International Conference on Sciences and Techniques of Automatic Control and Computer Engineering (STA).

Cao, Y., & Chen, X. B. (2014). Disturbance-Observer-Based Sliding-Mode Control for a 3-DOF Nanopositioning Stage. *IEEE/ASME Transactions on Mechatronics, 19*(3), 924-931.

Capitan, C. (2009). *Torque Control in Field Weakening Mode.* Aalborg University, Denmark.

Castanos, F., & Fridman, L. (2006). Analysis and design of integral sliding manifolds for systems with unmatched perturbations. *IEEE Transactions on Automatic Control, 51*(5), 853-858.

Castillo-Zamora, J., Camarillo-Gómez, K. A., Pérez-Soto, G. I., & Rodríguez-Reséndiz, J. (2018). Comparison of PD, PID and Sliding-Mode Position Controllers for V–Tail Quadcopter Stability. *IEEE Access, 6*, 38086-38096.

Chen, K., Tang, R., Li, C., & Wei, P. (2018). Robust adaptive fractional-order observer for a class of fractional-order nonlinear systems with unknown parameters. *Nonlinear Dynamics, 94*(1), 415-427.

Chen, S.-Y., & Lee, C.-Y. (2017). Digital signal processor based intelligent fractional-order sliding-mode control for a linear voice coil actuator. *IET Control Theory & Applications, 11*(8), 1282-1292.

Chen, S. Y., & Lin, F. J. (2011). Robust Nonsingular Terminal Sliding-Mode Control for Nonlinear Magnetic Bearing System. *IEEE Transactions on Control Systems Technology, 19*(3), 636-643.

Chen, W. H., Yang, J., Guo, L., & Li, S. (2016). Disturbance-Observer-Based Control and Related Methods - An Overview. *IEEE Transactions on Industrial Electronics, 63*(2), 1083-1095.

Chiang, H. K., & Tseng, C. H. (2004). Integral variable structure controller with grey prediction for synchronous reluctance motor drive. *IEE Proceedings - Electric Power Applications, 151*(3), 349-358.

Chih-Lyang, H., Li-Jui, C., & Yuan-Sheng, Y. (2007). Network-Based Fuzzy Decentralized Sliding-Mode Control for Car-Like Mobile Robots. *IEEE Transactions on Industrial Electronics, 54*(1), 574-585.

Chopade, A. S., Khubalkar, S. W., Junghare, A. S., Aware, M. V., & Das, S. (2018). Design and implementation of digital fractional order PID controller using optimal pole-zero approximation method for magnetic levitation system. *IEEE/CAA Journal of Automatica Sinica, 5*(5), 977-989.

Choudhury, A., Pillay, P., & Williamson, S. S. (2014). Comparative Analysis Between Two-Level and Three-Level DC/AC Electric Vehicle Traction Inverters Using a Novel DC-Link Voltage Balancing Algorithm. *IEEE Journal of Emerging and Selected Topics in Power Electronics, 2*(3), 529-540.

Chuan-Kai, L. (2006). Nonsingular Terminal Sliding Mode Control of Robot Manipulators Using Fuzzy Wavelet Networks. *IEEE Transactions on Fuzzy Systems, 14*(6), 849-859.

Damiano, A., Gatto, G. L., Marongiu, I., & Pisano, A. (2004). Second-order sliding-mode control of DC drives. *IEEE Transactions on Industrial Electronics, 51*(2), 364-373.

Dasmahapatra, S., Sarkar, B. K., Saha, R., Chatterjee, A., Mookherjee, S., & Sanyal, D. (2015). Design of an Adaptive Fuzzy-Bias SMC and Validation for a Rugged Electrohydraulic System. *IEEE/ASME Transactions on Mechatronics, 20*(6), 2708-2715.

Davijani, N. Z., Jahanfarnia, G., & Abharian, A. E. (2017). Nonlinear Fractional Sliding Mode Controller Based on Reduced Order FNPK Model for Output Power Control of Nuclear Research Reactors. *IEEE Transactions on Nuclear Science, 64*(1), 713-723.

Delavari, H., Ghaderi, R., Ranjbar, A., & Momani, S. (2010). Fuzzy fractional order sliding mode controller for nonlinear systems. *Communications in Nonlinear Science and Numerical Simulation, 15*(4), 963-978.

Deng, Y., Wang, J., Li, H., Liu, J., & Tian, D. (2019). Adaptive sliding mode current control with sliding mode disturbance observer for PMSM drives. *ISA Transactions, 88*, 113-126.

Ebrahimi, B., Tafreshi, R., Mohammadpour, J., Franchek, M., Grigoriadis, K., & Masudi, H. (2014). Second-Order Sliding Mode Strategy for Air-Fuel Ratio Control of Lean-Burn SI Engines. *IEEE Transactions on Control Systems Technology, 22*(4), 1374-1384.

Efe, M. O. (2008). Fractional Fuzzy Adaptive Sliding-Mode Control of a 2-DOF Direct-Drive Robot Arm. *IEEE Transactions on Systems, Man, and Cybernetics, Part B: Cybernetics, 38*(6), 1561-1570.

Efe, M. O. (2011). Fractional Order Systems in Industrial Automation - A Survey. *IEEE Transactions on Industrial Informatics, 7*(4), 582-591.

Eker, İ. (2010). Second-order sliding mode control with experimental application. *ISA Transactions, 49*(3), 394-405.

El-Sousy, F. F. M. (2011). Robust wavelet-neural-network sliding-mode control system for permanent magnet synchronous motor drive. *IET Electric Power Applications, 5*(1), 113-132.

El-Sousy, F. F. M. (2013). Adaptive Dynamic Sliding-Mode Control System Using Recurrent RBFN for High-Performance Induction Motor Servo Drive. *IEEE Transactions on Industrial Informatics, 9*(4), 1922-1936.

Elmas, C., & Ustun, O. (2008). A hybrid controller for the speed control of a permanent magnet synchronous motor drive. *Control Engineering Practice, 16*(3), 260-270.

Elsayed, B. A., Hassan, M., & Mekhilef, S. (2013). Decoupled third-order fuzzy sliding model control for cart-inverted pendulum system. *Applied Mathematics & Information Sciences, 7*(1), 193-201.

Elsayed, B. A., Hassan, M. A., & Mekhilef, S. (2015). Fuzzy swinging-up with sliding mode control for third order cart-inverted pendulum system. *International Journal of Control, Automation and Systems, 13*(1), 238-248.

Energy, I. A. U. S. (2016). *International Energy Outlook*.

Errouissi, R., Ouhrouche, M., Wen-Hua, C., & Trzynadlowski, A. M. (2012). Robust Nonlinear Predictive Controller for Permanent-Magnet Synchronous Motors With an Optimized Cost Function. *IEEE Transactions on Industrial Electronics, 59*(7), 2849-2858.

Faa-Jeng, L., Chih-Kai, C., & Po-Kai, H. (2007). FPGA-Based Adaptive Backstepping Sliding-Mode Control for Linear Induction Motor Drive. *IEEE Transactions on Power Electronics, 22*(4), 1222-1231.

Faa-Jeng, L., & Po-Hung, S. (2006). Robust Fuzzy Neural Network Sliding-Mode Control for Two-Axis Motion Control System. *IEEE Transactions on Industrial Electronics, 53*(4), 1209-1225.

Fallaha, C. J., Saad, M., Kanaan, H. Y., & Al-Haddad, K. (2011). Sliding-Mode Robot Control With Exponential Reaching Law. *IEEE Transactions on Industrial Electronics, 58*(2), 600-610.

Feng, Y., Yu, X., & Man, Z. (2002). Non-singular terminal sliding mode control of rigid manipulators. *Automatica, 38*(12), 2159-2167.

Ferrara, A., & Incremona, G. P. (2015). Design of an Integral Suboptimal Second-Order Sliding Mode Controller for the Robust Motion Control of Robot Manipulators. *IEEE Transactions on Control Systems Technology, 23*(6), 2316-2325.

Garcia, X. d. T., Zigmund, B., Terlizzi, A. A., Pavlanin, R., & Salvatore, L. (2011). Comparison between FOC and DTC Strategies for Permanent Magnet Synchronous Motors. *Advances in Electrical and Electronic Engineering, 5*(1), 76-81.

Gi-Taek, K., & Lipo, T. A. (1996). VSI-PWM rectifier/inverter system with a reduced switch count. *IEEE Transactions on Industry Applications, 32*(6), 1331-1337.

Gou-Jen, W., Chuan-Tzueng, F., & Chang, K. J. (2001). Neural-network-based self-tuning PI controller for precise motion control of PMAC motors. *IEEE Transactions on Industrial Electronics, 48*(2), 408-415.

Gudey, S. K., & Gupta, R. (2016). Recursive fast terminal sliding mode control in voltage source inverter for a low-voltage microgrid system. *IET Generation, Transmission & Distribution, 10*(7), 1536-1543.

Haibo, L., Heping, W., & Junlei, S. (2019). Attitude control for QTR using exponential nonsingular terminal sliding mode control. *Journal of Systems Engineering and Electronics, 30*(1), 191-200.

Han Ho, C., & Jin-Woo, J. (2013). Discrete-Time Fuzzy Speed Regulator Design for PM Synchronous Motor. *IEEE Transactions on Industrial Electronics, 60*(2), 600-607.

Han Ho, C., Nga Thi-Thuy, V., & Jin-Woo, J. (2011). Digital Implementation of an Adaptive Speed Regulator for a PMSM. *IEEE Transactions on Power Electronics, 26*(1), 3-8.

Han, S. I., & Lee, J. M. (2015). Balancing and Velocity Control of a Unicycle Robot Based on the Dynamic Model. *IEEE Transactions on Industrial Electronics, 62*(1), 405-413.

Hardik Shahane, S. O., Prashik Khandekar, Zalendra Bhagat, Resham Tondare. (2018). Review of Different PWM Techniques. *International Journal of Engineering Research in Electrical and Electronic Engineering, 4*(3), 206-208.

Hsien, T. L., Sun, Y. Y., & Tsai, M. C. (1997). H∞ control for a sensorless permanent-magnet synchronous drive. *IEEE Proceedings on Electric Power Applications, 144*(3), 173-181.

Huang, J., Cui, L., Shi, X., Li, H., & Xiang, Z. (2014). *Composite integral sliding mode control for PMSM.* Paper presented at the 33rd Chinese Control Conference (CCC), Nanjing, China.

Huang, J., Li, H., Teng, F., & Liu, D. (2012). *Fractional order sliding mode controller for the speed control of a permanent magnet synchronous motor.* Paper presented at the 24th Chinese Control and Decision Conference (CCDC).

Huixian, L., & Shihua, L. (2012). Speed Control for PMSM Servo System Using Predictive Functional Control and Extended State Observer. *IEEE Transactions on Industrial Electronics, 59*(2), 1171-1183.

Hung, J. Y., Gao, W., & Hung, J. C. (1993). Variable structure control: a survey. *IEEE Transactions on Industrial Electronics, 40*(1), 2-22.

Jafarov, E. M., Parlakci, M. N. A., & Istefanopulos, Y. (2005). A new variable structure PID-controller design for robot manipulators. *IEEE Transactions on Control Systems Technology, 13*(1), 122-130.

Jeng-Dao, L., Suiyang, K., & Zhi-Bin, W. (2013). DSP-Based Sliding-Mode Control for Electromagnetic-Levitation Precise-Position System. *IEEE Transactions on Industrial Informatics, 9*(2), 817-827.

Jian-Bo, C., & Bing-Gang, C. (2009). Fuzzy-Logic-Based Sliding-Mode Controller Design for Position-Sensorless Electric Vehicle. *IEEE Transactions on Power Electronics, 24*(10), 2368-2378.

Jingqing, H. (1995). The "Extended State Observer" of a Class of Uncertain Systems. *Control and Decision, 10*(1), 85-88.

Junejo, A. K., Xu, W., Mu, C., Ismail, M. M., & Liu, Y. (2020). Adaptive Speed Control of PMSM Drive System Based a New Sliding-Mode Reaching Law. *IEEE Transactions on Power Electronics, 35*(11), 12110-12121.

Kaynak, O., Erbatur, K., & Ertugnrl, M. (2001). The fusion of computationally intelligent methodologies and sliding-mode control - a survey. *IEEE Transactions on Industrial Electronics, 48*(1), 4-17.

Ke, Z., Xiao-guang, Z., Li, S., & Chang, C. (2011). *Sliding mode control of high-speed PMSM based on precision linearization control.* Paper presented at the International Conference on Electrical Machines and Systems (ICEMS).

Khan, M. K., & Spurgeon, S. K. (2006). Robust MIMO water level control in interconnected twin-tanks using second order sliding mode control. *Control Engineering Practice, 14*(4), 375-386.

Kommuri, S. K., Rath, J. J., Veluvolu, K. C., Defoort, M., & Soh, Y. C. (2015). Decoupled current control and sensor fault detection with second-order sliding mode for induction motor. *IET Control Theory & Applications, 9*(4), 608-617.

Komurcugil, H. (2011). *Fast terminal sliding mode control for single-phase UPS inverters.* Paper presented at the IEEE International Symposium on Industrial Electronics.

Krishnan, R. (2001). *Electric Motor Drives : Modeling, Analysis and Control.* Upper Saddle River, NJ: Prentice Hall.

Kuo, C.-F. J., Hsu, C.-H., & Tsai, C.-C. (2007). Control of a permanent magnet synchronous motor with a fuzzy sliding-mode controller. *The International Journal of Advanced Manufacturing Technology, 32*(7), 757-763.

Ladaci, S., & Charef, A. (2006). On Fractional Adaptive Control. *Nonlinear Dynamics, 43*(4), 365-378.

Laghrouche, S., Plestan, F., Glumineau, A., & Boisliveau, R. (2003). *Robust second order sliding mode control for a permanent magnet synchronous motor.* Paper presented at the American Control Conference.

Lanusse, P., Oustaloup, A., & Sabatier, J. (2014). *Robust factional order PID controllers: The first generation CRONE CSD approach.* Paper presented at the International Conference on Fractional Differentiation and Its Applications (ICFDA), Catania.

Leu, V. Q., Choi, H. H., & Jung, J. (2012). Fuzzy Sliding Mode Speed Controller for PM Synchronous Motors With a Load Torque Observer. *IEEE Transactions on Power Electronics, 27*(3), 1530-1539.

Levant, A. (1993). Sliding order and sliding accuracy in sliding mode control. *International Journal of Control, 58*(6), 1247-1263.

Levant, A. (2007). Principles of 2-sliding mode design. *Automatica, 43*(4), 576-586.

Levant, A., & Fridman, L. (2004). Robustness issues of 2-sliding mode control. In *Control, Robotics & Sensors. Variable Structure Systems: from principles to implementation,* 131-156.

Levine, W. S. (2010). *The Control Systems Handbook.* (Second ed.): CRC Press.

Li, M., Wang, F., & Gao, F. (2001). PID-based sliding mode controller for nonlinear processes. *Industrial and Engineering Chemistry Research, 40*(12), 2660-2667.

Li, W., Xuan, S., Gao, Q., & Luo, L. (2019). Investigation of a Four-Switch Four-Leg Inverter: Modulation, Control, and Application to an IPMSM Drive. *IEEE Transactions on Power Electronics, 34*(6), 5655-5666.

Liang, Y. W., Ting, L. W., & Lin, L. G. (2012). Study of Reliable Control Via an Integral-Type Sliding Mode Control Scheme. *IEEE Transactions on Industrial Electronics, 59*(8), 3062-3068.

Lin, F. J., Hung, Y. C., & Ruan, K. C. (2014). An Intelligent Second-Order Sliding-Mode Control for an Electric Power Steering System Using a Wavelet Fuzzy Neural Network. *IEEE Transactions on Fuzzy Systems, 22*(6), 1598-1611.

Ling, R., Maksimovic, D., & Leyva, R. (2016). Second-Order Sliding-Mode Controlled Synchronous Buck DC-DC Converter. *IEEE Transactions on Power Electronics, 31*(3), 2539-2549.

Liu, P., & Liu, H. P. (2012). Permanent-magnet synchronous motor drive system for electric vehicles using bidirectional z-source inverter. *IET Electrical Systems in Transportation, 2*(4), 178-185.

Liu, X., & Li, K. (2018). A novel sliding mode single-loop speed control method based on disturbance observer for permanent magnet synchronous motor drives. *Advances in Mechanical Engineering, 10*(12), 1-10.

Liu, X., Yu, H., Yu, J., & Zhao, L. (2018). Combined Speed and Current Terminal Sliding Mode Control With Nonlinear Disturbance Observer for PMSM Drive. *IEEE Access, 6*, 29594-29601.

Lu, E., Li, W., Yang, X., & Liu, Y. (2019). Anti-disturbance speed control of low-speed high-torque PMSM based on second-order non-singular terminal sliding mode load observer. *ISA Transactions, 88*, 142-152.

Lu, E., Li, W., Yang, X., & Xu, S. (2017). Composite Sliding Mode Control of a Permanent Magnet Direct-Driven System For a Mining Scraper Conveyor. *IEEE Access, 5*, 22399-22408.

Luo, Y., Chen, Y., Ahn, H.-S., & Pi, Y. (2010). Fractional order robust control for cogging effect compensation in PMSM position servo systems: Stability analysis and experiments. *Control Engineering Practice, 18*(9), 1022-1036.

Luo, Y., Chen, Y. Q., Ahn, H. S., & Pi, Y. G. (2012). Fractional Order Periodic Adaptive Learning Compensation for State-Dependent Periodic Disturbance. *IEEE Transactions on Control Systems Technology, 20*(2), 465-472.

Maddahi, A., Sepehri, N., & Kinsner, W. (2019). Fractional-Order Control of Hydraulically Powered Actuators: Controller Design and Experimental Validation. *IEEE/ASME Transactions on Mechatronics, 24*(2), 796-807.

Maleki, N., Pahlavani, M. R. A., & Soltani, I. (2015). A Detailed Comparison Between FOC and DTC Methods of a Permanent Magnet Synchronous Motor Drive. *Journal of Electrical and Electronic Engineering, 3*(2), 92-100.

Man, Z., & Xing Huo, Y. (1997). Terminal sliding mode control of MIMO linear systems. *IEEE Transactions on Circuits and Systems I: Fundamental Theory and Applications, 44*(11), 1065-1070.

Mathworks. (2019). Interior PMSM.

Matignon, D. (1996). Stability results for fractional differential equations with applications to control processing. *IEEE-SMC Computational Engineering in Systems Applications, 2*, 963–968.

Matraji, I., Laghrouche, S., Jemei, S., & Wack, M. (2013). Robust control of the PEM fuel cell air-feed system via sub-optimal second order sliding mode. *Applied Energy, 104*, 945-957.

Mobayen, S. (2015). Fast terminal sliding mode tracking of non-holonomic systems with exponential decay rate. *IET Control Theory & Applications, 9*(8), 1294-1301.

Mohanty, A., Patra, S., & Ray, P. K. (2016). Robust fuzzy-sliding mode based UPFC controller for transient stability analysis in autonomous wind-diesel-PV hybrid system. *IET Generation, Transmission & Distribution, 10*(5), 1248-1257.

Mu, C., & He, H. (2018). Dynamic Behavior of Terminal Sliding Mode Control. *IEEE Transactions on Industrial Electronics, 65*(4), 3480-3490.

Mu, C., Sun, C., & Xu, W. (2015). Fast sliding mode control on air-breathing hypersonic vehicles with transient response analysis. *Proceedings of the Institution of Mechanical Engineers, Part I: Journal of Systems and Control Engineering, 230*(1), 23-34.

Mu, C., Xu, W., & Sun, C. (2016). On Switching Manifold Design for Terminal Sliding Mode Control. *Journal of the Franklin Institute, 353*(7), 1553-1572.

Mu, C., Zong, Q., Tian, B., & Xu, W. (2015). Continuous sliding mode controller with disturbance observer for hypersonic vehicles. *IEEE/CAA Journal of Automatica Sinica, 2*(1), 45-55.

Mujumdar, A., Tamhane, B., & Kurode, S. (2015). Observer-Based Sliding Mode Control for a Class of Noncommensurate Fractional-Order Systems. *IEEE/ASME Transactions on Mechatronics, 20*(5), 2504-2512.

Nguyen, A. T., Basit, B. A., Choi, H. H., & Jung, J. (2020). Disturbance Attenuation for Surface-Mounted PMSM Drives Using Nonlinear Disturbance Observer-Based Sliding Mode Control. *IEEE Access, 8*, 86345-86356.

Ohnishi, K. (1987). A new servo method in mechatronics. *Transactions of Japanese Society of Electrical Engineering, 107*, 83-86.

Oustaloup, A. (1991). *La Commande CRONE: Commande Robuste D'ordre Non Entire, Herme's.* Paris, France: Hermes Science Publications.

Oustaloup, A., Melchior, P., Lanusse, P., Cois, O., & Dancla, F. (2000). *The CRONE toolbox for Matlab.* Paper presented at the IEEE International Symposium on Computer-Aided Control System Design (CACSD).

Pan, H., & Xia, L. Z. (2008). Efficient Object Recognition Using Boundary Representation and Wavelet Neural Network. *IEEE Transactions on Neural Networks, 19*(12), 2132-2149.

Petráš, I. (2011). *Fractional-Order Nonlinear Systems: Modeling, Analysis and Simulation.* Springer Berlin Heidelberg.

Pillay, P., & Krishnan, R. (1989). Modeling, simulation, and analysis of permanent-magnet motor drives. I. The permanent-magnet synchronous motor drive. *IEEE Transactions on Industry Applications, 25*(2), 265-273.

Pisano, A., Davila, A., Fridman, L., & Usai, E. (2008). Cascade Control of PM DC Drives Via Second-Order Sliding-Mode Technique. *IEEE Transactions on Industrial Electronics, 55*(11), 3846-3854.

Podlubny, I. (1999). *Fractional Differential Equations.* San Diego: Academic Press.

Podlubny, I. (2002). Geometric and Physical Interpretation of Fractional Integration and Fractional Differentiation. . *Fractional Calculus and Applied Analysis, 5*(4), 367-386.

Pundir Avdesh, S., & Singh, K. (2019). Chattering Free Sliding Mode Control with Observer Based Adaptive Radial Basis Function Neural Network for Temperature Tracking in a Fixed Bed Reactor. *International Journal of Chemical Reactor Engineering, 17*(10).

Pupadubsin, R., Chayopitak, N., Taylor, D. G., Nulek, N., Kachapornkul, S., Jitkreeyarn, P., Somsiri, P., & Tungpimolrut, K. (2012). Adaptive Integral Sliding-Mode Position Control of a Coupled-Phase Linear Variable Reluctance Motor for High-Precision Applications. *IEEE Transactions on Industry Applications, 48*(4), 1353-1363.

Purwadi, A., Hutahaean, R., Rizqiawan, A., Heryana, N., Heryanto, N. A., & Hindersah, H. (2015). *Comparison of maximum torque per Ampere and Constant Torque Angle control for 30kw Interior Interior Permanent Magnet Synchronous Motor.* Paper presented at the Proceedings of the Joint International Conference on Electric Vehicular Technology and Industrial, Mechanical, Electrical and Chemical Engineering (ICEVT & IMECE).

Qi, L., & Shi, H. (2013a). Adaptive position tracking control of permanent magnet synchronous motor based on RBF fast terminal sliding mode control. *Neurocomputing, 115*(0), 23-30.

Qi, L., & Shi, H. (2013b). A Novel Second Order Sliding Mode Control Algorithm for Velocity Control Permanent Magnet Synchronous Motor. In K. Li, S. Li, D. Li, & Q. Niu (Eds.), *Intelligent Computing for Sustainable Energy and Environment: Second International Conference* (213-220). Berlin, Heidelberg: Springer Berlin Heidelberg.

Rong-Jong, W., Kun-Lun, C., & Jeng-Dao, L. (2010). On-Line Supervisory Control Design for Maglev Transportation System via Total Sliding-Mode Approach and Particle Swarm Optimization. *IEEE Transactions on Automatic Control, 55*(7), 1544-1559.

Saghafinia, A., Wooi Ping, H., & Nasir Uddin, M. (2014). Fuzzy sliding mode control based on boundary layer theory for chattering-free and robust induction motor drive. *The International Journal of Advanced Manufacturing Technology, 71*(1), 57-68.

Salehtavazoei, M., & Tavakoli-Kakhki, M. (2014). Compensation by fractional-order phase-lead/lag compensators. *IET Control Theory & Applications, 8*(5), 319-329.

SangJoo, K., & Wan Kyun, C. (2003). A discrete-time design and analysis of perturbation observer for motion control applications. *IEEE Transactions on Control Systems Technology, 11*(3), 399-407.

Schweizer, M., & Kolar, J. W. (2013). Design and Implementation of a Highly Efficient Three-Level T-Type Converter for Low-Voltage Applications. *IEEE Transactions on Power Electronics, 28*(2), 899-907.

She, J. H., Fang, M., Ohyama, Y., Hashimoto, H., & Wu, M. (2008). Improving Disturbance-Rejection Performance Based on an Equivalent-Input-Disturbance Approach. *IEEE Transactions on Industrial Electronics, 55*(1), 380-389.

Sheng, L., Xiaojie, G., & Lanyong, Z. (2017). Robust Adaptive Backstepping Sliding Mode Control for Six-Phase Permanent Magnet Synchronous Motor Using Recurrent Wavelet Fuzzy Neural Network. *IEEE Access, 5*, 14502-14515.

Shihua, L., Mingming, Z., & Xinghuo, Y. (2013). Design and Implementation of Terminal Sliding Mode Control Method for PMSM Speed Regulation System. *IEEE Transactions on Industrial Informatics, 9*(4), 1879-1891.

Shihua, L., & Zhigang, L. (2009). Adaptive Speed Control for Permanent-Magnet Synchronous Motor System With Variations of Load Inertia. *IEEE Transactions on Industrial Electronics, 56*(8), 3050-3059.

Shihua Li, Kai Zong, & Huixian Liu. (2011). A composite speed controller based on a second-order model of permanent magnet synchronous motor system. *Transactions of the Institute of Measurement and Control, 33*(5), 522-541.

Shtessel, Y. B., Shkolnikov, I. A., & Levant, A. (2009). Guidance and Control of Missile Interceptor using Second-Order Sliding Modes. *IEEE Transactions on Aerospace and Electronic Systems, 45*(1), 110-124.

Shuo, Z. (2015). *Nonsingular fast terminal sliding mode control method and its application on permanent magnet synchronous motor.* Paper presented at the 34th Chinese Control Conference (CCC).

Sioud, H., Sharafin, A., Eliker, K., & Zhang, W. (2018). *Chebyshev neural network observer based RBF neural network terminal sliding mode controller for a class*

of nonlinear system. Paper presented at the 2018 Chinese Control And Decision Conference (CCDC).

Song, Q., & Jia, C. (2016). Robust Speed Controller Design for Permanent Magnet Synchronous Motor Drives Based on Sliding Mode Control. *Energy Procedia, 88*, 867-873.

Song, Z., Hou, Z., Jiang, C., & Wei, X. (2006). Sensorless control of surface permanent magnet synchronous motor using a new method. *Energy Conversion and Management, 47*(15), 2451-2460.

Spanier, K. B. O. J. (1974). *The Fractional Calculus.* New York: Academic Press.

Su, Y. X., Zheng, C. H., & Duan, B. Y. (2005). Automatic disturbances rejection controller for precise motion control of permanent-magnet synchronous motors. *IEEE Transactions on Industrial Electronics, 52*(3), 814-823.

Sun, G., Ma, Z., & Yu, J. (2018). Discrete-Time Fractional Order Terminal Sliding Mode Tracking Control for Linear Motor. *IEEE Transactions on Industrial Electronics, 65*(4), 3386-3394.

Sun, G., Wu, L., Kuang, Z., Ma, Z., & Liu, J. (2018). Practical tracking control of linear motor via fractional-order sliding mode. *Automatica, 94*, 221-235.

Susperregui, A., Martinez, M. I., Tapia, G., & Vechiu, I. (2013). Second-order sliding-mode controller design and tuning for grid synchronisation and power control of a wind turbine-driven doubly fed induction generator. *IET Renewable Power Generation, 7*(5), 540-551.

Syuan-Yi, C., & Faa-Jeng, L. (2011). Robust Nonsingular Terminal Sliding-Mode Control for Nonlinear Magnetic Bearing System. *IEEE Transactions on Control Systems Technology, 19*(3), 636-643.

Szewczyk, R., Zieliński, C., & Kaliczyńska, M. (2015). *Progress in Automation, Robotics and Measuring Techniques: Control and Automation.* Springer International Publishing.

Tepljakov, A., Petlenkov, E., & Belikov, J. (2011). *FOMCON: Fractional-order modeling and control toolbox for MATLAB.* Paper presented at the 18th International Conference Mixed Design of Integrated Circuits and Systems (MIXDES).

Uddin, M. N., Abido, M. A., & Rahman, M. A. (2004). Development and implementation of a hybrid intelligent controller for interior permanent-magnet synchronous motor drives. *IEEE Transactions on Industry Applications, 40*(1), 68-76.

Utkin, V. (1977). Variable structure systems with sliding modes. *IEEE Transactions on Automatic Control, 22*(2), 212-222.

Utkin, V., Guldner, J., & Shi, J. (1999). *Sliding mode control in electromechanical systems.* Boca Raton, Fla.: CRC Press.

Utkin, V., & Jingxin, S. (1996). *Integral sliding mode in systems operating under uncertainty conditions.* Paper presented at the 35th IEEE Conference on Decision and Control.

Utkin, V. I. (1993). Sliding mode control design principles and applications to electric drives. *IEEE Transactions on Industrial Electronics, 40*(1), 23-36.

Valerio, D., & Da Costa, J. S. (2004). *Ninteger: a non-integer control toolbox for MatLab.* Paper presented at the First IFAC Workshop on Fractional Differentiation and Applications, Bordeaux.

Van, M., Mavrovouniotis, M., & Ge, S. S. (2019). An Adaptive Backstepping Nonsingular Fast Terminal Sliding Mode Control for Robust Fault Tolerant Control of Robot Manipulators. *IEEE Transactions on Systems, Man, and Cybernetics: Systems, 49*(7), 1448-1458.

Veselic, B., Perunicic-Drazenovic, B., & Milosavljevic, C. (2010). Improved Discrete-Time Sliding-Mode Position Control Using Euler Velocity Estimation. *IEEE Transactions on Industrial Electronics, 57*(11), 3840-3847.

Vu, N. T.-T., Choi, H. H., & Jung, J.-W. (2012). Certainty equivalence adaptive speed controller for permanent magnet synchronous motor. *Mechatronics, 22*(6), 811-818.

Wai, R. J. (2001). Total sliding-mode controller for PM synchronous servo motor drive using recurrent fuzzy neural network. *IEEE Transactions on Industrial Electronics, 48*(5), 926-944.

Waide, P., & Brunner, C. U. (2011). *Energy-Efficiency Policy Opportunities for Electric Motor-Driven Systems*.

Wang, J., Li, S., Yang, J., Wu, B., & Li, Q. (2015). Extended state observer-based sliding mode control for PWM-based DC-DC buck power converter systems with mismatched disturbances. *IET Control Theory & Applications, 9*(4), 579-586.

Wang, Y., Feng, Y., Zhang, X., & Liang, J. (2019). A New Reaching Law for Anti-disturbance Sliding-mode Control of PMSM Speed Regulation System. *IEEE Transactions on Power Electronics, 35*(4), 4117 - 4126.

Wang, Z., Chen, J., Cheng, M., & Zheng, Y. (2015). Fault-Tolerant Control of Paralleled-Voltage-Source-Inverter-Fed PMSM Drives. *IEEE Transactions on Industrial Electronics, 62*(8), 4749-4760.

Wang, Z., Zheng, Y., Zou, Z., & Cheng, M. (2012). Position Sensorless Control of Interleaved CSI Fed PMSM Drive With Extended Kalman Filter. *IEEE Transactions on Magnetics, 48*(11), 3688-3691.

Wu, Y., Yu, X., & Man, Z. (1998). Terminal sliding mode control design for uncertain dynamic systems. *Systems & Control Letters, 34*(5), 281-287.

Xia, C., Wang, X., Li, S., & Chen, X. (2011). Improved integral sliding mode control methods for speed control of PMSM system. *International Journal of Innovative Computing, Information and Control, 7*(4), 1971-1982.

Xiaoguang, Z., Lizhi, S., Ke, Z., & Li, S. (2013). Nonlinear Speed Control for PMSM System Using Sliding-Mode Control and Disturbance Compensation Techniques. *IEEE Transactions on Power Electronics, 28*(3), 1358-1365.

Xinghuo, Y., & Kaynak, O. (2009). Sliding-Mode Control With Soft Computing: A Survey. *IEEE Transactions on Industrial Electronics, 56*(9), 3275-3285.

Xinghuo, Y., & Man, Z. (2002). Fast terminal sliding-mode control design for nonlinear dynamical systems. *IEEE Transactions on Circuits and Systems I: Fundamental Theory and Applications, 49*(2), 261-264.

Xu, S. S. D., Chen, C. C., & Wu, Z. L. (2015). Study of Nonsingular Fast Terminal Sliding-Mode Fault-Tolerant Control. *IEEE Transactions on Industrial Electronics, 62*(6), 3906-3913.

Xu, W., Jiang, Y., & Mu, C. (2016). Novel Composite Sliding Mode Control for PMSM Drive System Based on Disturbance Observer. *IEEE Transactions on Applied Superconductivity, 26*(7), 1-5.

Xu, W., Jiang, Y., Mu, C., & Yue, H. (2015). *Nonsingular terminal sliding mode control for the speed regulation of permanent magnet synchronous motor with parameter uncertainties.* Paper presented at the 41st Annual Conference of the IEEE Industrial Electronics Society (IECON).

Xu, W., Junejo, A. K., Liu, Y., & Islam, M. R. (2019). Improved Continuous Fast Terminal Sliding Mode Control with Extended State Observer for Speed Regulation of PMSM Drive System. *IEEE Transactions on Vehicular Technology, 68*(11), 10465 - 10476.

Yan, L., Ju-Beom, S., & Jang-myung, L. (2009). *PMSM speed controller using switching algorithm of PD and Sliding mode control.* Paper presented at the ICROS-SICE International Joint Conference, Fukuoka, Japan.

Yang Quan, C., Petras, I., & Dingyu, X. (2009). *Fractional order control - A tutorial.* Paper presented at the American Control Conference (ACC), St. Louis, Missouri, USA.

Yaonan, W., Xizheng, Z., Xiaofang, Y., & Guorong, L. (2011). Position-Sensorless Hybrid Sliding-Mode Control of Electric Vehicles With Brushless DC Motor. *IEEE Transactions on Vehicular Technology, 60*(2), 421-432.

Yin, X. X., Lin, Y. G., Li, W., Liu, H. W., & Gu, Y. J. (2015). Fuzzy-Logic Sliding-Mode Control Strategy for Extracting Maximum Wind Power. *IEEE Transactions on Energy Conversion, 30*(4), 1267-1278.

Yin, Y., Liu, J., Sánchez, J. A., Wu, L., Vazquez, S., Leon, J. I., & Franquelo, L. G. (2019). Observer-Based Adaptive Sliding Mode Control of NPC Converters: An

RBF Neural Network Approach. *IEEE Transactions on Power Electronics, 34*(4), 3831-3841.

Ying, L., Yang Quan, C., Hyo-Sung, A., & Youguo, P. (2009). *Fractional order periodic adaptive learning compensation for cogging effect in PMSM position servo system.* Paper presented at the American Control Conference (ACC), St. Louis, Missouri, USA.

Yu, X., Fu, Y., Li, P., & Zhang, Y. (2018). Fault-Tolerant Aircraft Control Based on Self-Constructing Fuzzy Neural Networks and Multivariable SMC Under Actuator Faults. *IEEE Transactions on Fuzzy Systems, 26*(4), 2324-2335.

Zadeh, L. A. (1965). Fuzzy sets. *Information and Control, 8*(3), 338-353.

Zaihidee, F. M., Mekhilef, S., & Mubin, M. (2019). Application of Fractional Order Sliding Mode Control for Speed Control of Permanent Magnet Synchronous Motor. *IEEE Access, 7,* 101765-101774.

Zaky, M. (2012). Adaptive and robust speed control of interior permanent magnet synchronous motor drives. *Electrical Engineering, 94*(1), 49-58.

Zhang, B., Pi, Y., & Luo, Y. (2012). Fractional order sliding-mode control based on parameters auto-tuning for velocity control of permanent magnet synchronous motor. *ISA Transactions, 51*(5), 649-656.

Zhang, J., Liu, X., Xia, Y., Zuo, Z., & Wang, Y. (2016). Disturbance Observer-Based Integral Sliding-Mode Control for Systems With Mismatched Disturbances. *IEEE Transactions on Industrial Electronics, 63*(11), 7040-7048.

Zhang, R., Dong, L., & Sun, C. (2014). Adaptive nonsingular terminal sliding mode control design for near space hypersonic vehicles. *IEEE/CAA Journal of Automatica Sinica, 1*(2), 155-161.

Zhang, X., Wang, Y., Liu, G., & Yuan, X. (2016). Robust Regenerative Charging Control Based on T-S Fuzzy Sliding-Mode Approach for Advanced Electric Vehicle. *IEEE Transactions on Transportation Electrification, 2*(1), 52-65.

Zhang, X., Zhao, K., & Sun, L. (2011). *A PMSM sliding mode control system based on a novel reaching law.* Paper presented at the International Conference on Electrical Machines and Systems (ICEMS).

Zhao, K., Yin, T., Zhang, C., He, J., Li, X., Chen, Y., Zhou, R., & Leng, A. (2019). Robust Model-Free Nonsingular Terminal Sliding Mode Control for PMSM Demagnetization Fault. *IEEE Access, 7,* 15737-15748.

Zhao, Y., & Dong, L. (2019). Robust current and speed control of a permanent magnet synchronous motor using SMC and ADRC. *Control Theory and Technology, 17*(2), 190-199.

Zhong, X., Shao, X., Li, X., Ma, Z., & Sun, G. (2018). Fractional Order Adaptive Sliding Mode Control for the Deployment of Space Tethered System With Input Limitation. *IEEE Access, 6,* 48958-48969.

Zhou, J., & Wang, Y. (2002). Adaptive backstepping speed controller design for a permanent magnet synchronous motor. *IEE Proceedings - Electric Power Applications, 149*(2), 165-172.

Zhou, Z., Zhang, B., & Mao, D. (2018). Robust Sliding Mode Control of PMSM Based on Rapid Nonlinear Tracking Differentiator and Disturbance Observer. *Sensors, 18*(4), 1031.

Zhu, C., Zeng, Z., & Zhao, R. (2017a). Comprehensive Analysis and Reduction of Torque Ripples in Three-Phase Four-Switch Inverter-Fed PMSM Drives Using Space Vector Pulse-Width Modulation. *IEEE Transactions on Power Electronics, 32*(7), 5411-5424.

Zhu, C., Zeng, Z., & Zhao, R. (2017b). Torque ripple elimination based on inverter voltage drop compensation for a three-phase four-switch inverter-fed PMSM drive under low speeds. *IET Power Electronics, 10*(12), 1430-1437.